Spectral Photoresponse Tuning and Enhancement in Organic Ultraviolet Photodetectors through Active Layer Optimization and Plasmonic Nanostructures

Monica R. Esopi

A dissertation

submitted in partial fulfillment of the

requirements for the degree of

Doctor of Philosophy

University of Washington

2019

Reading Committee:

Qiuming Yu, Chair

Samson A. Jenekhe

Vincent C. Holmberg

Program Authorized to Offer Degree:

Department of Chemical Engineering

University of Washington

Abstract

Spectral Photoresponse Tuning and Enhancement in Organic Ultraviolet Photodetectors through Active Layer Optimization and Plasmonic Nanostructures

Monica R. Esopi

Chair of the Supervisory Committee:
Professor Qiuming Yu
Department of Chemical Engineering

Ultraviolet photodetectors are important in a wide variety of applications including scientific measurement, environmental monitoring, imaging, and flame and missile detection. Organic active materials offer a low-cost, flexible, solution-processable alternative to inorganic materials. Strong, sensitive photoresponse with wavelength selectivity and tunability is highly desired, and can be achieved through material selection, active layer manipulation, and plasmonic nanostructure incorporation. In this work, 3D-finite-difference time domain (FDTD) electromagnetic simulations, transfer-matrix method (TMM) optical simulations, and experimental approaches were integrated to understand the relationship between physical parameters, underlying device physics, and photoresponse mechanisms to develop organic UV photodetectors with strong, sensitive, tunable photoresponse.

Conventional organic photodiodes with active layers composed of blends of wide bandgap polymers and fullerene derivatives or ZnO nanoparticles were used to achieve strong and narrowband UV photoresponse via the mechanisms of photomultiplication and charge collection narrowing (CCN). By reducing the content of [6,6]-phenyl-C_{71}-butyric acid methyl ester

($PC_{71}BM$) in a polymer poly(9,9-dioctylfluorene-alt-bithiophene) (F8T2) active layer, isolated $PC_{71}BM$ clusters were formed and trapped electrons near the device cathode, resulting in band bending and hole injection, thus enabling multiple holes to be collected per incident photon and achieving photomultiplication. A peak EQE of 5600%, under 360 nm illumination and -40 V bias, was achieved by devices utilizing a 100:4 w:w blend of F8T2:$PC_{71}BM$. Devices with active layers composed of poly[bis(4-phenyl)(2,4,6-trimethylphenyl)amine] (PTAA) and ZnO nanoparticles had photoresponse that could be tuned from broad and photomultiplicative to spectrally narrowband by using thin and thick active layers, respectively, via the CNN mechanism. A single EQE peak at 424 nm with a full-width at half-maximum of just 12 nm was demonstrated when a thick active layer was used. UV photoresponse was further tuned and enhanced by incorporating Al plasmonic nanostructure arrays, either as a transparent bottom electrode or a top electrode in conventional UV photodetectors. Al nanohole arrays (Al-NHAs) were incorporated into UV photodetectors as transparent electrodes and the resulting photoresponse spectra varied from having two peaks under reverse bias to a distinct, single peak under forward bias. This novel bias-dependent photoresponse switching was enabled by plasmonic enhancements to the electric field in the active layer, which acted as an additional forward bias in Al-NHA-based devices. Plasmonic Al nanostructures were also incorporated into the top device electrode in the form of a nanohemisphere array (NHSA) to engage the mechanisms of light scattering and electric field enhancement, which improve the strength and speed of photoresponse. This work sheds light on the improvement of UV photodetection through active layer optimization and plasmonic nanostructure incorporation, and opens up avenues to develop sensitive, spectrally selective photodetectors to meet the expanding photodetection needs of modern technology.

TABLE OF CONTENTS

LIST OF FIGURES

LIST OF TABLES

ACKNOWLEDGEMENTS

I must first extend a most emphatic thanks to my advisor, Prof. Qiuming Yu. I cannot adequately express how happy and grateful I am that I completed my PhD in her research group and under her guidance. Her technical knowledge and insight, scientific enthusiasm and curiosity, and general support and mentorship were essential components in the successes I have had throughout my graduate degree. The responsibilities and projects she assigned me, and her guidance through them, allowed me to grow as an engineer, researcher, and person, and I am ever grateful for her example, encouragement, and leadership.

I am also sincerely grateful to Professors Samson A. Jenekhe, Vincent C. Holmberg, and Lih Y. Lin for sharing their time and expertise by serving on my dissertation committee. The insights, feedback, and suggestions they provided were always unique and valuable, and I am immensely appreciative. I would like to doubly thank Prof. Jenekhe and Prof. Lin, and their research group members, for the use of several pieces of equipment that were essential to my research.

I would like to acknowledge financial support from the UW Department of Chemical Engineering, the UW Clean Energy Institute, the National Science Foundation, and the Defense Threat Reduction Agency. Additionally, I would like to acknowledge various facilities at the UW campus, including the Photonics Research Center, Molecular Analysis Facility, Bindra Lab, Washington Nanofabrication Facility, and Washington Clean Energy Testbeds, that provided access to and training on essential fabrication and characterization equipment.

I would next like to thank both past and present members of the Yu Research Group. The mentorship, comradery, and knowledge of each member has helped me to innovate and grow both technically and personally. I consider myself lucky to have completed my PhD alongside Dr. Beau Richardson, Dr. David Galvan, Gabriella Tosado, Erjin Zheng, Emerson Chen, Julie Blanchfield,

Yu-Han Ho, Vidit Parehk, Yi-Yu Lin, Xiaoyu Zhao, Beiying Zhou, Hao Dong, and Zhiyin Niu. I would also like to thank the undergraduate students who worked with me, aiding in my research and helping me to grow as a teacher and mentor, including Graham Henry, Max Calcagno, Dat Nguyen, Henry Armas-Amaya, and Aayush Mitra. I am also grateful to the Department of Chemical Engineering at UW for continually striving to create an inclusive and welcoming culture that all folks can thrive in. I am especially grateful to Prof. Elizabeth Nance for founding the Women in Chemical Engineering organization, which greatly enhanced my sense of community at UW and provided me with opportunities to build my soft skills, reflect on my past experiences, identify positive workplace cultures and make improvements wherever I can.

Finally, I would like to express my heartfelt thanks to my friends and family. To my husband, Jake, I cannot overstate the value of your constant and comprehensive support. You give me the strength and confidence to be and do exactly what I want and ensure that life is enjoyable and fulfilling along the way. I will never be able to thank you enough but I will always keep trying. I would like to thank my parents, whose examples and lifelong confidence in me made me believe that I really can be anything I want to be when I grow up. I will always be grateful to my sister, Mia, for convincing me at a young age that reading and being my weird self were the coolest things I could ever do, and to my brother, Steven, for being the best person I know and inspiring me to find and meet my full potential. I am grateful to my extended family and my in-laws for their enthusiastic support, and I am particularly grateful to the Mazzas for stepping up as my Seattle-family. I am also immensely grateful to all of my friends, from childhood, Penn State, and UW/Seattle, for creating a dynamic, fun, and supportive community around me. Lastly, I would like to thank my cat, Whiskey, for being a constant source of comfort, affection, and amusement, thus contributing significantly to my sanity and happiness throughout my graduate studies.

Chapter 1. INTRODUCTION

1.1 PHOTODETECTORS IN MODERN TECHNOLOGY

Optoelectronic devices are an essential component of modern technology. These devices, which convert between light and electricity, have enabled advances in industries including manufacturing, computing, imaging, telecommunications, automotive, and consumer products. LASERs and LEDs, which convert electrical energy into light, are used in fiber optic communications, lighting, displays, motion sensors, and consumer products.[1, 2] Devices that convert light into electricity, like solar cells and photodetectors, are equally important. While solar cells are primarily used for power generation, photodetectors are utilized in a wide variety of applications, some of which are demonstrated in Fig. 1-1.

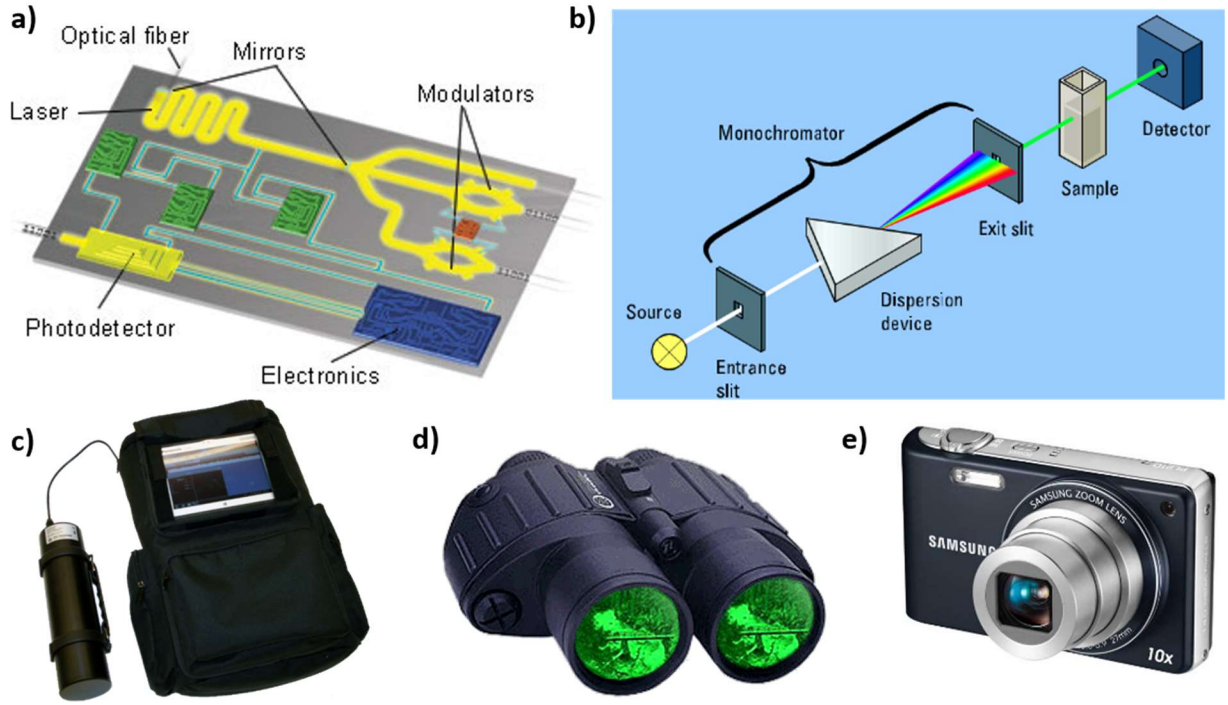

Figure 1-1. Examples of applications of photodetectors, including (a) chip-to-chip fiber optic communication,[3] (b) scientific spectral measurement system,[4] (c) personal radiation exposure monitor utilizing a photomultiplier tube,[5] (d) night-vision goggles relying on infrared photodetection,[6] and (e) a digital camera based on visible-range photodetectors.[7]

Many of these overlap with the applications of LASERs and LEDs, because any time light is used to send a signal, transfer information, or provide a quantitative measurement, a photodetector is required to receive and analyze that light. Motion sensors, disk drives and fiber optics are some commercially available applications of photodetectors,[2, 8, 9] but they are also applied in scientific research, environmental monitoring, missile detection and industrial process control.[10-12]

Photodetectors have undergone many of the same technological advancements as other optoelectronic devices, including the development and increased utilization of organic active materials. Photodetectors based on organic materials are becoming increasingly popular as a durable, cost-effective option, just as televisions and other electronic displays based on OLEDs (organic LEDs) are more widely available and organic solar cells continue to offer a promising alternative to current commercial technologies.[13] Compared to their inorganic counterparts, organic materials tend to be cheaper, lighter and more abundant, and they offer the added benefits of flexibility, solution processability and tunable optoelectronic properties.[14] This tunability is of particular interest for photodetectors, as different applications require devices be sensitive to different wavelength ranges. The ability to reliably and predictably control the spectral response of a photodetector is therefore strongly desired.

1.2 Classifications of Photodetectors

Photodetectors can be classified in many ways, including their spectral response range, their dominant working mechanism, and their active materials. The spectral response of a device, or the type of light it responds to, is perhaps the most obvious classification criterion. Some devices, referred to as broadband, respond to a wide range of wavelengths of light, but many are more selective and can be classified based on their spectral response. The focus of this work is on ultraviolet (UV) photodetectors, which have a wide variety of applications. The electromagnetic

spectrum, with the UV region specified,[15] is shown in Fig. 1-2. In many areas of scientific research, such as materials analysis and astronomical research, the ability to reliably quantify UV light is essential.[10] The measurement and tracking of UV light is also critical in environmental monitoring and can be used for checking personal radiation exposure.[11] Additionally, UV photodetectors are implemented in many industrial arc flash protection systems, as well as general flame detection applications.[16, 17] Missile detection also depends on UV photodetection, as background radiation produced by missiles can be captured by a scintillator and detected and measured by an attached UV photodetector.[18] For this type of application, a low-noise, wavelength-selective photodetector that can be produced cheaply and employed easily is essential.

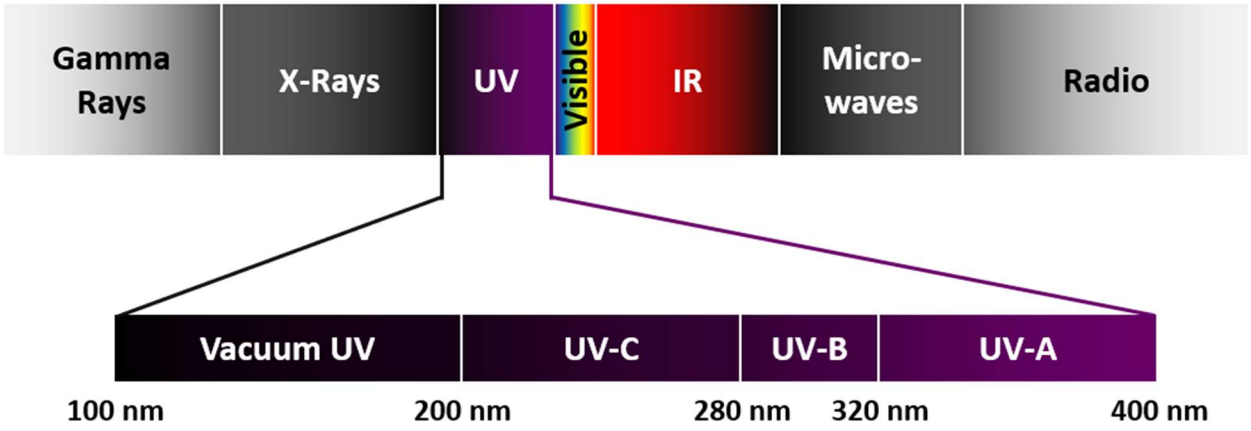

Figure 1-2. The electromagnetic spectrum, with the UV spectral region specified by wavelength.

Photodetectors can also be classified by their dominant working mechanisms, and an overview of these is given in Fig. 1-3. Thermal photodetectors do not directly detect incident photons, but rather rely on a temperature-dependent property that is modified by incident radiation.[19] Those that directly detect photons typically produce an electrical current upon illumination. These can be broadly classified as either photoemissive, where absorbed photons cause electrons to be excited to the point of emission into a surrounding material, or solid state, where electrons are excited, though not emitted, thus altering the electronic energetic state of a material.[19] These solid state detectors can be further classified as phototransistor, photoconductor or photodiode devices.[14]

Phototransistors operate much the same way as a field-effect transistor, but current production is enabled by photon absorption rather than an applied voltage.[14]

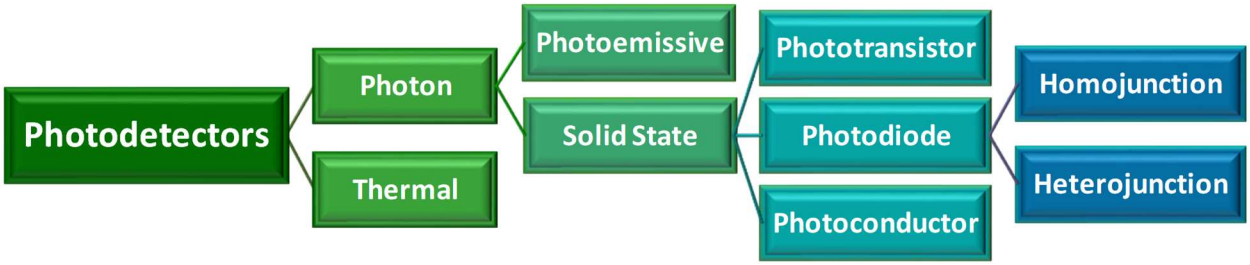

Figure 1-3. Overview of photodetectors classified by their dominant working mechanism.

In a photoconductor, the absorption of light causes the conductivity of the active material to increase, allowing excited charge carriers to readily move through the active layer and be collected at device electrodes.[14] Typically, the conductivity is improved for either holes or electrons, so that one type of charge carrier can exit the active layer and be collected before the other, in which case an additional charge carrier will be injected from an electrode to maintain charge neutrality.[14] If one type of charge carrier can be injected and collected multiple times before the other type of charge carrier can be collected once, photoconductive gain is achieved and the photoresponse is enhanced. Photodiodes typically exhibit rectification and employ a p-n junction, where a p-type electron donor and n-type electron acceptor material are used together in the active layer. Light is absorbed and excites an electron, which moves through the n-type material to be collected at the cathode while the photogenerated hole transports through the p-type material and is collected at the anode. In inorganic devices, this can be accomplished with a homojunction, where the same material is doped differently to form both sides of the p-n junction, or with a heterojunction, where two distinct materials are used to form the p-n junction. In organic devices, heterojunctions are typically used because they provide a significant energy offset at their interface. Photogenerated electron-hole pairs, or excitons, are more strongly bound in organic materials, so the energetic offset between materials aids in their dissociation, which is required for charge collection.[14]

Whether the active layer material in a photodetector is inorganic, organic, or a hybrid provides another method for categorization. Solid-state inorganic photodetectors utilizing wide-bandgap semiconductors such as ZnO, GaN, SiC, AlN, BN and diamond have been widely used in UV photodetectors.[14, 20] In some cases, these materials provide strong, UV-selective photoresponse through a process called photomultiplication, where multiple electronic charge carriers can be produced per incident photon. GaN was successfully used in a doped homojunction device that achieved a responsivity (R) of about 0.1 A/W under no applied bias with a very sharp cutoff around 360 nm.[21] A device based on a ZnO film reached over 100 A/W responsivity, under a forward bias of 5 V, with a sharp cutoff around 400 nm, although it should be noted that photodetectors are typically operated under reverse bias to minimize dark current and enhance sensitivity.[22] A device utilizing a heterojunction between these two semiconductors (n-ZnO/p-GaN) has been reported with a very sharp R peak around 375 nm, though the R value was very low, around 1 x 10^{-4} A/W.[23] Inorganic photodiode devices are sometimes operated at a strong bias so that photogenerated carriers pick up energy while moving through the active layer and excite multiple additional carriers through impact, a process called impact ionization of avalanche photoresponse.[2] A ZnO-based device with a MgO insulating layer produced R values on the order of 104 under a 73 V bias and 350-400 nm illumination.[24] An additional MgO insulating layer enhanced the avalanche photoresponse mechanism in another ZnO-based device, producing a 10-fold increase in photoresponse strength.[25] Photomultiplier tubes (PMTs) are another inorganic technology that is commonly used for photoemissive UV detection. PMTs work through impact ionization, where a photogenerated electron is emitted into a vacuum tube and makes contact with dynodes, exciting multiple additional electrons that each repeat this mechanism as they proceed to the cathode.[26] PMTs are inherently fragile because they are based on vacuum tubes, and they require extremely

high working voltages (often up to 1000 V) and protection from the earth's magnetic fields, making them bulky and ill-suited for many applications.[26] As mentioned previously, organic and organic-inorganic hybrid devices provide a more durable, cost-effective alternative to inorganic devices.

1.3 Organic and Organic-Inorganic Hybrid Ultraviolet Photodetectors

In this work, we have focused on organic photodetectors with a vertical device structure, rather than lateral devices, which require a larger electrode gap and therefore have slower response speeds than vertical devices.[14] In a vertical architecture, shown in Fig. 1-4, devices are built layer by layer, with each layer directly deposited onto the layers below it. The device is typically illuminated from the bottom, through the substrate, so every layer below the active layer must have good transparency. A typical device structure includes a transparent substrate, transparent conducting electrode, transparent charge selective layer, active layer, charge selective layer, and conducting electrode. The charge selective layers are either a hole transport layer (HTL) or electron transport layer (ETL), and sometimes these materials also serve as an electron blocking layer (EBL) or hole blocking layer (HBL), respectively. The active layer is typically a heterojunction composed of a blend of a p-type electron donor and an n-type electron acceptor. A conventional device (Fig. 1-4a) has a structure of substrate/anode/HTL/active layer/ETL/cathode, and an inverted device (Fig. 1-4b) has a structure of substrate/cathode/ETL/active layer/HTL/anode.

The general device working mechanism, illustrated in Fig. 1-4c, begins with light absorption in the active layer. When light is absorbed, typically in the electron donor, it excites an electron from the highest occupied molecular orbital (HOMO) to the lowest unoccupied molecular orbital (LUMO), leaving behind a positively charged hole in the HOMO. These two charge carriers are bound together and collectively referred to as an exciton. Photogenerated excitons diffuse to

donor-acceptor interfaces, where the energetic offset between the two materials enables exciton dissociation. Organic active layers have undergone steady improvement since their introduction, one of the most significant steps being the incorporation of a bulk heterojunction (BHJ) morphology (Fig. 1-4c), which improves charge transport in the active layer and increases the surface area of the heterojunction interface. In a BHJ device, the donor and acceptor materials form an interpenetrating network throughout the active layer, providing continuous pathways so that separated holes and electrons can each transport through the active layer to be collected at the anode and cathode, respectively.[27, 28]

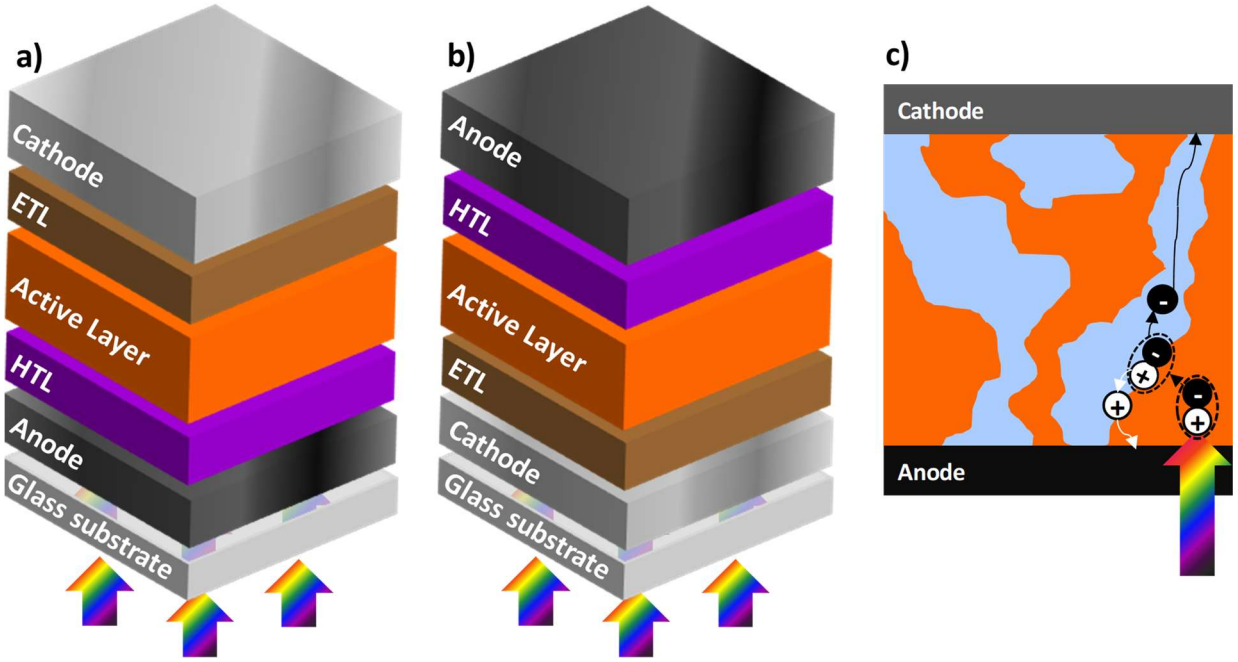

Figure 1-4. Diagram of the device structure for (a) a conventional device and (b) an inverted device. (c) Illustration of the general working mechanism for a device with a bulk heterojunction active layer.

The general device working mechanism, illustrated in Fig. 1-4c, begins with light absorption in the active layer. When light is absorbed, typically in the electron donor, it excites an electron from the highest occupied molecular orbital (HOMO) to the lowest unoccupied molecular orbital (LUMO), leaving behind a positively charged hole in the HOMO. These two charge carriers are bound together and collectively referred to as an exciton. Photogenerated excitons diffuse to

donor-acceptor interfaces, where the energetic offset between the two materials enables exciton dissociation. Organic active layers have undergone steady improvement since their introduction, one of the most significant steps being the incorporation of a bulk heterojunction (BHJ) morphology (Fig. 1-4c), which improves charge transport in the active layer and increases the surface area of the heterojunction interface. In a BHJ device, the donor and acceptor materials form an interpenetrating network throughout the active layer, providing continuous pathways so that separated holes and electrons can each transport through the active layer to be collected at the anode and cathode, respectively.[27, 28] The first use of an organic BHJ, composed of poly(3-hexylthiophene) (P3HT) and methanofullerene (PCBM), yielded strong photoresponse between 400-600 nm, with the external quantum efficiency (EQE) peaking around 76% at 500 nm.[29] The EQE represents the ratio of charge carriers collected per incident photon.

To achieve a BHJ, the donor and acceptor materials are blended in a ratio that is close to 1:1, w:w. If the materials are blended in an unbalanced weight ratio where the acceptor is present at a much lower content than the donor, by perhaps two orders of magnitude, a different active layer morphology is achieved. In this case, the acceptor forms isolated clusters within the donor matrix, rather than each material forming a continuous pathway throughout the active layer as they would in a BHJ. In a BHJ, the EQE can never exceed 100%, but in this alternate morphology, a mechanism for photomultiplication is enabled. Electrons that transfer from the donor layer into the isolated clusters of acceptor material become trapped, since there is no physical pathway for them to transport through the active layer and there is an energetic barrier to escape into the donor. If these trapped charges accumulate, the energy bands of the active layer bend down, and under an applied reverse bias hole injection from the cathode is enabled. Multiple holes can be injected from the external circuit that the cathode is connected to, so multiple holes can be collected per incident

photon. When this occurs, photomultiplication and EQE values exceeding 100% are achieved. The same components of the previously mentioned BHJ device, P3HT and PCBM, were utilized in a ratio of 100:1, w:w to achieve EQE values as high as 16,700% and 37,500%, with and without an ETL/HBL of LiF respectively, under 380 nm illumination and a -19 V bias.[30, 31]

Another way to achieve this isolated charge trap morphology is to embed inorganic electron-accepting quantum dots and nanoparticles in a polymer active layer. This can also benefit device performance because many nanoparticles and quantum dots absorb light while the common organic acceptor material [6,6]-phenyl-C_{71}-butyric acid methyl ester ($PC_{71}BM$) does not. Additionally, nanoparticles and quantum dots can tolerate a higher content of charge traps, compared to $PC_{71}BM$, without forming a continuous network of acceptor material. For example, n-type ZnO nanoparticles have been embedded into p-type polymer active layers of P3HT and poly(9-vinylcarbazole) (PVK) to engage photomultiplication in an organic-inorganic hybrid photodetector, yielding peak EQE values of 340,600% and 245,300%, respectively, under 360 nm illumination and a -9 V bias.[32]

1.4 Photodetector Figures of Merit

Because solar cells are primarily utilized as a power source, maximizing the power conversion efficiency is the clear design objective. For photodetectors, the design criteria selection is more complicated and depends on the intended application. For example, a photodetector utilized in a fiber optic communication system should be designed primarily for a high response speed.[2] In missile detection, a photodetector needs to respond to a specific wavelength range and be able to operate in ambient conditions. The broad applicability of photodetectors and corresponding performance criteria complicates the design process and necessitates a variety of figures of merit to evaluate different aspects of photodetector performance.[19]

The measurement of current density-voltage characteristics is often the first step in photodetector evaluation. The current produced by a device is measured, typically over a voltage range that sweeps between negative voltage (reverse bias) and positive voltage (forward bias), and this current is divided by the active device area to obtain a current density (J). The resulting data are referred to as J-V curves, and their shape and magnitude are indicative of device performance and can often provide insight into the underlying response mechanisms and device physics. Dark current density (J_D) is the current produced by a device when it is not illuminated, and it should be minimized. Photocurrent density (J_{PH}) is the current produced by a device under incident illumination. It should be maximized, and the wavelength and power of the incident light should always be noted. The on/off ratio is the ratio of J_{PH} to J_D.

External quantum efficiency (EQE) is the ratio, typically reported as a percentage, of charge carriers produced to incident photons. EQE provides an indication of photoresponse strength, it should be maximized and is calculated by Eq. 1.1, where q is the elementary charge, P_λ is the measured incident optical power at a given wavelength (λ), A_{spot} is the illumination spot area, h is Planck's constant, and c is the speed of light.

$$EQE = \frac{J_{PH}}{q} \Big/ \frac{P_\lambda \lambda}{A_{spot} hc} \tag{1.1}$$

Responsivity (R), the output current per incident optical power, accounts for the variation of optical power with wavelength. R provides an indication of photoresponse strength, it should be maximized and is calculated by Eq. 1.2:

$$R = EQE * \frac{q\lambda}{hc} \tag{1.2}$$

The noise current (I_n) in a photodetector can arise from multiple sources, including shot noise, Johnson (thermal) noise, and 1/f noise, and is either measured directly or obtained by taking a Fast

Fourier Transform (FFT) of the dark current, measured at a steady applied bias over a period of time, thereby accounting for the measurement frequency and bandwidth.[19, 33, 34] Noise equivalent power (NEP) is the lowest optical power that a detector can distinguish from noise and represents the sensitivity of a device. Specific detectivity (D*) is the inverse of NEP, normalized by the device bandwidth, as accounted for by the noise current, and the active area. This figure of merit can therefore be compared across devices and measurement systems and encompasses both the strength and sensitivity of photoresponse. D* should be maximized and is calculated by Eq. 1.3. Table 1-1 shows some state of the art D* values for organic, inorganic, and hybrid systems.

$$D^* = R\sqrt{A}/I_n \tag{1.3}$$

Table 1-1. State of the art D* values for organic, inorganic, and hybrid systems. The wavelength and applied bias for each value correspond to the reported peak detectivity value. A * on the reference indicates that the work used a shot noise approximation to calculate the noise current, yielding less reliable D* values.[35]

Device Active Layer	Wavelength (nm)	Bias (V)	D* (Jones)	Reference
P3HT:$PC_{71}BM$	400	-19	3.5×10^{13}	36*
PCDTBT:$PC_{71}BM$	400	-2	2.0×10^{13}	37*
PVK:4CzPN	350	-9	1.1×10^{12}	38*
PVK:$PC_{71}BM$	350	-1.5	5.6×10^{12}	39*
NPB:BAlq	270	-12	8.3×10^{11}	40*
F8T2:$PC_{71}BM$	330	0	4.2×10^{10}	this work
mCP:TiO_2 nanoparticles	351	-10	3.7×10^{14}	41*
P3HT:ZnO nanoparticles	360	-9	2.5×10^{14}	32
PVK:ZnO nanoparticles	360	-9	3.4×10^{15}	32
C nanodots:ZnO quantum dots	360	14	3.1×10^{17}	42
ZnO nanorods	360	-5	4.1×10^{15}	43
Si	254	0	3.5×10^{12}	44
Si	410	0	5.0×10^{12}	44
Si:graphene	365	0	1.6×10^{13}	45*
$Bi_{0.041}Sn_{0.959}O_2$	280	1	6.1×10^{15}	46*
GaN	340	1	5.3×10^{14}	47*

Linear dynamic range (LDR) is the range of incident optical power intensities over which the detector's current output changes linearly, and it should be maximized. There is inconsistency in the literature around the calculation of LDR, but it is always dependent on the number of orders

of magnitude over which the relationship between produced current and incident optical power is linear. If the incident optical power is decreased by an order of magnitude, and the output current also drops by an order of magnitude, this is considered a linear response.

The response speed is quantified by the rise time and fall time, which represent the time it takes for a device to reach 90% and 10%, respectively, of the maximum photoresponse level when illumination is introduced and removed, respectively. In this work, our primary focus has been on minimizing J_D and maximizing EQE, which inherently optimizes R, and D*, with a secondary focus on maximizing the response speed.

1.5 Tuning Spectral Photoresponse

The ability to reliably and easily tune the spectral selectivity of a photodetector's response is strongly desired, at it enables quick, easy, cost-effective production of multiple devices with varied photoresponse, thereby improving device applicability. Some applications may require device photoresponse to be selective to certain regions, such as UV, visible, or IR. For example, UV-selective photodetection is required for flame and missile detection, technologies like digital cameras and disk drives rely on visible-range detection, and IR-selective photodetection is used for many remote control and motion sensing applications. Sometimes, very specific wavelength-selectivity is required, such as for colorimetry or imaging, while other applications, such as laboratory measurements and environmental monitoring, may call for even photoresponse across a wide range of incident illumination. Therefore, in addition to tuning photoresponse to different spectral regions, the response can also be tuned within a spectral window to be broad or narrowband, demonstrated in Fig. 1-5.

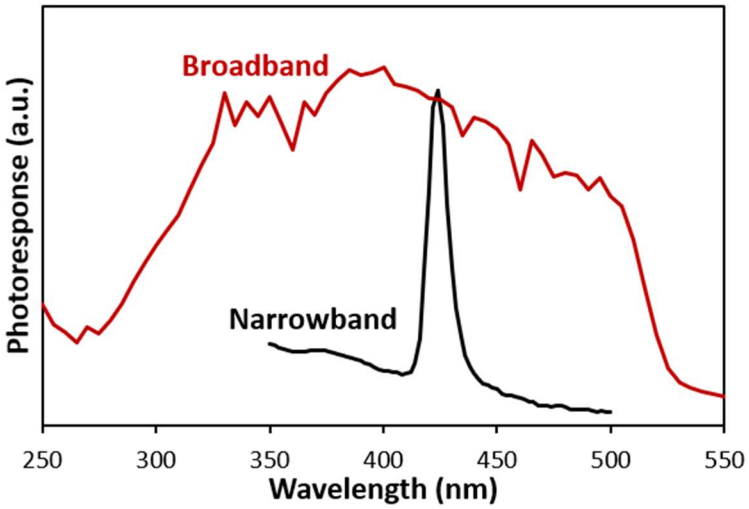

Figure 1-5. Representative photoresponse spectra of a broadband and narrowband device.

One method for tuning spectral photoresponse is active material selection, which determines both the optical and electronic properties of organic devices. Electronically, polymer selection is dominated by high hole mobility and HOMO/LUMO level alignment with the electron accepter, HTL/ETL, and electrodes. Optically, a polymer with an absorption spectrum that aligns with the desired response window must be selected, though this is not always sufficient to guarantee the desired spectral response. In this work, UV-selectivity is maintained by the selection of wide-bandgap, UV-absorbing active materials. Physically controllable film conditions such as weight ratio, annealing temperature, and precursor solution concentration provide a handle for controlling active layer thickness and morphology, which in turn control the optical properties of the film.[30, 48-52] Liquid crystalline polymers, with multiple phase transitions, can produce films with varying optical properties depending strongly on the annealing temperature of the films.[48-50] Film processing conditions also affect the distribution of charge traps, such as acceptor clusters, nanoparticles, or quantum dots, which impacts both the optical and electronic properties of the film.[30, 32, 51-53] Generally, the films in this work are processed so that charge traps concentrate towards the top portion of the active layer, which is beneficial to device performance.

Tuning the spectral photoresponse between broad and narrowband can be accomplished by manipulating the active layer thickness to engage a mechanism called charge collection narrowing (CCN). This mechanism was first established in red and near-infrared (NIR) photodetectors, composed of poly[N-900-heptadecanyl-2,7-carbazole-alt-5,5-(40,70-di-2-thienyl-20,10,30-benzothiadiazole)] (PCDTBT) and poly[2,5-(2-octyldodecyl)-3,6-diketopyrrolopyrrole-alt-5,5-(2,5-di-(thien-2-yl)thieno[3,2-b]thiophene)] (DPP-DTT) respectively, blended with $PC_{71}BM$.[33] This phenomenon is based on bulk exciton generation, where light that penetrates the active layer can be absorbed, and generate excitons, throughout the entire layer, which enables it to contribute significantly to the photoresponse. In devices with relatively thin active layers, up to a few hundred nanometers, most light can penetrate the active layer and produce bulk exciton generation, leading to broadband photoresponse. If a device has a thicker active layer, on the order of microns, only light with longer wavelengths can penetrate the entire active layer. Light within the peak absorption range of the material is absorbed quickly. Therefore, this light only generates excitons in the lower portion of the active layer, creating an extended depletion region that diminishes charge transport and suppresses photoresponse.[33] In contrast, light at the edges of the absorption peak is absorbed only weakly. Light at the short-wavelength edge of the absorption peak still cannot penetrate the thick active layer, due to its inherently low penetration depth, but light at the long-wavelength edge of the absorption peak can penetrate through the entire active layer. This light is reflected off the top electrode and establishes an interference pattern, which enables it to be absorbed and generate excitons throughout the active layer and contribute significantly to the photoresponse. Because only light at the long-wavelength edge of the absorption peak can establish bulk exciton generation in thick devices, a dramatic narrowing of photoresponse is achieved by simply increasing the thickness of the active layer.

Another method for tuning and controlling the photoresponse window is through filters, but adding an extra layer to a device with the sole purpose of tuning the photoresponse complicates the device architecture, increases the overall cost of the device, and limits resolution in imaging applications.[54] However, incorporating nanostructures into existing device layers, such as an electrode, could control and tune the spectral photoresponse of devices without adding a filter onto the device. This layer could therefore act as both an electrode and an optical filter for devices, as has been accomplished with nanostructured metal electrodes,[55, 56] in addition to providing both optical and electrical enhancements to device performance.[57, 58]

1.6 Plasmonic Enhancements in Photodetectors

The device flexibility enabled by organic active materials is negated by the commonly used bottom electrode material of indium tin oxide (ITO). ITO has good conductivity and visible transparency, but it has relatively low UV transparency, is expensive due to the scarcity of indium, and is brittle and requires relatively difficult processing.[59] We intend to replace ITO with an Al nanostructured film, utilizing a much cheaper and more abundant material without sacrificing conductivity. While planar Al has poor transparency, incorporating an array of nanoholes provides sufficient transmission of UV light and additional plasmonic enhancements to device performance.

Surface plasmonics are a popular approach for improving the performance of optoelectronic devices. Excited free electrons at a metal-dielectric interface form collective oscillations of surface charges called surface plasmons (SPs).[60] These SPs can couple to incident light when the frequency and momentum match, forming a quasiparticle called a surface plasmon polariton (SPP) that propagates along the surface,[57, 60-62] as illustrated in Fig. 1-6a.[60] SPPs trap light at the surface and significantly enhance the local electric field intensity at both sides of the interface.[63] This is illustrated in Fig. 1-6b,[60] which also illustrates how the electric field decays quickly with distance

from the interface, and is therefore concentrated near the surface.[64] This phenomenon makes plasmonic nanostructures attractive for photodetectors, which often rely on charge dynamics and response mechanisms that are sensitive to the internal electric field throughout devices and especially at device interfaces.[60, 65]

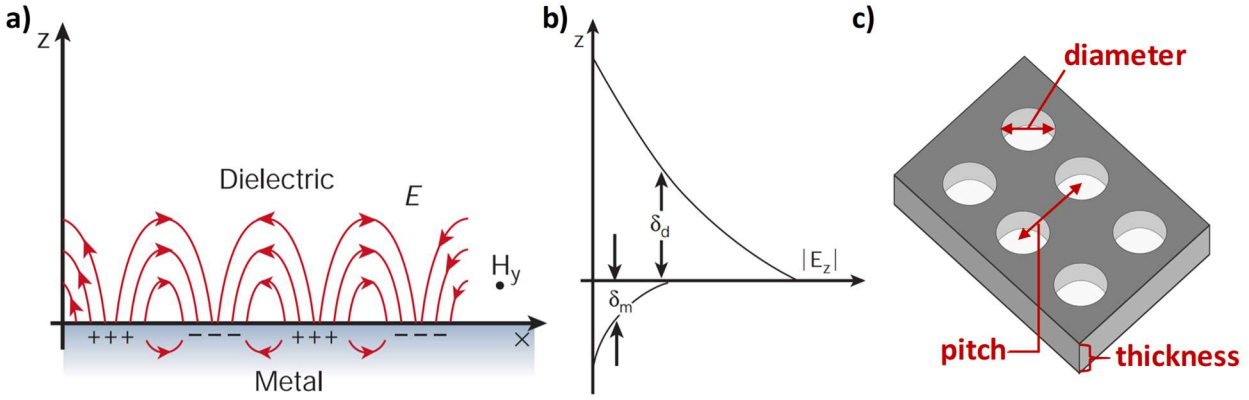

Figure 1-6. (a) Schematic of an SPP, from ref. 60, illustrating the surface charge and electric field (E) involved in the SPP formation at a metal-dielectric interface, as well as the magnetic field (H) in the y direction.[60] (b) Schematic of the electric field decay, from ref. 60, showing the exponential decay of electric field strength with distance from the interface through the decay lengths in the metal (δ_m) and dielectric (δ_d).[60] (c) Illustration of the relevant geometric parameters for a nanohole array, including the diameter (size of the nanohole), pitch (center-to-center distance between holes), and thickness of the layer.

Using SPPs for optical and electronic enhancements to device performance is a particularly attractive approach because the controllable physical properties directly impact the optical properties of SPPs, so they can be tuned relatively easily.[58, 61, 62] A periodic array of nanostructures enables metal films to engage in the coupling of incident light to SPs in the surface, supporting SPPs in the form of a standing wave on the metal surface by diffracting incident light so that its momentum can be readily matched to the SPs.[57, 60-62, 64] Only SPPs with certain frequencies, coupling to incident light of certain frequencies, can be excited and propagate along the surface, and this depends directly on the geometry and periodicity of the nanostructure array.[61, 62, 66] Therefore, if a nanohole array, incorporated into a device as a transparent conducting electrode, is utilized for SPP production and support, the diameter, pitch, and thickness (Fig. 1-6c) of the array

provide physical handle for tuning the optical properties of SPPs, and therefore the spectral range of incident light for which they will provide plasmonic photoresponse enhancements.[61, 62, 65, 67, 68]

When incorporated into optoelectronic devices, SPPs can engage a variety of both optical and electronic enhancement mechanisms and can be supported on a variety of nanostructures including gratings, nanoparticles, and nanohole arrays.[65] Plasmonic nanostructures employed in thin film solar cells enable devices with thinner active layers, which have superior charge transport properties, to compete optically with thicker devices by improving light absorption through three main methods.[61] On the illuminated side of the active layer, plasmonic nanostructures scatter incident light, increasing its path length in the active layer; within the active layer, embedded plasmonic nanostructures enhance the local electric field and subsequently improve absorption; and at the rear of the active layer, plasmonic nanostructures trap light in SPPs that propagate along the rear active layer interface.[61] The same absorption improvements resulting from plasmonic nanostructures in thin film organic solar cells[69-73] can similarly be utilized in photodetectors.[58, 65, 68] Plasmonic nanostructures can also concentrate light into small volumes, which is attractive for photodetectors as increasingly small devices are desired to decrease response time and power consumption, particularly for information technology and communication applications.[57]

In addition to enabling smaller photodetectors with absorption enhancements, incorporating SPPs into photodetectors can also improve the responsivity, spectral selectivity and tunability of devices.[65] Responsivity improvements can be realized through the same mechanisms of light trapping and absorption enhancement applied in thin film solar cells.[65, 67, 74-78] For spectral selectivity and tunability, arrays of nanoholes in metal films can be used as internal filters, simultaneously serving as a device electrode and tuning the spectral photoresponse simply by varying the geometry of the pattern.[55, 65, 67, 68, 79] Al is an attractive material for UV photodetectors

due to its relative abundance and low cost, compared to the more commonly used plasmonic metals of Ag and Au, and because of its plasmonic activity and tunability in the UV spectral range.[55, 80, 81] The suitability of Al for UV plasmonics is demonstrated in Fig. 1-7.[82-84]

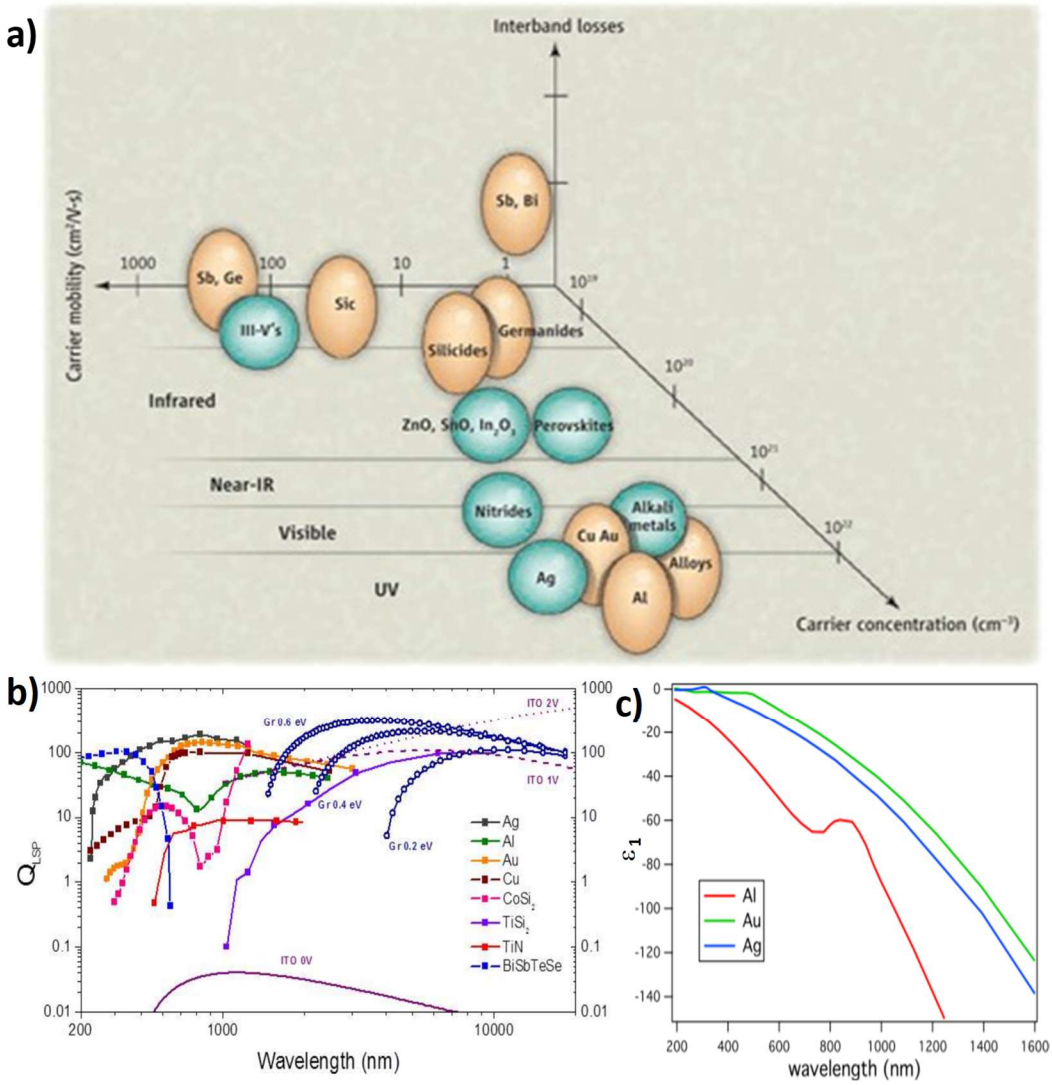

Figure 1-7. (a) Plot of various materials for plasmonics, from ref. 82, illustrating the carrier mobility and concentration, as well as the relevant spectral ranges for each material and the interband losses.[82] (b) Plot of the quality factor of localized surface plasmon resonance against incident wavelength for a variety of plasmonic materials, from ref. 83.[83] (c) Plot of the real part of the dielectric function for the common plasmonic metals of Al, Au, and Ag, from ref. 84.[84]

In Fig. 1-7a, plasmonic materials are plotted for various spectral rangesaccording to their carrier mobility and concentration. Interband losses are also represented, with a more spherical point corresponds to lower losses.[82] Clearly, due primarily to its large carrier concentration, Al is well-

suited for UV plasmonics. Fig. 1-7b shows the quality factor of localized surface plasmon resonance (Q_{LSPR}) for various materials plotted against incident wavelength, which represents the ratio of the stored electromagnetic energy to the absorbed energy, and therefore gives some insight into which materials will support SPPs most effectively.[83] It is calculated, in this case, based on the intrinsic properties of each material, including its dielectric constant.[83] Al works well for UV plasmonics because the real part of its dielectric constant is negative throughout the entire UV spectral range (Fig. 1-7c),[84] and it is clear that Al (green curve, Fig. 1-7b) has among the highest Q_{LSPR} values in the UV spectral region.[83]

In addition to the theory represented in Fig. 1-7, Al has been shown experimentally to have strong UV plasmonic activity. Al nanodisks and nanoparticles produce tunable plasmonic resonances in the UV spectral range,[80, 81] and Al nanostructured films have been used to filter transmission to and within the UV spectral range.[55] Additionally, Al nanostructures can be used to accomplish sub-bandgap photoresponse, via hot-electron injection, making them a viable option for improving and controlling the response of visible-range photodetectors and solar cells.[73, 79, 85]

1.7 Objectives and Goals

The overarching goal of this work has been to explore and expand the "toolbox" of methods available for tuning and improving the photoresponse of UV photodetectors. The wide variety of applications and performance criteria for photodetectors complicates their design, so it is important for the field to have a comprehensive understanding of the photoresponse mechanisms available, the controllable physical parameters that can produce, engage, and tune those mechanisms, and how they impact device performance. By understanding the tools available and their interdependent relationships to response mechanisms and device performance, photodetectors for all applications can be designed and produced quickly and effectively. Investigating established

response mechanisms and extending them into the UV spectral range through active layer material choice, thickness, and morphology has been a main focal point of this work, as has been as the design, fabrication and incorporation of plasmonic nanostructured electrodes. Contributing to the constantly expanding knowledge around photodetectors and their working mechanisms, and utilizing that knowledge to produce devices with predictable, tunable, strong, UV-selective photoresponse is the primary aim of the work. The objectives of this research include:

1. Extend an established photomultiplication mechanism for organic photodetectors into the UV range through active layer material choice and deepen the understanding of this mechanism and the factors that impact its function;
2. Tune the photoresponse of UV photodetectors between spectrally broad and narrowband through the active layer thickness and investigate the impact of the active layer composition and morphology on the efficacy of this mechanism;
3. Design, fabricate, and characterize plasmonic nanostructured electrodes and fully understand their impact on device performance so that they can be incorporated into devices in a way that will result in strong, sensitive, and tunable photoresponse.

Chapter 2. PHOTOMULTIPLICATION VIA CHARGE INJECTION IN UV PHOTODETECTORS BASED ON A BLEND OF F8T2 AND $PC_{71}BM$

2.1 INTRODUCTION

The first observation of photomultiplication in an organic photodetector was in thin organic pigment films, where photogenerated holes were trapped at the interface of the active layer and the anode, inducing band bending in the active layer and consequential electron injection from the anode.[86, 87] A single layer of n-methyl-3,4,9,10-perylenetetracarboxyl-diimide (Me-PTC) was utilized as an active layer and yielded an EQE that peaked around 5000% at -20 V applied bias.[86] Since then, photomultiplication has been further studied and improved in organic devices. Recently photomultiplication has been successfully utilized in a device with an active layer composed of the polymer donor P3HT and the fullerene-derivative acceptor $PC_{71}BM$, with a device architecture of ITO/poly(2,3-dihydrothieno-1,4-dioxin)-poly(styrenesulfonate) (PEDOT:PSS)/P3HT:$PC_{71}BM$/LiF/Al.[30] The active layers in these devices were designed with weight ratios that drastically favored P3HT, forcing $PC_{71}BM$ to form isolated clusters instead of an interpenetrating network like it would in a BHJ. Therefore, when excitons were separated at acceptor/donor junctions, the electrons that moved into the acceptor $PC_{71}BM$ became trapped near the cathode and enhanced hole-injection from the cathode.[30, 36] EQE and R values as high as 16,700% and 51.7 A/W, respectively, were reported for the P3HT:$PC_{71}BM$ devices under 380 nm illumination and a -19 V bias.[30] Even higher values for EQE, 37,500% under 625 nm illumination and a -19 V bias, were obtained when the ETL/HBL LiF was removed from the device architecture.[31] This photomultiplication mechanism was also utilized in a fullerene-free

photodetector that was based on a 100:1 blend of P3HT and DC-IDT2T to achieve EQE values of 28,000% under 380 nm illumination and a -20 V bias.[88]

Increasing EQE to maximize R is a common design goal of photodetectors, but decreasing J_D is also important because it allows for a more sensitive device, manifested as a higher D*. Low dark current density is often achieved by incorporating charge-blocking layers, which limit the thermally generated current present in devices under dark conditions. The incorporation of an electron blocking layer of polystyrene-N,N-diphenyl-N,N-bis(4-n-butylphenyl)-(1,10-biphenyl)-4,4-diamine-erfluorocyclobutane (PS-TPD-PFCB) and a hole blocking layer of C_{60} into a device based on a BHJ composed of poly[2,6-(4,4-bis-(2-ethylhexyl)-4H-cyclopenta[2,1-b;3,4-b]dithiophene)-alt-4,7-(2,1,3-benzothiadiazole)] (PCPDTBT) and $PC_{71}BM$ lowered the J_D from 10^{-2} to 10^{-5} mA/cm^2 at a -1 V bias.[89] Recently, a dark current of 6.4 x 10^{-7} mA/cm^2 at -0.5 V was achieved for an organic BHJ photodetector with a structure of glass/ITO/(poly-TPD or PEDOT:PSS)/poly[(2,5-bis(2-hexyldecyl)-2,3,5,6-tetrahydro-3,6-dioxopyrrolo[3,4-c]pyrrole-1,4-diyl)-alt-([2,2':5',2''-terthiophene]-5,5''-diyl)](PDPP3T):$PC_{71}BM$/Al, which is among the lowest reported for organic devices and enabled a D* of 1 x 10^{13} Jones under NIR illumination, despite unimpressive EQE values around 27.7% under a -0.5 V bias and 850 nm illumination.[90] The J_D of the P3HT:$PC_{71}BM$ device with an EQE of 16,700% was around 10^{-4} mA/cm^2.

These P3HT-based devices had impressive response between 360-380 nm and maintained relatively strong response throughout the visible region. However, many applications such as missile detection, arc flash protection, and scientific measurement require UV-selective photodetection.[14, 17] For a device to be UV-selective, it must have a much stronger response to UV light than other spectral regions, and ideally the response should have a sharp cutoff outside of the UV region. To accomplish the design goals of high EQE, low dark current and UV-selectivity,

photomultiplication can be utilized in a UV-selective system. The liquid crystalline polymer poly[(9,9-dioctylfluorenyl-2,7-diyl)-alt-co-(bithiophene)] (F8T2) is a p-type semiconductor with a hole mobility of 0.01-0.02 cm^2/V^-s and a typical bandgap of 2.4 eV.[91] F8T2 has been implemented in thin film transistors, and it was shown that the alignment, whether the polymer backbones are parallel or perpendicular to the lateral charge flow, significantly impacts hole mobility, which can be 6.5 times larger for parallel-oriented films.[49] F8T2 has also been blended with $PC_{61}BM$ and used in photodetectors with a ITO/F8T2:$PC_{61}BM$/Au structure that showed good rectification and J_{PH} around 2 mA/cm^2 under 460 nm illumination and a -1 V bias.[92] As a liquid crystalline polymer, F8T2 has several different phase regions and transitions, leading to variations in microstructure and morphology that can affect optical absorption, charge dynamics and energy level alignment.[48-50] The bandgap of F8T2, which is well-suited for UV absorption, can vary between 2-3 eV depending on whether the film is amorphous, mesophase, or ordered liquid-crystal.[48]

In this work, F8T2 was blended with small amounts of $PC_{71}BM$ in an effort to take advantage of photomultiplication in a UV-selective, entirely organic active layer for a conventional device with the structure ITO/PEDOT:PSS/F8T2:$PC_{71}BM$/LiF/Al. Devices with F8T2:$PC_{71}BM$ weight ratios of 100:1 and 100:4, with and without the LiF ETL were fabricated and evaluated, primarily through J-V curves and EQE measurements. All devices experienced photomultiplication and produced EQE values over 100%, and most were stable under strong reverse biases up to -40 V. Devices with 100:4 F8T2:$PC_{71}BM$ blends with the LiF layer included were found to be optimal, producing peak EQE and R values of 5600% and 15.9 A/W, respectively, under 360 nm illumination and a -40 V bias. Strong UV-selectivity was achieved, and there is a response cutoff around 420 nm with limited response throughout the rest of the visible range. Under a -40 V bias,

the ratio of EQE at 360 and 510 nm is 6.65, and the ratio of EQE at 360 and 650 nm is 247. The dark current at -1 V was extremely low at just 2.7 x 10^{-7} mA/cm^2. The devices presented here offer an entirely organic alternative for sensitive, UV-selective photomultiplication that can be utilized in large-area, flexible devices that would be cheaper and easier to produce than current technologies.

2.2 EXPERIMENTAL

2.2.1 *Precursor Solution Preparation*

F8T2 was purchased from American Dye Source, Baie D'Urfe, Quebec, Canada three separate times, providing three distinct samples: high-MW, mid-MW, and low-MW with molecular weights (MW) of 82,000, 43,000, and 29,000 g/mol and polydispersity indexes (PDI) of 2.6, 3.9, and 3.3, respectively. Low-MW F8T2 was used unless otherwise stated. $PC_{71}BM$ was purchased from Nano-C Inc. (Westwood, MA). All solution preparation was completed in a nitrogen-filled glovebox. F8T2 and $PC_{71}BM$ were dissolved separately in 1,2-dichlorobenzene (anhydrous, 99.9% purity, Sigma-Aldrich, St. Louis, MO) at a concentration of 40 mg/mL and stirred at 700 rpm and 70ºC for at least 12 h. These solutions were then combined in varying F8T2:$PC_{71}BM$ ratios including 100:1, 100:4, and 1:1, v:v. Because the F8T2 and $PC_{71}BM$ solution concentrations were the same, the volume ratio was equivalent to a weight ratio. When high-MW and mid-MW F8T2 were used it was with total concentrations of 15 and 20 mg/mL, respectively, in which case a solution with a total concentration of 40 mg/mL was made and then diluted by adding additional 1,2-dichlorobenzene. The blended solutions were stirred for at least one additional hour at 700 rpm and 70ºC.

2.2.2 *Film Fabrication and Analysis*

Plain glass slides were cut into 1.5 cm x 1.5 cm squares and cleaned by ultrasonication for 15 min each in soapy deionized (DI) water, DI water, acetone and isopropanol, in sequence, and then by oxygen plasma cleaning at 100 W for 30 s. All film fabrication steps, after the preparation of the substrates, were completed in a nitrogen-filled glovebox. The F8T2:$PC_{71}BM$ blend precursor solutions were filtered through a 0.2 μm PTFE syringe filter (except for high-MW solutions, which were too viscous to filter by our methods) and deposited via spin coating at 1000 rpm, unless otherwise stated, for 30 s. The films were then annealed for 10 min at 80ºC, unless otherwise stated. Film analysis was performed in ambient conditions. UV/Vis spectra were collected using a Perkin Elmer Lambda 900 UV/Vis spectrophotometer. Photoluminescence data were collected with a Horiba Fluorolog 3 Spectrofluorometer. Film thicknesses were measured using a KLA Tencor Alpha-Step 500 Profiler. AFM images were collected with a Bruker/Veeco/DI Multimode AFM-2.

2.2.3 *Device Fabrication and Characterization*

ITO coated glass substrates (≤ 10 Ω/sq, Colorado Concept Coatings LLC, Loveland, CO) were prepared by the same methods of ultrasonication and plasma treatment as described in Section 2.2.2. PEDOT:PSS solution (Clevios P VP AI 4083, Heraeus, Hanau, Germany) was filtered through a 0.45 μm PTFE syringe filter and spin-coated on the ITO-coated glass substrates at 5000 rpm for 40 s, then baked at 120ºC for 10 min in air. The chips were then transferred into a nitrogen-filled glovebox. F8T2:$PC_{71}BM$ active layers were deposited via spin coating, under the same conditions as the films in section 2.2.2. A thin 0.8 nm layer of LiF (99.995%, Sigma-Aldrich), followed by 100 nm Al (99.999%, R.D. Mathis, Long Beach, CA, were deposited via thermal

evaporation using an Angstrom Engineering Amod PVD Platform. LiF was deposited without the use of any mask, and Al electrodes were deposited with rectangular masks so that the active area of each device was 0.1 cm^2, and four devices were on each chip.

All device characterization measurements were performed in air. J-V curves, J_D versus time, EQE spectra, and response speed data were obtained using a Keithley 6430 sub-fA sourcemeter or a Keithley 2635B sourcemeter. Unless otherwise noted, scan direction was from forward bias to reverse bias (+2 to -2 V, or +2 to -40 V). Light was provided using a tungsten light source and Acton Research SpectraPro 275 Monochromator, or a Xenon arc lamp and an Oriel Cornerstone 130 Monochromator. Optical intensity was measured using a Newport 1830-C Power Meter with a Newport 818-UV Si Fiber Optic Detector, or a Newport 1918-R Power Meter and Newport UV-Si Photodiode. The lamps' power spectra are shown in Fig. 2-1. The response speed was obtained by manually switching between dark/light conditions.

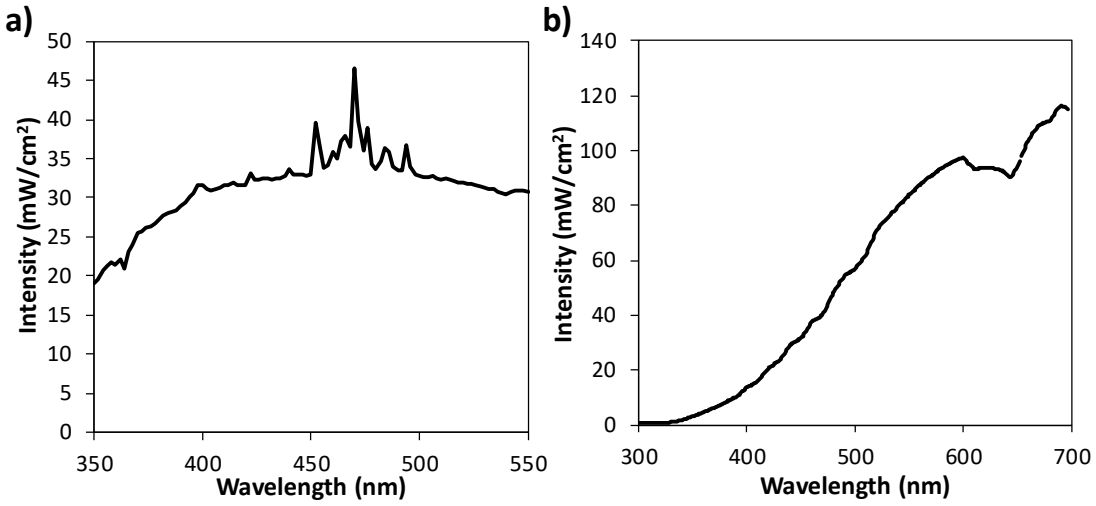

Figure 2-1. The power curves for (a) the xenon arc lamp and (b) the tungsten lamp.

2.2.4 *Optical and Electromagnetic Simulations*

Transfer matrix method[93, 94] (TMM) and 3-dimensional finite-difference time-domain (3D-FDTD, Lumerical FDTD Solutions[95]) simulations were performed to obtain the

exciton generation rate and electric field distribution, respectively, within devices. The simulated devices have a similar structure to experimentally fabricated devices, with the same layer compositions and thicknesses. Specifically, the simulated device structure was glass (100 nm)/ITO (100 nm)/PEDOT:PSS (40 nm)/F8T2:$PC_{71}BM$ (100:4, 350 nm)/Al (100 nm). The optically thin LiF layer was not included. The exciton generation rate was calculated for incident light at 375 and 425 nm. Electric field distributions were collected with a frequency-domain field monitor positioned at a cross section through the middle of the devices. For each material utilized in a simulated device, in both TMM and FDTD simulations, the wavelength-dependent optical constants of refractive index (n) and extinction coefficient (k) had to be defined. For Al, these optical properties were provided in the material library of the Lumerical program,[96] and data from an online database were used for the glass substrates.[97, 98] For all other materials the wavelength-dependent optical constants were obtained from ellipsometry with a Woollam M-2000 Spectroscopic Ellipsometer and are shown in Fig. 2-2. A more detailed description of the 3D-FDTD simulations is provided in Chapter 4, Section 4.2.

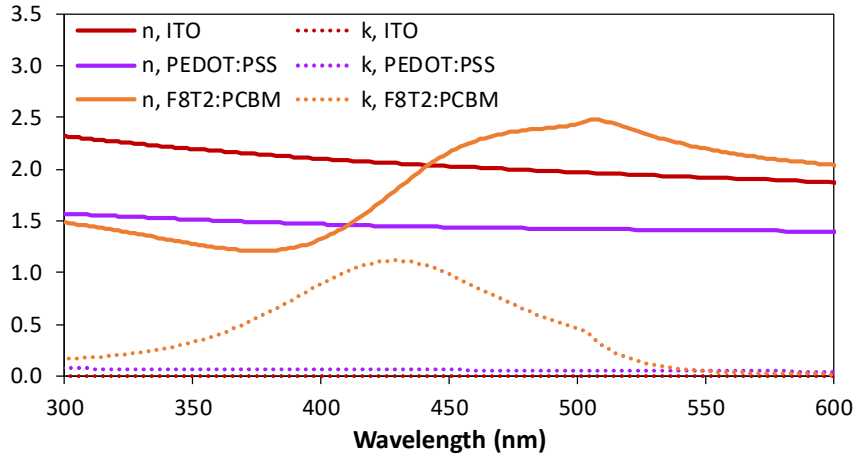

Figure 2-2. Wavelength-dependent optical constants of refractive index, n, and extinction coefficient, k. For F8T2:PC71BM, fitted using CompleteEASE software with a General Oscillator model with a mean square error of 21, and for the other materials the data was the same as that used in reference 69.[69]

2.3 Results and Discussion

2.3.1 *Active Layer Morphology Control*

The processing conditions of the active layer must be optimized, as they have a direct impact on the morphology and thickness of the active layer, and therefore its optical and electronic properties.[99] These conditions include the MW of the polymer used, ratio of the blended materials, precursor solution concentration, spin speed, and annealing temperature. One of the most important parameters for device performance was found to be the average molecular weight (low-MW, mid-MW, or high-MW) of the polymer used. Absorption, photoluminescence, and EQE spectra of films and devices fabricated using F8T2 with different molecular weights are given in Fig. 2-3a-c, respectively.

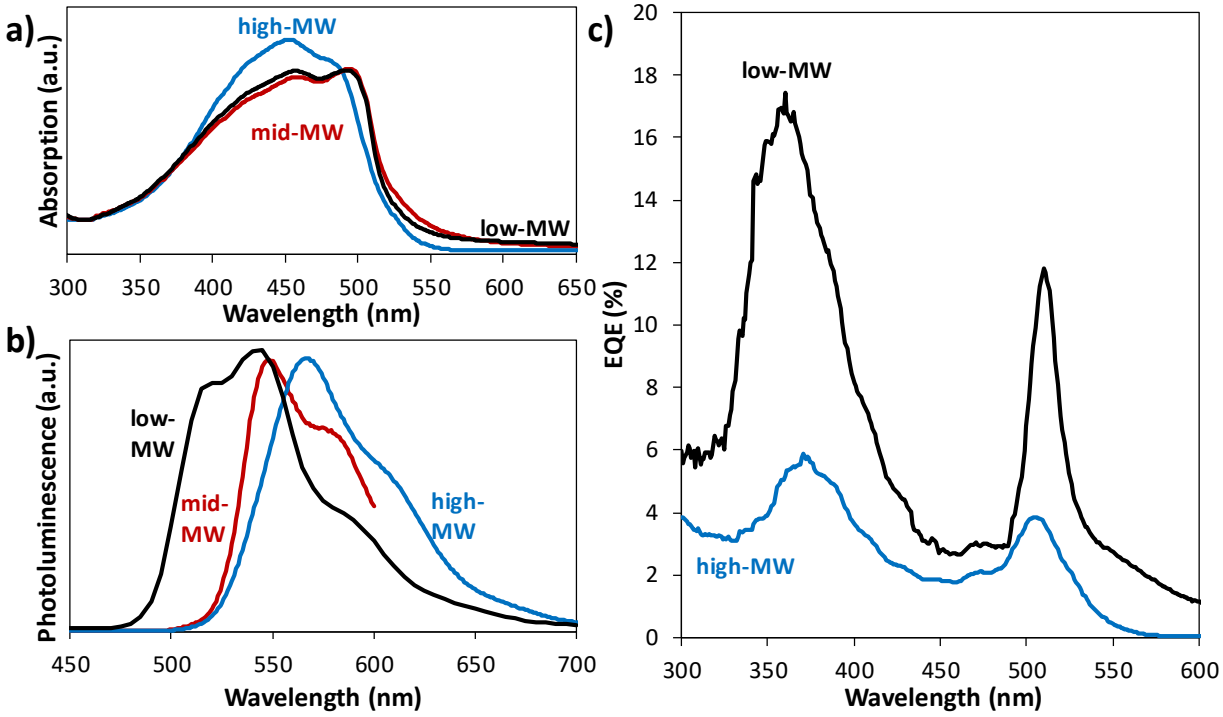

Figure 2-3. (a) UV-Vis absorption spectra for pure F8T2 films with high-, mid-, and low-MW at concentrations of 15, 20, and 40 mg/mL, respectively, normalized by the absorption of each film at 315 nm. (b) Photoluminescence spectra for blend films with a F8T2:$PC_{71}BM$ ratio of 100:1, w:w. The total concentration for the low-, mid-, and high-MW films was 40, 40, and 15 mg/mL, respectively. Each spectrum was normalized by film thickness. (c) EQE spectra at a -20 V bias for devices with active layers corresponding to the low-MW and high-MW films in (b).

The absorption spectra for pure high-MW F8T2 films (Fig. 2-3a) exhibit a different shape compared to the low- and mid-MW samples, which behave similarly to each other. These curves were normalized by the absorption at 315 nm to account for film thickness variation due to the different molecular weights and precursor solution concentrations used. The photoluminescence spectra were normalized, by film thickness, to be between 0 and 1 and these spectra for 100:1 blend films (Fig. 2-3b) show a clear blue-shift, indicating better UV-selectivity, for decreasing molecular weight. Using low-MW polymer also enhanced the EQE performance (Fig. 2-3c). The values obtained from low-MW devices are significantly higher, peaking around 18% at 360 nm compared to about 5% for high-MW devices with a -20 V applied bias. The devices made with low-MW F8T2 also proved to be more stable under strong reverse biases (up to -40 V) while the devices made with high-MW F8T2 were not stable under applied reverse biases higher than -20 V. It should also be noted that solutions and films were easier to fabricate using low-MW and mid-MW F8T2; high-MW solutions were too viscous to filter by our methods, and produced films with diminished consistency and uniformity.

Active layer thickness, controlled by precursor solution concentration and spin speed, can also impact device performance. EQE spectra of devices with an identical structure except for the active layer film thickness are shown in Fig. 2-4a to illustrate the impact of an active layer that is too thin. The device structure was ITO/PEDOT:PSS/F8T2:$PC_{71}BM$(100:4)/LiF/Al, made with high-MW F8T2 with a total precursor solution concentration of 15 mg/mL. The thick device had an active layer spin cast at 1000 rpm and the thin device had an active layer spin cast at 1600 rpm, both for 30 s, resulting in respective thicknesses of 130 nm and 90 nm.

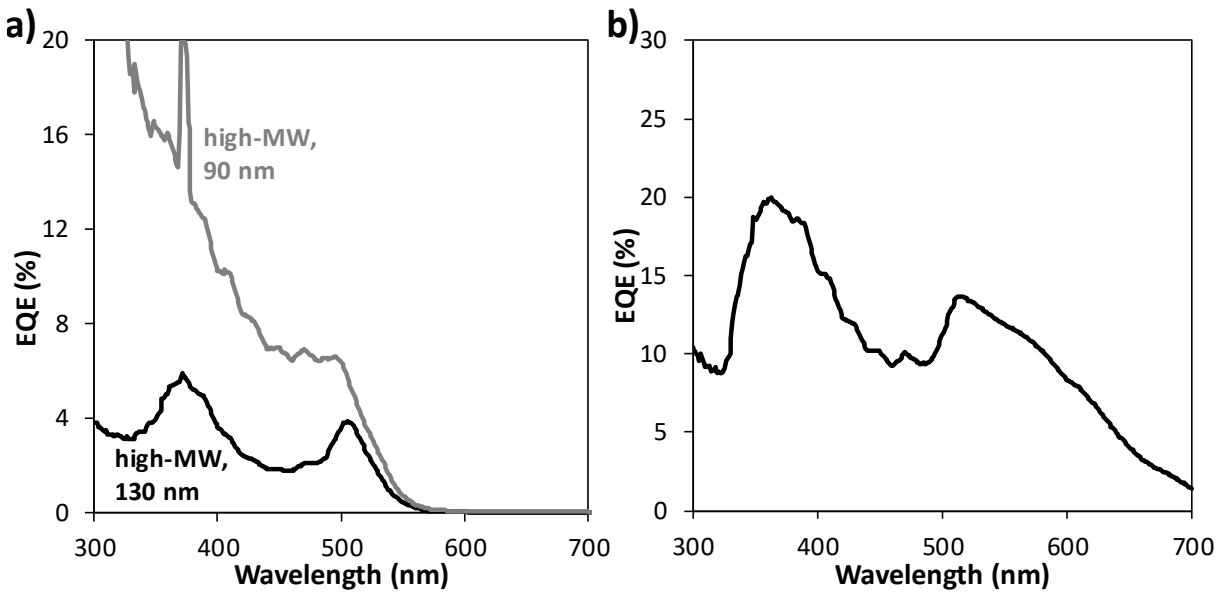

Figure 2-4. (a) EQE spectra of two devices, with high-MW F8T2 blended in a 100:4 weight ratio with $PC_{71}BM$, with different active layer thicknesses under a reverse bias of -20 V. (b) EQE of a device based on an active layer with an F8T2:$PC_{71}BM$ ratio of 1:1, w:w, using mid-MW F8T2 and annealed at 100°C, tested under an applied reverse bias of -2 V. The device structure is ITO/PEDOT:PSS/F8T2:$PC_{71}BM$/LiF/Al.

This work focused on F8T2:$PC_{71}BM$ blends that heavily favored F8T2, so the $PC_{71}BM$ would form isolated clusters and enable photomultiplication via charge trapping, band bending, and charge injection. To contextualize this response, devices with an F8T2:$PC_{71}BM$ ratio of 1:1, w:w, forming a BHJ in the active layer, were also fabricated and evaluated. The EQE under a -2 V applied bias is shown in Fig. 2-4b, having a different shape than the spectra produced with photomultiplication, discussed in section 2.3.3. Importantly the EQE of BHJ-based photodiode devices can never exceed 100% and they are far less stable under strong reverse biases. The EQE spectrum for a device with a BHJ active layer also has a spectrally distinct shape, indicating that mechanistic differences exist between the BHJ photodiode device and those that undergo photomultiplication. Notably, the dip between peaks is mild and there is no sharp cutoff outside the UV region. Instead, the photoresponse gradually decreases throughout the visible range, like the absorption of $PC_{71}BM$ (Fig. 2-5a) which becomes significant in films that are 50% $PC_{71}BM$.

Fig. 2-5 demonstrates the film properties resulting from blends of F8T2:$PC_{71}BM$ with 100:4 and 100:1 weight ratios. The UV-Vis absorption spectrum of pure F8T2 (Fig. 2-5a) shows strong absorption between 350-550 nm with a sharp cutoff around 550 nm. A pure $PC_{71}BM$ film absorbs a relatively small amount of light throughout the visible region, gradually decreasing as wavelength increases. Blended films with F8T2:$PC_{71}BM$ weight ratios of 100:4 and 100:1, also represented in Fig. 2-5a, absorb light similarly to pure F8T2 films, with strong UV absorption and a sharp cutoff around 550 nm, but the absorption decreases with increasing $PC_{71}BM$ content. Because the F8T2-based films have similar thicknesses and each curve was normalized by the absorption at 315 nm, this decrease can be attributed to the increase in $PC_{71}BM$ content.

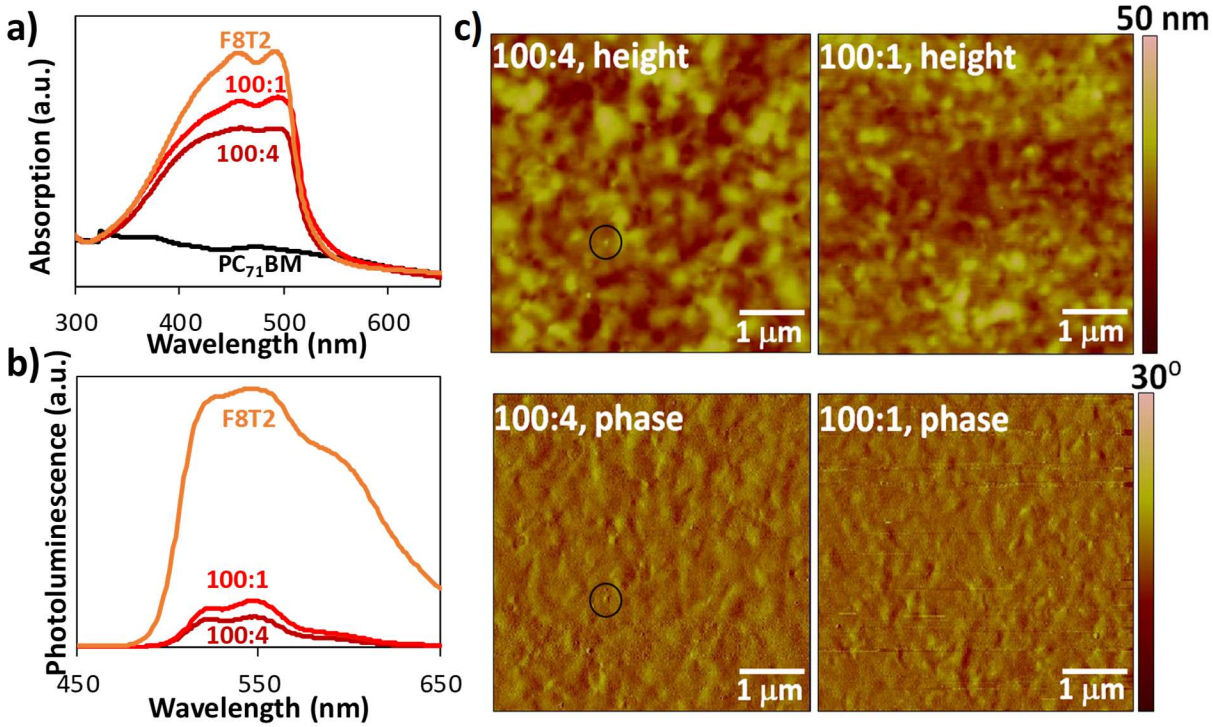

Figure 2-5. (a) UV-Vis absorption spectra of F8T2, $PC_{71}BM$, and F8T2:$PC_{71}BM$ blend films with 100:4 and 100:1 weight ratios, normalized by the absorption of each film at 315 nm. (b) Photoluminescence spectra of F8T2 and F8T2:$PC_{71}BM$ blend films with 100:4 and 100:1 weight ratios with light incident from the top of the films. (c) AFM images for F8T2:$PC_{71}BM$ blend films with 100:4 and 100:1 weight ratios.

Figure 2-5b shows a significant decrease in photoluminescence for both blended films compared to pure F8T2, signifying that even a small amount of $PC_{71}BM$ quenches

photoluminescence by allowing excitons to separate at F8T2:$PC_{71}BM$ junctions rather than recombine in F8T2.[27] Height and phase AFM images of the blend films are shown in Fig. 2-5c. The morphology and surface roughness of both films are similar but small spots, which might be $PC_{71}BM$ aggregates, are visible in the 100:4 film images (one is circled as an example) much more prominently than in the 100:1 film images. The active layers of all four types of devices discussed in this work were fabricated using low-MW F8T2, blended with $PC_{71}BM$ at a total concentration of 40 mg/mL in either a 100:1 or 100:4 weight ratio, spin cast at 1000 rpm for 30 s, and annealed at 80°C for 10 min.

2.3.2 *Photomultiplication Mechanism*

We fabricated photodetectors with a conventional device structure of ITO/PEDOT:PSS/F8T2:$PC_{71}BM$/LiF/Al (Fig. 2-6a), where ITO and Al are the anode and cathode, respectively, and PEDOT:PSS and LiF are the HTL and ETL/HBL, respectively. Low $PC_{71}BM$ content films with F8T2:$PC_{71}BM$ weight ratios of 100:4 and 100:1 were used as the active layer for the devices labeled Device 100:4-LiF and 100:1-LiF, respectively. Since it has been reported that the absence of an ETL can lead to more efficient photomultiplication,[31] we also fabricated devices without the LiF ETL/HBL layer with the same F8T2:$PC_{71}BM$ weight ratios of 100:4 and 100:1, which are labelled Device 100:4-noLiF and 100:1-noLiF, respectively. In the dark, without or with a reverse bias (Fig. 2-6b and c, respectively), the large hole-injection barrier of 1.2 eV from the Al cathode into the HOMO of F8T2 can effectively block hole injection. Despite the relatively low electron-injection barrier of 0.4 eV from the anode into the LUMO of $PC_{71}BM$, isolated $PC_{71}BM$ aggregates do not provide a physical pathway for electron injection to occur. Therefore, low dark current is maintained in these devices, even under strong reverse biases. Under illumination, excitons are generated in F8T2 domains and diffuse to the boundaries of $PC_{71}BM$

clusters, unless they are generated too far from $PC_{71}BM$ clusters, in which case the excitons simply recombine. The electrons that cross the junction into $PC_{71}BM$ become trapped, as shown in Fig. 2-6d, due to the high barrier of about 1.2 eV between the LUMO levels of F8T2 (-3.1 eV) and $PC_{71}BM$ (-4.3 eV). Under illumination and an applied reverse bias, as in Fig. 2-6e, these trapped electrons accumulate near the Al cathode and cause the active layer energy bands to bend at the interface, which lowers the tunneling distance and therefore the barrier for holes to inject from the Al cathode into the HOMO of F8T2. By this mechanism of electron trapping, band bending and hole injection, multiple charge carriers can be collected per incident photon, so photomultiplication and an EQE over 100% can be obtained.

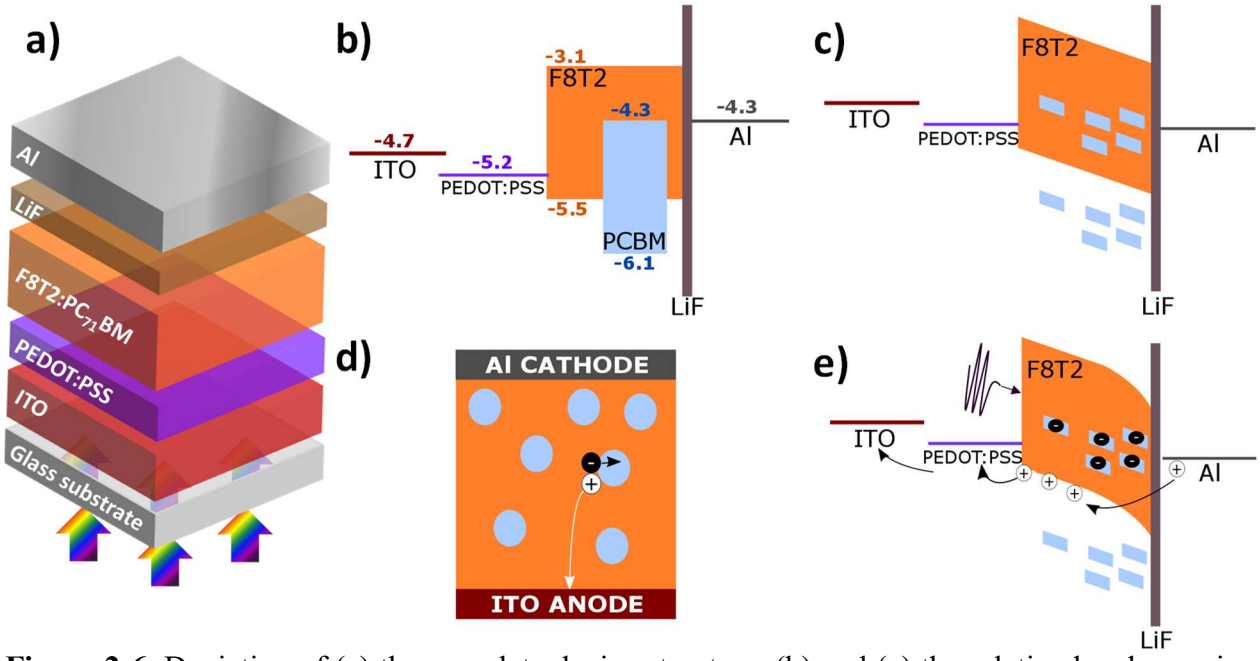

Figure 2-6. Depiction of (a) the complete device structure, (b) and (c) the relative band energies of the layers in the dark without and with applied reverse bias, respectively, (d) the active layer morphology with isolated $PC_{71}BM$ clusters and the resulting charge trapping, and (e) the relative band energies of the layers under illumination and a reverse bias, illustrating the photomultiplication mechanism.

2.3.3 *EQE Strength and Spectral Analysis*

EQE spectra for Device 100:4-LiF measured under varied reverse bias are shown in Fig. 2-7. Each spectrum was taken under constant applied reverse bias, starting at 0 V and increasing by 2 or 4 V intervals to -40 V. To maintain legibility, only some of these spectra are shown in Fig. 2-7, but most measured spectra followed the same trends. EQE values increased with applied reverse bias, due to the enhanced hole tunneling injection and improved hole transport resulting from the increasing strength of the internal electric field of the device.[30, 36] Two peaks are observed, one between 330-420 nm cresting at 360 nm and a second sharp, narrow peak at 510 nm, with a dip in between. At low biases (Fig. 2-7a) all EQE values are very small, remaining under 1% even for a -6 V applied bias, but when the applied bias is over -24 V (Fig. 2-7b) the EQE reaches values over 100% and photomultiplication is realized.

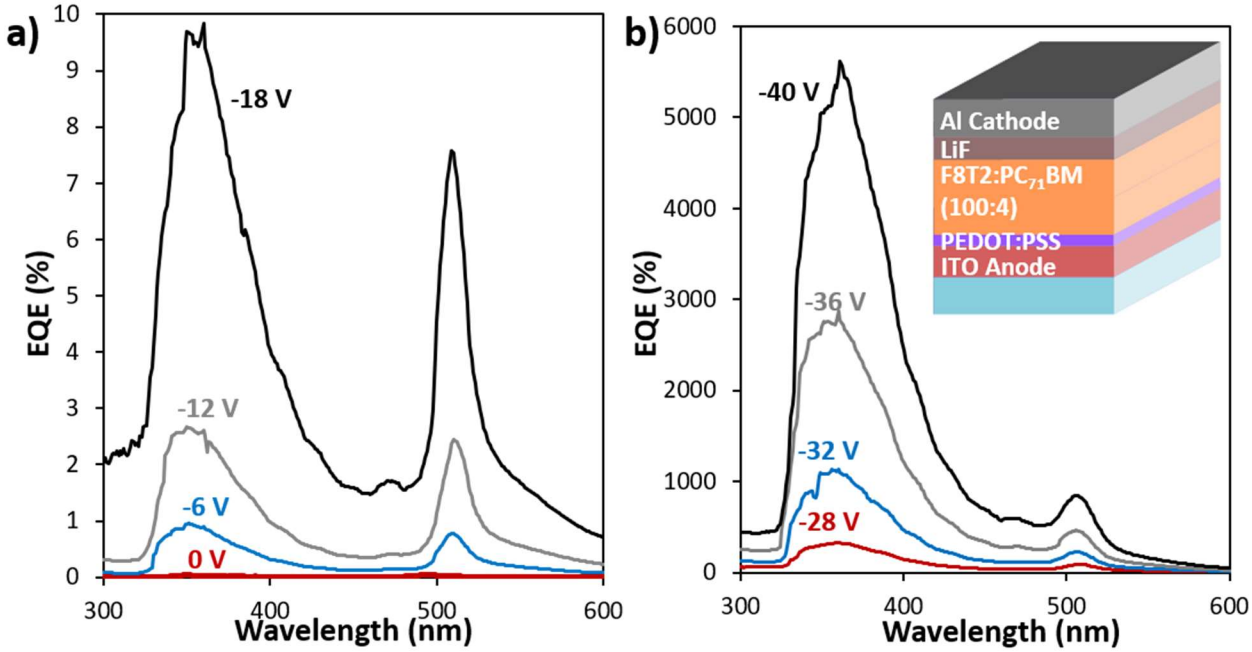

Figure 2-7. EQE spectra for Device 100:4-LiF taken under (a) moderate to no reverse bias and (b) strong reverse bias. The device structure is shown as an inset in (b).

Notably, the device maintains good behavior under reverse biases as strong as -40 V, resulting in a peak EQE value of 5600% at 360 nm. Comparing Fig. 2-7a and b demonstrates that the relative

size of the 360 and 510 nm peaks depends on the bias. At lower applied biases (Fig. 2-7a), the two peaks are very similar in height, but at a -18 V applied bias the 360 nm peak starts to grow stronger than the 510 nm peak. In Fig. 2-7b, with reverse biases between -28 and -40 V, the 360 nm peak dominates the curve and the peak at 510 nm becomes almost negligible. Because the peak at 360 nm increases more rapidly with increasing reverse bias than the peak at 510 nm does, it can be concluded that the device response becomes more UV-selective as the bias is increased, and strong UV-selectivity is achieved under strong reverse biases.

We further increased the F8T2:$PC_{71}BM$ ratio to 100:1, w:w, for Device 100:1-LiF to evaluate the impact of lower $PC_{71}BM$ content on device performance. The EQE spectra of Device 100:1-LiF tested under strong reverse biases (-28, -32, -36 and -40 V) are shown in Fig. 2-8a. Like the spectra of Device 100:4-LiF, the EQE values increase with reverse bias and display two peaks around 360 nm and 510 nm with a dip between. However, the EQE values obtained from Device 100:1-LiF are much smaller than those from Device 100:4-LiF, peaking at just over 1600% at 360 nm under a -40 V bias. The lower EQE could be due to a smaller number of $PC_{71}BM$ electron traps near the Al cathode in Device 100:1-LiF compared to Device 100:4-LiF, and thus less efficient photomultiplication. As observed in the AFM images in Fig. 2-5c, there are small, prominent spots in the image of the 100:4 blend film, which we hypothesize to be $PC_{71}BM$ aggregates. The obscurity of spots in the image of the 100:1 blend film would then correspond to fewer $PC_{71}BM$ clusters near the top of the film, leading to the inferior EQE performance of Device 100:1-LiF compared to Device 100:4-LiF.

The EQE spectra of Device 100:4-noLiF, with a 100:4, w:w, F8T2:$PC_{71}BM$ ratio but without LiF, are shown in Fig. 2-8b. The device yielded EQE values of 10,200%, 25,900%, 48,000% and 68,900% at 360 nm with the applied reverse biases of -28, -32, -36 and -40 V, respectively. These

EQE values are much higher than those of 330%, 1,100%, 2,800% and 5,600% obtained under the same respective biases from Device 100:4-LiF at 360 nm, which is consistent with the literature.[31] In Device 100:4-LiF and 100:1-LiF, LiF functions as both an ETL and HBL, so its removal makes hole injection easier, increasing the amount of current collected but also destabilizing the device. Devices 100:4-noLiF and 100:1-noLiF both exhibited unstable and inconsistent behavior, which will be discussed further in section 2.3.5.

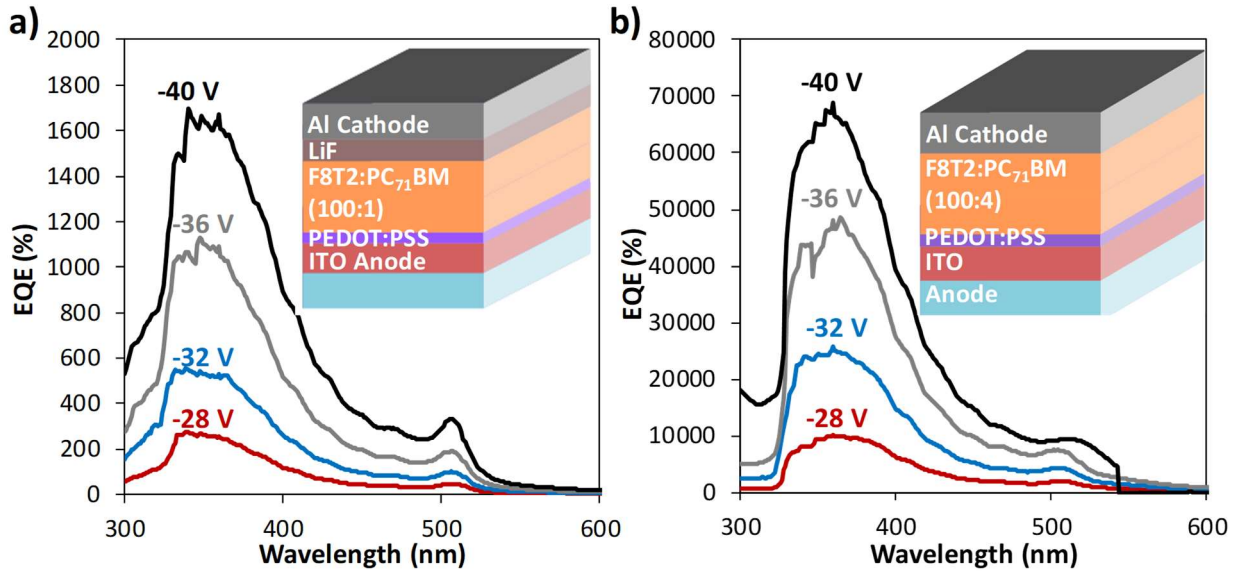

Figure 2-8. EQE spectra obtained under strong reverse biases for (a) Device 100:1-LiF and (b) Device 100:4-noLiF. Device structures are shown as insets.

The spectral shape of the EQE obtained from these devices is not immediately intuitive because the EQE dips where the F8T2 absorption is the strongest. The phenomenon has been similarly reported for a P3HT:$PC_{71}BM$ system[30] and can be understood using the distributions of the electric field intensity and the exciton generation rate throughout the device as a function of incident light wavelength. Fig. 2-9 shows simulated (Fig. 2-9a,c) and experimental (Fig. 2-9b) results of Device 100:4-LiF with the simulation structure of ITO(100 nm)/PEDOT:PSS(40 nm)/F8T2:$PC_{71}BM$(100:4, 350 nm)/Al(100 nm) for Fig. 2-9a and c. The LiF layer of Device

100:4-LiF was thin enough (0.8 nm) that it did not have a significant impact on the simulations and was therefore excluded for simplicity.

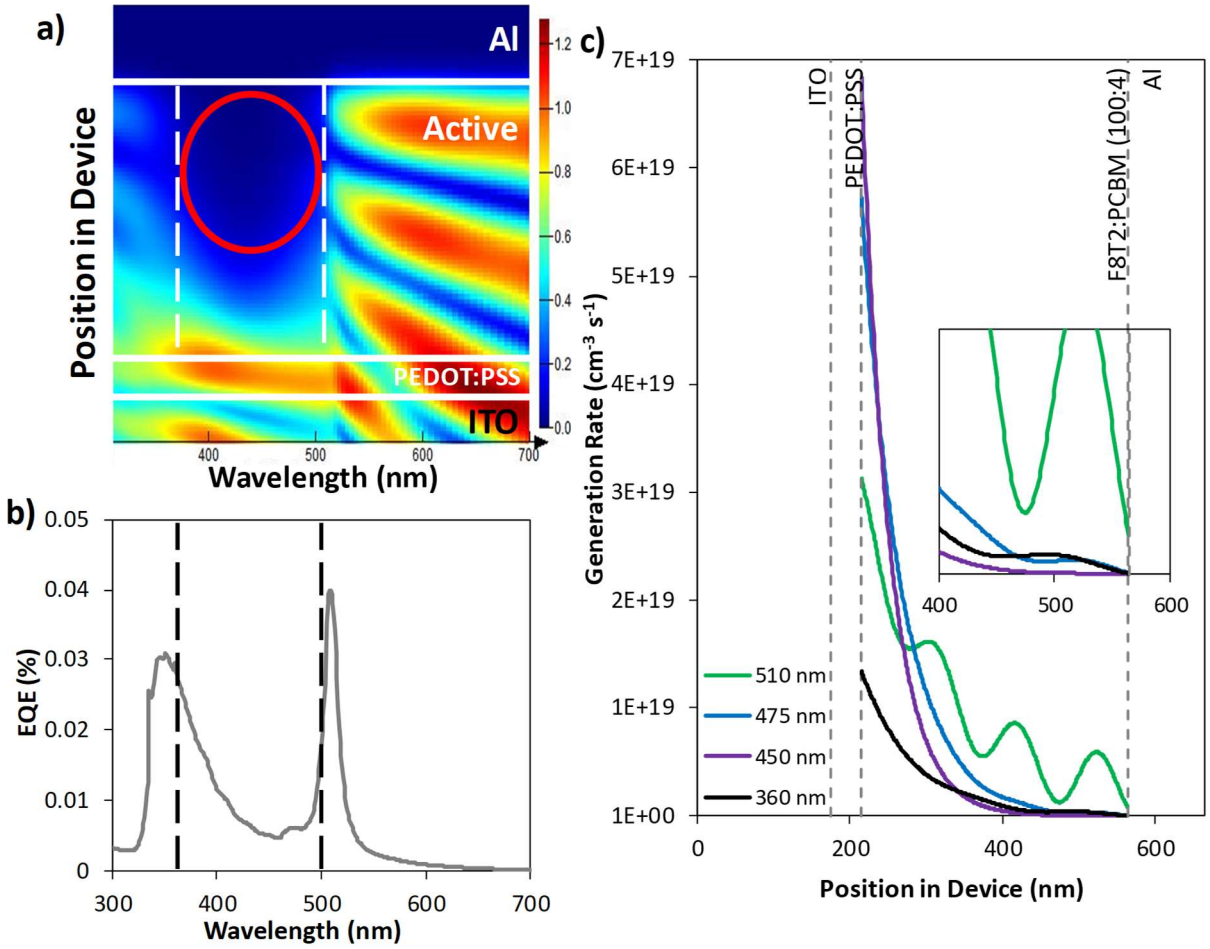

Figure 2-9. (a) The simulated electric field ($|E/E_0|$) present throughout the device, with no applied bias, upon illumination with light in the wavelength range of 300 to 700 nm, from the ITO side. (b) A sample EQE curve for Device 100:4-LiF with no applied bias. Low intensity in the internal electric field is marked with a red circle in (a) and the affected wavelength range is indicated with dashed lines in both (a) and (b). (c) The simulated exciton generation rate throughout the device for monochromatic 360, 450, 475, and 510 nm illumination, with no applied bias. The inset shows a close-up on the active layer near the Al cathode.

FDTD simulations were performed to obtain the internal electric field distribution under illumination. TMM simulations were performed to obtain the exciton generation rate results. Light within the peak absorption of F8T2, from about 400-500 nm generates a strong electric field near the active layer/PEDOT:PSS interface, but it decays quickly as it moves up into the rest of the active layer, as shown in Fig. 2-9a. This range corresponds directly to the dip in EQE in Fig. 2-9b.

This light is absorbed quickly within the active layer, so it only generates excitons in the lower portion of the active layer, as demonstrated by the position-dependent exciton generation rate for 450 and 475 nm light in Fig. 2-9c.

On either side of this range, the electric field extends much further into the active layer (Fig. 2-9a) generating a strong photoresponse at the edges of the F8T2 absorption range, around 360 and 510 nm (Fig. 2-9b). Illumination at 360 nm generates excitons further into the active layer than light at 450 or 475 nm, and has a second, smaller peak near the top of the active layer, shown in the inset of Fig. 2-9c. Since the photomultiplication mechanism relies on trapped charges accumulating at the top of the active layer, this peak enables the device to utilize this photomultiplication mechanism. Light at 510 nm also generates excitons throughout the entire active layer (Fig. 2-9c), so a photoresponse is also produced at this wavelength (Fig. 2-9b). Because this peak is a result of light being absorbed and generating excitons throughout the active layer, it is not as sensitive to the applied bias as the peak at 360 nm, which is the result of electrons being trapped near the top of the active layer and enabling hole injection. Both the processes of hole injection and the subsequent transport of holes across the entire thickness of the active layer to be collected at the ITO anode will be enhanced by the application of stronger reverse biases, so the peak at 360 nm is very sensitive to bias.

Fig. 2-10a plots the ratio of the EQE peak heights at 360 and 510 nm against applied bias. This ratio is always above unity, even without any applied bias, and generally increases with reverse bias, quantitatively confirming that the devices become more UV-selective under stronger biases. Device 100:4-LiF possesses the clearest demonstration of this, quantifying the dramatic growth of the 360 nm peaks in Figs. 2-7 and 2-8. The ratio remains close to 1 between 0 and -20 V, then increases significantly with bias to 6.65 at -40 V. The ratio could not be calculated reliably for

Devices 100:1-LiF and 100:4-noLiF at biases between 0 and -14 V, due to noise and inconsistency in the data. It was obtainable at stronger biases, but for Device 100:1-LiF, the ratio fluctuated between 4 and 7 instead of following any clear trend. The ratio for Device 100:4-noLiF remained around 5 until a bias of -30 V was reached, at which point it steadily increased to 7.25 at -40 V. It should be noted that this comparison is for two peaks, and the EQE at 360 nm can also be compared to the EQE in the unresponsive region, for example at 650 nm. The ratios of EQE at 360 and 650 nm for Devices 100:4-LiF, 100:1-LiF, 100:4-noLiF, and 100:1-noLiF are 247, 143, 1100, and 47.3, respectively, demonstrating strong UV-selectivity.

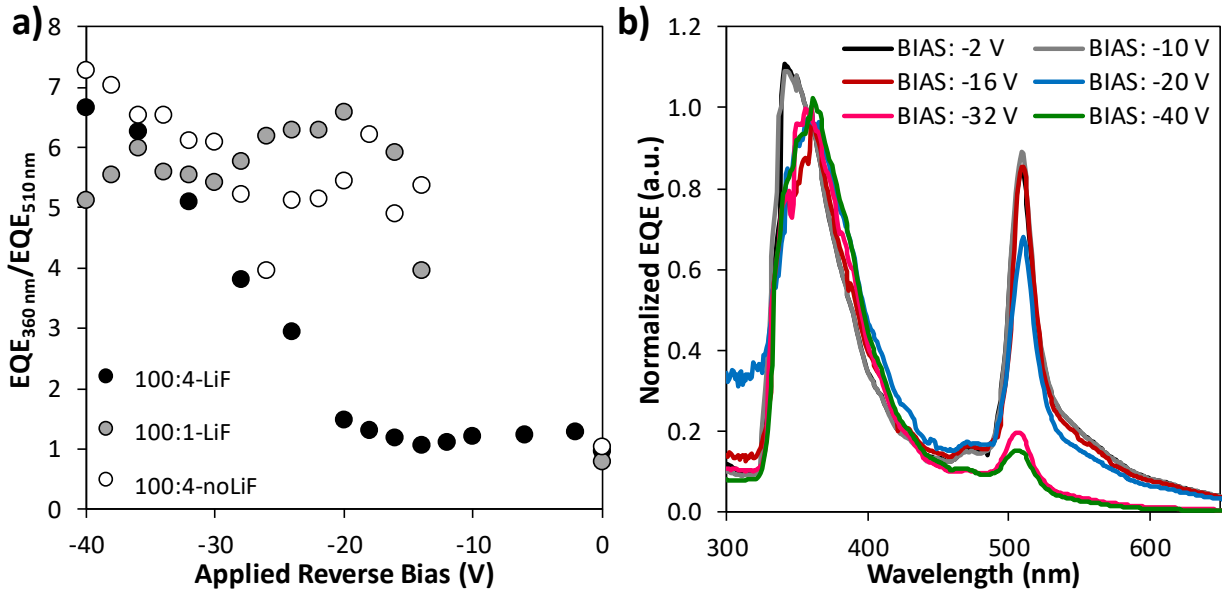

Figure 2-10. (a) The ratio of the EQE at 360 nm to the EQE at 510 nm for Devices 100:4-LiF, 100:1-LiF and 100:4-noLiF under varied reverse biases. (b) EQE spectra for Device 100:4-LiF at varied applied reverse biases, normalized by the EQE value at 360 nm.

Fig. 2-10b shows the EQE spectra normalized by the value at 360 nm. Unlike photodetectors made with P3HT:$PC_{71}BM$,[36] there is no obvious increase of EQE values within the dip region with increasing reverse bias in Fig. 2-10b. This suggests that the clusters of $PC_{71}BM$ in the blend film of F8T2:$PC_{71}BM$ (100:4) are concentrated towards the top of the film, rather than uniformly distributed in the active layer, as was hypothesized based on the AFM image in Fig. 2-5c. The EQE in the dip region was reported to increase with reverse bias in devices with P3HT:$PC_{71}BM$

blends because $PC_{71}BM$ traps were present throughout the film. Electrons trapped in the lower portion of the film could hop from trap to trap and contribute to photomultiplication, and this hopping was enhanced under strong reverse biases.[36] In our F8T2:$PC_{71}BM$ devices, however, this dip in EQE remains deep even with increasing reverse bias, confirming our hypothesis that $PC_{71}BM$ clusters are more concentrated near the cathode. When excitons are generated near the bottom of the film as they are in the peak absorption range of F8T2 (Fig. 2-5a), corresponding to the dip in EQE between about 400-500 nm, they do not result in trapped charges due to the lack of isolated $PC_{71}BM$ clusters in the lower portion of the active layer. Therefore, as reverse bias is increased, there is no trap-to-trap hopping possible to increase the EQE in this spectral range.

2.3.4 *J-V Characteristics and Shifting Behavior*

Fig. 2-11a-b shows the J-V curves of Device 100:4-LiF in the dark and under illumination where the photocurrents were normalized with respect to the incident optical intensity at each wavelength (360 or 510 nm), shown in Fig. 2-1. A small voltage range is shown in Fig. 2-11a for both fresh devices and devices after exposure to strong reverse bias and illumination during EQE measurements. Fig. 2-11b extends the measurements on exposed devices out to -40 V, demonstrating the stable response of Device 100:4-LiF under strong reverse bias. In general, J_D obtained from our devices is much lower than that obtained from P3HT-based devices, due to the higher injection barrier between Al and F8T2 (Fig. 2-11c) as compared to Al and P3HT (Fig. 2-11d). Values were taken from the literature for the work function of Al[100] and for the HOMO and LUMO levels of LiF,[101] F8T2,[91] and P3HT.[91] The larger injection barrier for F8T2 compared to P3HT also explains the smaller EQE values obtained for F8T2-based devices as compared to analogous P3HT-based devices.[30] Fig. 2-11 also shows that J_{PH} produced is higher under 360 nm than 510 nm illumination, confirming UV-selective photoresponse.

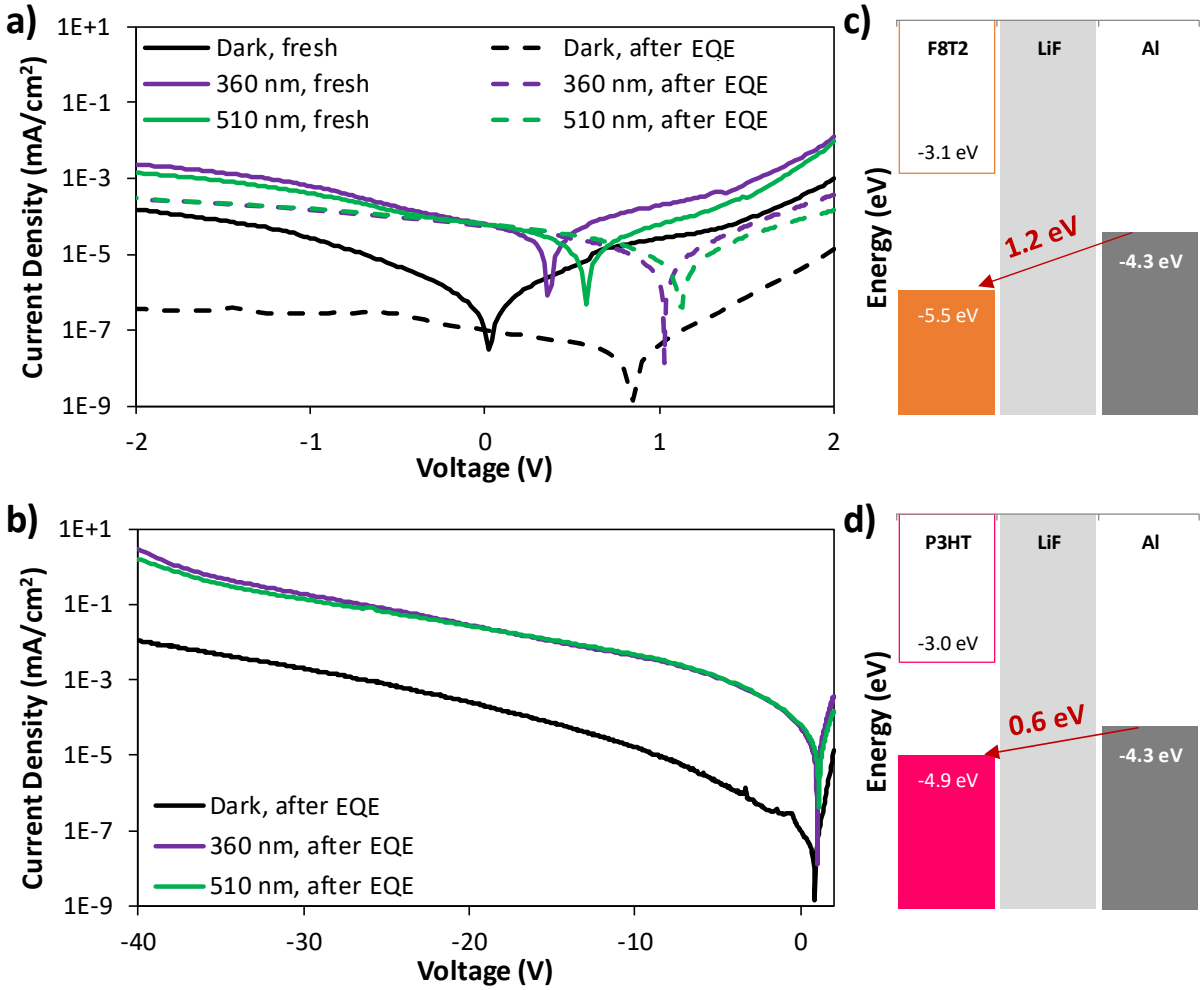

Figure 2-11. (a) Dark and illuminated J-V curves for fresh devices and the same devices after exposure to illumination and strong reverse bias. (b) Dark and illuminated J-V curves measured under reverse biases up to -40 V. All curves were taken by starting at forward bias and scanning towards reverse bias (+2 V to -2 or -40 V), and all illuminated curves were normalized by the optical intensity of the lamp (shown in Figure 2-1) at the corresponding wavelength. Diagrams of the energy barriers to hole injection from the cathode into the HOMO of (c) F8T2 and (d) P3HT.

After the devices underwent EQE measurements, they showed a decrease in both J_D and J_{PH}, as well as a shift in the voltage corresponding to the minimum dark current (V_0) and the open-circuit voltage (V_{OC}). Similarly structured devices with 100:1 P3HT:$PC_{71}BM$ blend active layers were studied under a "burn-in", where devices were exposed to 400 nm illumination and a -25 V, and then a -19 V, bias for 1000 s each.[36] This yielded J_D values, under a -19 V bias, before and after burn-in of 1.3 x 10^{-2} and 7.5 x 10^{-3} mA/cm^2, respectively.[36] Our observed change in behavior before and after EQE measurements (Fig. 2-11a) is similar to this phenomenon, though our dark

current decreases more significantly, by two orders of magnitude from 3.6 x 10^{-5} to 2.7 x 10^{-7} mA/cm^2 under a -1 V bias. Both the reported "burn-in" and our EQE measurements expose the devices to strong reverse bias and direct illumination, so it must be this exposure that causes the change in behavior.

To investigate this shifting J-V behavior, we fabricated three devices that were identical to Device 100:4-LiF and exposed them individually to each of the relevant exposures: strong reverse bias, illumination not resulting in a strong photoresponse (450 nm), and illumination resulting in a strong photoresponse (360 nm). Resulting J-V curves are given in Fig. 2-12. Exposure to strong reverse bias (-40 V) in the dark is explored in Fig. 2-12a for the first device. The current density output was almost constant throughout the exposure to strong reverse bias, in the dark, for 1000 s. This exposure lowered the dark current significantly, as shown in Fig. 2-12a, by about two orders of magnitude as had been observed in Fig. 2-11a, which might be due to a number of effects including an increased capacitive effect induced by strong reverse bias. Interestingly, reverse bias alone had no influence on V_0, which remained around 0 V for both the freshly made device and the device after exposure to strong reverse bias.[1]

Because the change in J-V behavior observed in Fig. 2-11 may be related to charge trapping, we hypothesized that exposure to illumination that would not induce charge trapping would not result in any change in the dark J-V behavior. We used monochromatic 450 nm illumination to test this hypothesis because this wavelength is within the peak absorption of F8T2. It generated the dip in EQE as shown in Fig 2-7, not a photomultiplicative response, indicating that this light was absorbed in the lower portion of the active layer where charge traps are not abundant, so it would not generate a significant amount of trapped electrons. The second device was exposed to 450 nm monochromatic illumination (32.9 μW cm^{-2}) for ~700 s, and the current output remained

constant during this exposure. Dark J-V curves were measured both before and after this exposure and are given in Fig. 2-12b. Clearly, exposure to monochromatic 450 nm illumination with no applied bias did not cause any significant shift in the dark J-V behavior, confirming the hypothesis that this shifting behavior may be related to charge trapping.

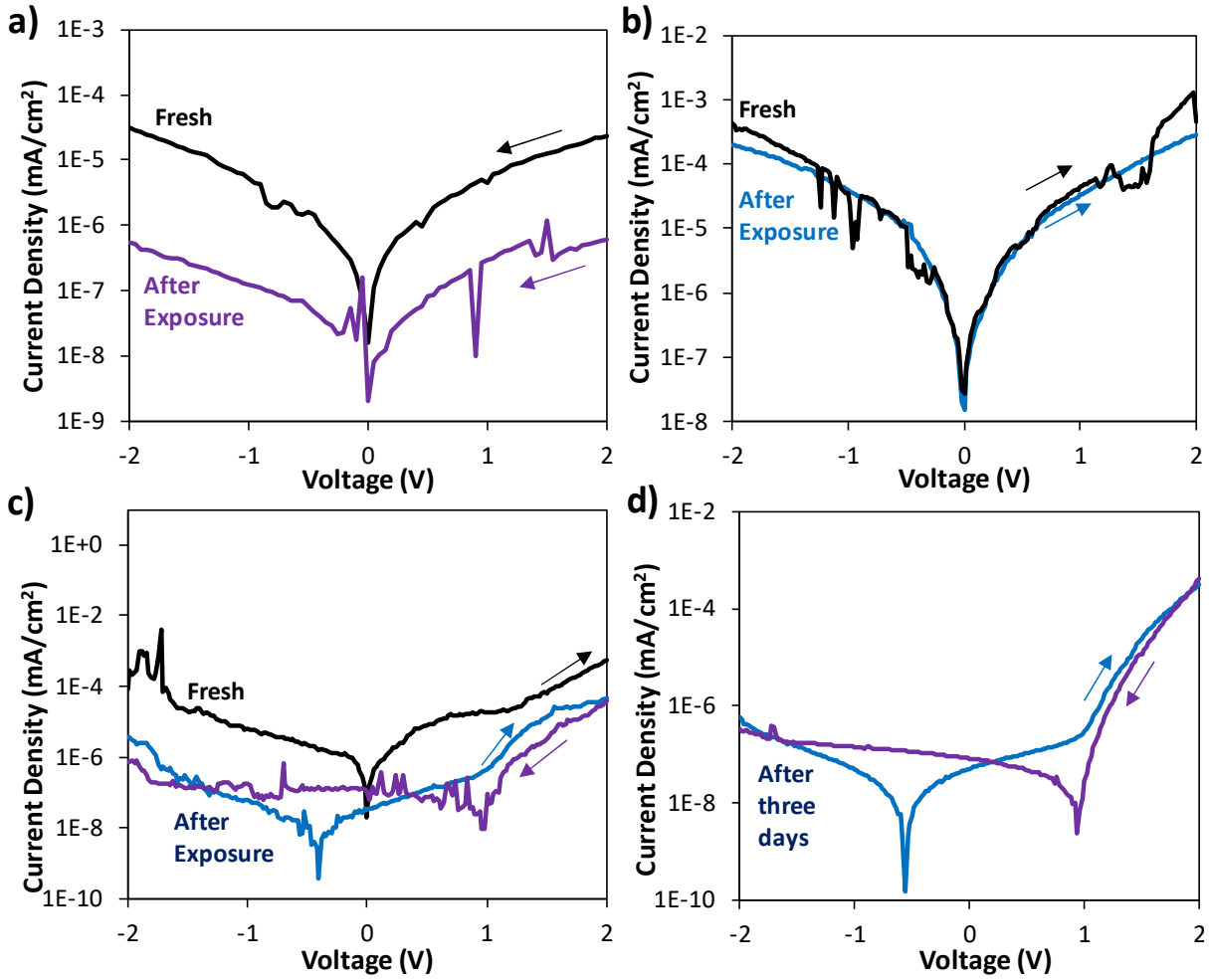

Figure 2-12. (a) Dark J-V measured on the freshly made device and the device immediately after exposure to a reverse bias of -40 V in the dark for 1000 s. (b) Dark J-V measured on the freshly made device and the device immediately after exposure to 450 nm monochromatic illumination with no applied bias. (c) Dark J-V measured on the freshly made device and the device immediately after exposure to 360 nm illumination with no applied bias (d) Dark J-V curves measured on the same device three days after the initial exposure to 360 nm illumination with no applied bias. Scan direction for each curve is indicated with an arrow.

To further confirm this, a third device was exposed to 360 nm monochromatic illumination (21.5 μW cm^{-2}) with no bias applied for >500 s, and the current output again remained constant

during this exposure. Dark J-V curves were taken before and after this exposure and are shown in Fig. 2-12c. After exposure to monochromatic 360 nm illumination alone, not only was the dark current lowered compared to that of a fresh device, but an obvious hysteresis was also observed, with the V_0 shifted away from 0 V to about 1 or -0.4 V, depending on the scan direction (from +2 to -2 V or from -2 to +2 V, respectively). Additionally, when the device was retested after being stored for three days in a N_2-filled glovebox under no exposure to light or bias, it retained this shifted J-V behavior, shown in Fig. 2-12d, rather than returning to its initial behavior. The different impacts of exposure to 360 and 450 nm illumination confirms that the illumination-induced change in J-V behavior observed after EQE measurements may be related to the trapping of charges and the non-uniform distribution of charge traps, which could contribute to an asymmetrical space charge accumulating in the active layer. Ultimately, the J-V behavior shifting observed after exposure to strong reverse bias and charge-trap-inducing illumination in Fig. 2-12 may be caused by a combination of effects including charge trapping, energy level shifting, space charge accumulation, and capacitance.[33, 36, 99, 102, 103]

2.3.5 *Impact of Device Architecture on Stability*

Despite the higher EQE values produced by Device 100:4-noLiF compared to Device 100:4-LiF (Fig. 2-8 and 2-7, respectively), Device 100:4-noLiF exhibited inconsistent performance when different Al electrodes on the same chip were tested. Fig. 2-13 shows the resulting EQE spectra from two different electrodes on Device 100:4-noLiF (Fig. 2-13a) and Device 100:4-LiF (Fig. 2-13b). The performance of Device 100:4-noLiF changes significantly between the two electrodes and is therefore determined to be unstable. Device 100:4-LiF, with less variation between the two electrodes, is shown for comparison. There is some variation between the spectra obtained from Device 100:4-LiF, about 37% difference in peak heights, but this is much smaller than the variation

in the spectra obtained from Device 100:4-noLiF, with about a 77% difference in peak heights. For all devices, the results from the best-performing electrode (100:4-LiF $_1$, 100:4-noLiF $_1$) were shown and discussed throughout the rest of the discussion.

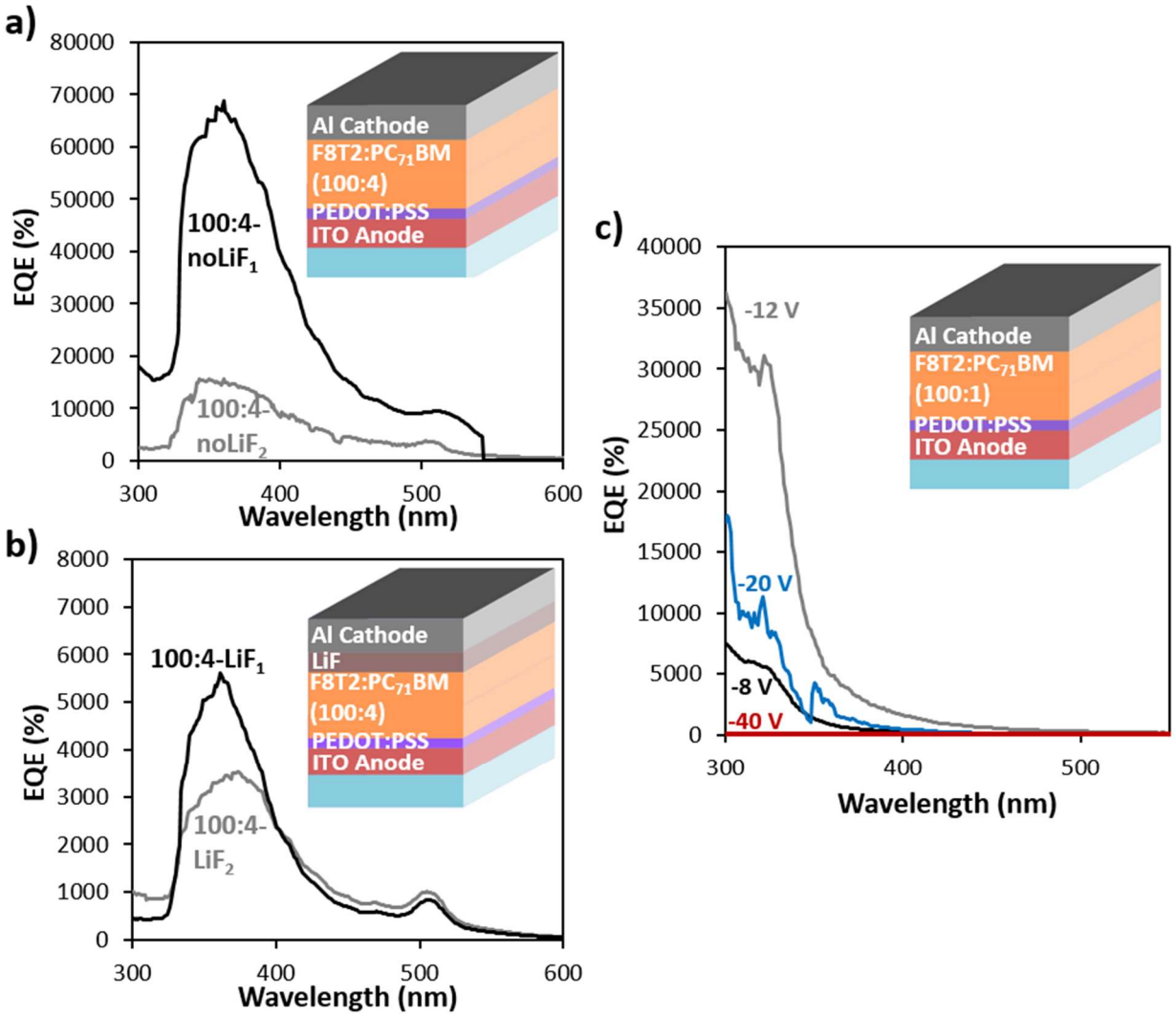

Figure 2-13. (a) EQE spectra for Device 100:4-noLiF under a -40 V reverse bias, where 100:4-noLiF$_1$ and 100:4-noLiF$_2$ represent two different Al electrodes on the same chip. (b) EQE spectra for Device 100:4-LiF under a -40 V bias, where 100:4-LiF$_1$ and 100:4-LiF$_2$ represent two different Al electrodes on the same chip. (c) EQE spectra for one electrode on Device 100:1-noLiF, under varied applied biases.

Lowering the F8T2:PC$_{71}$BM ratio to 100:1, w:w, and excluding LiF for Device 100:1-noLiF resulted in devices with both instability issues and poor performance. EQE spectra for Device 100:1-noLiF are given in Fig. 2-13c under varied applied bias. The performance of this device was

very unstable, following no discernable trend and showing characteristics indicative of avalanche-like breakdown. In general, stable and consistent devices are preferable, even if unstable devices produce higher EQE values, so Device 100:4-LiF is confirmed as the optimal device as analyzed by photoresponse strength, UV-selectivity and device stability.

An inverted device structure, where the cathode is at the bottom of the device and the anode at the top, has also been pursued in this work. In an inverted device, the top electrode can be a metal with a higher work function than Al, such as Ag or Au, which are more stable in air than the lower work function materials used in conventional device.[104, 105] This has been a popular approach in the field of solar cells and to some extent in photodetectors,[48, 59, 104-107] but does not always result in improved performance. In fact, devices with biplanar active layers of F8T2 and C_{60} were reported to produce better performance in a conventional, not inverted, structure.[48] When inverted devices were evaluated in this work, their behavior was unstable and unpredictable. This device structure has therefore not been pursued thoroughly, though some results are given in Fig. 2-14.

The devices represented in Fig. 2-14 had a structure of glass/ITO cathode/ZnO ETL(thickness varied)/F8T2:$PC_{71}BM$(100:4, thickness varied)/MoO_3 HTL(10 nm)/Ag anode(100 nm) and is shown in Fig. 2-14a. ZnO films were prepared from a sol-gel solution, where zinc acetate dihydrate and ethanolamine were dissolved in 2-methoxyethanol with concentrations of 0.1 and 0.3 M to produce 10 and 30 nm films, respectively. The films were spin cast at 6000 rpm for 60 s followed by a 1 h bake at 200°C. All active layers were spun at 1000 rpm for 30 s and annealed at 80°C for 10 min. The device represented in Fig. 2-14b and c had a 30 nm ZnO layer, and an active layer utilizing high-MW F8T2 with a total concentration of 15 mg/mL for the precursor solution, yielding an active layer thickness around 120 nm. The same electrode was used to obtain the J-V curves and EQE spectra shown in Fig. 2-14b and c, respectively. This electrode yielded a low dark

current, around 1 x 10^{-7} mA/cm^2, and a high peak EQE of 320% under 375 nm illumination and a -3 V bias, achieving photomultiplication under a relatively small applied bias. However, it was the only electrode on any inverted device that yielded this good behavior. Generally, the performance of inverted devices was inconsistent and unstable. In fact, even this high-performing device showed a steep increase at short wavelengths, indicating response instability.

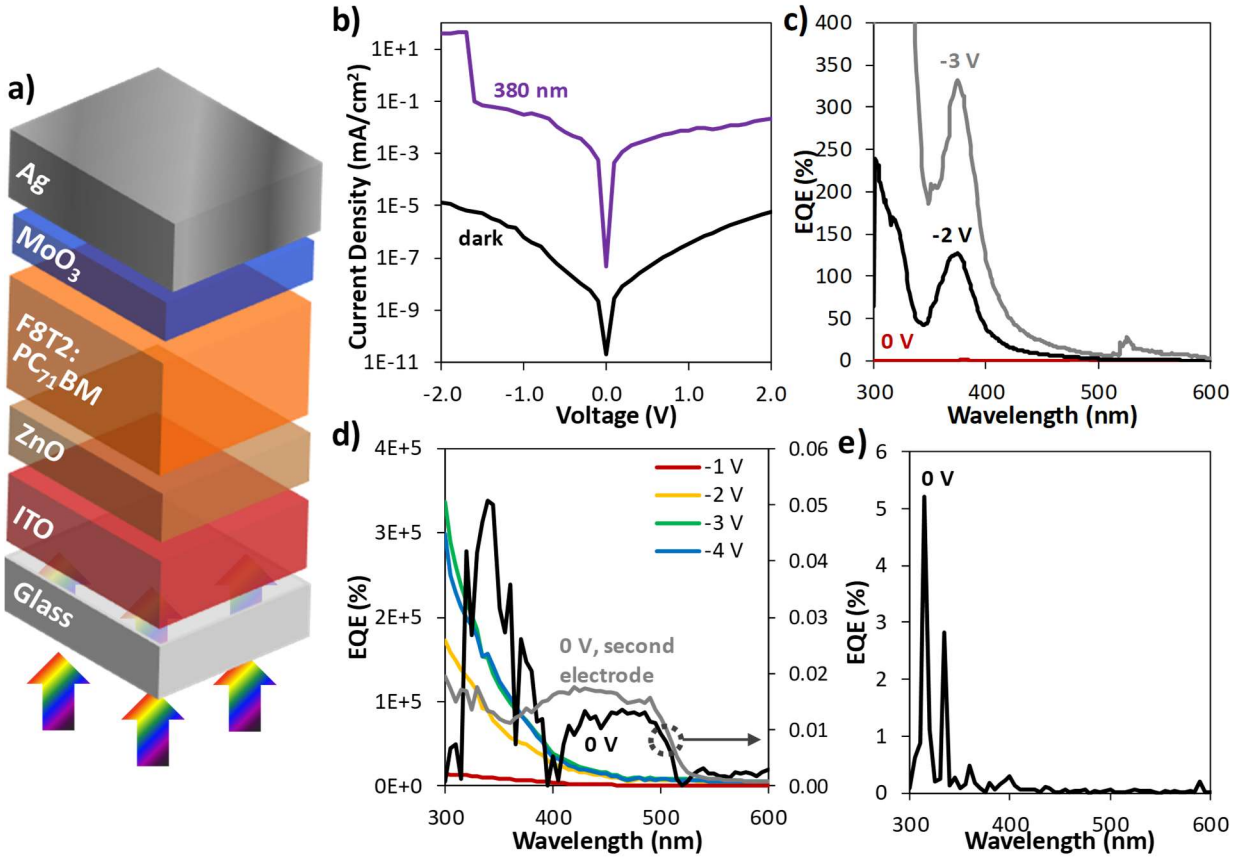

Figure 2-14. (a) J-V curves and (b) EQE spectra for the high-performing inverted device. EQE spectra for unstable inverted devices with ZnO thicknesses of (c) 30 nm and (d) 10 nm. The inverted device structure is given as an inset.

The devices represented in Fig. 2-14d and e were fabricated with low-MW F8T2, and the active layers were fabricated with the same conditions as for conventional devices. In Fig. 2-14d, EQE spectra for a device with a 30 nm ZnO layer are shown. Without any applied bias, this device produced EQE spectra with reasonable shapes that were relatively reproducible from one electrode to the next, but even small applied biases resulted in breakdown-like behavior. The EQE values

increased with increasing reverse bias, but the spectral shape indicates that these curves are unreliable. It was hypothesized that the ZnO ETL layer may be dominating the device response, since ZnO has absorbance in the UV range, so the thickness of this layer was decreased to 10 nm for the device evaluated in Fig. 2-14e. Unfortunately, this did not solve the problem of inconsistent and unstable performance, and in fact even the EQE spectra without any applied bias, shown in Fig. 2-14e, did not have a reasonable shape.

2.3.6 *Comprehensive Device Performance Analysis*

The ideal photodetector will maximize R, which characterizes the strength of the device response, while minimizing J_D, which corresponds to the noise present in the device. The peak R values, active layer thicknesses, and dark currents at -40 V are summarized in Table 2-1.

Table 2-1. Active layer thickness, responsivity (R), and dark current for all devices taken under a reverse bias of -40 V and 360 nm monochromatic illumination.

Device	Active Layer Thickness (nm)	Responsivity ($A\,W^{-1}$)	Dark Current (A)
100:4-LiF	330	15.9	-1.09×10^{-6}
100:1-LiF	360	4.84	-1.18×10^{-6}
100:4-noLiF	330	200	-3.30×10^{-6}
100:1-noLiF	360	7.7×10^{-4}	-1.76×10^{-4}

Peak R values, obtained under 360 nm illumination and -40 V bias, were 15.9, 4.84, 200, and 7.7×10^{-4} A/W for Devices 100:4-LiF, 100:1-LiF, 100:4-noLiF, and 100:1-noLiF, respectively. At 15.9 A/W, Device 100:4-LiF provided the highest R of all devices except for Device 100:4-noLiF, which yielded a responsivity of 200 A/W. However, Device 100:4-noLiF also had a higher dark current of -3.30×10^{-6} A that was more than three times as high as that of Device 100:4-LiF (-1.09×10^{-6} A) and Device 100:4-noLiF exhibited unstable and inconsistent behavior, so Device 100:4-noLiF cannot be presented as optimal. Devices 100:1-LiF and 100:1-noLiF had both lower R (4.84

and 7.7 x 10^{-4} A/W, respectively) and higher dark current (-1.18 x 10^{-6} and 1.76 x 10^{-4} A, respectively) as compared to Device 100:4-LiF. Therefore, the combination of high responsivity and low dark current for Device 100:4-LiF (Table 2-1) make it the apparent superior device of those tested in this work.

The response speeds of devices are shown in Fig. 2-15, where a squarer curve corresponds to a faster device response. Incident 360 nm illumination was turned on and off in 10 s intervals, and the photocurrent produced in the device was measured and then normalized to be between 0 and 1 so that curves obtained from different devices under varied applied biases could be compared. Fig. 2-15a shows the response speed for Device 100:4-LiF tested under two different reverse biases, -28 and -40 V, demonstrating that the device responds faster under stronger reverse bias, likely due to faster charge carrier diffusion and decreased capacitance.[1] In Fig. 2-15b, the response speeds of Devices 100:4-LiF, 100:1-LiF and 100:4-noLiF under the same bias of -40 V are compared. Having a higher $PC_{71}BM$ content increases the size and number of aggregates, making the photomultiplication mechanism more efficient and leading to an increase in both response speed and strength from Device 100:4-LiF compared to Device 100:1-LiF. Devices with and without LiF (Device 100:4-LiF and 100:4-noLiF) are also compared in Fig. 2-15b. The curve obtained from Device 100:4-noLiF is much noisier when the light is turned on than that obtained from Device 100:4-LiF, indicating that the response of Device 100:4-noLiF is unstable. Device 100:4-LiF also has a faster response than Device 100:4-noLiF, indicated by the squareness of the curves obtained from Device 100:4-LiF compared to Device 100:4-noLiF. The only difference between Device 100:4-LiF and C is the respective presence or absence of LiF, so it must be this layer that enhances the response speed of Device 100:4-LiF, most likely due to its impact on the energy level alignment between layers. Including a LiF layer decreases the effective electron transport barrier between the

cathode and active layer, thereby increasing the operating voltage and the charge carrier diffusion.[1, 108, 109] Again, Device 100:4-LiF is confirmed as optimal, both in terms of stability and response speed. A fall time for Device 100:4-LiF was roughly calculated to be 0.5 s, but the accuracy of this value is directly limited by the measurement system. The system took measurements at approximately 0.5 s intervals (Fig. 2-15c), so it is likely that the actual fall time is shorter than the value that was calculable.

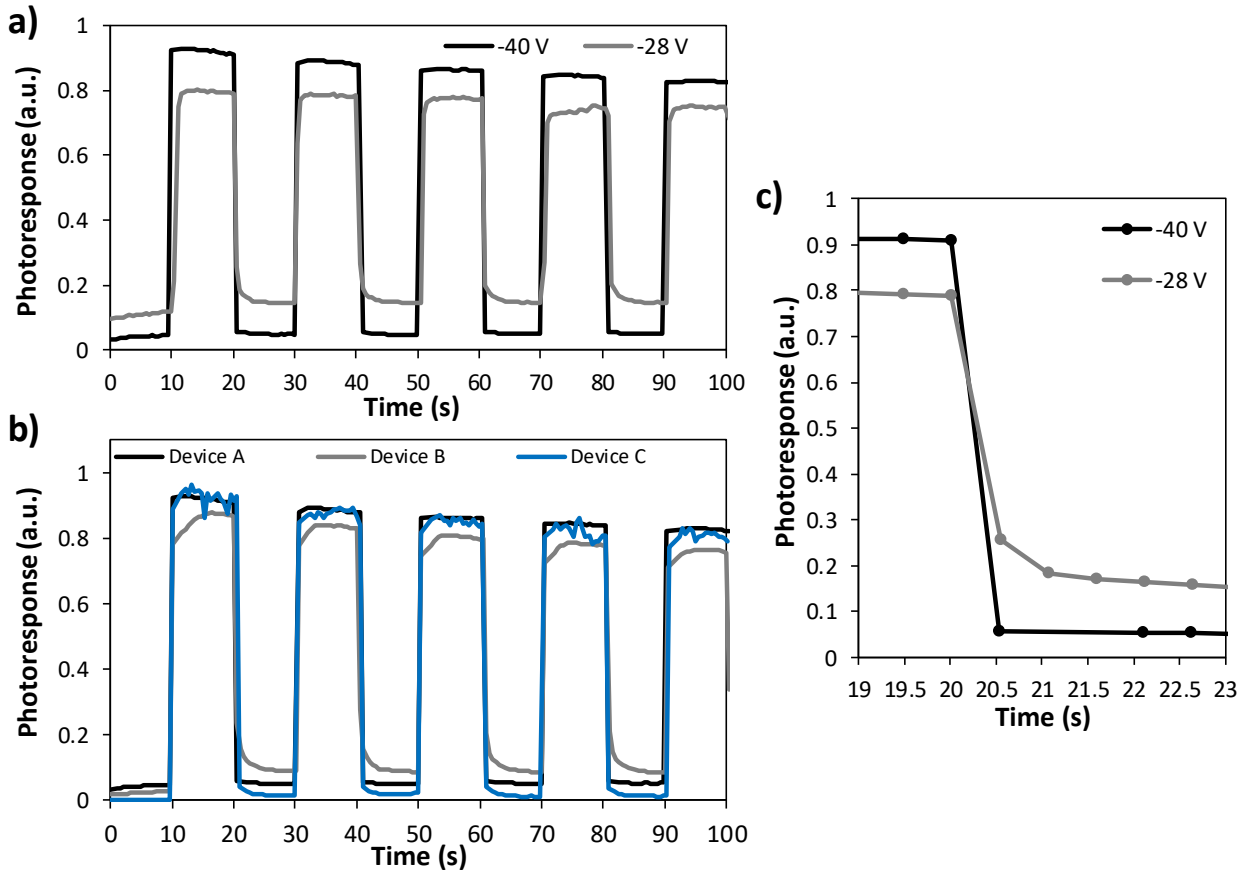

Figure 2-15. (a) The response speed of Device 100:4-LiF to 360 nm monochromatic illumination under two different reverse biases. (b) The response speed of Devices 100:4-LiF, 100:1-LiF and 100:4-noLiF, tested under a -40 V reverse bias with 360 nm monochromatic illumination. (c) A portion of the curves for Device 100:4-LiF in (a), showing the 0.5 s measurement interval.

2.4 CONCLUSIONS

We have fabricated organic, conventional photodetectors utilizing F8T2:$PC_{71}BM$ blend active layers with weight ratios of 100:1 and 100:4, with and without the presence of an ETL/HBL of

LiF. Generally, devices with LiF are more stable, and those with F8T2:$PC_{71}BM$ blend ratios of 100:4 provide the best overall performance, reaching an EQE and R of 5600% and 15.9 A/W, respectively, under 360 nm illumination and a -40 V applied bias, and an extremely low dark current of 2.7 x 10^{-7} mA/cm^2 at a -1 V bias. The F8T2-based devices possess a strong photoresponse that is more UV-selective than other reported organic systems utilizing photomultiplication because of the wide bandgap of F8T2. Strong reverse biases enhance photomultiplication, improve the UV-selectivity and response and demonstrate the stability of these devices. An inverted device architecture was explored but was found to be unstable enough to discourage further investigation. The impressive stability, high UV-selectivity, and impressive performance (high EQE and low dark current) of the conventional devices strengthen the pathway towards the development of large area, flexible organic UV photodetectors.

Chapter 3. TUNING THE SPECTRAL PHOTORESPONSE OF UV PHOTODETECTORS COMPOSED OF PTAA AND ZNO NANOPARTICLES THROUGH CHARGE TRAPPING AND CHARGE COLLECTION NARROWING

3.1 INTRODUCTION

There are many advantages to using organic materials and organic-inorganic hybrids in optoelectronic devices, including low material cost, facile processing and fabrication, and flexibility.[14] Another commonly touted benefit is the tunability of the optical characteristics of organic materials. For UV photodetectors, applications like environmental monitoring and laboratory instrumentation require a broadband UV response, while applications like filter-free imaging and colorimetry require wavelength-specific narrowband response.[14] It is therefore desirable to produce devices based on organic materials with responses that can be tuned between broadband and narrowband.

Organic photodetectors with broad spectral response from UV to NIR were first demonstrated by the Heeger group, using a narrow-bandgap conjugated polymer, poly(5,7-bis(4-decanyl-2-thienyl)-thieno(3,4-b)diathiazole-thiophene-2,5) (PDDTT), blended with $PC_{61}BM$ in a 1:1 weight ratio as the active layer.[110] The device had a structure of ITO/PEDOT:PSS/PDDTT:$PC_{60}BM$/Al and produced photoresponse ranging from 300-1450 nm with D* values exceeding 10^{12} Jones throughout the entire range.[110] Since then, organic-inorganic hybrid systems have also been used to fabricate broadband photodetectors, including many that incorporate quantum dots (QDs) into polymer active layers.[111] The integration of CdSe QDs into a layer of poly(2-methoxy,5-(2'-ethyl-

hexyloxy)-p-phenylenevinylene) (MEH-PPV) broadened the device photoresponse from a relatively narrow peak centered around 550 nm to a broader peak from 420 to 650 nm, due to the optical absorption of the QDs.[112] PbS QDs were incorporated into a P3HT:PCBM blend active layer, resulting in devices with NIR response that could be tuned to extend from 1000 nm to 1200-1700 nm depending on the size of the PbS QDs.[113]

Various mechanisms have been employed to spectrally tune and narrow photodetector response. Typically, a full width at half maximum (FWHM) around or below 100 nm is desired for narrowband devices. One method of achieving this narrow response is focusing on the absorption of the active layer materials. A new squarylium material was recently reported and utilized in thin-film devices producing EQE spectra with a 110 nm FWHM centered around 600 nm, peaking at 66% under a -2.5 V bias.[114] In other systems, active layer thickness and composition were controlled to achieve photoresponse narrowing and enhancement. One photoresponse mechanism relied on CdTe QDs acting as electron traps within a blended active layer of P3HT and PCBM.[53, 115] In devices with thinner active layers around 200-250 nm, the addition of CdTe QDs enabled photomultiplication under illumination between 350-650 nm and a -1 V bias.[115] In devices with active layer thicknesses around 3 μm, the active layer morphology was such that the CdTe QDs were concentrated towards the top of the active layer.[53] In this case, only light at the red edge of the P3HT:PCBM absorption peak, with a long penetration depth, generates significant response, resulting in EQE spectra with narrow response between about 650-750 nm.[53]

The active layer thickness itself can also be used to achieve the desired photoresponse tuning and narrowing. Increasing the thickness of the active layer can cause a narrowing in the photoresponse of the device caused by a mechanism called charge collection narrowing

(CCN).[33] For thick active layers, light within the absorption peak of the active layer is absorbed quickly and does not penetrate far into the active layer, and thus it cannot generate a photoresponse. Light on the edge of the absorption peak, however, penetrates the entire active layer. This light then reflects back into the active layer from the top metal electrode, establishing an interference pattern within the active layer. Because of this, it can be absorbed and generate excitons throughout the entire active layer, resulting in photoresponse only at this long wavelength at the edge of the absorption peak. The CCN mechanism was first demonstrated in devices with thick active layers (1.5, 2 and 3 mm) composed of (poly[N-900-heptadecanyl-2,7-carbazole-alt-5,5-(40,70-di-2-thienyl-20,10,30-benzothiadiazole) (PCDTBT) and poly[2,5-(2-octyldodecyl)-3,6-diketopyrrolopyrrole-alt-5,5-(2,5-di(thien-2-yl)thieno[3,2-b]thiophene)] (DPP-DTT) blended with $PC_{71}BM$ in weight ratios of 1:4 and 1:3, respectively.[33] These devices had spectral responses that specifically narrowed to the edge of the absorption peak for each polymer, producing red (~650 nm) and NIR (~950 nm) photodetectors with FWHM values around 70 and 90 nm, respectively.[33]

In this work, we investigated the spectral response tunability of organic-inorganic hybrid UV photodetectors composed of a wide-bandgap polymer poly[bis(4-phenyl)(2,4,6-trimethylphenyl)amine] (PTAA) blended with ZnO nanoparticles as the active layer in a device with a structure of ITO/PEDOT:PSS/PTAA:ZnO/BCP/Al. PTAA and ZnO were blended in 1:1 and 2:1 weight ratios, and both thin (150-200 nm) and thick (1400-1900 nm) active layers were used. By changing the active layer thickness, we can utilize CCN for UV photodetectors and narrow the photoresponse to the absorption edge of the active layer. The composition of the active layer, relating to the microstructure and thus charge transport

properties, determined the efficacy of CCN in these devices. In addition to enabling and controlling photoresponse tunability, active layer thickness and composition also impacted the J_D, R, D*, response speed, and stability of devices. Through TMM and 3D-FDTD simulations, we predicted that controlling the active layer thickness and composition would enable tuning between a broad photomultiplicative photoresponse and a selective narrowband photoresponse, which we achieved experimentally. This tunability, achieved by changing the simple conditions of active layer composition and thickness, could enable simple and cost-effective production of a variety of UV photodetectors.

3.2 EXPERIMENTAL

3.2.1 *ZnO Nanoparticle Synthesis and Precursor Solution Preparation*

ZnO nanoparticles were synthesized according to the procedure previously reported.[116] Briefly, 2.36 g of zinc acetate dihydrate (≥ 99.0%, Sigma-Aldrich) was dissolved in 100 mL of methanol (≥ 99.9%, Fisher Scientific (Hampton, NH)) at 60°C, and 1.256 g KOH (≥ 85.0%, Fischer Scientific) was dissolved in 52 mL of methanol. The two solutions were combined and stirred at 60°C for 1.5 h, at which point the solution became turbid and was stirred for an additional hour. The ZnO nanoparticles were then collected by centrifuge, washed three times in methanol, dissolved in 1,2-dichlorobenzene at 200 mg/mL, and stored in a refrigerator until use. The hydrodynamic diameter of the nanoparticles was determined using dynamic light scattering (DLS) with Malvern Zetasizer Nano. All solution preparation took place in a nitrogen-filled glovebox. Poly[bis(4-phenyl)(2,4,6-trimethylphenyl)amine] (PTAA) was purchased from Solaris Chem. Inc. (Quebec, Canada). PTAA and ZnO nanoparticles were each dissolved separately in 1,2-

dichlorobenzene with concentrations of 40 mg/mL and 200 mg/mL, respectively. The ZnO nanoparticle solution was removed from the storage refrigerator and handled at room temperature, and the PTAA solution was stirred for at least 12 h at 70°C. Before combining the two solutions, the PTAA solution was cooled to room temperature. The solutions were combined so that the resulting solution would have either a 1:1 or 2:1 weight ratio with total concentrations of 66.7 mg/mL and 55.6 mg/mL, respectively. The combined solution was stirred at room temperature for 5 min before use.

3.2.2 *Film Fabrication and Analysis*

Plain glass slides were cut into 1.5 cm x 1.5 cm squares and cleaned by ultrasonication for 15 min each in soapy deionized (DI) water, DI water, acetone and isopropanol, in sequence, and then by oxygen plasma cleaning at 100 W for 30 s. All film fabrication steps, after substrate preparation, were done in a nitrogen-filled glovebox. The PTAA:ZnO blend precursor solutions were filtered through a 0.45 μm PTFE syringe filter and deposited via spin coating. For thin films, the precursor solution with a ratio of 1:1 or 2:1, w:w, was spun at 1000 rpm or 800 rpm, respectively, for 30 s. For thick films, the precursor solutions for both weight ratios of 1:1 and 2:1 were spun at 400 rpm for 30 s. All films were annealed at 100°C for 10 min. Film analysis was performed in ambient conditions. UV/Vis spectra were collected using a Perkin Elmer Lambda 900 UV/Vis spectrophotometer. Film thicknesses were measured using a KLA Tencor Alpha-Step 500 Profiler. The distribution of ZnO nanoparticles in the thick active layer films was determined with the elemental analysis using energy dispersive X-ray spectroscopy (EDS) on an FEI Sirion SEM.

3.2.3 *Device Fabrication and Characterization*

ITO coated glass substrates (≤ 10 Ω/sq, Colorado Concept Coatings LLC, Loveland, CO) were prepared by the same methods of ultrasonication and plasma treatment as described in Section 3.2.2. PEDOT:PSS solution (Clevios P VP AI 4083, Heraeus, Hanau, Germany) was filtered through a 0.45 μm PTFE syringe filter and spin-coated onto the cleaned ITO-coated glass substrates at 5000 rpm for 40 s, then baked at 120°C for 10 min in air. The chips were then transferred into a nitrogen-filled glovebox. The PTAA:ZnO active layers were deposited via spin coating, under the same conditions as the films described in Section 3.2.2. A 10 nm layer of bathocuproine (BCP) (Sigma-Aldrich), followed by 100 nm Al (99.999%, R.D. Mathis, Long Beach, CA, were deposited via thermal evaporation using an Angstrom Engineering Amod PVD Platform. LiF was deposited without the use of any mask, and Al electrodes were deposited with rectangular masks so that the active area of devices was 0.1 cm^2, and four devices were on each chip.

All device characterizations were performed in ambient conditions. J-V curves, J_D versus time, and EQE spectra were obtained using a Keithley 2635B sourcemeter. Light was provided with a 150 W Xenon arc lamp and an Oriel Cornerstone 130 Monochromator. Optical intensity was measured using a Newport 1918-R Power Meter and Newport UV-Si Photodiode. The optical intensity of the Xenon arc lamp used is provided in Fig. 3-1.

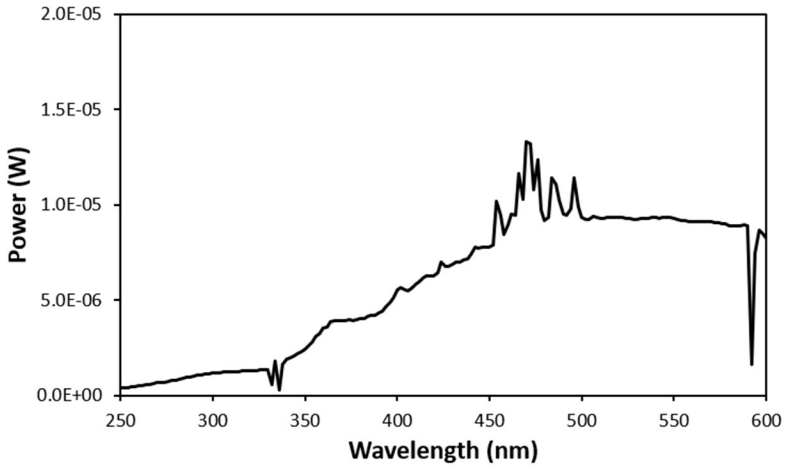

Figure 3-1. The optical power intensity of the lamp used for all device characterization measurements.

The on-off response of the devices was obtained using a Tektronix TBS 1052B Digital Oscilloscope and a chopper controlled by a Stanford Research Systems, Inc Model SR540 Chopper Controller. Bias was applied using the Keithley 2635B sourcemeter. The rise (fall) times are defined as the amount of time it takes for the device to transition from 10% to 90% (90% to 10%) of the photoresponse cycle. Matlab was used to perform Fast Fourier Transform (FFT) on dark current versus time data to obtain noise currents.

3.2.4 *Optical and Electromagnetic Simulations*

Transfer matrix method[93, 94] (TMM) and 3-dimensional finite-difference time-domain (3D-FDTD, Lumerical FDTD Solutions[95]) simulations were performed to obtain the exciton generation rate and electric field distribution, respectively, within the devices. The simulated devices have a similar structure as those experimentally fabricated, with the same layer compositions and thicknesses. Specifically, they are glass (100 nm)/ITO (100 nm)/PEDOT:PSS (40 nm)/PTAA:ZnO (weight ratio and thickness varied)/Al (100 nm). The thin BCP layer was not included. The exciton generation rate was calculated for incident light at 375 and 425 nm. Electric field distributions were collected with a

frequency-domain field monitor positioned at a cross section through the middle of the devices. For each material utilized in a simulated device, in both TMM and FDTD simulations, the wavelength-dependent optical constants of refractive index (n) and extinction coefficient (k) had to be defined. For Al, these optical properties were provided in the material library of the Lumerical program,[96] and data from an online database were used for the glass substrates.[97, 98] For all other materials the wavelength-dependent optical constants were obtained from ellipsometry with a Woollam M-2000 Spectroscopic Ellipsometer. These are shown in Fig. 2-2 for ITO and PEDOT:PSS, and in Fig. 3-2f for the PTAA:ZnO active layers. A more detailed description of the 3D-FDTD simulations is provided in Chapter 4, Section 4.2.

3.3 Results and Discussion

3.3.1 *Charge Collection Narrowing Mechanism*

The UV photodetectors have the structure of ITO/PEDOT:PSS/PTAA:ZnO/BCP/Al, shown in Fig. 3-2a. The ZnO nanoparticles had an approximate hydrodynamic diameter of 10 nm, and their distribution in the thick active layers is given in Fig. 3-2b,c. The four plotted curves were the result of vertical scans done in four positions across the films. As demonstrated in Fig. 3-2b,c, the ZnO nanoparticles are not evenly distributed throughout the blended active layer films but are more concentrated towards the top of the films. This trend is more apparent for the films with the 1:1 PTAA:ZnO weight ratio, which may be due to both the increased film thickness and the increased ZnO content. The energy diagram for each layer in the device is shown in Fig. 3-2d.

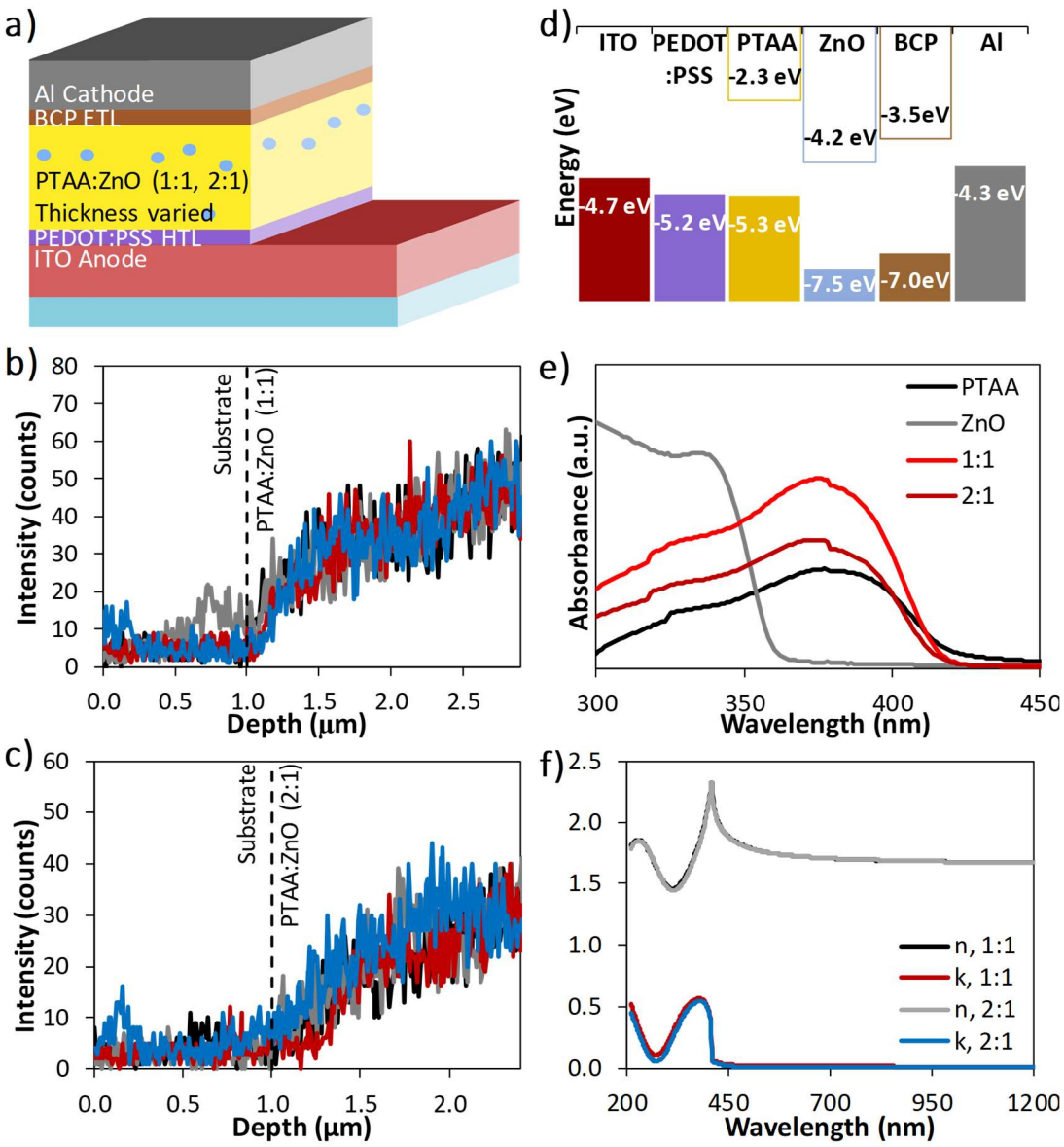

Figure 3-2. (a) Schematic of the device structure used in this work, (b,c) the distribution of ZnO in the thick blended films corresponding to the active layers of (b) Device 1900-1:1 and (c) Device 1400-2:1, obtained via EDS, (d) the energy diagram of each layer in the device used in this work, (e) absorption spectra of the pure components of the active layers and each blend film, normalized to the absorption at 600 nm, (f) optical constants for each blend film, obtained via ellipsometry.

The work function of PEDOT:PSS was provided by the vendor, as were the highest occupied molecular orbital (HOMO) and lowest unoccupied molecular orbital (LUMO) levels for BCP and PTAA. Values were taken from the literature for the work function of ITO[91, 117] and Al,[100] and for HOMO and LUMO levels of ZnO.[118, 119] ZnO is typically an n-type wide-bandgap material with a bandgap of 3.3 eV and electron mobility on the order

of 1-10 $cm^2/V\text{-}s$.[120] PTAA has been widely used as a hole transport material in perovskite photovoltaic devices[121] because of its hole mobility, which is around 5 x 10^{-3} $cm^2/V\text{-}s$.[122] PTAA is also a wide-bandgap material with a bandgap around 3.0 eV (Fig. 3-2d). As shown in Fig. 3-2e, the ZnO nanoparticle thin film has strong UV absorption, with a sharp cutoff around 360 nm. The PTAA thin film absorbs light from about 300-420 nm with a peak around 375 nm and a soft cutoff around 420 nm. The absorption spectra of the blended PTAA and ZnO resemble the absorption spectrum of a PTAA thin film with a peak around 375 nm. The addition of ZnO nanoparticles extends the absorption of the blended film deeper into the UV range and sharpens the cutoff observed around 420 nm.

TMM and 3D-FDTD simulations were used to fully investigate and understand the response as a function of active layer thickness and composition. For both TMM and 3D-FDTD simulations, the wavelength dependent refractive index, n, and extinction coefficient, k, of the PTAA:ZnO (1:1 and 2:1) films were obtained experimentally through ellipsometry and are shown in Fig. 3-2f. The exciton generation rates within the active layers induced by the light at two different wavelengths, 375 nm and 425 nm, corresponding to the absorption peak and edge, respectively, were obtained via TMM simulations and are plotted in Figs. 3-3a, b, e, and f. Electric field distributions for the wavelength range of 200-700 nm were obtained via 3D-FDTD simulations and are shown in Figs. 3-3c, d, g, and h. Two dramatically different active layer thicknesses were used for each weight ratio in these simulations, guided by the thicknesses of fabricated films for each composition: 150 (1:1, w:w), 200 (2:1, w:w), 1900 (1:1, w:w), and 1400 nm (2:1, w:w) were used as the active layer thicknesses for Devices 150-1:1, 200-2:1, 1900-1:1, and 1400-2:1, respectively.

As shown in Fig. 3-3a, while the two wavelengths of light interact differently with the Device 150-1:1 active layer, both generate excitons throughout the layer. The strong absorption of light at 375 nm results in a high exciton generation rate of 2.1 x 10^{19} $s^{-1}cm^{-3}$ at the PEDOT:PSS/active layer interface. Despite the quick decay, this light still produces significant exciton generation rates throughout the entire active layer, only dropping below 10^{18} $s^{-1}cm^{-3}$ within the top 10 nm of the active layer. Light at 425 nm induces a smaller exciton generation rate of 1.4 x 10^{19} $s^{-1}cm^{-3}$ at the PEDOT:PSS/active layer interface since it is near the edge of the absorption peak. The weak absorption by the active layer enables the light to penetrate the entire layer and reflect off the Al anode, establishing an interference pattern with a period of 106 nm. This interference leads to bulk exciton generation throughout the entire active layer, with peaks around 1.4 x 10^{19} $s^{-1}cm^{-3}$. Similar behavior is observed in Fig. 3-3b for Device 200-2:1. Again, light at 375 nm induces a high exciton generation rate of 1.7 x 10^{19} $s^{-1}cm^{-3}$ at the PEDOT:PSS/active layer interface, which decays throughout the active layer but stays above 10^{18} $s^{-1}cm^{-3}$ until the top 20 nm of the active layer. Light at 425 nm does not induce significant exciton generation at the PEDOT:PSS/active layer interface. This is because of the interference pattern, which has the same period of 106 nm due to the similarity between the optical constants for the 1:1 and 2:1, w:w, blends, as shown in Fig. 3-2f. As in Device 150-1:1, light at 425 nm establishes bulk exciton generation in Device 200-2:1 with peaks throughout the active layer around 6 x 10^{18} $s^{-1}cm^{-3}$.

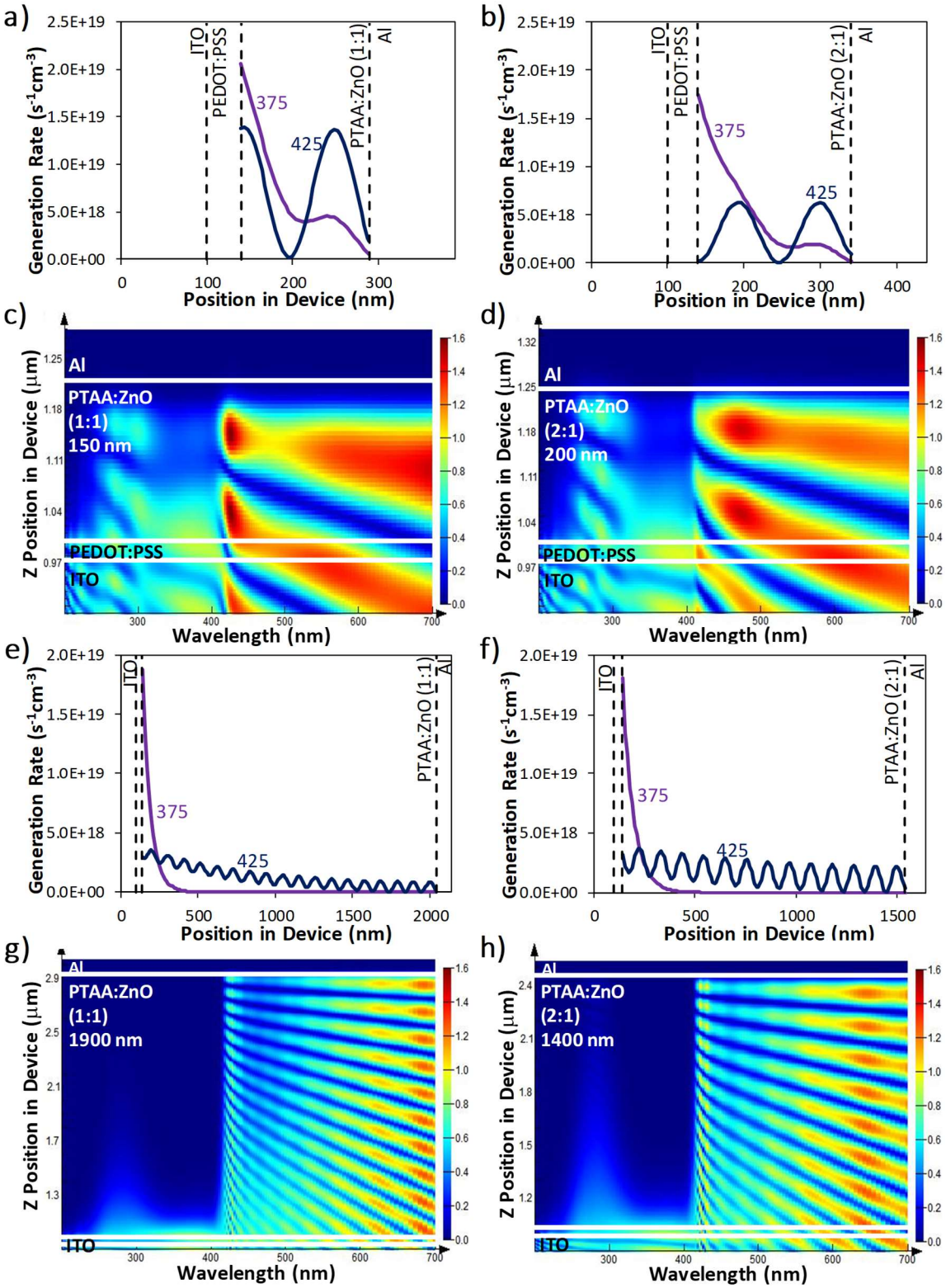

Figure 3-3. TMM-simulated exciton generation rate throughout the active layer for (a) Device 150-1:1, (b) Device 200-2:1, (e) Device 1900-1:1, and (f) Device 1400-2:1. 3D-FDTD-simulated electric field distribution throughout the device as a function of incident wavelength for (c) Device 150-1:1, (d) Device 200-2:1, (g) Device 1900-1:1, and (h) Device 1400-2:1.

The exciton generation rate in Device 200-2:1 is generally smaller than that in Device 150-1:1, so a weaker photoresponse is expected from Device 200-2:1. Because light of both simulated wavelengths generates excitons throughout the active layers, we expect these two thin devices to exhibit broad photoresponse when exposed to any light within the absorption range. The FDTD-simulated electric fields throughout Devices 150-1:1 and 200-2:1 (Figs. 3-3c,d) further support the expectation of a broad UV response for both thin devices. An electric field is present throughout the entirety of both active layers, for the wavelength range of ~250-420 nm, indicating that these devices will respond strongly to any light within this range. The electric field present in Device 150-1:1 (Fig. 3-3c) is slightly stronger than that in Device 200-2:1 (Fig. 3-3d), supporting the expectation that Device 150-1:1 will produce a stronger photoresponse than Device 200-2:1.

TMM simulations were performed at the same two wavelengths for Devices 1900-1:1 and 1400-2:1, shown in Figs. 3-3e,f. For Device 1900-1:1 (Fig. 3-3e), light at 425 nm still penetrates the entire active layer, establishing an interference pattern with a 105 nm period and bulk exciton generation with peaks that decay throughout the active layer but average around 1.6 x 10^{18} $s^{-1}cm^{-3}$. Because the exciton generation rate is sustained throughout the active layer, a photoresponse is expected from Device 1900-1:1 at this wavelength of 425 nm. The exciton generation rate induced by 375 nm light is still high, with a value of 1.9 x 10^{19} $s^{-1}cm^{-3}$, at the PEDOT:PSS/active layer interface. However, it falls off very quickly, dropping below 10^{18} $s^{-1}cm^{-3}$ within the first 150 nm of the active layer, which is less than 10% of its total width. Similar behavior is observed from Device 1400-2:1, shown in Fig. 3-3f. Light at 375 nm again induces a strong exciton generation rate of 1.8 x 10^{19} $s^{-1}cm^{-3}$ at the PEDOT:PSS/active layer interface, but it drops off quickly and falls below 10^{18} $s^{-1}cm^{-}$

^{3} about 150 nm into the active layer, which in this case is just over 10% of its total width. Light at 425 nm establishes a bulk exciton generation rate with the same period of 105 nm and peaks throughout the active layer averaging around 2.7 x 10^{18} $s^{-1}cm^{-3}$. This exciton generation rate is slightly higher than that of Device 1900-1:1, so a slightly stronger photoresponse at 425 nm is expected for Device 1400-2:1, compared to Device 1900-1:1. For both thick devices, under illumination by light within the absorption peak, the strong absorption causes excitons to only be generated within a small portion of the active layer close to the PEDOT:PSS layer. This unbalanced exciton generation creates a space charge and therefore a barrier to charge transfer, so no significant photoresponse should be observed at these wavelengths.[33] Therefore, a narrowband photoresponse centered around 425 nm, which generates excitons throughout the entire active layer, is expected from Devices 1900-1:1 and 1400-2:1. The exciton generation rates produced by both thick devices are smaller than those produced by thin devices, and thus the thin devices should generally produce a stronger photoresponse than thick devices. The expectation for the photoresponse to narrow with increasing thickness is also supported by the FDTD-simulated electric fields, shown in Figs. 3-3g and h. For Device 1900-1:1 (Fig. 3-3g), the electric field oscillates at the absorption edge of the active layer, around 425 nm, and is therefore strong throughout the entire active layer. The electric field falls off quickly in the rest of the UV range, with wavelengths below 425 nm, and does not extend significantly into the active layer due to the active layer absorption. Therefore, a photoresponse is only expected at the absorption edge wavelength of 425 nm. The same phenomenon is observed for Device 1400-2:1 (Fig. 3-3h), but it is not as clean. In fact, the electric field does extend, albeit weakly, throughout the active layer for wavelengths around 270-300 nm, indicating

that a photoresponse may be observed for these wavelengths. The electric field overall is stronger for Device 1400-2:1 than it is for Device 1900-1:1, so it is again expected that Device 1400-2:1 will produce a stronger photoresponse than Device 1900-1:1, but the narrowing of the response may not be as clean.

3.3.2 *Broadband Photomultiplicative Response in Thin Devices*

Devices with thin and thick PTAA:ZnO active layers were fabricated and their EQE spectra were taken under reverse biases, with the spectra obtained from thin devices shown in Fig. 3-4. As predicted by the simulation results in Fig. 3-3, these thin devices produce a broad UV response with high EQE values.

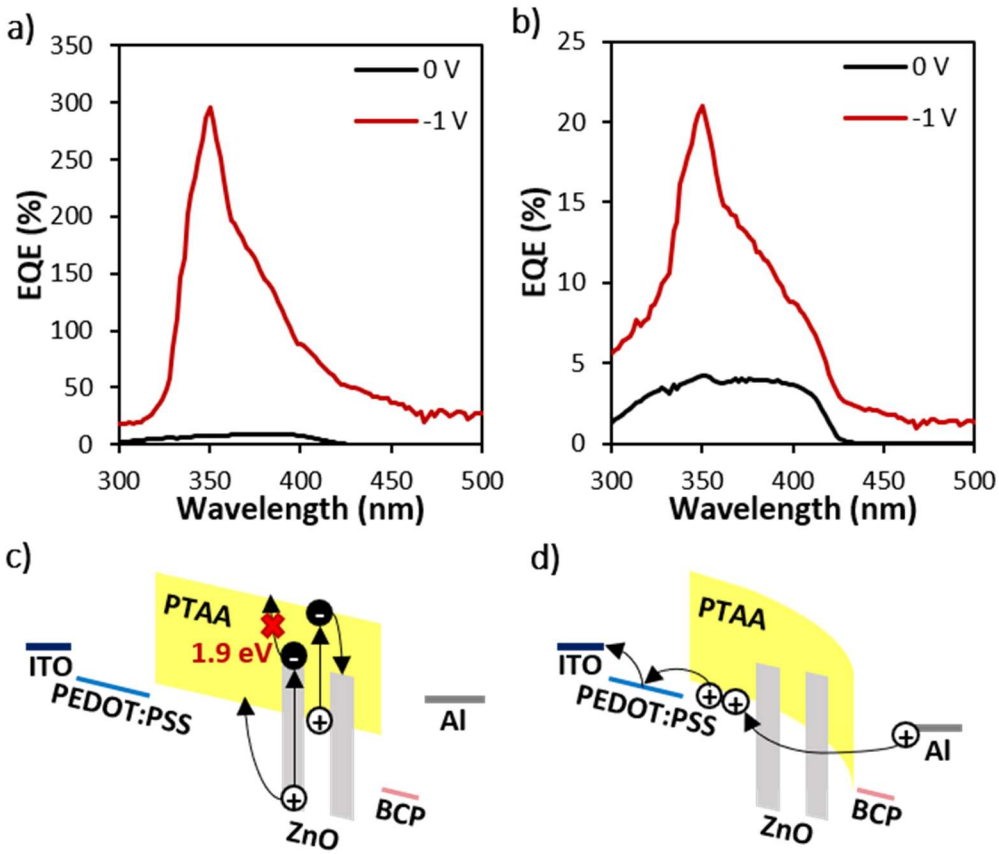

Figure 3-4. EQE spectra for (a) Device 150-1:1, (b) Device 200-2:1. Schematic illustration of (e) exciton generation in PTAA and ZnO and subsequent electron trapping in ZnO nanoparticles, (f) band bending and hole injection from the Al cathode, and subsequent collection of holes at the anode in a thin device.

Device 150-1:1 (Fig. 3-4a) produces the highest EQE values with a peak of 295% under 350 nm illumination and a -1 V bias. Device 200-2:1 (Fig. 3-4b) has a lower peak value of 21% under 350 nm illumination and a -1 V bias due to both the composition and the slightly thicker active layer compared to Device 150-1:1. The lower EQE values obtained from Device 200-2:1 compared to those from Device 150-1:1 are consistent with the trend predicted by the TMM and FDTD simulations, though the simulations do not consider bias.

By the definition of EQE as the ratio of charge carriers collected per incident photon, photomultiplication yields EQE values over 100%. As observed in Fig. 3-4a, photomultiplication is achieved in Device 150-1:1, in this case through charge trapping, band bending, and charge injection – a mechanism that has been well studied and evaluated in organic and inorganic-organic hybrid devices with active layer thicknesses in the range of 200-500 nm. The EQE values produced by Device 150-1:1 in this work, given the low applied bias, are comparable to those produced by similar systems in the literature utilizing the same photomultiplication mechanism. The organic system of P3HT and $PC_{71}BM$, blended with a ratio of 100:1, w:w, was utilized in devices with a structure of ITO/PEDOT:PSS/P3HT:$PC_{71}BM$/LiF/Al to obtain EQE values of 16,700% under 380 nm illumination and a -19 V bias through this photomultiplication mechanism.[30] The same mechanism was utilized in the more UV-selective system presented in Chapter 2, achieving EQE values of 5600% under 360 nm illumination and a -40 V bias.[51] Organic-inorganic hybrid systems, particularly polymer-nanoparticle blends, have also been employed to take advantage of this photomultiplication mechanism. Blending CdTe nanoparticles into a P3HT:$PC_{61}BM$ film yielded a peak EQE of 8000% under 350 nm illumination and a -4.5 V bias.[115] Additionally, ZnO nanoparticles have been incorporated into both P3HT and

PVK active layers in devices with the structure ITO/PEDOT:PSS/PVK:4,4′-bis[(p-trichlorosilylpropylphenyl) phenylamino]-biphenyl (TPD-Si2)/active layer/BCP/Al.[32] The PVK:ZnO device produced a more UV-specific response, from about 300-375 nm and peaking at 245,300% under 360 nm illumination and -9 V, while the P3HT:ZnO device produced a broader response from about 325-650 nm, due to the narrower bandgap of P3HT compared to PVK, peaking at 340,600% under 360 nm illumination and -9 V.[32]

The photomultiplication observed in Device 150-1:1 supports the idea that ZnO nanoparticles are isolated within the PTAA layer, because this is essential to the photomultiplication mechanism as illustrated in Fig. 3-4c and d. In the active layers, both PTAA and ZnO nanoparticles can absorb light, while PTAA acts as a hole transport material and the ZnO nanoparticles act as electron traps. Fig. 3-4c shows the exciton generation that occurs in the active layer upon illumination under an applied reverse bias. When the device is illuminated with light at wavelengths between 350 and 420 nm, excitons are generated in PTAA and diffuse throughout the active layer until they either recombine or come to an interface with ZnO. At this point the exciton can dissociate. The hole remains in the PTAA and moves through the active layer towards the ITO anode to be collected. The electron, however, is trapped in the isolated ZnO nanoparticle with a significant barrier of 1.9 eV to escape into the LUMO of PTAA. For illumination with light at wavelengths shorter than 350 nm, excitons can be generated in ZnO, in addition to PTAA. In this case, the electron is still trapped in the isolated ZnO nanoparticle by the same barrier to escape, but the hole can easily transfer into the HOMO of PTAA and move through the active layer to be collected at the anode. The trapped electrons in ZnO bend down the active layer energy bands, shortening the tunneling distance and therefore lowering the barrier for holes

to be injected from the Al cathode into the HOMO of PTAA (Figs. 3-4d). In thin devices, these injected holes can move through the active layer and be collected at the ITO anode. Multiple holes can be injected per incident photon, so this mechanism can lead to photomultiplication and an EQE over 100%.

3.3.3 *Narrowband Spectral Response in Thick Devices*

The EQE spectra for thick devices are shown in Fig. 3-5. As predicted by the simulations in Fig. 3-3, they generally produce narrower and weaker EQE spectra compared to the thinner devices. Device 1900-1:1 (Fig. 3-5a) shows good spectral narrowing to the edge of the PTAA absorption peak with a remarkably low FWHM of 12 nm, but a very low EQE of 0.66% under 424 nm illumination and a -1 V bias. Device 1900-1:1 maintained stable behavior under stronger applied biases and an EQE value of 2.8% was achieved under 424 nm illumination and a -10 V bias, but the stronger bias increased photoresponse throughout the UV range, producing EQE values above 1% for wavelengths shorter than 350 nm. The FWHM for the Device 1900-1:1 EQE peak at 424 nm remains narrow, below 16 nm, under subsequent testing with applied reverse biases up to -16 V (Fig. 3-5b) and is therefore considered a stable feature of the photoresponse. Device 1400-2:1 (Fig. 3-5c) produced a narrow EQE peak centered around 418 nm with a value of 1.1% under a -1 V bias, but response between 310-410 nm was also produced, with EQE values between 0.7-1% in this range. Generally, thick devices produce much lower EQE values for two reasons: the overall decrease in exciton generation rate compared to thinner devices, shown in Fig. 3-3, and the increased likelihood of charge recombination accompanying significant increases in film thickness, as illustrated in Fig. 3-5d.

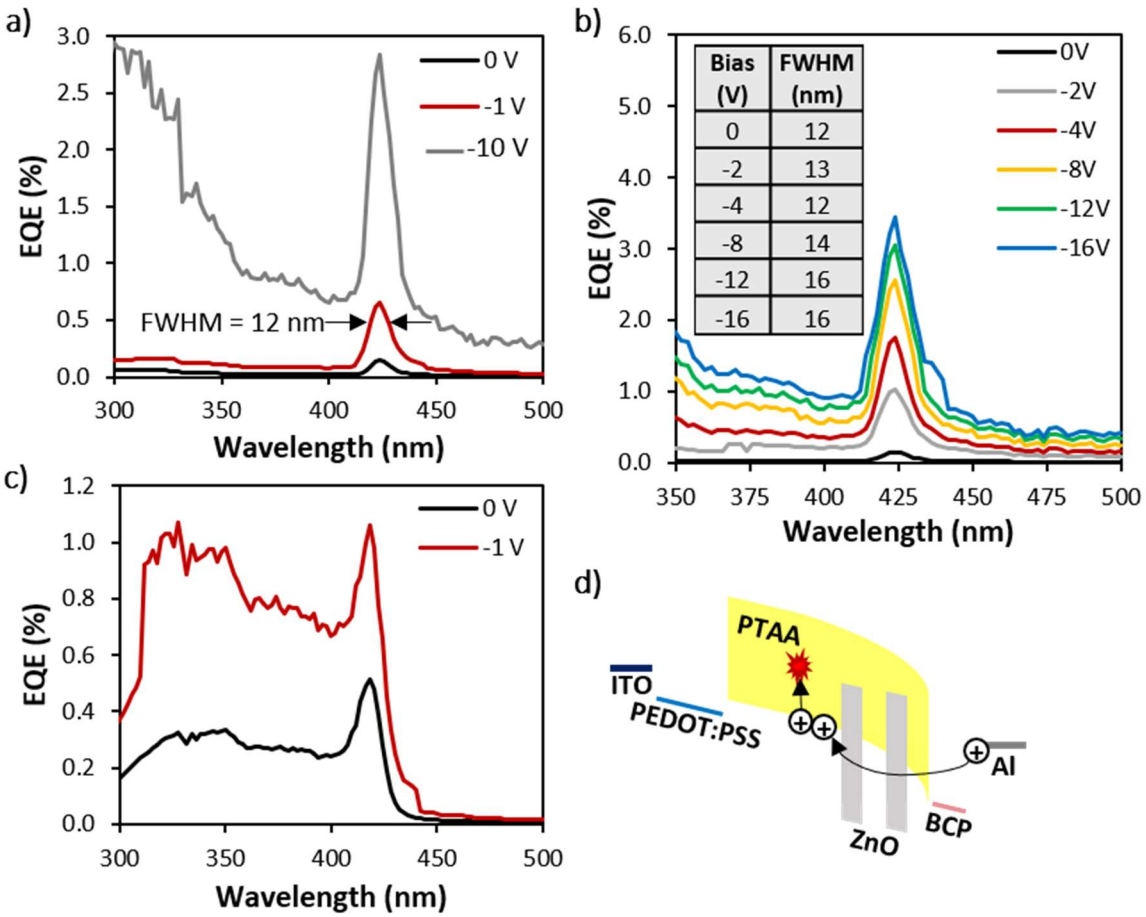

Figure 3-5. (a) EQE spectra for Device 1900-1:1, (b) Device 1900-1:1 under strong reverse biases, demonstrating the stable shape of the curve and the stability of the FWHM values. Inset: Table of the FWHM values for each subsequent scan, (c) EQE spectra for Device 1400-2:1 under zero and small reverse bias, and (d) schematic diagram of band bending and hole injection from the Al cathode and subsequent hole loss to recombination in a thick device

A few features of the photoresponse spectra of the thick devices in this work should be noted. First, the peak response of the thick devices occurs at a slightly longer wavelength than the absorption edge shown in Fig. 3-2e. As film thickness increases, a longer wavelength is required for light to penetrate through the active layer, resulting in a redshift in photoresponse.[33] Additionally, compared to the suppression of broad UV response achieved by Device 1900-1:1 under the same -1 V bias, the narrowing is not clean for Device 1400-2:1. This can be explained with the FDTD-simulated electric fields for Devices 1900-1:1 and 1400-2:1 (Figs. 3-3g,h). Both devices have a significant electric field

throughout the active layer at longer wavelengths, starting around the absorption edge, so both devices exhibit photoresponse at the edge of their absorption range. In reality, this occurs at the slightly longer wavelength of 424 nm for the thicker, 1900 nm active layer in Device 1900-1:1, compared to the peak response wavelength of 418 nm for the slightly thinner, 1400 nm active layer in Device 1400-2:1. This is because thicker films generally experience a redshift in their absorption.[33] It is clear in Fig. 3-3g and h that the electric field throughout the active layer in most of the UV range, with wavelengths shorter than 425 nm, is weaker in Device 1900-1:1 than in Device 1400-2:1, implying a weaker photoresponse throughout this region.

It also important to note that the photocurrent obtained from the devices in this work, both thick and thin, can be increased by applying a stronger reverse bias, as demonstrated in Fig. 3-5. This is due to an increase in the internal electric field, aiding the movement of holes through the active layer and improving the likelihood that they be collected at the anode. Strong biases have been applied to devices utilizing a blend of P3HT and $PC_{61}BM$ with a ratio of 100:1, w:w, in active layer thicknesses ranging from 0.3 to 7 μm, combining the response mechanisms of CCN and photomultiplication to produce very narrow, very strong photoresponse.[123, 124] A single, narrow EQE peak exceeding 50,000%, centered around 650 nm with a 30 nm FWHM, was achieved via hole injection from the Al cathode under a -60 V bias.[124] The same devices showed a U-shaped EQE spectrum under a +60 V bias, yielding EQE peaks around 40,000% under 340 nm illumination and 20,000% under 650 nm illumination.[123] Under forward bias, a larger peak was observed near the short-wavelength edge of the absorption peak because holes were injected from the ITO anode, rather than the Al cathode. Because of this, the photomultiplication mechanism occurred in

the portion of the active layer near the anode, so it was engaged by light with a short penetration depth.[123] With stronger applied biases, the EQE values obtained from our devices could be increased to be more competitive with those reported for similar systems, but for the sake of practical applicability, we have focused our evaluation on the low-bias region. For most applications, a small working voltage and minimal energy demands are desirable. Additionally, it has been previously reported[51] and observed in this work that thin devices can become unstable under strong biases.

3.3.4 *Impact of ZnO Nanoparticle Content*

From this, it seems that the weight ratio directly impacts the efficacy of the CCN mechanism, but it is plausible that the difference between the clean narrowing of Device 1900-1:1 and the broader response of Device 1400-2:1 could solely be due to the difference in film thickness. Experimentally, the effects of thickness and composition could not be easily isolated due to the difficulty in obtaining the same thickness for different compositions. We therefore used FDTD simulations to evaluate the electric field distributions for devices with both weight ratios of 1:1 and 2:1 at each thickness of 1400 and 1900 nm, shown in Fig. 3-6.

For each weight ratio, increasing the active layer thickness from 1400 nm (Fig. 3-6a,b) to 1900 nm (Fig. 3-6c,d) caused the electric field to decrease within the absorption peak, indicating that the photoresponse will be weaker at these wavelengths and the CCN mechanism will be more effective. Additionally, for each active layer thickness, the devices with a 1:1 weight ratio (Fig. 3-6a,c) exhibit a weaker electric field throughout the absorption peak than the devices with a 2:1 weight ratio (Fig. 3-6b,d), indicating that at any thickness, a device with a 1:1 weight ratio will engage the CCN mechanism more effectively and

produce a cleaner response-narrowing than a device with a 2:1 weight ratio. From these comparisons, it can be determined that both the increase in active layer thickness and the PTAA:ZnO ratio of 1:1, w:w, produce the superior photoresponse-narrowing observed in Device 1900-1:1 compared to Device 1400-2:1.

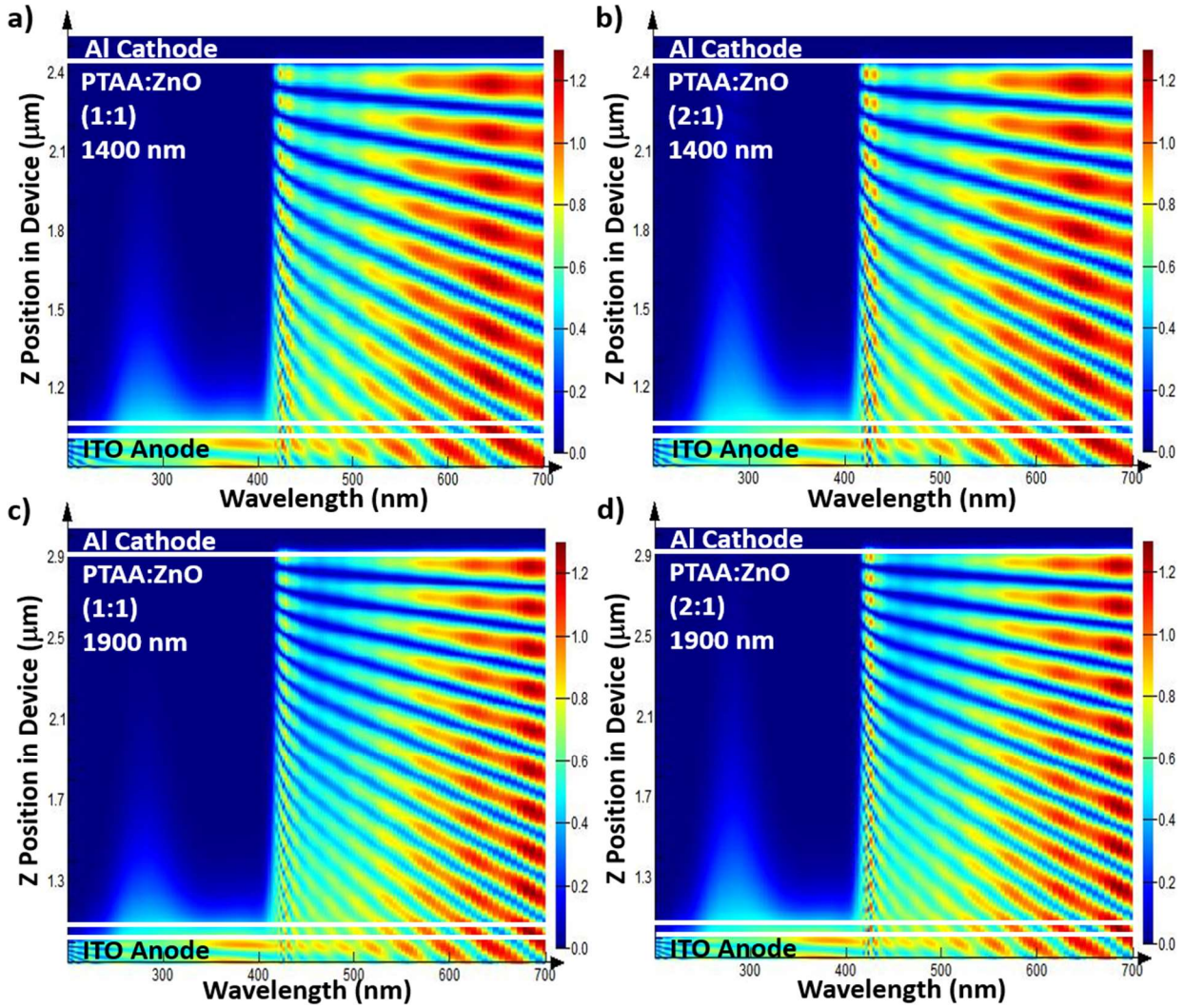

Figure 3-6. Electric field distribution obtained via 3D-FDTD simulations for devices with (a) a PTAA:ZnO ratio of 1:1, w:w, and active layer thickness of 1400 nm, (b) a PTAA:ZnO ratio of 2:1, w:w, and active layer thickness of 1400 nm (Device 1400-2:1), (c) a PTAA:ZnO ratio of 1:1, w:w, and active layer thickness of 1900 nm (Device 1900-1:1), and (d) a PTAA:ZnO ratio of 2:1, w:w, and active layer thickness of 1900 nm.

With PTAA:ZnO weight ratios of 1:1 and 2:1, there is a significant amount of ZnO nanoparticles, and the surface states and defects of these nanoparticles need to be

considered. The ZnO crystal structure introduces native defects, including vacancies (a missing atom), interstitial sites (an atom outside of a lattice site), and anti-sites (one atom in another's site).[125] Some of these defects – O vacancies, Zn interstitials, and Zn anti-sites – are donor-like defects that contribute to the inherent n-type behavior of ZnO.[125] These defects, particularly O vacancies at the nanoparticle surfaces, introduce extra electrons into the conduction band that enable the surface to adsorb O_2 from air.[126] Engaging electrons in this adsorption creates a depletion region of lowered conductivity on the ZnO surface, which is particularly impactful for nanoparticles.[127, 128] Under UV illumination and forward bias, the O_2 can be desorbed, freeing the electrons and increasing the conductivity of the ZnO.[126] This can be an effective photoresponse mechanism,[128, 129] but only if the dark/neutral-bias behavior can be immediately recovered. Depending on the system and the testing conditions, the conductivity increase is sometimes maintained even when the illumination/forward bias is removed. This is called persistent photoconductivity, and it results in the loss of a distinguishable photoresponse. Stable behavior can often be recovered upon aging in air and/or exposure to strong reverse biases.[127]

In this work, when persistent photoconductivity was observed, that is when dark current and photocurrent became indistinguishable, the devices were aged in air until the dark current returned to its original levels. This aging time was typically about 1 day, and then testing continued. Multiple electrodes on each chip were tested to ensure stable, reproducible behavior. Additionally, the dark current was repeatedly checked throughout testing to ensure that the device was stable and that any observed photoresponse was distinct from persistent photoconductivity. The extent to which persistent

photoconductivity affected device stability depended on the weight ratio of the active layer, as shown in Fig. 3-7.

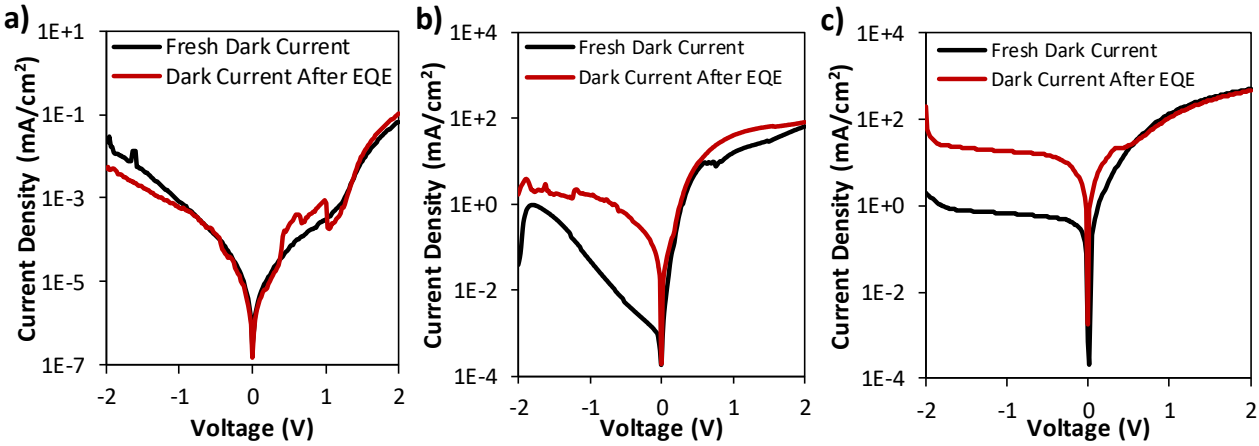

Figure 3-7. Current density-voltage characteristics for (a) a pure PTAA device (ITO/PEDOT:PSS/PTAA/BCP/Al) with a 200 nm active layer, (b) a pure ZnO device (ITO/PEDOT:PSS/ZnO/BCP/Al) with a 260 nm active layer, and (c) a device with a PTAA:ZnO ratio of 1:10, w:w, (ITO/PEDOT:PSS/PTAA:ZnO/BCP/Al) and a 150 nm active layer.

A pure PTAA device (Fig. 3-7a) does not experience any persistent photoconductivity, and has stable, reproducible dark current behavior before and after EQE measurements. For devices with a higher ZnO content, persistent photoconductivity was evident and stable behavior could not always be recovered. As shown in Fig. 3-7b and c, both pure ZnO devices and PTAA:ZnO devices with a ratio of 1:10, w:w, respectively, exhibited an increase in dark current, especially under reverse biases, after EQE measurements. The increased dark current could not be lowered to the level of freshly made devices even after aging in air or under forward bias. Generally, a higher ZnO content produces higher currents for both dark and illuminated conditions, while a higher PTAA content improves device stability. Considering both factors, the ratio of 1:1, w:w, was found as optimal among those investigated in this work.

3.3.5 *J-V Characteristics, Device Sensitivity and Response Speed*

The dark and illuminated current density-voltage characteristics (J-V curves) for all four devices are shown in Fig. 3-8. Generally, as predicted by the simulations in Fig. 3-3 and observed in the EQE spectra in Fig. 3-4, the thinner devices (Fig. 3-8a) produce higher currents under both dark and illuminated conditions than the thick devices (Fig. 3-8b).

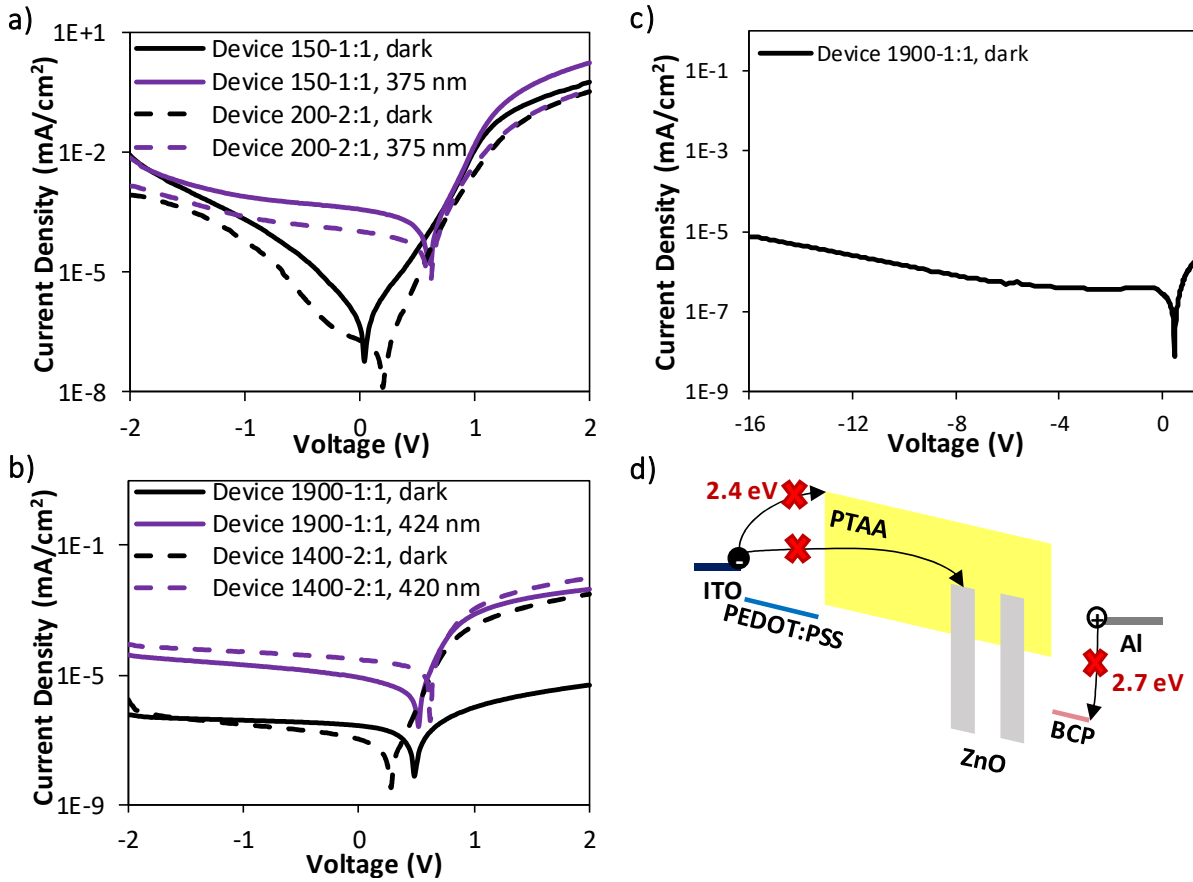

Figure 3-8. Dark and illuminated J-V curves for (a) Devices 150-1:1 and 200-2:1, and (b) Devices 1900-1:1 and 1400-2:1. (c) Dark current density under strong reverse bias for Device 1900-1:1. (d) Schematic illustration of the barriers to charge injection enabling the low dark current of Device 1900-1:1 to be maintained under strong reverse biases.

For both thin devices, the photocurrent and dark current, shown in Fig. 3-8a, are only distinguishable within a small bias range, from about -1.5 to 0.7 V, indicating that the device response is not stable outside of this range. Additionally, Device 150-1:1 produces a higher photocurrent than Device 200-2:1, with values of 7.9×10^{-4} and 2.4×10^{-4} mA/cm^2

under a -1 V bias and 375 nm illumination, respectively. Both thick devices produce a clearly distinguishable photoresponse throughout the relevant voltage range, with the photocurrent approximately two orders of magnitude greater than the dark current, as shown in Fig. 4b. For Device 1400-2:1, the dark current shows rectification and is very close to the photocurrent under forward bias. Device 1400-2:1 produces a stronger photocurrent than Device 1900-1:1, with values of 5.4 x 10^{-5} and 2.1 x 10^{-5} mA/cm^2 under a -1 V bias and 420 nm and 424 nm illumination, respectively.

For Device 1900-1:1, low dark current below 1 x 10^{-5} mA/cm^2 can be maintained even at strong reverse biases, shown in Fig. 3-8c. As illustrated in Fig. 3-8d, the low dark current is due to the relatively large barrier (2.7 eV) to hole injection from the Al cathode into the BCP layer and the even larger barrier (2.4 eV) to electron injection from the ITO anode into LUMO of PTAA. There could be electron injection from the ITO anode into the conduction band of ZnO based on their energy level alignment (0.5 eV barrier), but this injection is limited because ZnO nanoparticles may not directly contact the PEDOT:PSS interface. Additionally, even if some electrons were injected, they could not be transported through the active layer because the ZnO nanoparticles do not form a continuous pathway. The dark current of devices is indicative of the noise level that is present, which is obtained from a Fast Fourier Transform (f) of the dark current values.[34] Plots of the noise current versus frequency are given in Fig. 3-9 for each device.

For the thin devices (Fig. 3-9a), the application of a -1 V bias causes a significant increase in both dark and noise currents. For Device 150-1:1, the dark current increases from 5.0 x 0^{-8} mA/cm^2 under no bias, to 5.1 x 10^{-3} mA/cm^2 under a -1 V bias, and the noise current increases from 2.0 x 10^{-13} A/Hz$^{1/2}$ under no bias to 1.3 x 10^{-10} A/Hz1$^{/2}$ under a -1 V

bias. Similarly, for Device 200-2:1, the dark current increases from 3.4 x 10^{-7} mA/cm^2 under no bias to 1.1 x 10^{-5} mA/cm^2 under a -1 V bias, and the noise current increases from 2.4 x 10^{-13} A/Hz$^{1/2}$ under no bias to 2.0 x 10^{-12} A/Hz$^{1/2}$ under a -1 V bias. For the thicker devices (Fig. 3-9b), the impact of bias on the dark and noise currents is much less severe. For Device 1900-1:1, the dark current increases from 4.0 x 10^{-7} mA/cm^2 under no bias to 6.7 x 10^{-7} mA/cm^2 under a -1 V bias, and the noise increases mildly from 1.2 x 10^{-13} A/Hz$^{1/2}$ without any bias to 2.7 x 10^{-13} A/Hz$^{1/2}$ under a -1 V bias. Similarly, for Device 1400-2:1 the dark current is increased from 1.9 x 10^{-7} mA/cm^2 under no bias to 8.9 x 10^{-7} mA/cm^2 under a -1 V bias, and the noise decreased from 2.4 x 10^{-12} A/Hz$^{1/2}$ under no bias to 5.0 x 10^{-13} A/Hz$^{1/2}$ under a -1 V bias.

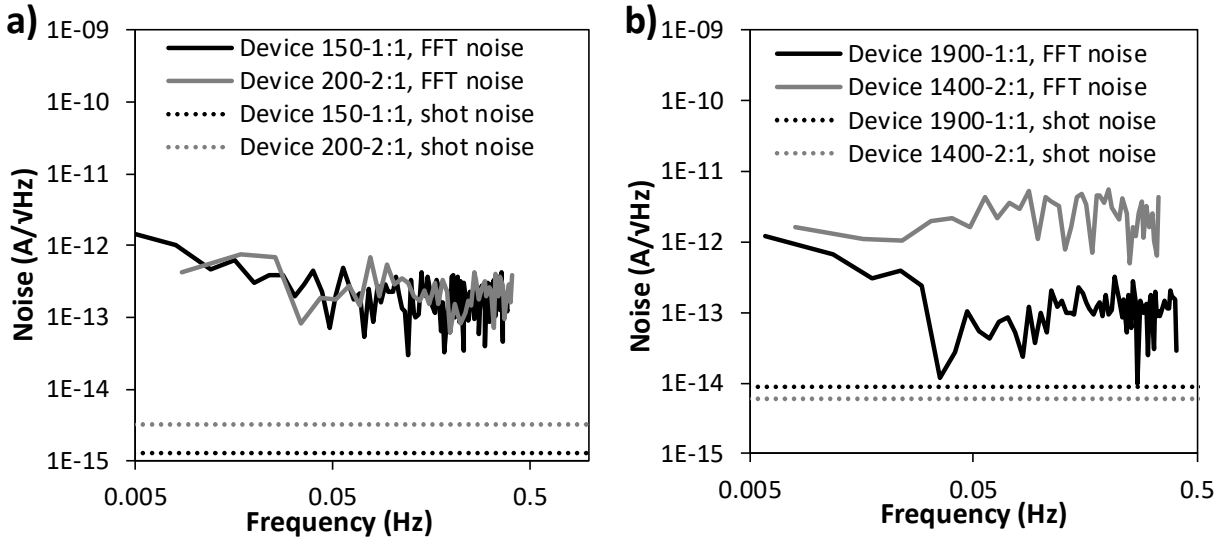

Figure 3-9. Noise currents under no bias obtained from FFT and calculated shot noise approximations for (a) Devices 150-1:1 and 200-2:1, and (b) Devices 1900-1:1 and 1400-2:1.

The R and D* results are plotted in Fig. 3-10, with results for thick and thin devices of the same weight ratios plotted together to illustrate the distinct broad or narrow spectral response. As shown in Fig. 3-10a, Device 150-1:1 obtained a peak R value of 83.2 A/W under 350 nm illumination and a -1 V bias, while Device 1900-1:1 maintained its narrowband spectral shape, with a peak R value of 0.23 A/W under 424 nm illumination

and a -1 V bias. As shown in Fig. 3-10b, Device 200-2:1 produced a spectral shape similar to that produced by Device 150-1:1, but much weaker in magnitude, with a peak R value of 5.93 A/W under 350 nm illumination and a -1 V bias. Device 1400-2:1, also shown in Fig. 3-10b, again demonstrates CCN, as evidenced by the peak of 0.36 A/W obtained under 420 nm illumination and a -1 V bias. However, R values around 0.25 A/W are maintained throughout most of the UV range between about 310-410 nm, indicating that this device does not engage the CCN mechanism as effectively as Device 1900-1:1, due to both its composition and thickness as previously discussed.

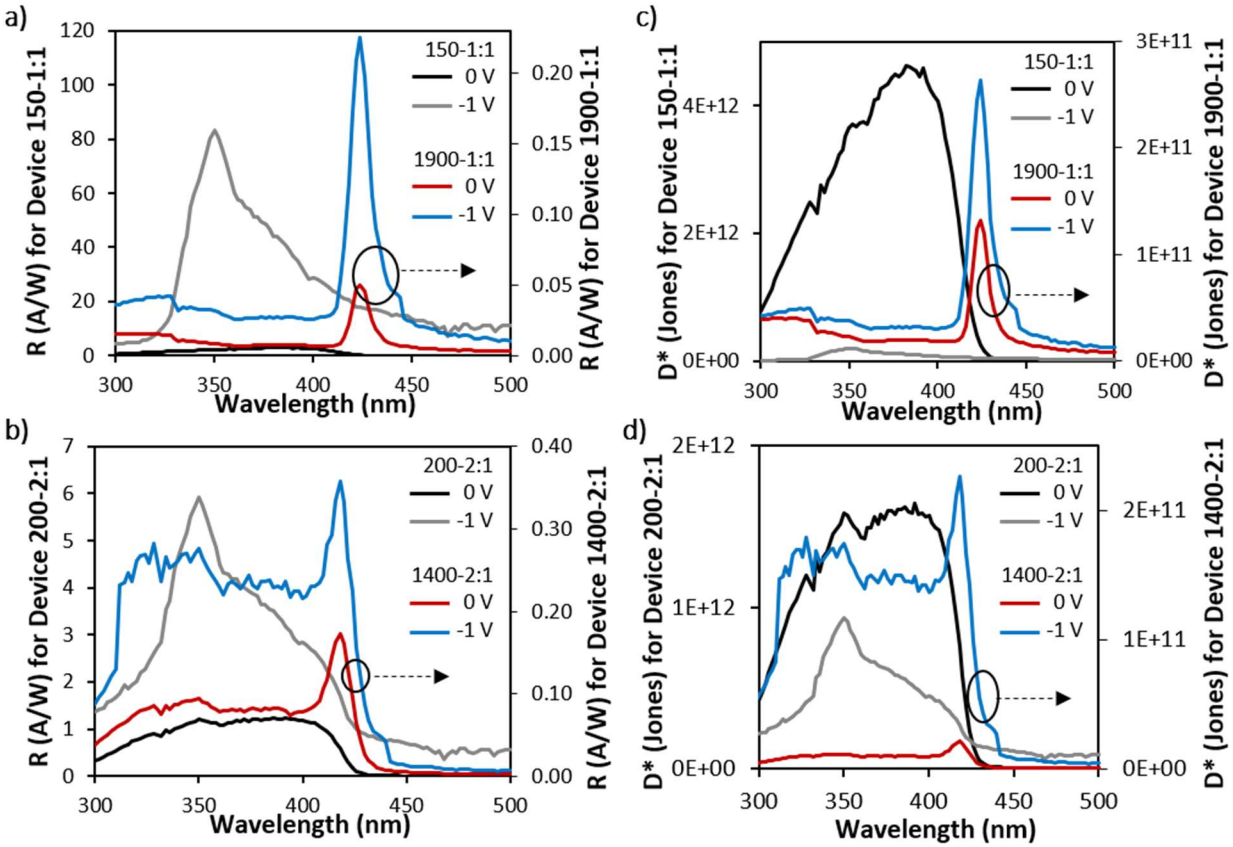

Figure 3-10. Responsivity (a and b) and specific detectivity (c and d) under 0 and -1 V biases. Responsivity for (a) Devices 150-1:1 and 1900-1:1, and (b) Devices 200-2:1 and 1400-2:1. Specific detectivity for (c) Devices 150-1:1 and 1900-1:1, and (d) Devices 200-2:1 and 1400-2:1.

Because both noise current and photoresponse are accounted for in D*, the values for the thin devices decreased under reverse bias while the values for the thick devices

increased. This is because thick devices produced only a slight increase in noise current when a reverse bias was applied, compared to the severe increase in noise current observed when a reverse bias was applied to the thinner devices. As shown in Fig. 3-10c, for Device 150-1:1 the peak D* value of 3.7 x 10^{12} Jones is obtained without any applied bias, under 382 nm illumination. Also shown in Fig. 3-10c are D* spectra for Device 1900-1:1. For this device, the applied bias improves D*, which peaks at 2.6 x 10^{11} Jones under 424 nm illumination and a -1 V bias. Similarly, shown in Fig. 3-10d Device 200-2:1 also produces its peak D* value of 1.6 x 10^{12} Jones without any applied bias, under 350 nm illumination, whereas for Device 1400-2:1 the peak D* value of 2.3 x 10^{11} Jones is obtained under 420 nm illumination and a -1 V bias.

The on-off response speed is shown for these devices in Fig. 3-11. The response was measured under 375 nm illumination for the two thin devices (Device 150-1:1 and Device 200-2:1), and under 424 and 420 nm illumination for Device 1900-1:1 and Device 1400-2:1, respectively. Because Device 150-1:1 produced higher photocurrents than the other devices, its on-off response could be measured with no applied bias. For Device 200-2:1, a -1 V bias was applied to produce a sufficient photoresponse for these measurements, and a -10 V bias had to be used for Devices 1900-1:1 and 1400-2:1. Generally, applying a bias should increase the response speed of a device.[1] Therefore, because Device 150-1:1 exhibits the fastest photoresponse when it is tested without any bias and compared to devices under bias, as in Fig. 3-11, it must have the fastest photoresponse overall of the devices tested. The rise and fall times for Device 150-1:1 were found to be around 50 and 60 ms, respectively. These response times are slower than the rise and fall times of 25 and 558 μs reported for a P3HT:ZnO system under a -9 V bias,[32] but faster than the rise and fall times,

below 200 ms, reported for a device based on ZnO nanoparticles embedded in a layer of poly(9,9-dihexylfluorene) (PFH) under a -1 V bias.[127]

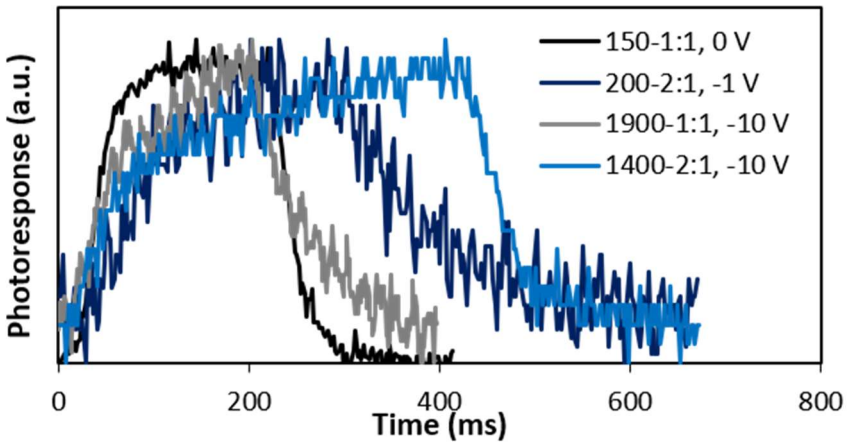

Figure 3-11. Photoresponse for (a) Device 150-1:1 under 375 nm illumination, (b) Device 200-2:1 under 375 nm illumination, (c) Device 1900-1:1 under 424 nm illumination, (d) Device 1400-2:1 under 420 nm illumination.

3.4 CONCLUSIONS

The effects of active layer film thickness and composition on the spectral response of UV photodetectors have been investigated. TMM and FDTD simulations were used to provide insights into the exciton generation rate and electric field distribution within the devices as a function of incident light wavelength. Experimentally, the active layer film thickness and composition were used to tune between broad and narrow spectral response for UV-selective photodetectors whose active layers are a blend of PTAA and ZnO nanoparticles with the weight ratios of 1:1 and 2:1. Devices with thin active layers (150-200 nm) exhibited a broad photoresponse, while devices with thick active layers (1400-1900 nm) showed a narrowed photoresponse centered at the edge of the absorption peak of the active layer, due to charge collection narrowing. The device with a 1900 nm active layer and PTAA:ZnO ratio of 1:1, w:w, showed an extremely narrow, single photoresponse peak centered at 424 nm with a FWHM of 12 nm. The corresponding responsivity and specific detectivity were 0.23 A/W and 2.6 x 10^{11} Jones under 424 nm illumination and a -1

V bias. Decreasing the active layer thickness to 150 nm with the same weight ratio resulted in a broad photoresponse in the wavelength range of ~320-420 nm, with a peak EQE of 295% under 350 nm illumination and a -1 V bias due to the charge trapping and injection enabled by the ZnO nanoparticles acting as electron traps. The photomultiplication produced a peak responsivity of 83.2 A/W under 350 nm illumination and a -1 V bias, but the peak specific detectivity of 3.7×10^{12} Jones was achieved under no bias and decreased to 2.0×10^{11} under a -1 V bias due to the increased noise current. Generally, increasing the ratio of PTAA:ZnO to 2:1, w:w, lowered dark and photocurrents, eliminated photomultiplication in the thin device, and diminished the spectral response narrowing in the thick device. The CCN mechanism was effectively extended into the UV photodetection range, and the response in this range can be easily tuned between a broad photomultiplicative response and a sensitive, selective narrowband response, simply by varying the thickness and composition of the active layer.

Chapter 4. PLASMONIC ALUMINUM NANOHOLE ARRAYS AS TRANSPARENT CONDUCTING ELECTRODES FOR ORGANIC UV PHOTODETECTORS WITH BIAS-DEPENDENT PHOTORESPONSE

4.1 INTRODUCTION

The incorporation of metallic nanostructured films and nanoparticles has become a popular approach for improving the performance of optoelectronic devices, including photodetectors, due to the performance enhancements resulting from their ability to support surface plasmon polaritons (SPPs) that can concentrate light into sub-wavelength volumes, improve the absorption in the active layer, and increase the internal electric field in devices.[57, 58] Additionally, metal films are conductive and could therefore enhance performance while serving as a device electrode, making them a flexible, cost-effective alternative to the commonly used material of ITO, which is expensive, brittle, and has poor UV transmittance.[59] These performance enhancements can be engaged by light of varying wavelengths depending on the design and material of the nanostructures.[60-62] This provides a mechanism for tuning the spectral photoresponse of devices, making plasmonic nanostructures attractive for a wide variety of applications including filter-free imaging and colorimetry, flame and missile detection, and environmental monitoring.[14]

While metal films patterned with sub-wavelength nanoholes have been shown to provide extraordinary optical transmission,[62, 130] in this and similar work the incorporation of a nanostructured metal electrode into devices has produced lower light absorption in the active layer compared to devices based on ITO electrodes.[69] However, the other effects of

plasmonic nanostructured electrodes, spectral tunability and electric field enhancement, remain attractive and worthwhile pursuits. A stronger electric field in a device, even just at the interface of the active layer and a charge transport layer, could improve charge dynamics and therefore photoresponse in a device. The spectral tunability enabled by plasmonic nanostructures is also desirable. The transmission of an array of nanoholes in a metal film can be tuned and controlled by the geometric parameters including the gap, the size of the holes, and the pitch, the spacing of the array.[58, 61, 62] These parameters directly impact the plasmonic properties through the standing wave SPPs that can be established on the nanostructured surface, which in turn determines the incident light that SPs will have resonance with and couple to.[60, 62]

Plasmonic nanostructures have been employed effectively in thin film solar cells, enabling devices with thinner active layers, which have superior charge transport properties, to compete optically with thicker devices by improving absorption through light scattering, local electric field enhancement, and light trapping.[61] This heightened absorption increases the short circuit density (J_{SC}) produced by thin film solar cells that incorporate plasmonic nanostructures, therefore improving device performance. Thin film perovskite solar cells, having a structure of fluorine-doped tin oxide (FTO)/TiO_2/$CH_3NH_3PbI_3$/2,2′,7,7′-Tetrakis(N,N-di-4-methoxy-phenyl-amino)-9,9′-spirobifluorene (spiro-OMeTAD)/Au produced a J_{SC} of 13.19 mA/cm^2 when plasmonic Ag nanoparticles were deposited between the FTO and TiO_2 layers, compared to 10.79 mA/cm^2 when no Ag nanoparticles were included.[71] Additionally, an Au nanohole array (Au-NHA) was shown to improve the J_{SC} with respect to active layer thickness when incorporated into inverted organic solar cells with a device structure of Au-NHA/ZnO/poly[[4,8-bis[(2-ethylhexyl)oxy]benzo[1,2-b:4,5-b′]dithiophene-2,6-diyl][3-fluoro-2-[(2-ethylhexyl)carbonyl] thieno[3,4-b]thiophenediyl]]

(PTB7):[6,6]-phenyl-C_{71}-butyric acid methyl ester ($PC_{71}BM$)/MoO_3/Ag.[69] The Au nanostructured electrode improved absorption in the active layer by trapping light via an optical cavity effect and thus enabled J_{SC} levels to be maintained when the active layer was decreased to sub-optimal thickness, offering a potential solution to the trade-off between optical absorption and charge extraction that persists in thin film solar cells.[69]

The coupling of light and surface charge into LSPPs enhances the electric field at both interfaces of the plasmonic electrode.[63] This phenomenon is very attractive for photodetectors, particularly those relying on charge injection and transport at device electrode interfaces.[60, 65] Photodetectors utilizing plasmonic nanostructures and nanoparticles produce improved responsivity (R) values, and improved spectral selectivity and tunability for device photoresponse.[65] A device with a structure of ITO/4,4-N,N′-bis[N-(1-naphthyl)-N-phenylamino]biphenyl (NPB)/C_{60}/bathocuproine (BCP)/Al incorporated Au nanoparticles at the top of the NPB active layer and, through plasmonic enhancements to the absorption and local electric field as well as hot carrier injection, the R values increased from 2.00 to 99.38 mA/W under 830 nm illumination and a -0.4 V bias.[76] In these devices, plasmonic excitements enable sub-bandgap photodetection, and this can also be pursued as the main design objective. An Ag nanohole array (Ag-NHA) was incorporated into the bottom transparent electrode of a device with a structure of Ag-NHA/2,2′,7,7′-tetrakis(N,N′-di-p-methylphenylamino)-9,9′-spiro-bi-fluorene (spiro-TTB)/Al and improved the photoresponse strength by two orders of magnitude under 830 nm illumination and a 5 V bias.[77]

Photodetectors that are sensitive to UV illumination are important in a variety of applications including environmental monitoring, scientific research, imaging, and flame and missile detection.[1, 2, 14] Despite their applicability, extension of plasmonic enhancement mechanisms to UV-selective devices has been relatively slow, because the common plasmonic metals of Ag and

Au cannot support surface plasmon polaritons (SPPs) when illuminated by light with wavelengths shorter than about 350 nm.[80] Al is well-suited to support and tune SPPs in the UV spectral range due to its carrier concentration, dielectric function, and high quality factor for long range surface plasmons when illuminated by UV light,[82-84] although oxide formation on the Al surface can interfere with and cause a redshift in its plasmonic properties.[55, 80, 81, 85, 131] In addition, Al provides an attractive material option for UV photodetectors due to its relative abundance and low cost compared to Ag and Au. A simulated Al nanogrid demonstrated optical transmittance that could be tuned between about 300-430 nm by varying the geometry of the grid,[55] and Al nanoparticle arrays produced plasmonic resonance peaks that could be shifted between about 270-340 nm by varying the particle size.[81] Acting as a hot electron injection material, plasmonic Al can provide performance enhancements both within and beyond the UV spectral range. A device consisting of Al and ITO electrodes separated by a thin Al_2O_3 layer produced a peak R value of 250 nA/W under 440 nm illumination and no bias.[85] Incorporating plasmonic Al nanowires into the same device resulted in significant enhancements to the sub-bandgap absorption, demonstrating that plasmonic Al nanostructures could improve solar cell performance in addition to photodetection.[85] In fact, simulated organic solar cells with a device structure of Al nanohole array (Al-NHA)/poly(3,4-ethylenedioxythiophene):polystyrene sulfonate (PEDOT:PSS)/poly(3-hexylthiophene) (P3HT):$PC_{61}BM$/ZnO/perfect electronic conductor (PEC) were reported to have enhanced absorbance throughout the visible range, compared to devices based on ITO, that could be precisely tuned by varying both the geometry of the Al-NHA and the thickness of the device layers, utilizing the optical cavity effect of the multi-layered device.[73] Because of its plasmonic properties and ability to induce sub-bandgap photoresponse, Al can be used as a filter for color-selective photoresponse throughout the UV and visible spectral ranges. An Al grating deployed on top of a

lateral photodetector, utilizing Al electrodes on a Si substrate with a thin oxide layer, was reported as an effective color-selective filter, as grating pitch values of 300, 400, and 500 nm resulted in blue, green, and red photodetection, respectively.[79]

In this work, Al nanohole arrays (Al-NHAs) were utilized as transparent conducting electrodes to optimize the UV-selectivity and response tunability of photodetectors having a conventional photodiode structure with organic active materials, which provide a low-cost, flexible alternative to inorganic materials.[14] UV-selectivity was ensured through the material selection of Al, for plasmonic activity within the UV spectral range, and the polymer donor of poly(9,9-dioctylfluorene-alt-bithiophene) (F8T2), for strong UV absorption with a cut-off around 515 nm. The active layer was a 350 nm film consisting of F8T2 and the fullerene-derivative electron acceptor $PC_{71}BM$, combined in a ratio of 100:4, w:w, based on the investigation and evaluation in Chapter 2.[51] While inverted devices offer a potential stability enhancement through their utilization high work function metals such as Ag in their top electrodes, rather than the lower work function metals such as Al used in conventional devices,[104, 105] inverted devices in this work were found to be unreliable, so only conventional devices were pursued for Al-NHA incorporation. PEDOT:PSS and LiF were used as hole and electron transport layers, respectively, for an overall device structure of Al-NHA/PEDOT:PSS/F8T2:$PC_{71}BM$/LiF/Al. 3-dimensional finite-difference time-domain (3D-FDTD) electromagnetic simulations were conducted to design the Al-NHA to produce strong UV absorption in the active layer and enhanced internal electric field intensity. A hexagonal Al-NHA with a diameter, pitch, and thickness of 175, 200, and 30 nm, respectively, is determined to be optimal. Notably, these parameters can be varied within a small range without severely diminishing the absorbance of the active layer, so imperfection in the fabrication of the nanostructures is tolerable. Al-NHA electrodes were successfully fabricated using nanosphere

lithography (NSL) and incorporated into photodetectors, which produced two narrow photoresponse peaks with specific detectivity (D*) values of 4.0 x 10^9 and 4.6 x 10^9 Jones under 340 and 515 nm illumination, respectively, and -2 V bias, and one broad photoresponse peak with a peak D* of 8.8 x 10^9 Jones under 450 nm illumination and 2 V bias. Compared to control ITO-based devices, Al-NHA-based devices had similar response under reverse bias and superior response under forward bias, as ITO-based devices became unstable under forward bias. The bias-dependent photoresponse switching is believed to benefit from plasmonic enhanced internal electric field that increases the driving force for hole diffusion. The mechanism was further confirmed by the investigation of conventional devices with planar Al electrodes and hole-only devices with both planar Al and Al-NHA electrodes. This novel bias-dependent response switching improves the applicability of UV photodetectors through the incorporation of cost-effective, flexible, and performance-enhancing plasmonic Al-NHA transparent conducting electrodes.

4.2 EXPERIMENTAL

4.2.1 *Finite-Difference Time-Domain Unit Cell Setup and Simulation Details*

3-dimensional finite-difference time-domain (3D-FDTD, Lumerical FDTD Solutions[95]) simulations were performed to obtain the transmission through each layer in the device and the electric field distribution throughout the device. An overview of the 3D-FDTD simulation setup used to design the Al-NHA electrodes is shown in Fig. 4-1. As discussed in Chapter 2, it was ultimately determined for F8T2:$PC_{71}BM$ blend active layers that the optimal device structure was conventional, the optimal active layer thickness was approximately 350 nm, and the optimal ratio for the blend was 100:4, w:w, so these conditions were used for simulated devices and active layers. The bottom-illuminated conventional device with a structure of Al-NHA (30

nm)/PEDOT:PSS (40 nm)/F8T2:$PC_{71}BM$ (350 nm, 100:4 weight ratio)/LiF (0.8 nm)/Al (100 nm) is illustrated in Fig. 4-1a. Film thicknesses were informed by experimental devices, and both the diameter and the pitch (spacing) of the NHAs were varied. When Al-NHAs were incorporated into simulated devices, the subsequent layer material, PEDOT:PSS, was used to fill the nanohole, and then was treated as a planar film on top of this filled hole. Therefore, the reported thickness of PEDOT:PSS refers to the thickness of the planar film on top of the filled Al nanohole. A cross-sectional view of the simulation unit cell is shown in Fig. 4-1b. The simulation boundary is represented by a blue border and the light source impinges normally from the bottom of the device with polarization in the x-direction. The boundary conditions used in the x, y, and z directions were anti-symmetric, symmetric, and perfectly matched layer, respectively, simulating a periodic array with free space above and below.[132] The simulation was run with 250 frequency points, and the auto-shut-off limit was reached in all cases. An auto-non-uniform mesh was used, with the mesh accuracy set to 4 and a minimum mesh step of 0.25 nm. Frequency-domain field monitors, which capture both transmittance of light and electric field distribution, were placed throughout the device. Monitors between device layers, indicated in Fig. 4-1b by light blue lines, were placed between layers to capture transmittance, and absorbance in a layer was calculated by subtracting the transmittance above and below the specified layer. Additional monitors, indicated by dashed yellow lines in Fig. 4-1b, were placed in vertical cross-sections in the xz- and yz-planes, intersecting at (0,0), to capture the internal electric field distribution. In this case, a specific x-y point was chosen from each monitor so that the electric field could be plotted along the z axis against incident wavelength. A top-view of the hexagonal Al-NHA is shown in Fig. 4-1c, indicating the nanohole diameter (D), and unit cell x- and y-lengths, pitch (p) and $p\sqrt{3}$,

respectively. The shape of the array was determined by the fabrication method of nanosphere lithography, which inherently produces a hexagonal array.

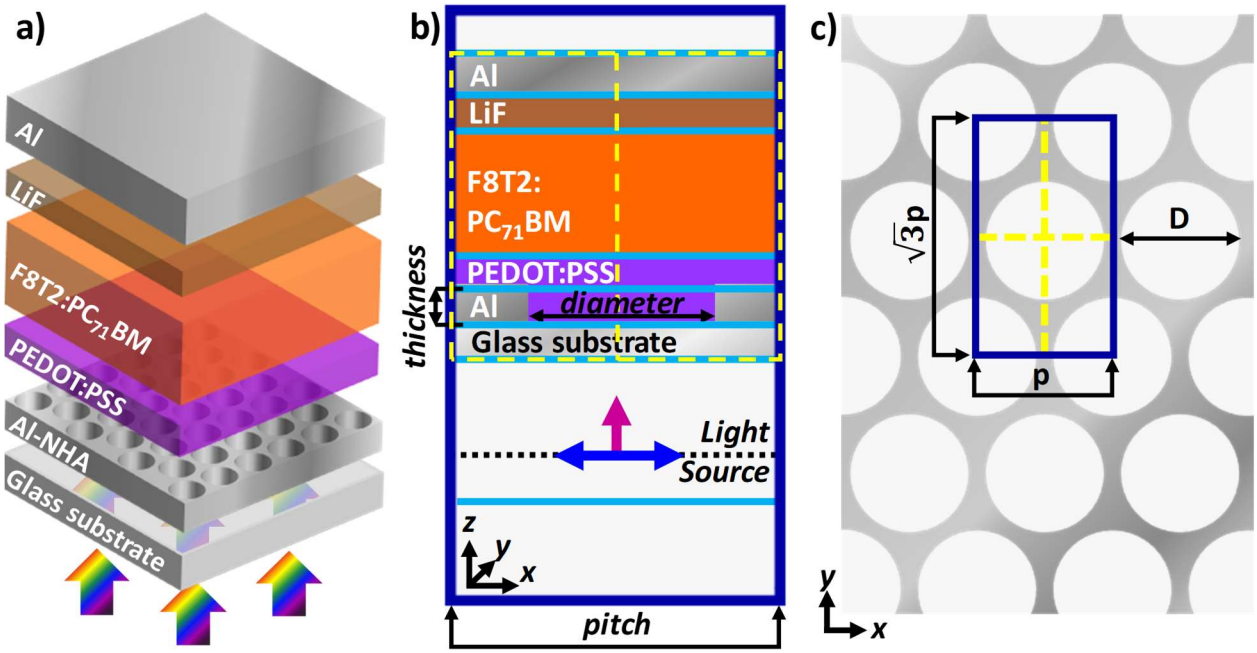

Figure 4-1. (a) Illustration of a conventional Al-NHA-based device. (b) A cross-sectional view of a simulation unit cell. (c-d) A top-view of the (c) hexagonal and (d) square Al-NHAs.

For each material utilized in a simulated device, the wavelength-dependent optical constants of refractive index (n) and extinction coefficient (k) had to be defined. For Al, these optical properties were provided in the material library of the Lumerical program,[96] and for LiF they were found in an online database.[133, 134] For all other materials the wavelength-dependent optical constants were obtained from ellipsometry with a Woollam M-2000 Spectroscopic Ellipsometer and fitted using CompleteEASE software from J. A. Woollam Co, and the resulting n and k data are shown in Fig. 4-2. F8T2:$PC_{71}BM$ data was fit with a General Oscillator (GenOsc) model consisting of two Cody-Lorentz and one Gaussian oscillator with a mean square error of 8. Corning EAGLE XG glass data was fitted with a Cauchy model with a mean square error of 6. ITO data was fitted with a GenOsc model consisting of two Tauc-Lorentz, one Gaussian and one Drude oscillator,

with a mean square error of 6. PEDOT:PSS data was fitted with a GenOsc model consisting of one Tauc-Lorentz and one Lorentz oscillator, with a mean square error of 9

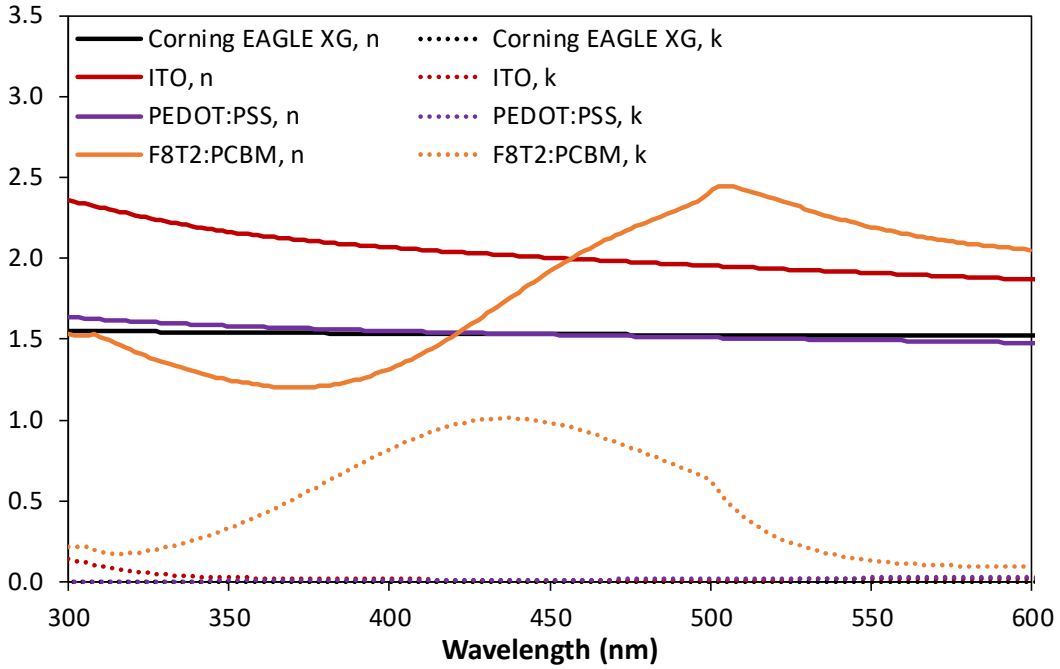

Figure 4-2. Wavelength-dependent optical constants of refractive index, n, and extinction coefficient, k, values for Corning EAGLE XG glass substrate, ITO, PEDOT:PSS and F8T2:$PC_{71}BM$ that were measured using ellipsometry.

4.2.2 *Al-NHA Fabrication via Nanosphere Lithography*

Carboxylate surface functionalized polystyrene beads with a diameter of 200 nm were purchased from Polysciences, Inc. (Warrington, PA). Before use, the stock solution (5.68×10^{12} particles/mL) was diluted (1.43×10^{12} particles/mL) with ultrapure water (18 MΩ). Polyethylene oxide (molecular weight 1,000,000 g/mol, Sigma-Aldrich, St. Louis, MO), was added at a concentration of 100 ppm. Corning EAGLE XG glass substrates, 1.1 mm thick, were cut into 1.5 cm x 1.5 cm squares and cleaned by ultrasonication for 15 min each in soapy deionized (DI) water, DI water, acetone and isopropanol, sequentially, followed by 20 min of UV-ozone (UVO) treatment. Immediately after UVO treatment, 5 µL of the nanosphere suspension was dropped onto the substrates, which were then moved in gentle circular motions to spread the suspension over the

surface before being laid flat to dry. The resulting nanosphere monolayer films were etched using a plasma treatment system (Yield Engineering Systems, Inc. CV200RF Series) with O_2 and Ar flow rates of 80 and 20 standard cubic centimeters per minute (SCCM), respectively, at 125 W for 90 s. 30 nm of Al was deposited on the etched spheres with a CHA Solution e-beam evaporator without any masks and the film thickness was controlled by a quartz crystal microbalance (QCM). Nanosphere liftoff was performed via ultrasonication in toluene (99.8%, Sigma-Aldrich). A scanning electron microscope (SEM, FEI Sirion) was used to characterize the nanostructures and evaluate each fabrication step.

4.2.3 *Device Fabrication and Characterization:*

Al-NHA electrodes were prepared as described in Section 4.2.2. ITO coated Corning EAGLE XG glass substrates (≤ 10 Ω/sq, Colorado Concept Coatings LLC, Loveland, CO) were cut into 1.5 cm x 1.5 cm squares and cleaned by the same procedure described in Section 4.2.2. Al^{Planar} electrodes were fabricated by depositing 10 nm of Al (99.999%, R.D. Mathis, Long Beach, CA) onto Corning EAGLE XG glass substrates, which had been cleaned by the same procedure described in Section 4.2.2, via thermal evaporation. Once prepared, all three electrodes were exposed to UVO treatment to improve the hydrophilicity before device fabrication was completed. PEDOT:PSS solution (AI 4083, Clevios P VP AI 4083, Heraeus, Hanau, Germany) was filtered through a 0.45 μm PTFE syringe filter and deposited via spin-coating at 5000 rpm for 40 s, followed by baking at 120ºC for 10 min in air. The chips were then transferred into a nitrogen-filled glovebox, where active layers were deposited from a previously-prepared precursor solution. F8T2 (molecular weight of 29,000 g/mol, polydispersity index of 3.3, American Dye Source, Baie D'Urfe, Quebec, Canada) and $PC_{71}BM$ (Nano-C Inc., Westwood, MA), were dissolved separately in 1,2-

dichlorobenzene (anhydrous, 99.9%, Sigma-Aldrich) at a concentration of 40 mg/mL and stirred at 700 rpm and 70ºC for at least 12 h, and then combined into a F8T2:$PC_{71}BM$ (100:4, w:w) precursor solution, which was stirred for at least one additional hour at 700 rpm and 70ºC before being filtered through a 0.2 μm PTFE syringe filter. The active layer was formed by spin-coating the precursor solution at 1000 rpm for 30 s and was then annealed at 80ºC for 10 min. A thin 0.8 nm layer of LiF (99.995%, Sigma-Aldrich), or 10 nm MoO_3 (99.9995%, Alfa Aesar, Haverhill, MA) for hole-only devices, followed by 100 nm Al were deposited via thermal evaporation using an Angstrom Engineering Amod PVD Platform, with film thickness controlled by a QCM. LiF and MoO_3 were deposited without the use of any mask, and Al electrodes were deposited with circular masks so that the active area of each device was 0.03 cm^2, and sixteen devices were on each chip.

All device characterization measurements were performed in air. J-V curves, dark current over time, EQE spectra, and response speed were obtained using a Keithley 2635B sourcemeter. Light for these measurements as well as transmission and reflection measurements was provided using a Xenon arc lamp (150 W) and Oriel Cornerstone 130 Monochromator. Optical intensity was measured using a Newport 1918-R Power Meter and Newport UV-Si Photodiode. The optical power intensity was the same as that shown in Section 3.2.3 (Fig. 3-1). The response speed was obtained by manually switching between dark/light conditions. The rise (fall) times are defined as the amount of time it takes for the device to transition from 10% to 90% (90% to 10%) of the photoresponse cycle. The same lamp, monochromator, photodiode and power meter were used to conduct transmittance and reflectance measurements. Matlab was used to perform Fast Fourier Transform (FFT) on dark current over time data to obtain noise currents. Active layer film

thickness was measured using a KLA Tencor Alpha-Step 500 Profiler, and ITO and PEDOT:PSS film thicknesses were confirmed during ellipsometry measurements. Sheet resistance was measured using a Jandel Cylindrical four-point probe connected to a Keithley 2450 sourcemeter. UV-Vis spectroscopy data were collected using a Perkin Elmer Lambda 900 UV-Vis spectrophotometer.

4.3 RESULTS AND DISCUSSION

4.3.1 *Optimizing the Nanopattern Geometry via 3D-FDTD Simulations*

The simulated active layer absorbance for conventional Al-NHA-based devices are shown in Fig. 4-3. The overall device structure was glass (100 nm)/ITO (200 nm) or Al-NHA (gap and pitch varied, 30 nm thickness)/PEDOT:PSS (40 nm)/F8T2:$PC_{71}BM$ (100:4, 350 nm)/LiF (0.8 nm)/Al (100 nm). The diameter was varied so that the Al wall between nanoholes would be either 25 or 50 nm, and the pitch was varied between the diameters of commercially available polystyrene nanospheres, which determines the pitch of nanopatterns produced via NSL. Devices based on Al-NHA electrodes with diameter/pitch combinations of 50/100 nm, 75/100 nm, 150/200 nm, 175/200 nm, 250/300 nm, and 275/300 nm were simulated, and the results are presented in Fig. 4-3. The simulated active layer absorbance for these Al-NHA-based devices, as well as for an ITO-based device, are shown in Fig. 4-3a. UV-Vis measurements were performed on an F8T2:$PC_{71}BM$ film (350 nm thick, 100:4 weight ratio) and an absorption spectrum is superimposed in Fig.4-3a for comparison and to indicate the photoactive range of the active layer. For all devices, the simulated active layer absorbance shows a clear cut-off around 530 nm, which aligns relatively well with the cut-off of the UV-Vis absorption spectrum. A peak around 580 nm, outside of the active layer absorption range, is observed for all simulated devices due to the nanocavity effect resulting from

the top reflective Al electrode. To confirm this, the absorbance of the active layer for both Al-NHA- and ITO-based devices without the top Al layer were simulated with a structure of glass (100 nm)/ITO (200 nm) or Al-NHA (175 nm diameter, 200 nm pitch, 30 nm thickness)/PEDOT:PSS (40 nm)/F8T2:$PC_{71}BM$ (100:4, 350 nm)/LiF (0.8 nm). The resulting absorbance spectra (Fig. 4-3b) do not exhibit a peak at 580 nm, confirming that this peak results from reflectance of the top Al electrode rather than true active layer absorbance.

For Al-NHA based devices, UV-selective plasmon-enhanced absorbance peaks around 350-400 nm are clearly shown for NHAs with small pitches (100-200 nm). The Al-NHA electrode with a diameter/pitch of 50/100 nm produces the lowest active layer absorbance, peaking at 330 nm at 0.26, because the volume fraction of nanoholes in the Al-NHA film is only 23%, resulting in low transmittance. Increasing the diameter to 75 nm, while keeping the same pitch of 100 nm, increases the volume fraction of nanoholes in the Al-NHA film to 51%, and the 330 nm absorbance peak broadens and increases in magnitude to 0.56. While hole volume fraction alone does not determine the final magnitude and spectral shape of electrode transmittance, which is also affected by the geometry of the nanopattern, increasing the hole volume fraction does correspond to an increase in electrode transmittance, which in turn results in higher absorbance in the active layer. Therefore, the electrode with a diameter/pitch of 75/100 produces active layer absorbance that is spectrally similar to that produced by the 50/100 electrode, but is higher in magnitude.

Because surface plasmon resonance is sensitive to the nanoarray pitch,[65, 135] a redshift of transmittance through Al nanogrids[55] and active layer absorbance of solar cells based on Au-NHA electrodes[69] were reported when the nanopattern pitch was increased. The same trend is observed for the devices represented in Fig. 4-3a. When the pitch is increased from 100 to 200 nm, the plasmon-enhanced absorption peak shifts from around 330 nm to around 400 nm, maintaining UV-

selectivity despite a significant redshift. For Al-NHA films with a diameter/pitch of 150/200 nm and 175/200 nm, the volume fractions of nanoholes are 51% and 69%, respectively, and in this case increasing the hole diameter also increases the magnitude of the active layer absorbance, particularly in the UV spectral range between about 300-400 nm. For the 200 nm pitch, diameters of 150 and 175 nm produce absorbance peaks around 400 nm of 0.61 and 0.71, respectively. Increasing the pitch to 300 nm results in a further redshift of plasmon-enhanced absorbance and the plasmonic peaks, observed around 450 nm, merge with the active layer absorbance between about 400-530 nm. The volume fractions of nanoholes in Al-NHA films with a diameter/pitch of 250/300 and 275/300 are 63% and 76%, respectively, and the absorbance between 450-515 nm is relatively unaffected when the hole diameter is increased.

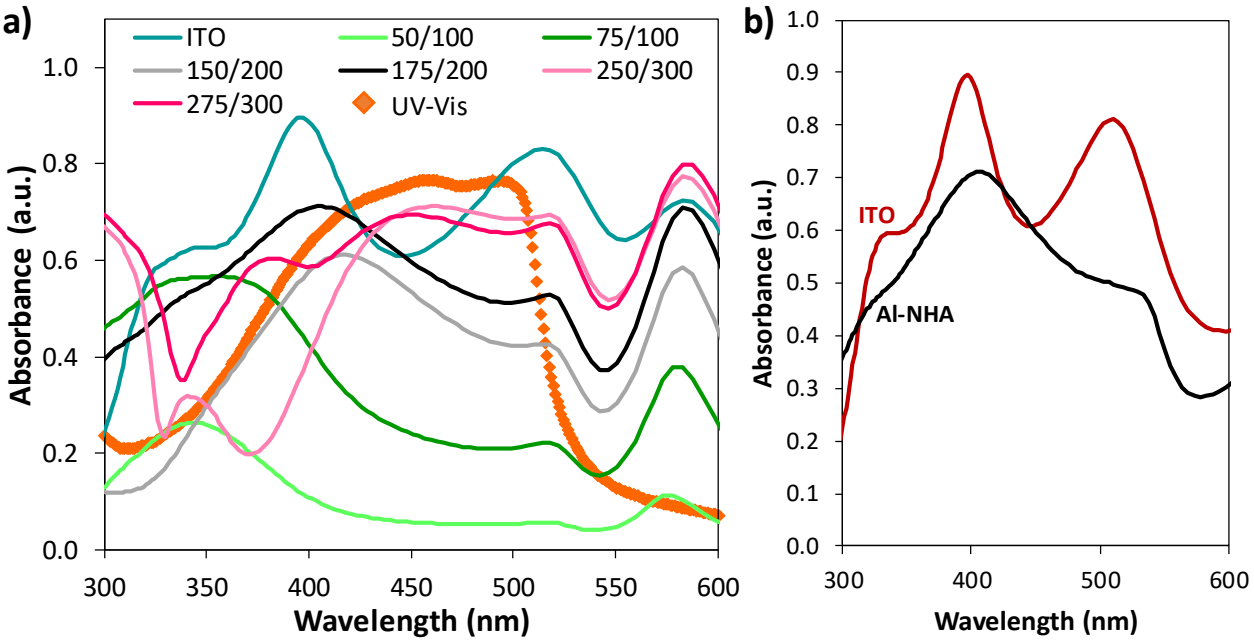

Figure 4-3. (a) FDTD-simulated active layer absorbance for Al-NHA-based devices with the diameter and pitch varied. Active layer absorbance for an ITO-based device and the UV-Vis absorbance data for an active layer film are included. The device structure is glass (100 nm)/ ITO (200 nm) or Al-NHA (diameter and pitch varied, 30 nm thickness)/PEDOT:PSS (40 nm)/F8T2:$PC_{71}BM$ (100:4, 350 nm)/LiF (0.8 nm)/Al (100 nm). (b) FDTD-simulated active layer absorbance for Al-NHA- and ITO-based devices without the top Al electrode. The device structure is glass (100 nm)/ ITO (200 nm) or Al-NHA (175 nm diameter, 200 nm pitch, 30 nm thickness)/PEDOT:PSS (40 nm)/F8T2:$PC_{71}BM$ (100:4, 350 nm)/LiF (0.8 nm).

With a few exceptions, the ITO-based control device produces stronger active layer absorbance than Al-NHA-based devices, due to the relatively high transmittance of ITO compared to Al-NHAs. Electrodes with a pitch of 300 nm produce higher active layer absorbance values than ITO in the spectral range between about 425-475 nm, and the electrode with a diameter/pitch of 175/200 yields active layer absorbance values at its peak, around 400 nm, that are competitive with ITO. In fact, this 175/200 electrode yields stronger active layer absorbance values than any other Al-NHA in the spectral range between about 360-425 nm. Therefore, due to its clear UV-selective plasmonic-enhanced absorbance and relatively strong active layer absorbance overall, the Al-NHA-based device with a diameter/pitch of 175/200 nm was chosen as the optimal geometry for pursuit in further theoretical investigation and device incorporation.

Generally, the absorbance onset and cut-off of the simulated spectra in Fig. 4-3 align well with the UV-Vis absorption spectrum of F8T2:$PC_{71}BM$, but the oscillations produced by the ITO-based device must be addressed. In the active layer absorbance, peaks around 400, 515, and 580 nm and dips around 445 and 555 nm were observed, which correspond respectively to dips and peaks in the total reflectance at the same wavelengths, shown in Fig. 4-4 for a widened wavelength range. The 3D-FDTD simulated and experimentally measured reflectance from an ITO-based device are both provided in Fig. 4-4 so that a strong comparison can be made. Compared to the simulated data, the experimental data is slightly broadened. In the spectral region between about 300-400, the experimental lamp power is relatively low, so the dip around 320 nm is not accurately captured, but the peaks around 455 and 555 nm are represented in both the simulated and measured data. Under longer wavelengths, the measured reflectance data broadens further. The peaks and dips in these spectra are attributed to the cavity effects that result from the multilayer device structure, which includes multiple interfaces between materials with different

refractive indices. At each interface that has a refractive index mismatch, a portion of light is reflected. When multiple interfaces are present both constructive and destructive interference result, producing peaks and valleys in the reflectance and absorbance spectra. The significant magnitude of the device reflectance is attributed to this phenomena, and particularly to the large difference in refractive index between the glass substrate (n = ~1.5) and air (n = ~1).[136]

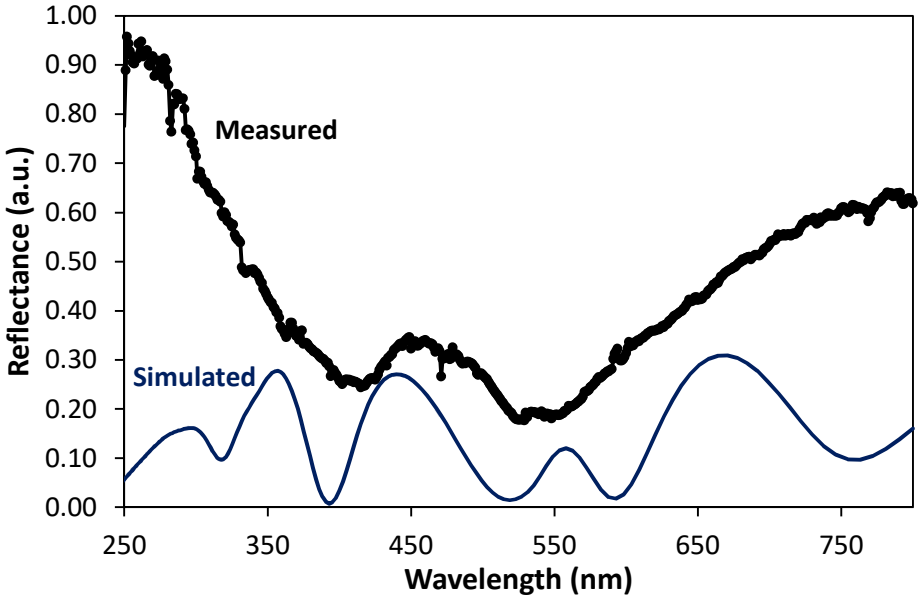

Figure 4-4. Simulated reflectance from an ITO-based device with a structure glass (100 nm)/ITO (200 nm)/PEDOT:PSS (40 nm)/F8T2:$PC_{71}BM$ (100:4, 350 nm)/LiF (0.8 nm)/Al (100 nm).

While the active layer absorbance is a useful tool for comparing similar NHA geometries, it does not provide a full understanding of all the factors that influence and contribute to spectral photoresponse and device behavior. Coupled with a working knowledge of device photoresponse mechanisms, the internal electric field distribution, which can also be calculated via 3D-FDTD simulations, can be used to investigate some of these factors. Therefore, electric field distributions were obtained for simulated Al-NHA- and ITO-based devices and are shown in Fig. 4-5. The optimal NHA geometry with a diameter/pitch of 175/200 nm was used for the Al-NHA-based device, so simulated devices had a structure of glass (100 nm)/ITO (200 nm) or Al-NHA (175 nm

diameter, 200 nm pitch, 30 nm thickness)/PEDOT:PSS (40 nm)/F8T2:$PC_{71}BM$ (100:4, 350 nm)/LiF (0.8 nm)/Al (100 nm).

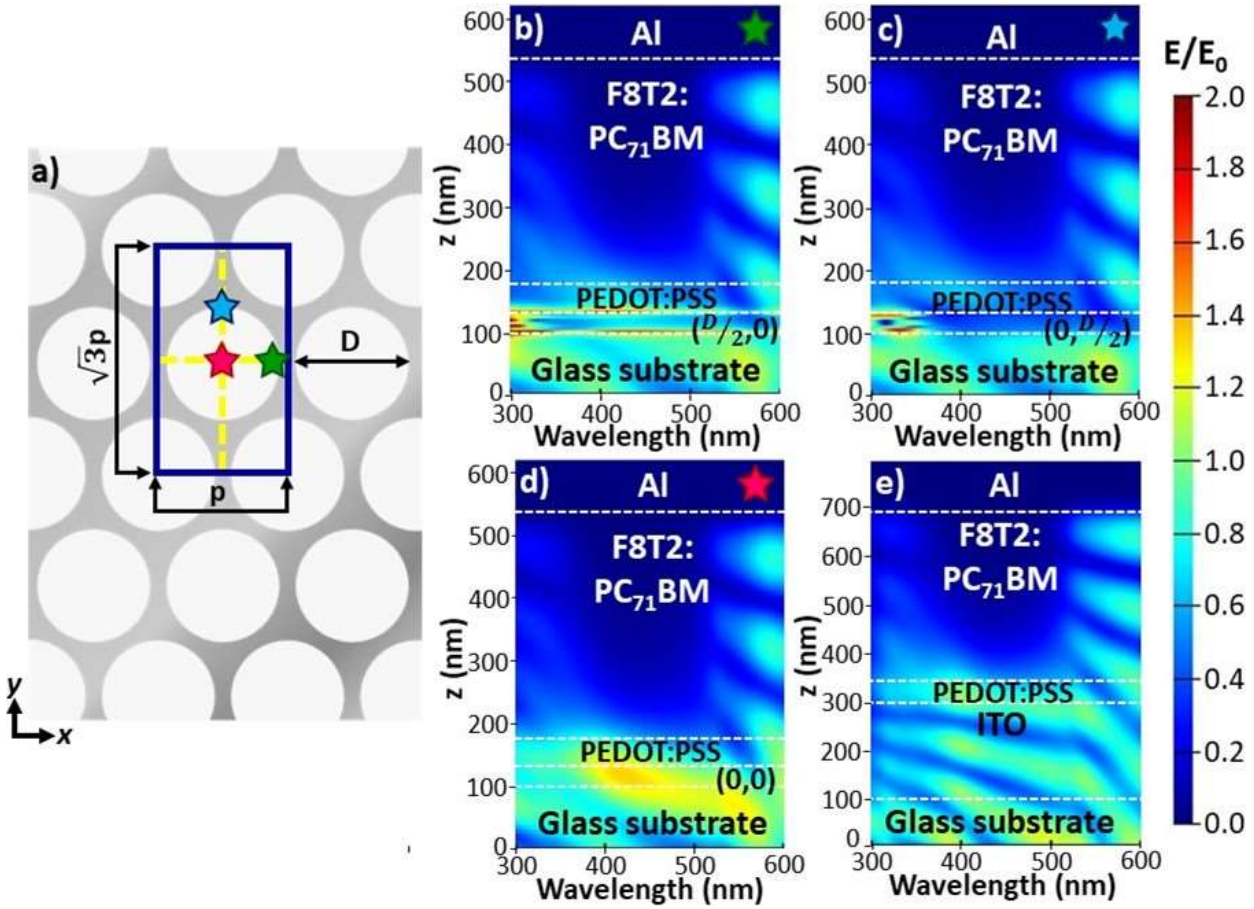

Figure 4-5. (a) Illustration of the top-view of the hexagonal Al-NHA. (b-d) 3D-FDTD-simulated internal electric field distributions as a function of wavelength for an Al-NHA-based device with a diameter/pitch of 175/200 nm at the x-y coordinate of (b) (D/2, 0), (c) (0, D/2) and (d) (0, 0) based on the coordinates defined in Figure 1c, and marked as green, blue and pink stars, respectively. (e) 3D-FDTD-simulated internal electric field distribution as a function of wavelength for an ITO-based device at any x-y point. The reference electric field (E_0) is 1 V/m.

The internal electric field is mapped along the z direction of each device, for a specific x-y point, against the incident illumination wavelength. The color scale represents the strength of the electric field relative to a reference electric field of 1 V/m, and is therefore unitless. For the Al-NHA-based device represented in Fig. 4-5, electric field distributions at three x-y points, corresponding to the x-edge, y-edge, and center-point of the central nanohole, were calculated to provide a representative evaluation of the internal electric field throughout the device. The wavelength

dependent electric field distributions at x-y points of (D/2, 0), (0, D/2), and (0,0), based on the coordinates defined in Fig. 4-5a and marked by green, blue, and pink stars, respectively, are shown in Fig. 2b, c, and d, respectively. For the ITO-based device (Fig. 4-5e), any x-y point can be used since the device, and the internal electric field, is uniform over x-y variation.

Since plasmonic enhancements to the internal electric field are a very near-field effect,[60] the Al-NHA does not produce any unique behavior in the top portion of the active layer, and in fact all simulated devices represented in Fig. 4-5 exhibit similar electric field distributions in this region. The strongest intensity is obtained under incident wavelengths at the edges of the active layer absorption peak, around 300-350 nm and above about 520 nm. Because active layer absorption at these wavelengths is relatively weak, this light can penetrate the active layer and be reflected off the top Al electrode, resulting in the electric field intensity oscillations at these wavelengths and enabling them to produce a significant electric field intensity at the top of the active layer.[33, 52, 123, 124] Light within the absorption peak, between about 350-520 nm, is absorbed strongly and therefore does not reach the top portion of the active layer, resulting in a weak electric field intensity in this spectral range at the top of the devices.

Distinct behavior is observed from the Al-NHA-based device in the lower portion of the active layer at each of the three x-y points in Fig. 4-5b-d due to the hexagonal NHA, the coupling of SPPs, and the polarization of incident light. In general, relatively strong electric fields occur at the interfaces of PEDOT:PSS/Al-NHA and Al-NHA/glass. Fig. 4-5b shows the internal electric field distribution at the point (D/2, 0), corresponding to the x-edge of the nanohole. Electric field intensities between about 1.0-2.0 are maintained throughout the spectral range evaluated at the Al-NHA interfaces, with the highest intensities obtained in the spectral ranges between about 300-350 and 400-500 nm. Fig. 4-5c shows the internal electric field at the point (0, D/2), corresponding

to the y-edge of the nanohole. High intensity values, between about 1.5-2.0, are achieved at the Al-NHA interfaces for incident light between about 300-360 nm. Fig. 4-5d shows the electric field distribution in the center of the nanohole, at the point (0,0). The electric field intensity in the lower portion of the device varies between about 0.6-1.2, with the highest intensities obtained in the spectral range of 350-550 nm. Notably, the highest electric field intensities in the Al-NHA-based are obtained in the spectral range between about 300-500 nm, which aligns well with the active layer absorbance and intended spectral range of photodetection. The ITO-based device, shown in Fig. 4-5e, produced electric field intensities between about 0.8-1.0 in the lower portion of the device, regardless of the incident wavelength. Oscillations are observed in the electric field intensity within the ITO and glass layers, which do not contribute to photoresponse, in the wavelength range corresponding to active layer absorption, confirming that cavity effects are present and likely responsible for the peaks and dips observed in the active layer absorbance for the simulated ITO-based device. At all three x-y points evaluated for the Al-NHA-based device, the electric field intensity in the lower portion of the device is stronger than that in the ITO-based device, demonstrating the plasmonic enhancements provided to the local electric field intensity in devices when metallic nanostructured films are incorporated into devices.

4.3.2 *Fabricating Al-NHAs via Nanosphere Lithography*

Al-NHAs were fabricated via NSL for integration into the photodiode devices. While nanoimprint lithography has been used to successfully fabricate similar NHAs,[69, 137] nanosphere lithography (NSL) has also been used to produce NHAs and proved a superior fabrication method for this work because of its cost-effectiveness, speed, and scalability.[137] The procedure is illustrated in Fig. 4-6 along with SEM images resulting from each step. NSL inherently produces a hexagonal NHA with the pitch determined by the nanosphere

diameter and the diameter controlled by the etch conditions. In this work, the monolayer of 200 nm diameter nanospheres was formed via drop-coating.

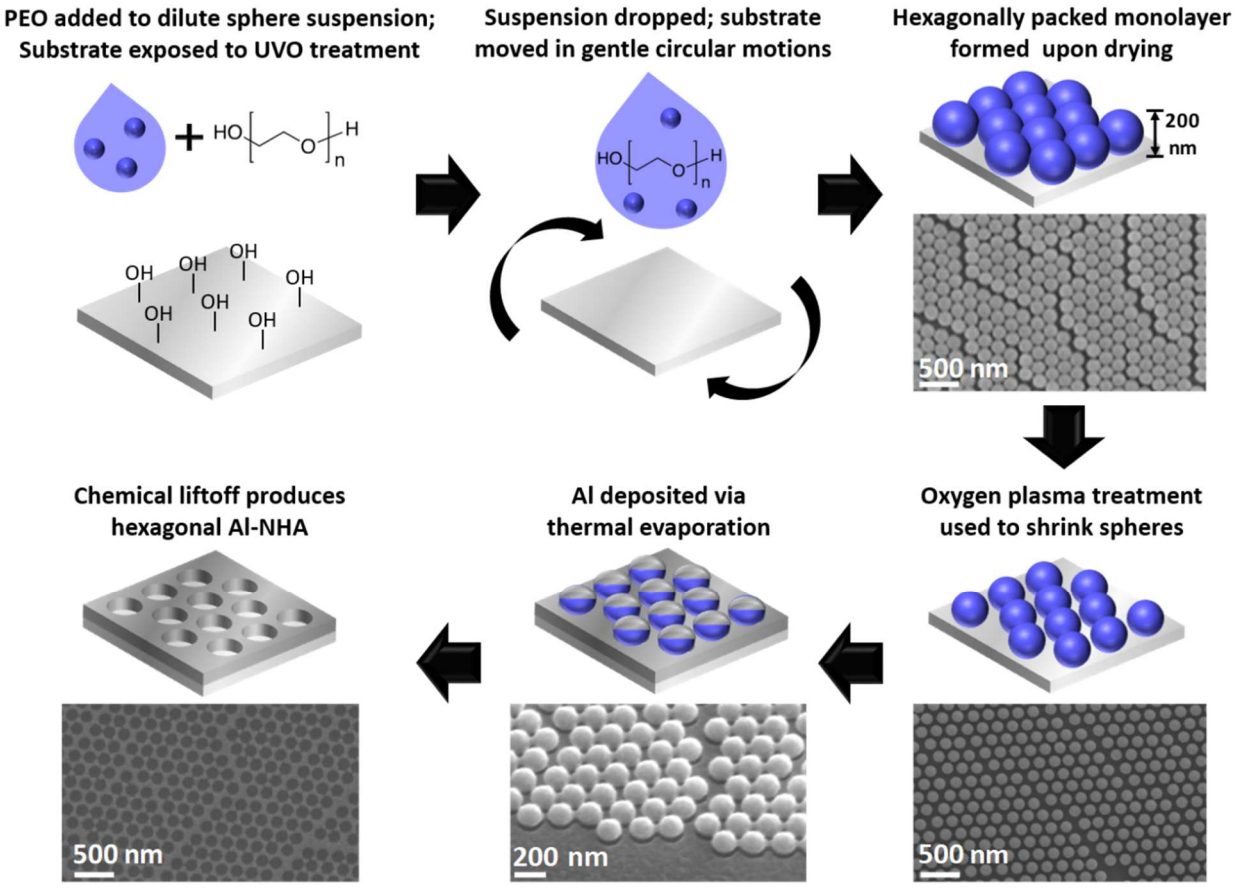

Figure 4-6. Schematics and corresponding SEM images for the nanosphere lithography process including the following steps: preparation of the substrate and nanosphere suspension, drop-coating with circular motions, the resulting nanosphere monolayer, shrinking the spheres via an oxygen plasma etch, Al deposition on top of and in between the spheres, and sphere removal via chemical liftoff.

Before drop-coating, Corning XG EAGLE glass substrates were exposed to UV-Ozone (UVO) treatment to activate hydroxyl groups on the surface and improve hydrophilicity and a small amount of polyethylene oxide (PEO) was added to the diluted nanosphere suspension to improve the resulting monolayer quality. It has been reported that adding PEO improves the quality of the monolayer formed via the air-water interface method.[138] After the nanosphere monolayers were deposited, they were exposed to an O_2 plasma to shrink the spheres and create clean space between, so that Al could be deposited both on

top of the spheres and on the glass substrate between them. Finally, the spheres were dissolved in toluene during liftoff to produce the desired Al-NHA.

A critical step in NSL is the formation of a large area, close-packed monolayer of nanospheres. As can be observed in Fig. 4-6, defects exist throughout these monolayers, which could be reduced by further optimization of drop-coating process. Different conditions, such as the solvent of the sphere suspension, concentration of spheres and PEO, other additives, volume dropped, and substrate material and treatment, could be explored as well as a deeper investigation of other sphere deposition techniques. Many such techniques have been reported in the literature, and several were attempted in this work including convective dragging,[139] spin-coating,[140] drop-coating[141-143] and the air-water interface method.[138, 144-150] Some results are shown in Fig. 4-7. Force assembly by directional rubbing was also attempted, but this technique could only be accomplished on polymer films, typically polydimethylsiloxane (PDMS).[70, 151, 152] In addition to complicating the dry etch step required to expose the glass substrate beneath the polymer lithography mask, the use of PDMS would require much harsher liftoff conditions, compared to the liftoff required for spheres alone, so this method was not pursued.

The films in Fig. 4-7a and b were produced by spin coating and drop coating, respectively. For both films, the nanosphere suspension was diluted with a 1:1 blend of water and ethanol to a final concentration of 9.47 x 10^8 spheres/mL. The film in Fig. 4-7a was spin cast by dropping 40 μL of suspension and spinning at 800 rpm for 30 s, followed by drying on a hot plate at 60°C for 5 min. This resulted in a film that visually looked opaque and white, and under SEM was shown to have sporadic and incomplete coverage. The drop-coated film in Fig. 4-7b was produced by dropping 20 μL of the same diluted

solution and drying on a hot plate set to 20°C, effectively drying at room temperature. This film was visually more transparent than the spin cast film. The entire area of the drop cast film was not covered uniformly, but there were sections with good monolayer formation, as shown in Fig. 4-7b.

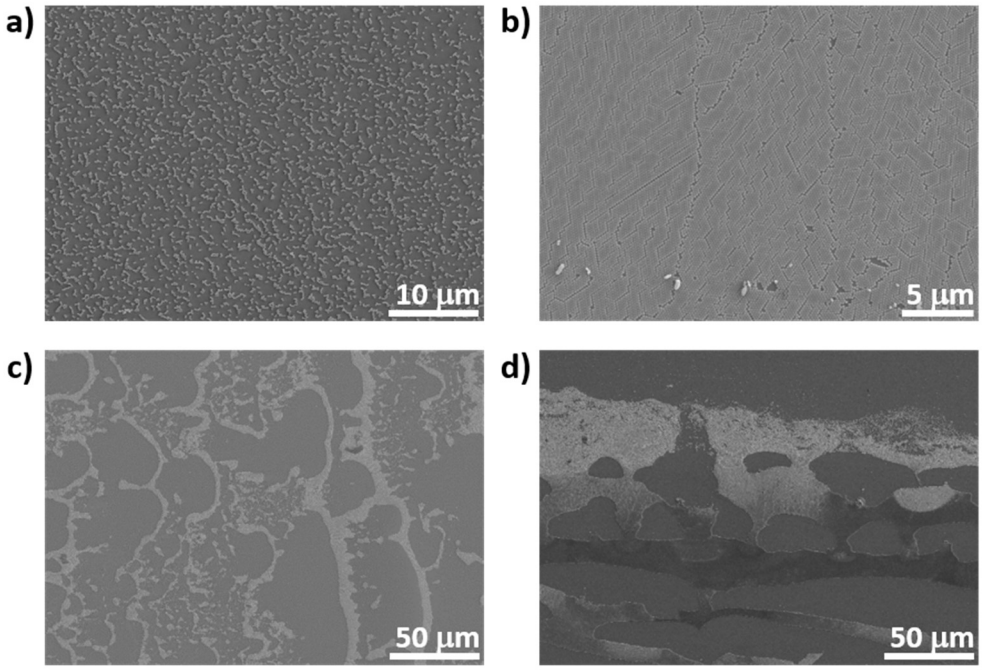

Figure 4-7. SEM images of the nanosphere films produced by (a) spin coating, (b) drop coating, (c) convective dragging, and (d) air/water interface. Lighter areas are spheres and darker areas are bare glass. The variation in the colors of the sphere-covered areas in (d) are due to variations in the sphere packing density.

The film in Fig. 4-7c was produced by convective dragging. 20 µL of diluted sphere suspension, 9.47 x 10^8 spheres/mL diluted in ultrapure water, was dropped onto a substrate, and a glass cover slip was then placed on top of the dropped solution and dragged across the substrate at a rate of 0.1 µm/s by a syringe pump attached to the cover slip. This was within the range of dragging rates reported in the literature, but the lines observed in Fig. 4-7c indicate that the dragging rate was too fast.[139] However, the process time was approximately 45 min, and only one sample could be produced at a time, so it was determined that this was not a practical method to pursue due to its extremely time-intensive

nature. The film in Fig. 4-7d was produced using the air/water interface method. Briefly, substrates are submerged in a water bath while spheres, diluted in a blend of water and ethanol,[145] are dropped onto the water surface so that a monolayer is formed. The water is then pumped out, often with the bath set at a small angle.[145, 149] A syringe pump was used in this work for both dropping the spheres and pumping out the water bath. As the water is pumped out, the water surface and monolayer lowers to and below the substrate level, depositing the sphere monolayer onto the substrate surface. For the film in Fig. 4-7d, the diluted solution of spheres had a concentration of 9.47 x 10^8 spheres/mL and was diluted in a 2:1 blend of water and ethanol. 50 μL of the solution was dropped at a rate of 0.01 mL/min, and the water was withdrawn at a rate of 0.1 mL/min. The variation in sphere color in the SEM image is related to variations in the packing density of the spheres. The air/water interface method has been relatively widely used and adapted in the literature,[145-147, 149, 150] and further adaptations were also pursued, but none produced monolayer coverage and uniformity superior to that of drop-coated films. Therefore, drop-coating was determined to be the most suitable method for producing the nanosphere monolayer and was fully pursued in this work.

The resulting hexagonal monolayer was exposed to an O_2 plasma etch to shrink the spheres. Ideally, this will shrink the spheres minimally, enough to create clean separation with no material between spheres, so that the eventual nanoholes will be separated by thin, continuous Al walls. The etch step is sensitive to etch power, time, and the flow rate ratio of the process gases O_2 and Ar. The etch condition optimization is summarized in Fig. 4-8. Fig. 4-8a shows SEM images of the nanosphere monolayers produced by varied etching powers and times, with the process gas flow kept constant at 50 SCCM each of O_2 and Ar.

The films in the first row were etched under 125 W for 30, 60, 90, and 120 s. 30 and 60 s were insufficient to create space between the spheres, and bridging is evident. After 90 s, clean separation is achieved but the spheres are significantly smaller. After 120 s, material redeposition occurs and clean separation is therefore not achieved.

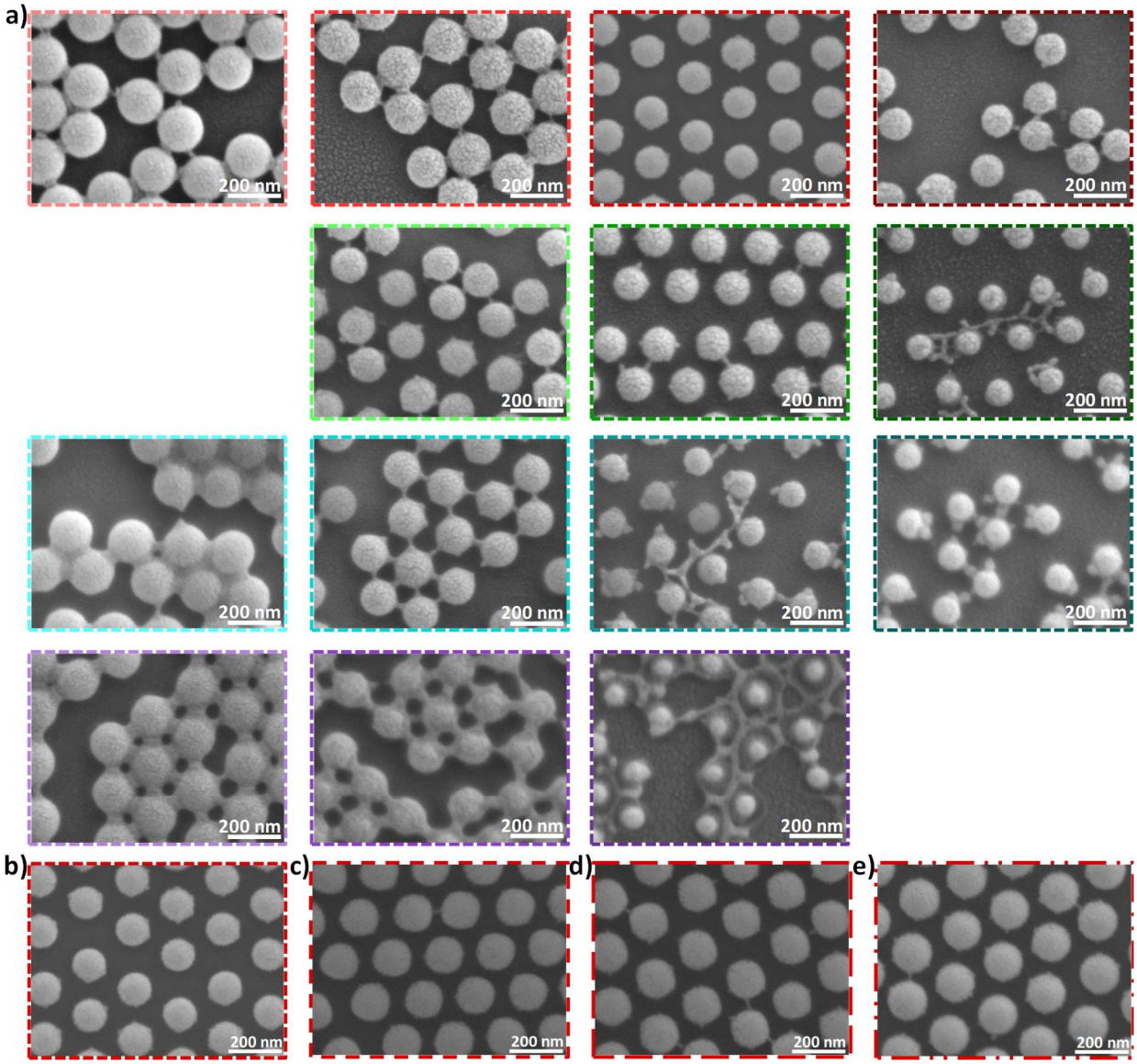

Figure 4-8. SEM images of the resulting nanosphere monolayers for varied etching conditions including (a) etch time and power with the O_2 and Ar gas flow rates each fixed at 50 SCCM, and (b-e) process gas flow rate ratio, utilizing O_2:Ar ratios of (b) 1:1, (c) 4:1, (d) 8:1, and (e) 1:0, with fixed etch power and time of 125 W and 90 s, respectively. In (a), the first, second, third, and fourth rows were etched at 125, 250, 300, and 400 W, respectively and the first, second, third, and fourth columns were etched for 30, 60, 90, and 120 s, respectively.

The films in the second row of Fig. 4-8a were etched at 250 W for 60, 90 and 120 s. While a 60 s etch is nearly enough for a clean separation without shrinking the spheres significantly, bridging persists between a significant number of the spheres. If the etch is held for 90 or 120 s, redeposition is apparent. The films in the third row were etched at 300 W for 30, 60, 90 and 120 s. Etch times of 30 and 60 s were insufficient but etch times of 90 and 120 s were too harsh, as material was redeposited between the spheres. The films in the fourth row of Fig. 4-8a were etched at 400 W for 30, 60 and 90 s. Bridging is observed for the films etched for 30 and 60 s and redeposition is observed for the film etched for 90 s. The etch at 125 W held for 90 s provided the best results of the etching power/time combinations evaluated, so it was used as a basis to optimize the ratio of the process gases. These results are shown in Fig. 4-8b-e, f O_2:Ar ratios of 1:1, 4:1, 8:1, and 1:0, respectively, with the total gas flow kept constant at 100 SCCM. The film in Fig. 4-8b is the same as the film in Fig. 4-8a etched at 125 W for 90 s, with a 1:1 ratio of O_2:Ar. This condition produced clean separation between the spheres, but a less severe size change for the spheres is desired. The film in Fig. 4-8c was etched with a 4:1 ratio of O_2:Ar, which also produced clean space between spheres, and the spheres were shrunk less severely. As the O_2:Ar ratio was further increased to 8:1 and 1:0, bridging was reintroduced, as seen in Fig. 4-8d and e, respectively. Based on the results in Fig. 4-8, the optimal etch conditions were determined to be 125 W for 90 s, with a 4:1 blend of O_2:Ar at a total flow rate of 100 SCCM.

After etching, 30 nm of Al was deposited via thermal evaporation onto the nanosphere monolayers with the impinging beam normal to the substrate to ensure that Al on top of the spheres remains physically separated from Al on the glass between the spheres, so that liftoff of spheres to generate nanoholes can be achieved. The SEM image in Fig. 4-6

corresponding to this step was taken at the edge of a patterned area, with a higher magnification and a 40° tilt, to clearly demonstrate that this deposition has been achieved. Finally, toluene was used as a solvent to achieve chemical liftoff[149, 150, 153, 154] by dissolving the spheres, resulting in the desired Al-NHA with a thickness of 30 nm.

4.3.3 *Performance of Al-NHA-based Conventional Photodetectors*

Fabricated Al-NHAs were then evaluated as device electrodes. For a transparent conducting electrode, optical transmittance directly affects device photoresponse strength. Transmission of Al-NHA and control ITO electrodes were measured and are shown in Fig. 4-9. The Al-NHA electrode does not exceed 40% transmission throughout the entire spectral range, peaking at 36.8% under 380 nm illumination. The ITO electrode has around 90% transmission in the range of 380-600 nm, but the transmission is lower, between 30-90%, in the range of 300-380 nm. Another critical characteristic of a transparent conducting electrode is its sheet resistance, which, if too high, will prevent the film from functioning as an effective electrode. The sheet resistance for an Al-NHA electrode was measured to be 3.4 Ω/sq using the four-point probe method. ITO electrodes, with a thickness of 200 nm, had a sheet resistance of 8.9 Ω/sq.

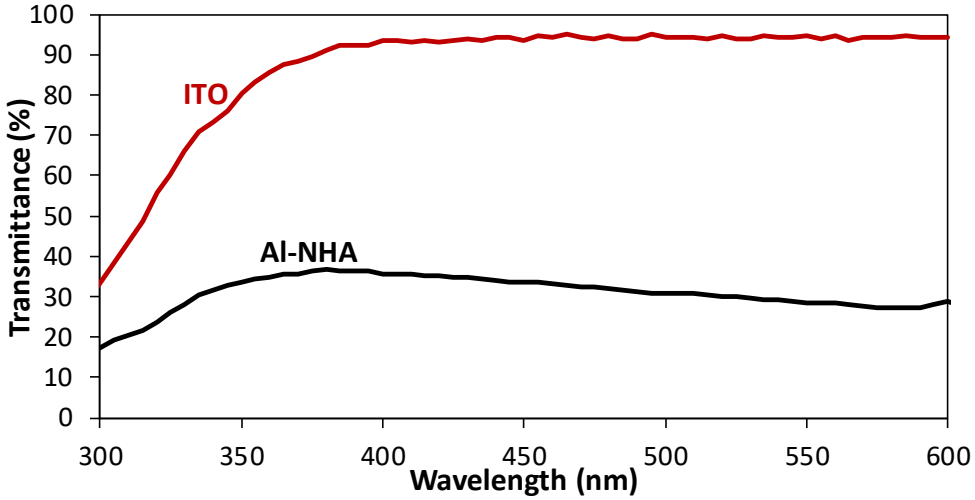

Figure 4-9. Measured transmittance for Al-NHA (30 nm) and ITO (200 nm) electrodes.

Devices were fabricated with a structure of Al-NHA (30 nm) or ITO (200 nm)/PEDOT:PSS (40 nm)/F8T2:$PC_{71}BM$ (350 nm, 100:4 weight ratio)/LiF(0.8 nm)/Al (100 nm) and evaluated. The dark current in Al-NHA-based devices is significantly reduced compared to ITO-based devices, as shown in Fig. 4-10a. The dark current density (J_D) values produced by Al-NHA- and ITO-based devices are 4.4 x 10^{-7} and 8.3 x 10^{-5} mA/cm^2, respectively, under a -2 V bias, and 9.2 x 10^{-8} and 5.2 x 10^{-4} mA/cm^2, respectively, under a 2 V bias. Low dark current typically corresponds to more sensitive photoresponse and is therefore a desired attribute of the Al-NHA-based devices. The photocurrent densities (J_{PH}) produced under 360 nm illumination are shown in Fig. 4-10b. Due to the higher transmittance of ITO compared to Al-NHAs, ITO-based devices produce higher J_{PH} values than Al-NHA-based devices. Under 360 nm illumination, Al-NHA- and ITO-based devices produce J_{PH} values of 2.5 x 10^{-6} and 1.0 x 10^{-4} mA/cm^2, respectively, under a -2 V bias, and 2.9 x 10^{-6} and 5.8 x 10^{-4} mA/cm^2, respectively, under a 2 V bias.

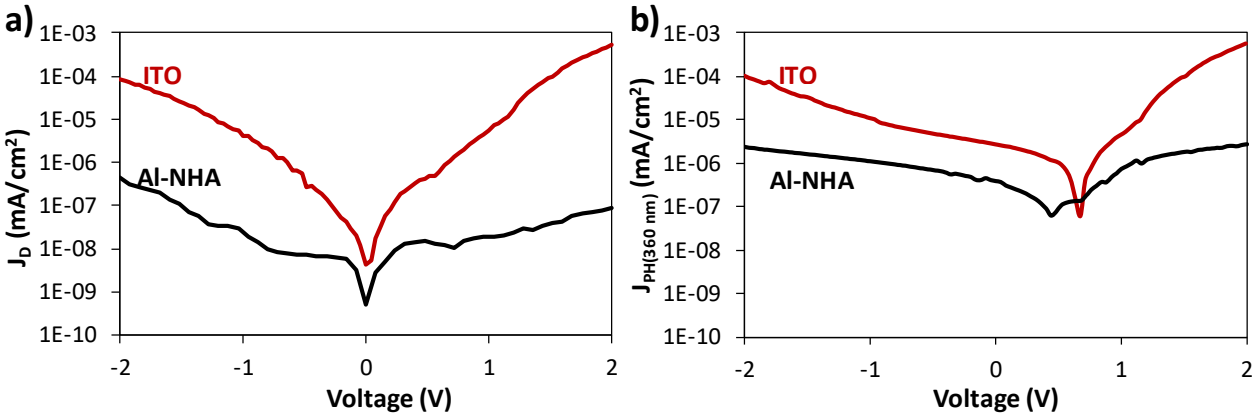

Figure 4-10. Current density produced by Al-NHA- and ITO-based devices under (a) dark conditions and (b) 360 nm illumination.

The dark current density of a device corresponds approximately, but not exactly, to the noise current present within the device. To obtain accurate values for noise currents, the dark current density was measured, at a steady applied bias, against time, and a Fast Fourier Transform (FFT)

was performed on the resulting data.[33, 34, 52] The noise current values for each device fabricated and evaluated in this work are shown in Table 4-1, under a variety of applied biases.

Table 4-1. Noise currents for Al-NHA- and ITO-based devices, calculated by a Fast Fourier Transform of the dark current measured against time, tested under forward and reverse biases.

Bottom Electrode	Bias (V)	Noise Current (A/√Hz)
Al-NHA	-2	4.4×10^{-13}
	-1	5.7×10^{-12}
	0	2.8×10^{-12}
	0.5	3.1×10^{-13}
	1	2.9×10^{-13}
	2	4.5×10^{-13}
ITO	-2	3.3×10^{-11}
	-1	1.2×10^{-11}
	0	4.4×10^{-11}
	0.5	3.0×10^{-12}

The EQE spectra of the Al-NHA- and ITO-based devices under 0, -1 and -2 V reverse biases are provided in Fig. 4-11a. EQE represents the ratio of collected charge carriers to incident photons, providing a measure of photoresponse strength. Peaks around 350 and 515 nm, corresponding to the edges of the active layer absorbance peak, are produced by both Al-NHA- and ITO-based devices. Light with these wavelengths is absorbed weakly, so it penetrates the active layer and is absorbed in the top portion, enabling it to contribute significantly to reverse-bias photoresponse, the mechanism of which will be discussed in detail later. This is true for both Al-NHA- and ITO-based devices and agrees with the simulated electric field distributions presented in Fig. 4-5, where the electric field at the top of the active layer is most intense for incident light with wavelengths at the edges of the active layer absorbance peak. Notably, Al-NHA-based devices produce photoresponse that is more UV-selective than the ITO-based devices, as demonstrated by two spectral features. First, the UV-peak is slightly blue-shifted for Al-NHA-based devices, occurring at 350 nm instead of 360 nm as it does for ITO-based devices. This agrees

with the simulated active layer absorbance shown in Fig. 4-3, where UV-peaks produced by Al-NHA-based devices were also blue-shifted from that of ITO-based devices. The other feature demonstrating the superior UV-selectivity of Al-NHA-based devices is the relative magnitude of EQE peaks. Under a -2 V bias, Al-NHA-based devices produce a UV-peak that is slightly higher than the 515 nm peak, while ITO-based-devices produce a UV-peak that is slightly lower than the 515 nm peak. The superior UV-selectivity exhibited by the Al-NHA-based devices could be due to the relatively high transmittance, compared to the rest of the Al-NHA transmittance spectrum, between 350-400 nm produced by the Al-NHA electrode (Fig. 4-9). The lower photoresponse strength produced by Al-NHA-based devices compared to that produced by ITO-based-devices, confirmed by the J_{PH} values in Fig. 4-10b, is attributed to the lower optical transmittance of Al-NHA electrodes compared to ITO (Fig. 4-9).

For applications where photoresponse sensitivity is more important than strength, the specific detectivity (D*) is a more meaningful figure of merit than EQE, as it accounts for the energy of incident photons at different wavelengths, the device active area, and the noise current in the device, which is lower in Al-NHA-based devices than in ITO-based devices, enabling Al-NHA-based devices to produce competitive D* values (Fig. 4-11b), despite their relatively weak photoresponse. The D* values obtained from Al-NHA- and ITO-based devices without any applied bias are very similar, with the Al-NHA- and ITO-based devices producing peaks at 2.0×10^8 and 2.8×10^8 Jones, respectively, under 340 nm illumination. Under applied reverse biases ITO-based devices achieve higher D* values than Al-NHA-based devices, but they are within an order of magnitude. Additionally, Al-NHA-based devices have a UV-peak that is slightly blue-shifted from the UV-peak produced by the ITO-based-device. Under a -2 V bias, Al-NHA- and ITO-based devices produce respective D* values of 4.0×10^9 and 1.2×10^{10} Jones under 340 and 350 nm

illumination, respectively. ITO can therefore be replaced by an Al-NHA electrode, which utilizes a cheap, flexible material, without significantly diminishing reverse-bias performance.

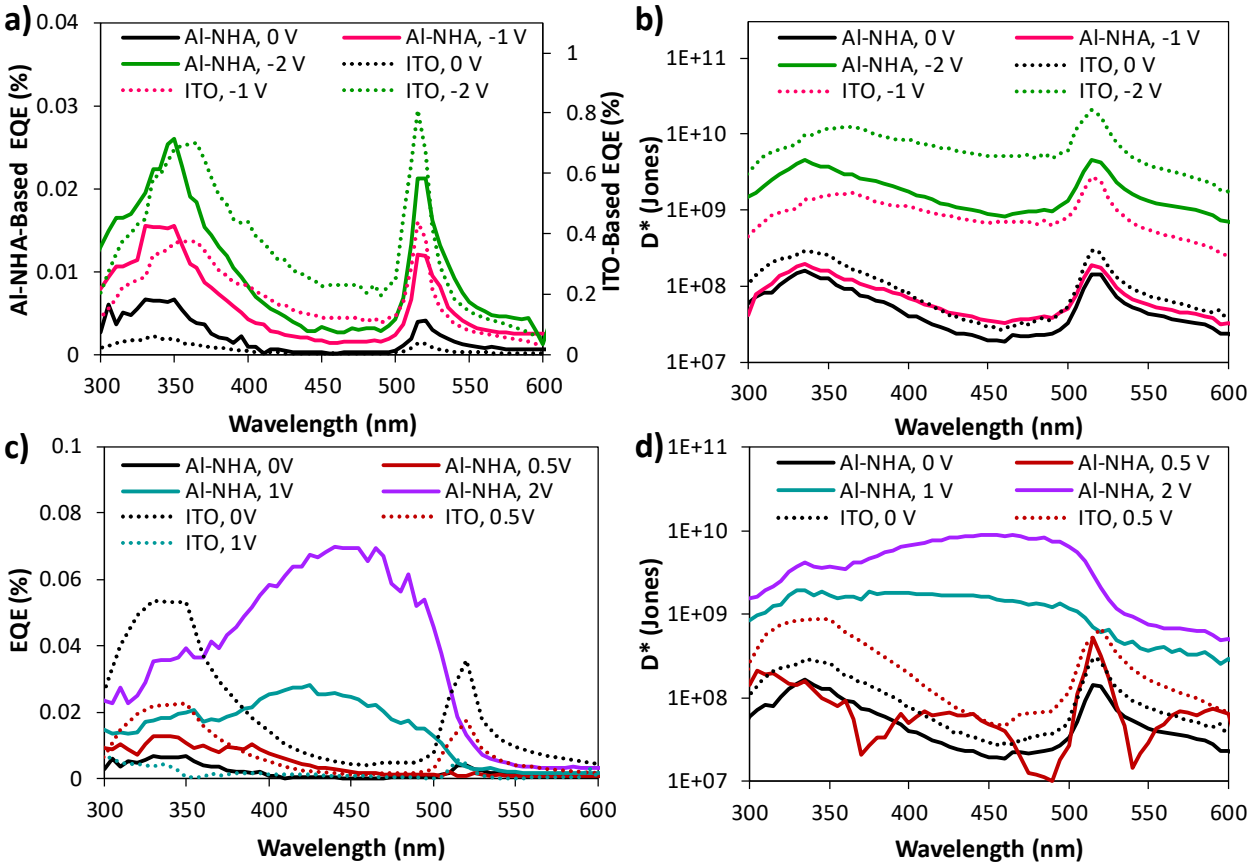

Figure 4-11. (a,b) EQE and D* spectra for Al-NHA- and ITO-based devices under reverse biases. (c,d) EQE and D* spectra for Al-NHA- and ITO-based devices under forward biases.

Under forward bias, Al-NHA-based devices produce superior photoresponse compared to ITO-based devices, as evaluated by response strength, stability, and sensitivity, and demonstrated in Fig. 4-11c-d. Al-NHA-based devices show a new, distinct spectral shape, exhibiting one broad peak that corresponds to the absorption of the active layer and increases in magnitude for increasing forward biases. A maximum EQE value of 0.069% under 450 nm illumination and a 2 V bias is obtained. Contrarily, the EQE values produced by ITO-based devices decrease with increasing forward bias, while maintaining the same spectral shape as is produced under reverse bias. When the bias was increased from 0 to 0.5 V, the peak EQE value obtained under 350 nm

illumination dropped from 0.053% to 0.023%. Increasing the forward bias to 1 V resulted in further reduced and unstable photoresponse. Due to both stronger EQE and lower dark (and noise) currents, Al-NHA-based devices produce superior D* values under forward bias compared to the ITO-based devices, as shown in Fig. 4-11d. Under a small forward bias of 0.5 V, the spectral shape produced by the Al-NHA-based device can be clearly observed, and will be discussed in the context of the general photoresponse mechanism later. As the forward bias was increased, the D* values produced by Al-NHA-based devices also increased, peaking at 8.8 x 10^9 Jones under 450 nm illumination and a 2 V bias. Under a small forward bias of 0.5 V the D* values produced by the ITO-based device also increased compared to the D* values produced without any bias, but values could not be obtained at higher biases because device instability prevented the reliable calculation of noise current. While the photoresponse values reported here are not among the strongest reported throughout the literature,[74-76] the novel bias-dependent response switching introduced in these Al-NHA-based devices is a significant achievement and could be applied to other systems to achieve photoresponse that is both strong and can be tuned by the bias applied.

4.3.4 *Drift- and Diffusion-Based Photoresponse Mechanisms*

The bias-dependent response switching achieved by the Al-NHA-based device is hypothesized to be related to electrode symmetry. Response switching has also been shown for a device with a structure of Al/P3HT:$PC_{71}BM$/Al, which produced two-peak EQE spectra under reverse bias and one-peak spectra under forward bias, corresponding to the edges and peak of the active layer absorbance, respectively.[30] The electrode symmetry allowed the assignment of cathode and anode to be determined by the applied bias, rather than the electrode material, thus enabling bias-dependent response switching.[30] Fig. 4-12a and b show band level diagrams for Al-NHA- and ITO-based devices, respectively, demonstrating the electrode symmetry introduced by the Al-

NHA electrode. It should be noted that, due to the conventional device structure, the interfacial layers remain asymmetric and so does the overall device. The proposed mechanism of the bias-dependent response switching is illustrated in Fig. 4-12c-f, which provides schematic representations of the photoresponse mechanisms for Al-NHA-based devices under reverse bias (Fig. 4-12c), no bias (Fig. 4-12d), and forward bias (Fig. 4-12e), and for ITO-based devices under any bias (Fig. 4-12f). For each case, a band diagram is drawn and includes the relevant band tilting and charge carrier flow. Arrows indicate the direction and relative strength of hole drift (denoted as h+ drift) and hole diffusion (denoted as h+ diffusion) currents. Generally, light absorption occurring in the top and bottom of the active layer, denoted with white and purple stars, respectively, are hypothesized to correspond to hole drift and diffusion, respectively.

For Al-NHA-based devices, the spectral shape of the photoresponse depends on the bias applied. Under reverse bias (Fig. 4-12c), the energy bands tilt to provide a driving force for hole drift. Light absorbed at the top of the active layer contributes most significantly to photoresponse, since photogenerated holes can successfully drift downwards to be collected at the bottom Al-NHA electrode (anode). Peak photoresponse is therefore achieved at the edges of the F8T2 absorption peak, around 350 and 515 nm, since these wavelengths can penetrate the active layer and be absorbed near the top of the layer. Light within the absorption peak is absorbed strongly in the bottom portion of the active layer and generates excitons there.[26] An applied reverse bias does not provide any driving force for photogenerated holes in the bottom of the active layer to diffuse upwards in the active layer, so a space charge region is established and suppresses the photoresponse for light absorbed in this region.[33]

An Al-NHA-based device without any applied bias is also dominated by hole drift, as illustrated in Fig. 4-12d and evidenced by the spectral shape observed in Fig. 4-11. The drift-dominated

photoresponse in this case is attributed to the presence of the LiF layer, which has two significant effects. First, LiF has hole-blocking capabilities, so it prevents any holes diffusing upwards through the active layer from being collected at the top Al cathode and contributing to photoresponse.[30, 51] Second, the presence of LiF has been shown to make the Al work function slightly less negative,[108, 109] resulting in a device that does not truly have symmetric electrodes but instead has a small built-in reverse bias, which provides a driving force for hole drift to dominate over diffusion, as it does under an applied reverse bias.

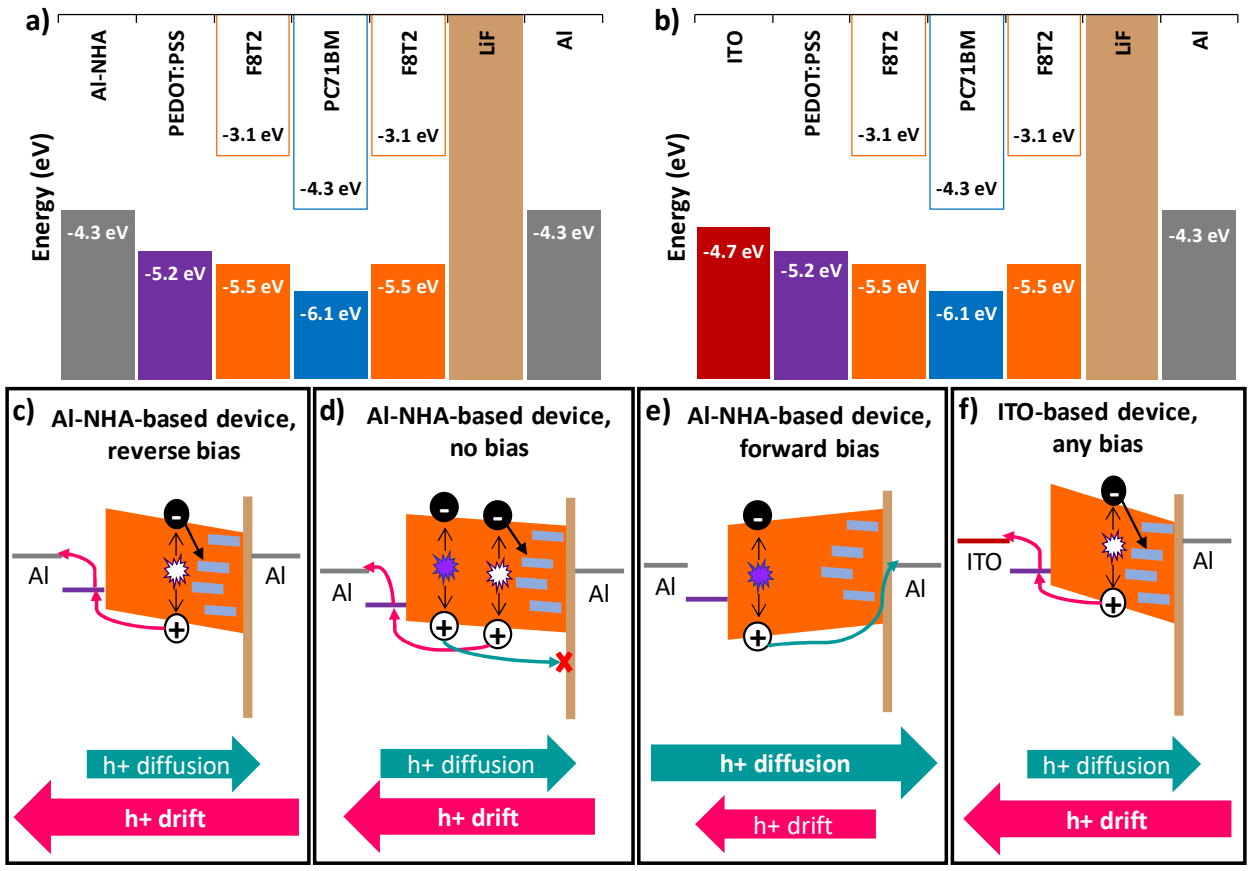

Figure 4-12. (a, b) Energy band diagrams for Al-NHA- and ITO-based devices. (c-e) Illustrations of response mechanism for an Al-NHA-based device under (c) applied reverse bias, (d) no applied bias, and (e) applied forward bias. (f) Illustration of response mechanism for an ITO-based device under any bias.

An applied forward bias enables the Al-NHA-based devices to produce spectrally distinct, diffusion-dominated photoresponse by effectively inverting the device, as illustrated in Fig. 4-12e.

In this case, the applied bias can overcome the built-in reverse bias introduced by the LiF layer and tilt the bands forward, providing a driving force for hole diffusion instead of drift. Light absorbed in the lower portion of the active layer, in the spectral range corresponding to the active layer absorption peak between about 350-515 nm, contributes most significantly to photoresponse in this case. The applied forward bias provides a driving force for photogenerated holes in the lower portion of the active layer to diffuse upwards through the layer, rather than form a response-suppressing space charge region. Beyond aiding the upwards diffusion of holes, this driving force also enables them to overcome the hole-blocking property of LiF and be collected at the top Al electrode. Further, the forward bias provides some resistance to hole drift, suppressing photoresponse at 350 and 515 nm and resulting in diffusion-dominated photoresponse spectra with a single peak around 450 nm.

For an ITO-based device, the asymmetry of the electrode work functions causes the bands to tilt and create a built-in reverse bias, as illustrated in Fig. 4-12f, resulting in behavior similar to that of an Al-NHA-based device under applied reverse bias (Fig. 4-12c). Because the built-in bias acts as a reverse bias, applying an additional reverse bias improves the photoresponse strength while applying a forward bias diminishes it (Fig. 4-11a and c, respectively). Two-peak photoresponse spectra are always produced, regardless of the bias applied, because the built-in reverse bias, resulting from the asymmetry of the electrode work functions, suppresses hole diffusion. Contrary to the response switching achieved in Al-NHA-based devices, the ITO-based device is locked in to a drift-dominated photoresponse, and any hole diffusion that occurs is blocked from contributing to the photoresponse by both the LiF hole blocking layer and the built-in reverse bias. Likewise, devices with a structure of ITO/poly[9,9-bis(60-(N,N-diethylamino)propyl)-fluorene-alt-9,9-bis-(3-ethyl(oxetane-3-ethyloxy)-hexyl)fluorene] (PFN-OX)/P3HT:$PC_{71}BM$/Al were reported to

produce spectrally similar photoresponse under both reverse and forward biases.[123] Even under a strong forward bias of 60 V, ITO-based devices produced EQE spectra with two peaks corresponding to the edges of the active layer absorbance.[123] In our case, ITO-based devices produce weak, unstable photoresponse under applied forward biases, whereas Al-NHA-based devices produce strong, stable photoresponse. Al-NHA electrodes enable distinct behavior simply by changing the bias applied to a device, effectively producing two devices in one.

The response mechanism described in Fig. 4-12 can be used to further explain some of the previously presented photoresponse results. Fig. 4-10 demonstrates that the dark current produced by Al-NHA-based devices is significantly lower than that produced by ITO-based devices, which can be attributed to two factors. First, as shown in Fig. 4-12a and b, the hole injection barrier from Al into PEDOT:PSS (0.9 eV) is higher than the injection barrier from ITO into PEDOT:PSS (0.5 eV), resulting in lower dark current in Al-NHA-based devices under forward bias. Second, the built-in reverse bias is weaker in Al-NHA-based devices than in ITO-based devices, due to the significant asymmetry between the ITO and Al work functions, yielding a stronger driving force for hole drift in ITO-based devices and a subsequently higher dark current. The stronger built-in reverse bias and resulting drift driving force in ITO-based devices, compared to Al-NHA-based devices, likely also contributes to the superior reverse-bias photoresponse strength achieved by ITO-based devices (Fig. 4-11).

The photoresponse of Al-NHA-based devices under the small applied forward bias of 0.5 V illustrates the transition between drift-dominated to diffusion-dominated photoresponse described in Fig. 4-12. Its spectral shape, which can be clearly observed in Fig. 4-11d, has three peaks centered around 350, 450, and 515 nm. The 350 and 515 nm peak correspond with the drift-based behavior produced under reverse or no bias, while the 450 nm peak corresponds to the diffusion-

based behavior produced under forward bias. The small forward bias of 0.5 V does not provide enough resistance to hole drift to prevent light absorbed at the top of the active layer from contributing to photoresponse, resulting in the peaks at 350 and 515 nm, but does provide a sufficient driving force for diffusion-based photoresponse to occur, resulting in the peak at 450 nm. Therefore, both drift- and diffusion-based responses are possible at this small forward bias.

4.3.5 *Impact of Device Structure and Plasmonic NHAs*

Devices with different F8T2:$PC_{71}BM$ weight ratios of 100:15 and 1:1 were also fabricated and evaluated. It was hypothesized that varying the active layer morphology may engage the plasmonically enhanced photoresponse mechanisms more effectively than the 100:4 weight ratio. A ratio of 100:15, w:w, was chosen so that the morphology of isolated $PC_{71}BM$ clusters would be maintained while increasing the amount of $PC_{71}BM$ clusters and providing a more uniform distribution of $PC_{71}BM$ throughout the active layer, rather than having a small amount of clusters concentrated towards the top of the film, as is the case for the 100:4 weight ratio. A ratio of 1:1, w:w, was chosen so that the bulk heterojunction (BHJ) morphology could be investigated in these Al-NHA-based devices, as it was hypothesized that photoresponse mechanisms that are more relevant to this morphology may benefit more directly from the plasmonic enhancements than the charge injection achieved by the active layers with a 100:4 weight ratio. Ultimately, the devices with a 100:15 weight ratio displayed the same behavior as devices with a 100:4 weight ratio, and devices with a 1:1 weight ratio were unstable under forward bias and exhibited typical BHJ behavior under reverse bias. Therefore, it was determined that increasing the $PC_{71}BM$ content did not improve the photoresponse or the engagement of the plasmonic enhancements, nor did it provide any additional information, so a ratio of 100:4, w:w, remained the focus of the work.

Devices based on 10 nm planar Al electrodes (denoted as Al^{Planar}, having a measured sheet resistance of 7.3 Ω sq^{-1}) and devices with a hole-only architecture based on both Al^{Planar} and Al-NHA electrodes were investigated to confirm the proposed photoresponse mechanism and to isolate the impact of the Al-NHA induced plasmonic effects from the effects of the electrode material. To make a full electrode comparison, the transmission of Al^{Planar} electrodes was measured and is shown in Fig. 4-13a. Clearly, this electrode produces much weaker transmission than the ITO and Al-NHA electrodes, as its transmission does not exceed 10% throughout the entire spectral range evaluated. An Al^{Planar}-based device was also simulated and evaluated, and the resulting active layer absorbance and device reflectance are provided and compared to those of Al-NHA- and ITO-based devices in Fig. 4-13b and c, respectively. The Al^{Planar}-based device produces a weaker and blue-shifted active layer absorbance compared to both the Al-NHA- and ITO-based devices (Fig. 4-13b), which is attributed to the lower transmittance and slightly blue-shifted peak transmittance of fabricated 10 nm Al thin films (Fig. 4-13a). Additionally, the simulated reflectance from the Al^{Planar}-based device (Fig. 4-13c) is significantly higher than the other two devices.

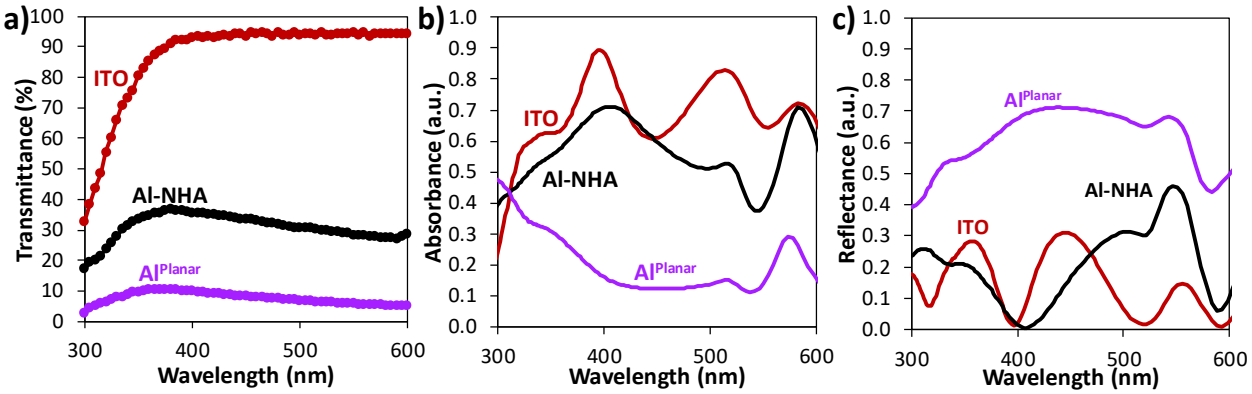

Figure 4-13. (a) Measured transmittance of ITO, Al-NHA, and Al^{Planar} electrodes with thicknesses of 200, 30, and 10 nm, respectively, (b-c) 3D-FDTD-simulated (b) active layer absorbance and (c) reflectance for devices based on ITO, Al-NHA, and Al^{Planar} electrodes with thicknesses of 200, 30, and 10 nm, respectively.

The internal electric field distribution for an AlPlanar-based device was also simulated and is shown in Fig. 4-14. The electric field intensity distributions for an ITO- and Al-NHA-based device are also included for comparison. Fig. 4-14 clearly shows that the incorporation of the NHA provides an electric field enhancement, as the Al^{Planar}-based device produces the weakest internal electric field intensities throughout the device. Stronger intensities are produced within the glass substrate due to the higher reflectance of the Al^{Planar} electrode, but electric field intensity within the substrate has no impact on device performance.

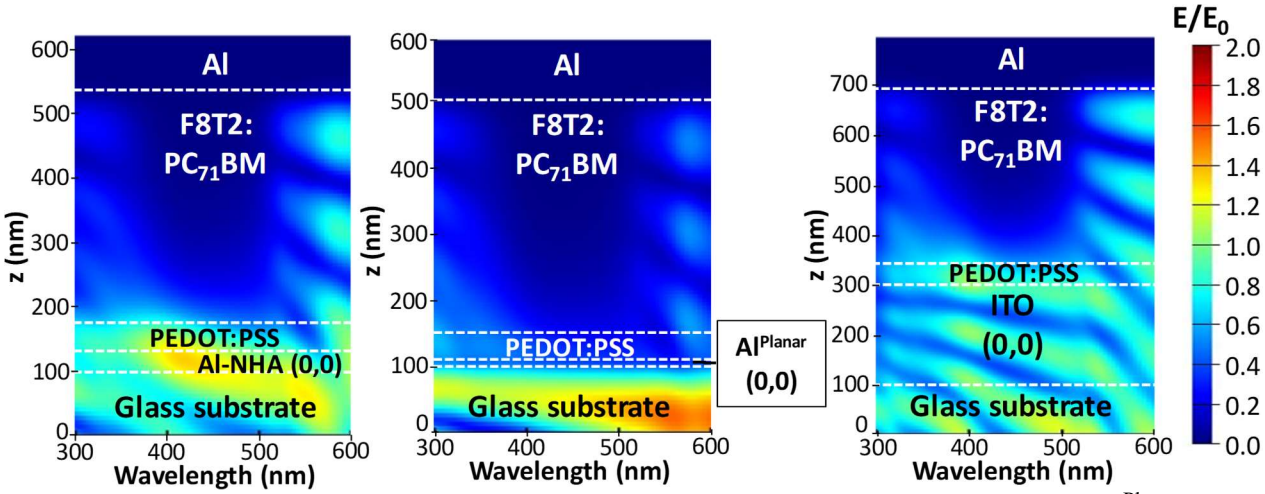

Figure 4-14. 3D-FDTD-simulated internal electric field distribution for Al-NHA-, Al^{Planar}-, and ITO-based devices.

The dark and photocurrent densities of Al-NHA and Al^{Planar} devices were also measured and are shown in Fig. 4-15. While the J_{PH} values produced by both devices are very similar in magnitude, the J_D produced by the Al^{Planar}-based device is significantly higher than that produced by the Al-NHA-based devices. Al-NHA- and Al^{Planar}-based devices produce dark current density values of --4.4 x 10^{-7} and 2.3 x 10^{-5} mA/cm^2, respectively, under -2 V bias, and 9.2 x 10^{-8} and 4.0 x 10^{-6} mA/cm^2, respectively, under 2 V bias. As both a high photocurrent and low dark current are desirable, Al-NHA-based devices exhibit better J-V performance overall, compared to Al^{Planar}-based devices.

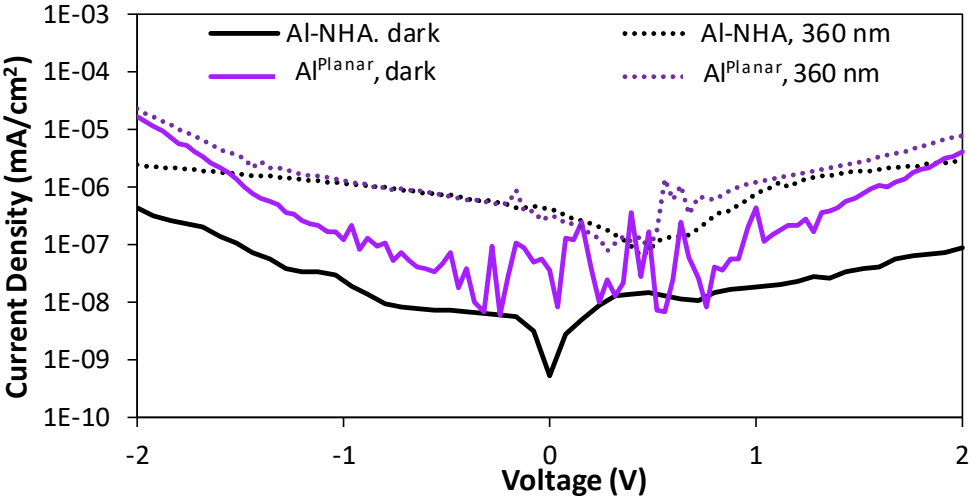

Figure 4-15. Current densities produced by Al-NHA- and Al^{Planar}-based devices in the dark and under 360 nm illumination.

The spectral photoresponse of Al-NHA- and Al^{Planar}-based devices are shown in Fig. 4-16. Al^{Planar}-based devices produce two EQE peaks that are similar, but slightly blue-shifted, compared to those of Al-NHA-based devices under a 0 or -1 V bias, as shown in Fig. 4-16a. Under 1 V forward bias, Al^{Planar}-based devices produce an EQE peak at 330 nm and a second peak around 390 nm which decreases throughout the spectral range between about 400-500 nm before it cuts off at 515 nm (Fig. 4-16a). This photoresponse is distinct from, and inferior to, the strong peak produced by the Al-NHA-based device under forward bias that clearly corresponds to the active layer absorption. The enhancement provided to the electric field intensity by the Al-NHA electrode is hypothesized to act as a small forward bias within the device, pushing the Al-NHA-based device towards diffusion-dominated behavior while the Al^{Planar}-based device produces drift- and diffusion-based photoresponse peaks with similar magnitudes. D* spectra for Al-NHA- and Al^{Planar}-based devices are shown in Fig. 4-16b and show the same trends. The noise currents calculated for Al^{Planar}-based devices under -1, 0, and 1 V biases 2.0×10^{-12}, 1.1×10^{-12}, and 3.6×10^{-12} A/√Hz, respectively.

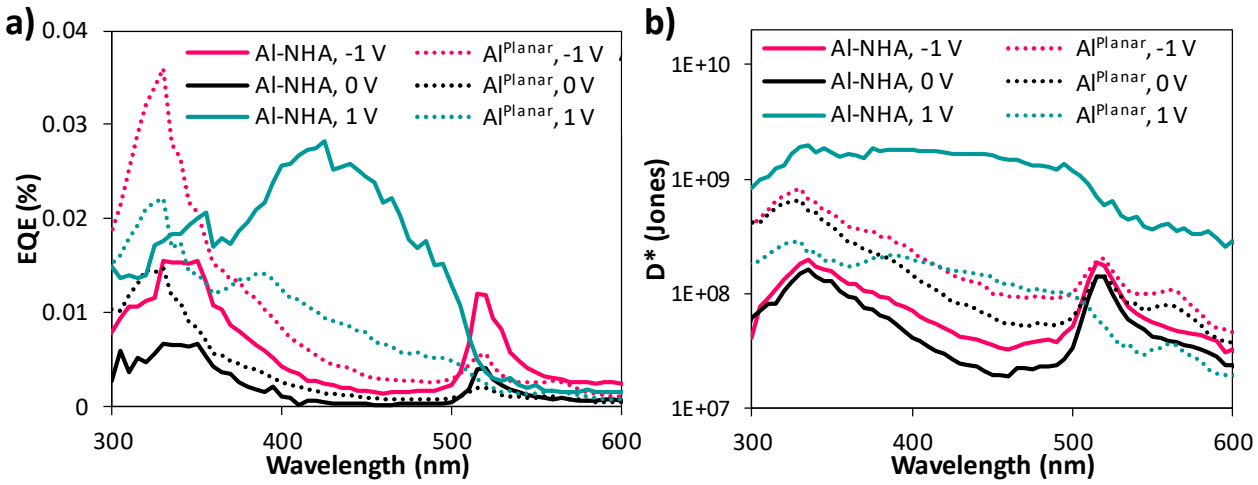

Figure 4-16. (a) EQE and (b) D* spectra for Al-NHA- and Al^{Planar}-based conventional devices.

Notably, when the electrode is changed from ITO to Al-NHA and then to Al^{Planar}, the UV-peak blue-shifts and grows in magnitude relative to the peak at 515 nm, a phenomenon that is summarized in Table 4-2. For ITO-, Al-NHA-, and Al^{Planar}-based devices, the UV-peak in EQE occurs at 360, 350 and 330 nm, respectively, and the ratio between the UV-peak in EQE and the peak at 515 nm is 0.84, 1.3, and 6.7, respectively.

Table 4-2. Summary of the UV- and 515 nm-peak in of ITO-, Al-NHA, and Al^{Planar}-based devices under a reverse bias of -2 V, along with the transmittance (T) of each electrode at the relevant wavelengths, ratios of the EQE and transmittance at the UV- and 515 nm-peak wavelengths, and the thickness of each electrode.

Bottom Electrode	Electrode Thickness (nm)	UV Peak			515 nm Peak		T_{UV}/T_{515}	EQE_{UV}/EQE_{515}
		Position (nm)	EQE (%)	T (%)	EQE (%)	T (%)		
ITO	200	360	0.37	85.4	0.44	94.0	0.908	0.84
Al-NHA	30	350	0.016	33.6	0.012	30.3	1.11	1.33
Al^{Planar}	10	330	0.036	8.09	0.0054	6.71	1.21	6.67

It is the balance between transmittance (Fig. 4-13a) and penetration depth, shown in Fig. 4-17, that determines the spectral position and relative strength of the UV-peak. The light penetration depth was calculated by Eq. 4.1,[1]

$$L_P = \frac{\lambda}{4\pi k} \tag{4.1}$$

where L_P is the penetration depth, λ is the incident wavelength, and k is the wavelength-dependent extinction coefficient at each incident wavelength. The extinction coefficient data is the same as that used in the FDTD simulations.

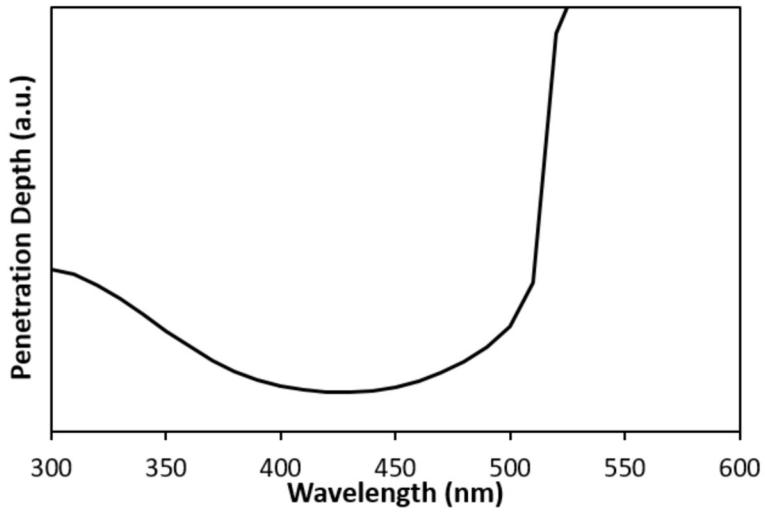

Figure 4-17. Penetration depth of light into the F8T2:$PC_{71}BM$ active layer.

As the wavelength of incident light increases within the UV spectral range, the transmittance increases while the penetration depth decreases. Both factors are directly proportional to photoresponse strength, so the balance between the two determines the spectral position of the UV peak. When transmittance is low, as for Al^{Planar}-based devices, penetration depth is the primary determinant of the spectral position of the UV-peak. As shown in Fig. 4-17, the penetration depth is higher for 330 nm than at 350 or 360 nm, so light with a wavelength of 330 nm can contribute most significantly to the reverse-bias photoresponse in Al^{Planar}-based devices. For the Al-NHA and ITO electrodes, the transmittance is higher overall than for the Al^{Planar} electrode, so the relative transmittance at different wavelengths is more impactful. For these devices, the transmittance is significantly stronger at the slightly longer wavelengths of 350-360 nm, compared to 330 nm, so these wavelengths dominate the UV photoresponse. In these cases, both the

transmittance and penetration depth play a role in determining exactly where the UV-peak in the photoresponse occurs. The penetration depth is slightly longer at 350 nm compared to 360 nm, but the transmittance is slightly higher at 360 nm than at 350 nm. For the Al-NHA electrode, the transmittance is only slightly higher at 360 nm than at 350 nm, with respective values of 34.9% and 33.6%, but for the ITO electrode the transmittance values at 360 and 350 nm are 85.4% and 80.5%, respectively. The smaller variation of about 1.3% in the transmittance of the Al-NHA electrode at these two wavelengths enables the Al-NHA-based device to produce a photoresponse peak at the shorter wavelength of 350 nm, while the almost 5% difference in the transmittance of the ITO electrode at these two wavelengths results in the ITO-based device producing a photoresponse peak at the longer wavelength of 360 nm. The relative magnitude of the peaks in the photoresponse spectra can also be understood through the relative transmittance of these electrodes at different wavelengths. The ratio of the transmittance at the UV-peak wavelength and at 515 nm for each electrode is also shown in Table 4-2 and increases as the electrode is changed from ITO to Al-NHA and then to Al^{Planar}.

To further confirm the proposed photoresponse mechanism, hole-only devices were fabricated by replacing the hole-blocking LiF layer with a hole-transporting MoO_3 layer.[155] Without the hole-blocking behavior and built-in bias resulting from the LiF layer, true electrode symmetry, and overall device symmetry, was achieved and the Al-NHA- and Al^{Planar}-based devices produce diffusion-dominated photoresponse without any applied bias. It is reasonable that hole diffusion would dominate over drift without any applied or internal bias, since light corresponding to diffusion-based response is absorbed more strongly than that corresponding to drift-based response. Further, the Al-NHA-based device should produce stronger photoresponse since

plasmonic enhancements to the electric field intensity should improve the hole diffusion driving force. Indeed, as shown in Fig. 4-18a and b, the Al-NHA-based devices exhibit stronger EQE and D* values, respectively, with spectra that are clearly dominated by hole diffusion, compared to those of Al^{Planar}-based devices, which are weaker and are similarly affected by hole drift and diffusion. The noise currents calculated for hole-only Al-NHA- and Al^{Planar}-based devices were 9.5 x 10^{-13} and 1.9 x 10^{-12} A/√Hz, respectively.The comparison of Al-NHA- and Al^{Planar}-based devices shown in Fig. 4-18 indicates that Al-NHA electrodes positively impact forward-bias photoresponse through plasmonic enhancements to the internal electric field, as Al-NHA-based devices outperform both Al^{Planar}- and ITO-based devices for response strength and stability.

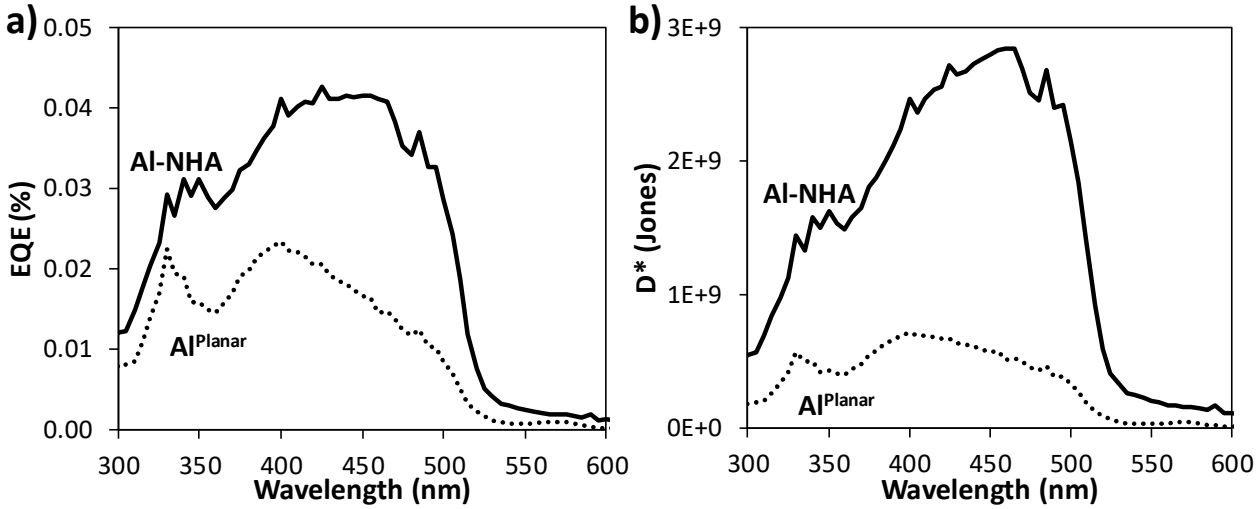

Figure 4-18. (a) EQE and (b) D* spectra for Al-NHA- and Al^{Planar}-based hole-only devices.

The response speed of Al-NHA-, Al^{Planar}- and ITO-based devices were tested under 360 nm illumination and 1 and -1 V biases (Fig. 4-19a and b, respectively), further indicating that device performance benefits from plasmonic enhancements to the internal electric field of Al-NHA-based devices. The wavelength of 360 nm was chosen because all devices generate photoresponse at that wavelength under both forward and reverse biases, and it is within the spectral range where plasmonic enhancements are expected. The rise (and fall) times were 0.35 s (0.49 s) and 0.45 s (0.51 s) under 1 V bias for the Al-NHA- and Al-P^{lanar}-based devices, respectively. The faster

response speed of the Al-NHA-based devices indicates that the devices benefit from plasmonic enhancements to the internal electric field intensity, which acts as a small forward bias and improves diffusion-based photoresponse resulting from light absorbed in the lower portion of the active layer. In Fig. 4-19b, the response speed of all three devices are compared under -1 V bias. The rise (fall) times are 0.37 s (0.39 s), 0.42 s (0.45 s), and 0.3 s (0.44 s) for the Al-NHA-, Al-P^{planar}-, and ITO-based devices, respectively. Under reverse bias, the Al-NHA-based devices undergo drift-dominated photoresponse and rely on light absorption in the top of the active layer, so plasmonic enhancements to the electric field are not relevant to the response speed.

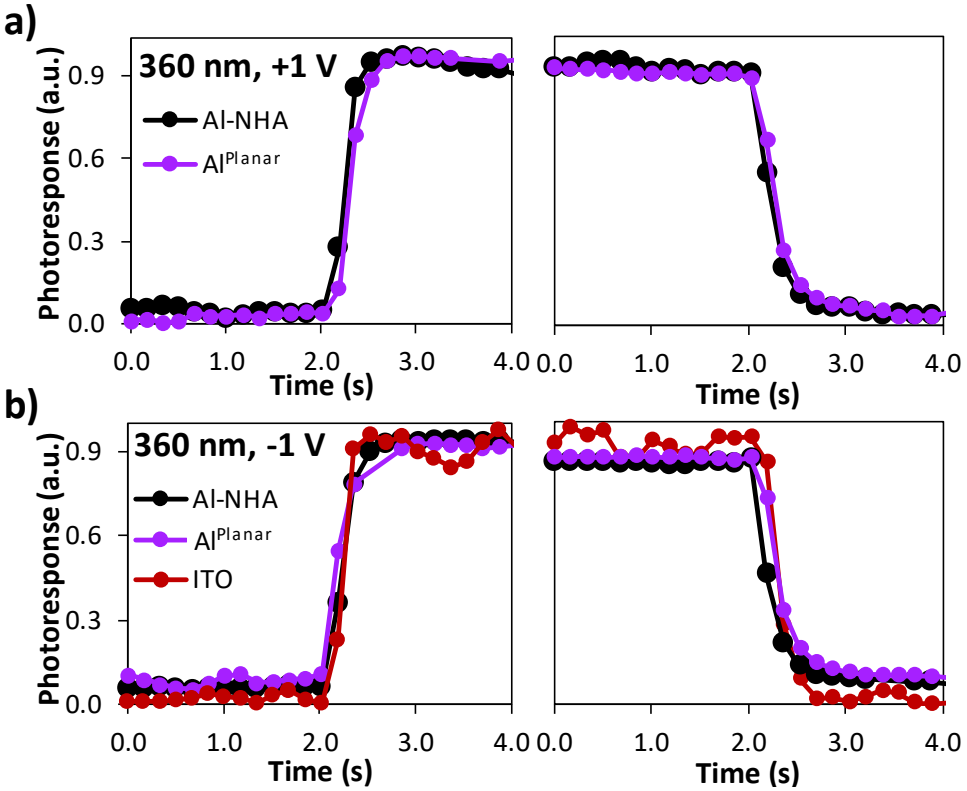

Figure 4-19. Response speed under 360 nm illumination for (a) Al-NHA- and Al^{Planar}-based devices at 1 V bias, and (b) Al-NHA-, Al^{Planar}-, and ITO-based devices at -1 V bias.

4.4 CONCLUSIONS

Plasmonic Al-NHA electrodes have been designed by 3D-FDTD simulations, fabricated by nanosphere lithography, and incorporated as transparent conducting electrodes in organic

ultraviolet photodetectors. The hexagonal Al-NHA with a diameter and pitch of 175 and 200 nm, respectively, produces both strong UV-selective active layer absorbance and enhanced internal electric field intensity in devices simulated and evaluated through 3D-FDTD simulations. This plasmonically enhanced internal electric field increases the driving force for hole diffusion, resulting in bias-dependent response switching. Fabricated Al-NHA-based devices produce two narrow photoresponse peaks with D* values of 4.0×10^9 and 4.6×10^9 Jones under 340 and 515 nm illumination, respectively, and -2 V bias, and one broad photoresponse peak with a peak D* of 8.8×10^9 Jones under 450 nm illumination and 2 V bias. ITO-based devices exhibit spectrally similar behavior under reverse bias, producing stronger photoresponse values due to the increased transmittance of ITO compared to Al-NHAs, and become unstable under forward bias. The EQE values produced by these devices are relatively low, but the mechanisms investigated and demonstrated in this work could be applied to other systems. With different active materials, such as perovskites and other polymers, stronger photoresponse could be produced while the novel bias-dependent response-switching enabled by Al-NHA electrodes is also achieved. The ability to tune the spectral photoresponse of devices by applying either reverse or forward bias improves device applicability, making Al-NHA electrodes a promising option for ITO-free organic UV photodetectors with improved photoresponse and bias-dependent response tunability.

Chapter 5. INCORPORATING ALUMINUM PLASMONIC NANOHEMISPHERE ARRAYS INTO ORGANIC ULTRAVIOLET PHOTODETECTORS FOR IMPROVED PHOTORESPONSE

5.1 INTRODUCTION

Incorporating plasmonic nanostructures at the active layer interfaces is a popular approach to improve the performance of optoelectronic devices because of performance-enhancing surface plasmon polaritons (SPPs) that are generated at metal-dielectric interfaces under illumination.[60, 68] Nanostructures can be incorporated at the light-incident surface or at the rear surface of the active layer to utilize scattering and reflection of light in the active layer and enhanced local electric fields near the active layer-metal electrode interface.[61, 65, 68, 69, 71] The rear surface of the active layer, corresponding to the top of the film in a vertical photodiode architecture, is of particular interest for nanostructure incorporation since the nanostructures can be transferred to the top metal electrode, providing two main advantages. First, the nanostructured top metal electrode can increase the light path through the active layer due to angular reflection, thus improving light absorption in the active layer.[61, 65] Second, the enhanced local electric field can positively affect light absorption and charge generation, separation and transport in the rear portion of the active layer.[1, 65] It has been previously reported that light absorption at the top of the active layer dominates the spectral photoresponse produced by conventional organic photodiode photodetectors,[30, 36, 51] so nanostructures incorporated in the rear surface of the active layer could be an effectie way to improve device performance.

In photodetectors, incorporating nanostructures into the rear surface of device active layers has resulted in improved current production, often measured by responsivity (R). These have been incorporated both in lateral phototransistor detectors and in vertical photodiode detectors, the latter of which has been utilized exclusively in our work. In a lateral metal-semiconductor-metal photodetector, based on a Si/SiO_2 substrate with gold electrodes, the incident interface of the perovskite ($CH_3NH_3PbI_3$) active layer was imprinted with Si molds with either no pattern, a pillar array, or a 1-D grating, both nanopatterns having a pitch of 600 nm and the grating was oriented perpendicular to the device electrodes.[74] Since the imprint process itself was shown to improve perovskite crystallinity and subsequently device performance, devices with both as-cast and flat-imprinted active layers were evaluated and used as controls to investigate the impacts of the nanostructure arrays.[74] Both nanopatterns, most significantly the nanograting, reduced the reflectance and transmittance of the active layer films, thereby increasing absorbance, compared to flat films, both of which produced similar transmittance and reflectance spectra.[74] The increased absorption and improved crystallinity enabled the nanograting-imprinted device to achieve a 30-fold increase in R, compared to non-imprinted devices, yielding a peak value of 58.5 A/W under 635 nm illumination and a 1 V bias.[74] Another lateral perovskite ($CH_3NH_3PbI_3$) photodetector, with a similar structure again utilizing gold electrodes and a Si/SiO_2 substrate, incorporated Au plasmonic nanosquare arrays into the multi-layered substrate, effectively structuring the rear interface of the active layer.[75] These Au nanosquare arrays, having a pitch of 350 nm, coupled with incident light to produce SPPs that enhanced the device performance through enhancements to the local electric field that resulted in reduced reflectance and increased light absorption.[74] Thus, nanostructured devices produced stronger photocurrent values throughout the desired near-infrared spectral range, producing about a 50-fold photocurrent enhancement under a 0.5 V bias

and incident illumination with wavelengths of 725 and 800 nm, and this response enhancement could be redshifted by increasing the size of the nanosquares used.[75]

Inspired by the structure of insect eyes and designed for green light detection, a multi-pattern nanostructure array consisting of nanoposts (64 nm average diameter) on a larger grating pattern (273 nm pitch) was incorporated into the top surface of an active layer composed of poly(3-hexylthiophene-2,5-diyl) (P3HT) and [6,6]-phenyl-C_{71}-butyric acid methyl ester ($PC_{71}BM$), which was included in a conventional vertical photodiode photodetector with a flexible device structure of polyethylene naphthalate (PEN)/ITO/poly(3,4-ethylenedioxythiophene) polystyrene sulfonate (PEDOT:PSS)/P3HT:$PC_{71}BM$ (1:1, w:w)/Al.[78] The performance of multi-pattermed devices was compared to the performance of devices with active layers with no pattern, only the grating, and only nanoposts. Under 1 V bias and 532 nm illumination, multi-patterned devices exhibited a responsivity (R) of 7.95 A/W and a specific detectivity (D*) of 11.4 x 10^{12} Jones, compared to R values of 1.48 , 3.80, and 2.03 A/W and D* values of 1.6 x 10^{12}, 4.2 x 10^{12}, and 3.9 x 10^{12} Jones achieved by devices with no pattern, only the grating, and only nanoposts, respectively.[78] The superior performance was arrtibuted to enhanced light trapping and absorption enabled by the multiple scaled nanostructures. Similarly, plasmonic nanostructures have been incorporated into the top active layer surface of solar cells to decrease reflection and improve light absorption, and therefore increase charge generation and photocurrent production. A 2-D square array was imprinted into the top surface of a soft polymer active layer, composed of poly[[4,8-bis[(2-ethylhexyl)oxy]benzo[1,2-b:4,5-b′]dithiophene-2,6-diyl][3-fluoro-2-[(2-ethylhexyl)carbonyl] thieno[3,4-b]thiophenediyl]] (PTB7):$PC_{71}BM$, so that the pattern transferred to the subsequent MoO_3 hole transport layer and Ag top electrode in inverted organic solar cells with a structure of ITO/ZnO/PTB7:$PC_{71}BM$/MoO_3/Ag.[72] The power conversion efficiency (PCE) was increased from

6.94% for the planar control devices to 7.74% for the devices with the plasmonic nanostructured tops due to enhancements to the short-circuit current density (J_{SC}). A nanohemisphere array (NHSA) was imprinted into the top active layer surface of quantum dot (QD) solar cells with a structure of ITO/ZnO/PbI_2-QD/PbS-QD/Au, so the pattern transferred to the top Au electrode.[70] The patterned devices produced an average J_{SC} of 27.8 mA/cm^2, compared to 25 mA/cm^2 from the flat devices, demonstrating a plasmonic enhancement to the device performance achieved by incorporating nanostructures in the rear active layer/Au electrode interface.

UV photodetectors are important in a variety of applications including environmental monitoring, scientific research, imaging, and flame and missile detection.[1, 2, 14] However, plasmonic enhancement mechanisms have not been widely applied to optoelectronic devices in the UV spectral range. Unlike the common plasmonic metals of Ag and Au, which work well in the visible and near infrared spectral ranges, Al is well-suited to support and tune SPPs in the UV spectral range due to its carrier concentration and dielectric function.[55, 80-83, 85, 131] Organic UV photodetectors with a conventional device structure typically have Al as the top electrode, deposited by thermal evaporation. Therefore, incorporating nanostructures at the rear surface of the active layer inherently produces an Al nanostructure array that can utilize the unique UV plasmonic properties of Al and enhance UV photodetector performance.

In this work, nanohemisphere arrays (NHSAs) were imprinted into the top active layer surface in conventional organic UV photodetectors and were transferred to the top Al cathode to generate plasmonic Al nanostructures. The impact of plasmonic NHSA on device performance was investigated using both 3-dimensional finite-difference time-domain (3D-FDTD) electromagnetic simulations and experimental methods. The wide band gap polymer poly(9,9-dioctylfluorene-alt-bithiophene) (F8T2) was blended with $PC_{71}BM$ in a weight ratio of 100:4 and used as the active

layer. Conventional UV photodetectors with this weight ratio demonstrated photomultiplication under large reverse biases.[51] The active layer thickness, which has a significant impact on device performance with regards to the spectral selectivity,[33, 52, 123] strength,[30] and photoresponse stability,[51] was varied between 125-470 nm. For comparison, devices with flat top active layers and electrodes were also investigated. 3D-FDTD simulations revealed that the devices with plasmonic NHSA top electrodes, referred to in this work as NHSA-top devices, exhibit stronger UV absorption in the active layer and enhanced electric fields at the interface of the top of the active layer and the Al electrode, especially for devices with thinner active layers. NHSA-top devices were fabricated by imprinting nanostructured molds into the top surface of the active layer, followed by thermal evaporation of the LiF electron transport layer and Al electrode, and evaluated alongside flat-top control devices whose active layers were imprinted with flat molds. The inclusion of a NHSA was found to improve the photoresponse strength, sensitivity and speed through increased UV absorption and enhanced electric fields resulting from angular reflection of light in the active layer and the plasmonic effects of the Al NHSA electrode. This work demonstrates that imprinting an NHSA into the top of the active layer, thus structuring the top metal electrode, is an effective approach for incorporating performance-enhancing plasmonic nanostructures into organic UV photodetectors.

5.2 EXPERIMENTAL

5.2.1 *Finite-Difference Time-Domain Unit Cell Setup*

Three-dimensional, finite-difference time-domain (3D-FDTD) electromagnetic simulations (Lumerical, Inc[96]) were used to investigate the incorporation of NHSA-tops on the light absorption in the active layer and the internal electric field distribution throughout the device, and an overview

of the simulations is provided in Fig. 5-1. The simulated device structure was Corning XG EAGLE glass (100 nm)/ITO (200 nm)/PEDOT:PSS (40 nm)/F8T2:$PC_{71}BM$ (100:4, w:w, varied thickness)/LiF (0.8 nm)/Al (100 nm) (Fig. 5-1a). The active layer is composed of a planar bulk portion with a hexagonal array of nanohemispheres, 200 nm in diameter (D), incorporated at its top surface. The thicknesses of the planar portion of the active layer were 100, 205, 355 and 445 nm, and a detailed discussion of the determination of these thicknesses and the comparison to the flat-top active layer thicknesses is provided in Section 5.3.2. The hexagonal array of nanohemispheres was subsequently incorporated into the LiF and Al layers. A cross-sectional and top-view of the simulation unit cell are provided in Fig. 5-1b and c, respectively. The simulation unit cell is defined by the blue border in Fig. 5-1b and c and has the x- and y-lattice constants of D and D$\sqrt{3}$, respectively. The light source was placed 600 nm below the glass substrate and impinged normally with polarization in the x-direction. For comparison, flat-top devices were simulated with the same configuration and unit cell with active layer thicknesses of 125, 230, 380 and 470 nm. The wavelength-dependent refractive index (n) and extinction coefficient (k) of each material and other simulation details were the same as those provided in Section 4.2.1.

Vertical frequency-domain field monitors (dashed yellow lines in Fig. 5-1b and c) were placed in the x-z and y-z planes of the device, intersecting at the origin (0,0), which corresponds to the center of the central nanohemisphere in the unit cell, to obtain the electric field distribution throughout the device under 330 nm monochromatic illumination. Electric field distributions were also mapped along the z-axis at individual x-y points and plotted against incident wavelength. For NHSA-top devices, three x-y points were used to accurately represent the electric field, since both the device geometry and internal electric field vary along x and y. These points, corresponding to the center of a nanohemisphere (0,0), the x-edge of a nanohemisphere (D/2, 0), and the y-edge of

a nanohemisphere (0, D/2) are marked in Fig. 5-1c by pink, green, and blue stars, respectively. For flat-top devices, one x-y point was plotted (0,0) since all x-y points are identical.

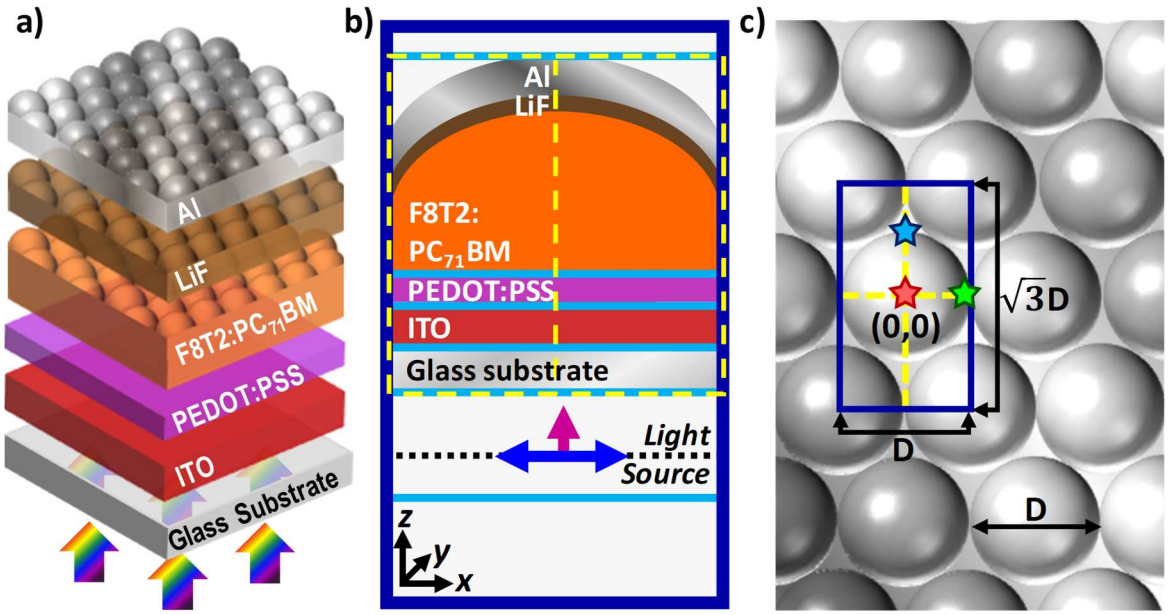

Figure 5-1. (a) 3D schematic of the device structure with NHSA incorporated into the active layer and subsequent layers. (b) Cross-sectional view of a simulation unit cell for a sample NHSA-top device. (c) Top-view schematic of an NHSA-top electrode showing the unit cell, the origin and the locations for vertical frequency-domain field monitors.

5.2.2 *Active Layer Absorbance Calculation*

Horizontal frequency-domain field monitors (light blue lines in Fig. 5-1b) were placed throughout the device between planar layers, at the top of the device, and below the light source to calculate the absorbance in planar layers, device transmittance, and device reflectance, respectively. Absorbance in planar device layers was calculated by subtracting the transmittance above the layer from the transmittance below it. In NHSA-top devices, the relative absorbance within device active layers was determined from the device reflectance, transmittance, and absorbance in the layers below the active layer, by Eq. 5.1:

$$A_{ACTIVE} = 1 - R - T - A_{ITO} - A_{PEDOT:PSS} - A_{GLASS} \quad (5.1)$$

where A_{ACTIVE} is the absorbance of the device active layer, R is the total reflectance from the device, T is the transmittance through the top of the device, and A_{ITO}, $A_{PEDOT:PSS}$, and A_{GLASS} are the absorbance in the ITO electrode, PEDOT:PSS layer and glass substrate, respectively. As demonstrated in Fig. 5-2a-b, the absorbance in the layers below the active layer, ITO and PEDOT:PSS, used to calculate A_{ACTIVE} does not vary significantly between NHSA- and flat-top devices. It should be noted that device transmittance and glass absorbance (A_{GLASS}), which are also used to calculate A_{ACTIVE}, are negligibly small.

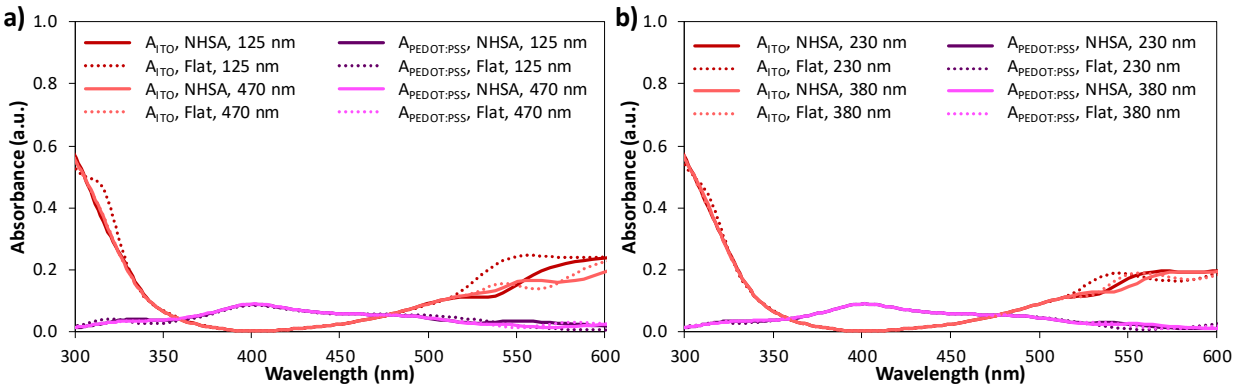

Figure 5-2. 3D-FDTD-simulated absorbance in ITO and PEDOT:PSS layers, A_{ITO} and $A_{PEDOT:PSS}$, respectively, in NHSA- and flat-top devices with active layer thicknesses of (a) 125 and 470 nm, and (b) 230 and 380 nm.

5.2.3 *Nanohemisphere Array Fabrication and Incorporation into Active Layer*

To fabricate the mold for NHSA imprinting, nanosphere monolayers were first deposited on glass substrates, as described in Section 4.2.2. To aid in the eventual mold separation, the anti-adhesive material trichloro(1H,1H,2H,2H-perfluorooctyl)silane (97%, Sigma-Aldrich, St. Louis, MO) was deposited on the hexagonal nanosphere monolayers by placing glass substrates covered with the monolayers and a separate dish containing 200 µL silane in a vacuum dessicator for 2 h. Polydimethylsiloxane (PDMS, Sylgard 184, Thermo Fisher Scientific, Waltham, MA) was poured over the treated nanosphere monolayers, degassed in a dessicator for 15 min, and cured at 70°C for 5 h on a hot plate. After curing, the PDMS was separated from the nanosphere monolayer,

producing a mold with a hexagonal array of 200 nm diameter hemispheric dimples. Flat molds were prepared by pouring PDMS on a silane-treated bare glass substrate. To imprint the NHSA onto the top surface of the active layer, the NHSA PDMS molds, wetted with 20 μL of 1,2-dichlorobenzene (anhydrous, 99.9% purity, Sigma-Aldrich, St. Louis, MO), were placed on F8T2:$PC_{71}BM$ films immediately after they were annealed at 80°C for 10 min, remained on the hot plate at 80°C for 5 min, and were then removed. The flat PDMS mold was imprinted onto the top of active layers by the same method to produce flat-top active layers for control devices. A scanning electron microscope (SEM, FEI Sirion) was used to evaluate each fabrication step.

5.2.4 *Device Fabrication and Characterization.*

ITO coated glass substrates (≤ 10 Ω/sq, Colorado Concept Coatings LLC, Loveland, CO) were cleaned and coated with a PEDOT:PSS (Clevios P VP AI 4083, Heraeus, Hanau, Germany) hole transport layer as in Section 4.2.3. In a nitrogen-filled glovebox, F8T2 (molecular weight of 29,000 g/mol, polydispersity index of 3.3, American Dye Source, Baie D'Urfe, Quebec, Canada) and $PC_{71}BM$ (Nano-C Inc., Westwood, MA) were each dissolved in 1,2-dichlorobenzene and stirred at 700 rpm and 70ºC for at least 12 h. The equal concentration F8T2 and $PC_{71}BM$ solutions were mixed in a F8T2:$PC_{71}BM$ weight ratio of 100:4 to yield precursor solutions with total concentrations of 20, 30 and 40 mg/mL, which were stirred at 700 rpm and 70ºC for at least 1 h and then filtered through a 0.2 μm PTFE syringe filter. Active layers with the target film thicknesses of 125, 230, 380, and 470 nm were produced by spinning 20, 30, 40, and 40 mg/mL precursor solutions at 1000, 1000, 1000, and 800 rpm, respectively for 30 s, and annealing at 80ºC for 10 min. A NHSA or flat PDMS mold was imprinted on the top surface of each active layer following the method described above. UV-Vis absorption spectra were collected using a Perkin

Elmer Lambda 900 UV-Vis spectrophotometer. Film thickness was measured using a Bruker OM-DektakXT Profilometer. A thin 0.8-1.0 nm layer of LiF (99.995%, Sigma-Aldrich) was then deposited via thermal evaporation, without the use of any mask. Finally, 100 nm Al electrodes were deposited via thermal evaporation through a mask with 16 circular holes to generate 16 devices per substrate with each having an 0.03 cm^2 active area. Both LiF and Al were deposited using an Angstrom Engineering PVD Platform, with stage rotation turned on to avoid any shadowing effects on the NHSA-tops, and thickness was monitored by a quartz crystal microbalance.

All device and film characterizations were performed in air. Current density-voltage (J-V) curves, dark current over time, external quantum efficiency (EQE) spectra, and response speed were measured using a Keithley 2635B sourcemeter. Light was provided using a Xenon arc lamp (150 W) and Oriel Cornerstone 130 Monochromator. Optical intensity was measured using a Newport 1918-R Power Meter and Newport UV-Si Photodiode. The optical power intensity was the same as that shown in Section 3.2.3 (Fig. 3-1). The response speed was obtained by manually switching between dark and light conditions. Matlab was used to perform Fast Fourier Transforms on dark current over time data to obtain noise currents.

5.3 Results and Discussion

5.3.1 *Anticipated Performance Enhancements Provided by a NHSA-Top*

3-dimensional finite-difference time-domain (3D-FDTD) electromagnetic simulations were performed to evaluate the impact of NHSA-tops on the absorbance and electric field distribution in the active layers of conventional UV photodetectors with the configuration shown in Fig. 5-1a. NHSA-top devices have active layers composed of a planar portion with a NHSA incorporated

into the top surface. The thicknesses of the planar portions were 100, 205, 305 and 455 nm and the diameter of the nanohemispheres was 200 nm. Accounting for the topography of nanohemispheres in the overall film thickness, corresponding flat-top active layer thicknesses of 125, 230, 380 and 470 nm, respectively, were used. Details regarding the simulated and experimental active layer structure and thickness can be found in Section 5.3.2. To simplify the discussion throughout, we use the flat-top active layer thickness to indicate the active layer thickness for both flat- and NHSA-top devices and refer to 125 and 470 nm active layers as thin and thick devices, while 230 and 380 nm active layers are referred to as intermediate devices.

The active layer absorbance (A_{ACTIVE}) and device reflectance (R) for devices with both NHSA- and flat-tops were calculated and are shown in Fig. 5-3. The oscillations exhibited in the A_{ACTIVE} and R spectra are attributed to the reflectance between layers and nanocavity effects that exist in any device composed of multiple thin layers, and to the mismatch in refractive index between the glass substrate (n = ~1.5) and air (n = ~1). These could be minimized by adding anti-reflection coating on the glass substrate or at the rear of the active layer, or by manipulating the substrate refractive index and device layer thicknesses.[136]

The results in Fig. 5-3a show that the thin device is significantly affected by NHSA-top incorporation, and Fig. 5-3b-d demonstrates that the influence of NHSA-top on active layer absorbance gradually diminishes with increasing active layer thickness. For the 125 nm active layer (Fig. 5-3a), NHSA- and flat-top devices produce reflectance values of 0.11 and 0.25, respectively, under 330 nm illumination, demonstrating that the NHSA-top provides a significant reflectance reduction. Consequently, the NHSA-top device has a higher absorbance of 0.63 compared to the flat-top device, which has an absorbance of 0.50, under 330 nm illumination. For the intermediate devices with a 230 nm active layer (Fig. 5-3b) a reduction in reflectance under

UV illumination is observed upon NHSA incorporation, so the NHSA enhancement to active layer absorbance is present but less significantly than in the thin device in Fig. 5-3a. As is observed for the thicker device in Fig. 5-3c, with a 380 nm active layer, the reflectance and active layer absorbance are nearly unchanged by the incorporation of the NHSA-top. For the thick device (Fig. 5-3d), the impact of NHSA-tops on active layer absorbance virtually disappears, and the simulated absorbance and reflectance of NHSA- and flat-top devices are identical except for minor differences under long-wavelength illumination.

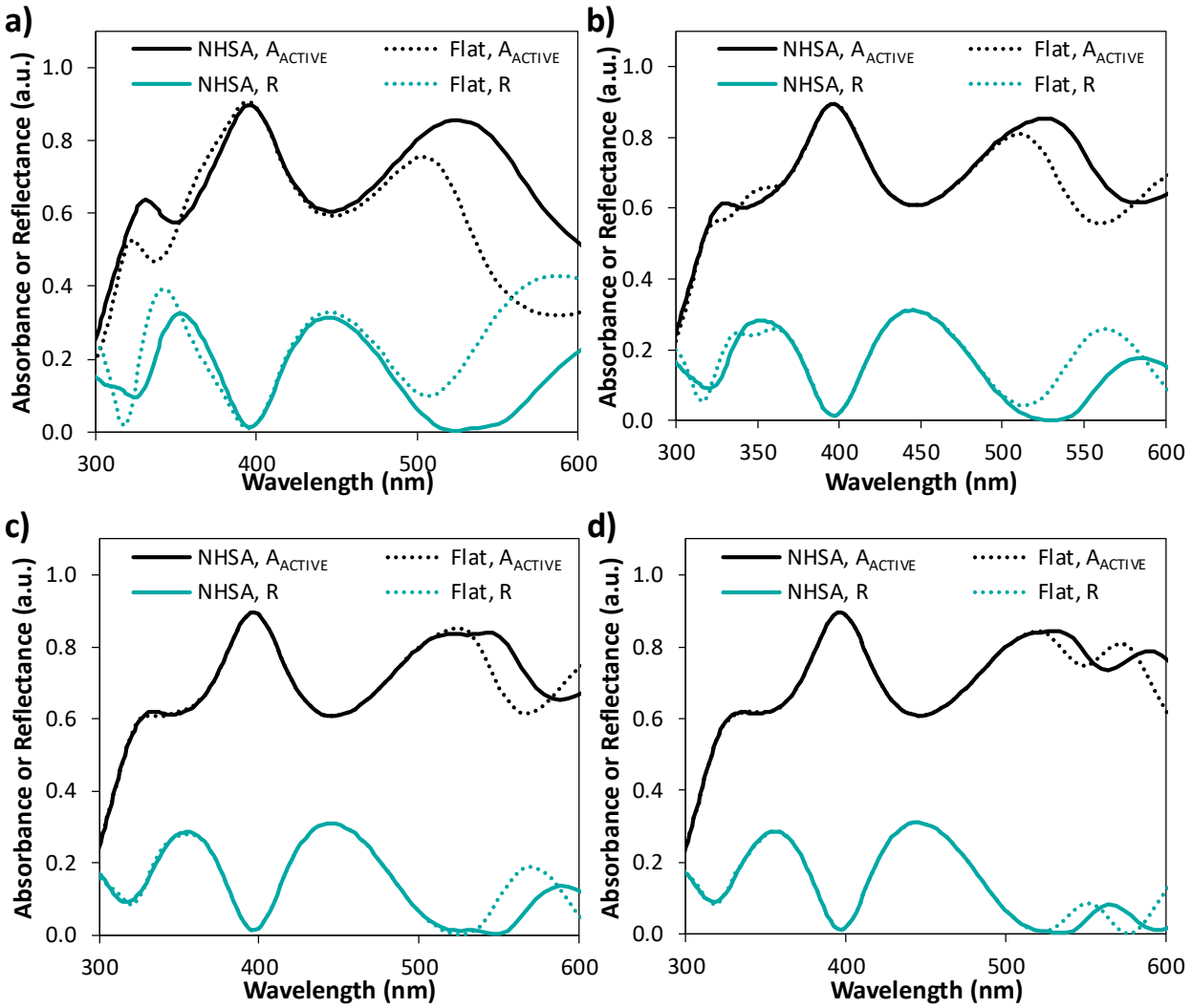

Figure 5-3. 3D-FDTD-simulated active layer absorbance (A_{ACTIVE}) and total device reflectance (R) for NHSA- and flat-top devices with active layer thicknesses of (a) 125 nm, (b) 230 nm, (c) 380 nm, and (d) 470 nm.

To confirm that the structuring of the active layer/LiF/Al interface causes the enhanced UV absorption observed in Fig. 5-3, rather than the structuring of the polymer film itself, UV-Vis absorption spectra were obtained for thin NHSA- and flat-top films without the subsequent layers deposited, and these are shown in Fig. 5-4. Clearly, NHSA incorporation does not impact the absorption of the active layer film by itself, so the impact observed in Fig. 5-3 must result from the structuring of the active layer/LiF/Al interface. Additionally, enhanced absorbance for NHSA-top devices was observed under long-wavelength incident illumination, in addition to UV illumination, because the behavior in the spectral region beyond ~530 nm is dominated by reflectance of the top electrode. As demonstrated by the experimentally measured UV-Vis absorption spectrum of F8T2:$PC_{71}BM$ (100:4, w:w) in Fig. 5-4, the active layer does not have significant absorption in this spectral region.

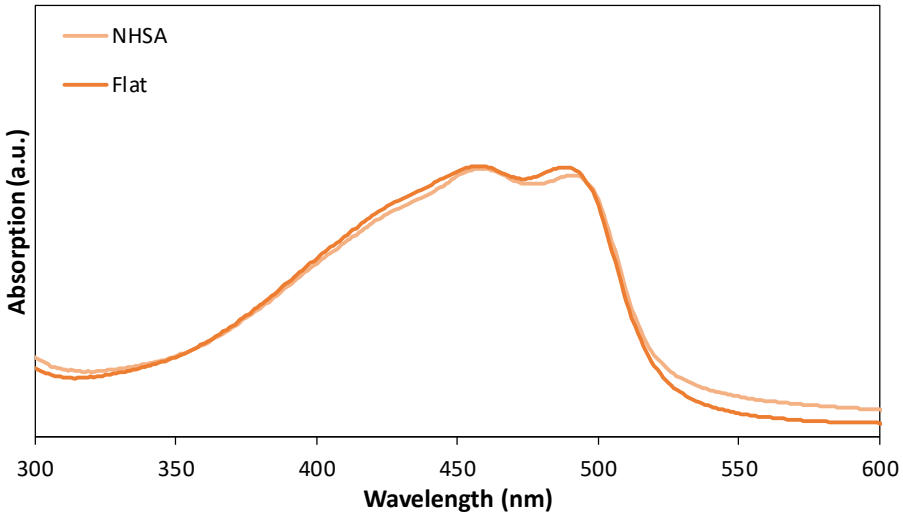

Figure 5-4. UV-Vis absorption spectra for NHSA- and flat-top active layer films with an average thickness of ~125 nm.

The electric field distribution under 330 nm illumination, which corresponds to a peak in active layer absorbance, is mapped in the x-z and y-z cross-sections of NHSA-top devices and the x-z cross-section of flat-top devices. Figure 5-5 shows the electric field distributions in the active layers and subsequent top layers for all simulated devices. The LiF electron transport layer was

included in the simulations but is too thin (0.8-1.0 nm) to be seen clearly in Fig. 5-5. Again, the impact of the NHSA-top on the electric field distribution is most significant for the thin device and gradually decreases as active layer thickness increases.

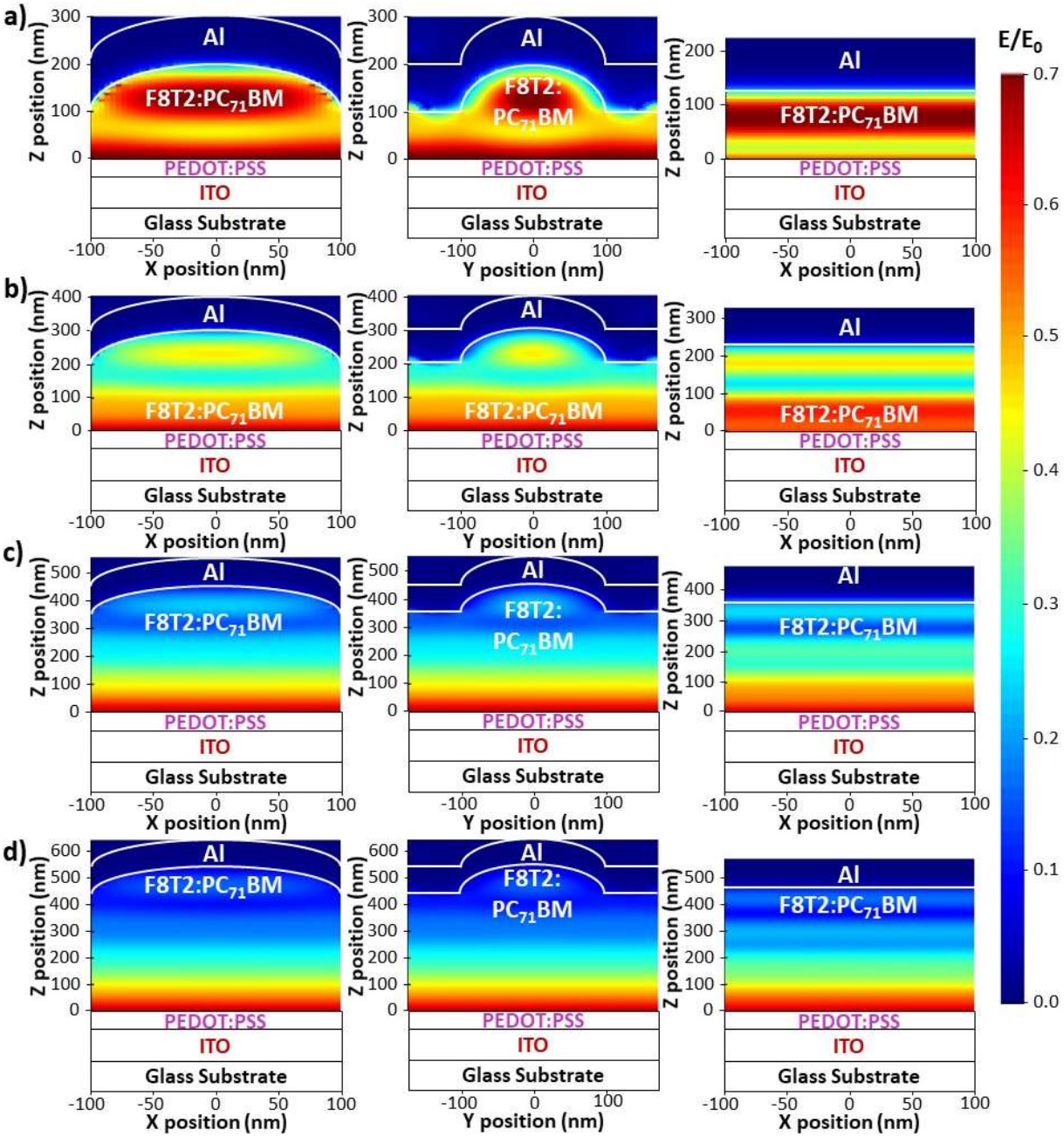

Figure 5-5. 3D-FDTD simulated electric field distributions, under 330 nm illumination, of the x-z cross-section (y = 0) and y-z cross-section (x = 0) in NHSA-top devices and the x-z cross-section (y = 0) in flat-top devices with active layer thicknesses of (a) 125 nm, (b) 230 nm, (c) 380 nm, and (4) 470 nm. The color scale is consistent for all plots and represents the ratio of the electric field intensity (E) to the incident field (E_0), which has an intensity of 1 V/m.

Figure 5-5a shows that strong electric fields are confined in the nanohemispheric region of the active layer in the thin device and extend to the edge of the active layer/LiF/Al electrode interface in the x-z cross-section, because incident light is polarized in the x-direction. Although the flat-top thin device shows a similar electric field intensity, the high-intensity region is more concentrated toward the middle of the active layer, away from the Al interface. As shown in Fig. 5-5b and c, the intensity of the confined electric field in the nanohemispheric active layer region deceases gradually with increasing active layer thickness. For the thick device (Fig. 5-5d), this confinement is almost completely diminished, and the electric field distribution for the thick NHSA-top device is very similar to that of the flat-top device. Clearly, NHSA-tops provide a plasmonic enhancement to the electric field intensity at the active layer/LiF/Al electrode interface, especially for thinner devices. The enhanced electric field could improve charge separation, transport, and injection at the top of device active layers, and subsequently improve the photoresponse strength and speed.

Electric field distributions were also mapped along the z-axis, at individual x-y points, and plotted against incident wavelength in the spectral range of 300-600 nm. The resulting plots are shown in Fig. 5-6 for all simulated devices, at three distinct points for NHSA-top devices, and at a single point for flat-top devices, because both the geometry and electric field distribution vary across the NHSA-top devices while they are uniform in flat-top devices. The three points plotted for NHSA-top devices correspond to the center (0,0), x-edge (D/2, 0), and y-edge (0, D/2), of the central nanohemisphere, according to the coordinate system defined in Fig. 5-1c and marked by pink, green, and blue stars, respectively, in Fig. 5-1c. These stars are also included in the relevant electric field distributions in Fig. 5-6 so that the corresponding x-y points can be easily discerned.

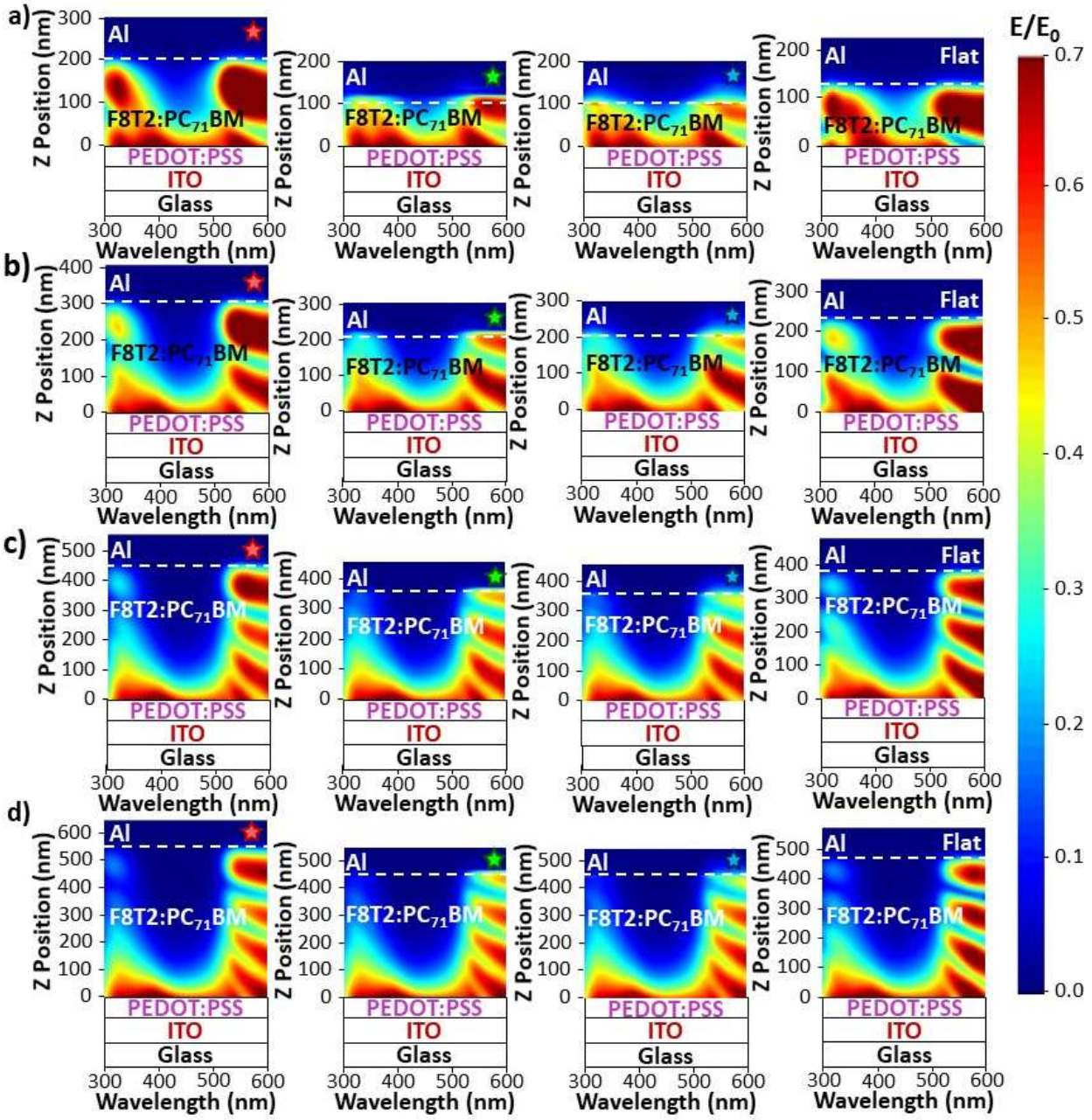

Figure 5-6. 3D-FDTD-simulated electric field distributions at a single x-y point, mapped along the z-axis against incident wavelength for both NHSA- and flat-top devices with active layer thicknesses of (a) 125 nm, (b) 230 nm, (c) 380 nm, and (d) 470 nm. From left to right across each panel, electric field distributions are shown at the center ((0,0), marked by a pink star), x-edge ((D/2,0), marked by a green star), and y-edge ((0,D/2), marked by a blue star) of the central nanohemisphere in NHSA-top devices, and at any x-y point in a flat-top device. The color scale is consistent for all plots, and represents the ratio of the electric field intensity (E) to the incident field (E_0) which has an intensity of 1 V/m.

As observed in Fig. 5-6a, the thin device exhibits a stronger electric field than the thick device, especially in the top portion of the active layer in the spectral ranges of 300-350 nm and 530-600

nm. The fringes in the electric field intensity observed in the spectral range between 530-600 nm occur because this light is beyond the absorption range of the active layer (Fig. 5-4), so it penetrates the active layer and reflects off the top electrode, establishing an interference pattern throughout the active layer. Because this light will not contribute to the photoresponse of fabricated devices, our discussion focuses on the UV spectral range, which is more relevant for understanding and predicting experimental results. In the center of the nanohemisphere of the thin device, marked by a pink star in Fig. 5-6a, the highest intensity area is located near the middle of the nanohemispheric region of the active layer, between z values of about 100-200 nm, and the intensity decreases towards the active layer/LiF/Al electrode interface under incident illumination between about 300-350 nm. The thin flat-top device exhibits a similar electric filed distribution. However, at the x- and y-edges of the nanohemisphere, marked by green and blue stars, respectively, the strongest electric field occurs directly at the active layer/LiF/Al electrode interface under incident illumination with wavelengths between about 330-350 nm, indicating UV-selective plasmonic enhancements to the local electric field. The strong local electric fields at the x- and y-edges of the nanohemisphere at the active layer/LiF/Al electrode interface can be seen in Table 5-1, which summarizes the ratios of E/E_0, under 330 nm illumination, for each device at three x-y points for NHSA-top devices and a single x-y point for flat-top devices.

With increasing active layer thickness, the electric field intensity decreases under illumination with wavelengths between about 300-350 nm as shown in Fig. 5-6b and c and Table 5-1 for the intermediate devices with the active layer thickness of 230 and 380 nm, respectively. For the thick devices shown in Fig 5-6d, the electric field intensities at the active layer/LiF/Al electrode interface for the NHSA-top device at three x-y points and for the flat-top device at one x-y point are relatively weak under illumination with wavelengths between about 300-350 nm. Similar to thin

and intermediate devices, the electric field at the center of the nanohemisphere exhibits similar behavior to flat-top devices, but the electric field at the edges of the nanohemisphere is enhanced due to localized surface plasmon resonance induced by the NHSA Al top electrodes, which can be seen in Table 5-1.

Table 5-1. Summary of the ratios of E/E_0 at the active layer/LiF/Al electrode interface for all simulated devices under 330 nm illumination at three x-y points for NHSA-top devices and a single x-y point for flat-top devices.

Average Active Layer Thickness (nm)	E/E_0 under 330 nm illumination			
	Center of Hemisphere	x-edge of Hemisphere	y-edge of Hemisphere	Flat-Top
125	0.17	0.44	0.53	0.27
230	0.12	0.28	0.33	0.17
380	0.063	0.14	0.17	0.091
470	0.042	0.095	0.11	0.060

5.3.2 *NHSA Fabrication and Incorporation*

3D-FDTD simulation results clearly show the plasmonic effect of the NHSA top Al electrode in the increase of UV absorption in the active layer and the enhancement of the electric field at the active layer/LiF/Al electrode interface under UV illumination, especially for the thin device. We therefore fabricated photodetectors with both NHSA- and flat-top active layers, inherently incorporating the NHSA into the subsequent LiF and Al layers, and evaluated their performance. The procedure for fabricating and imprinting NSHA molds into device active layers to produce NHSA-top devices is summarized in Fig. 5-7. It has been reported that the imprinting procedure alone, regardless of whether a flat or patterned mold is used, can have an impact on the active layer morphology and thus affect the device performance,[74] so control flat-top devices in this work were imprinted with a flat mold by the same procedure that is illustrated in Fig. 5-7.

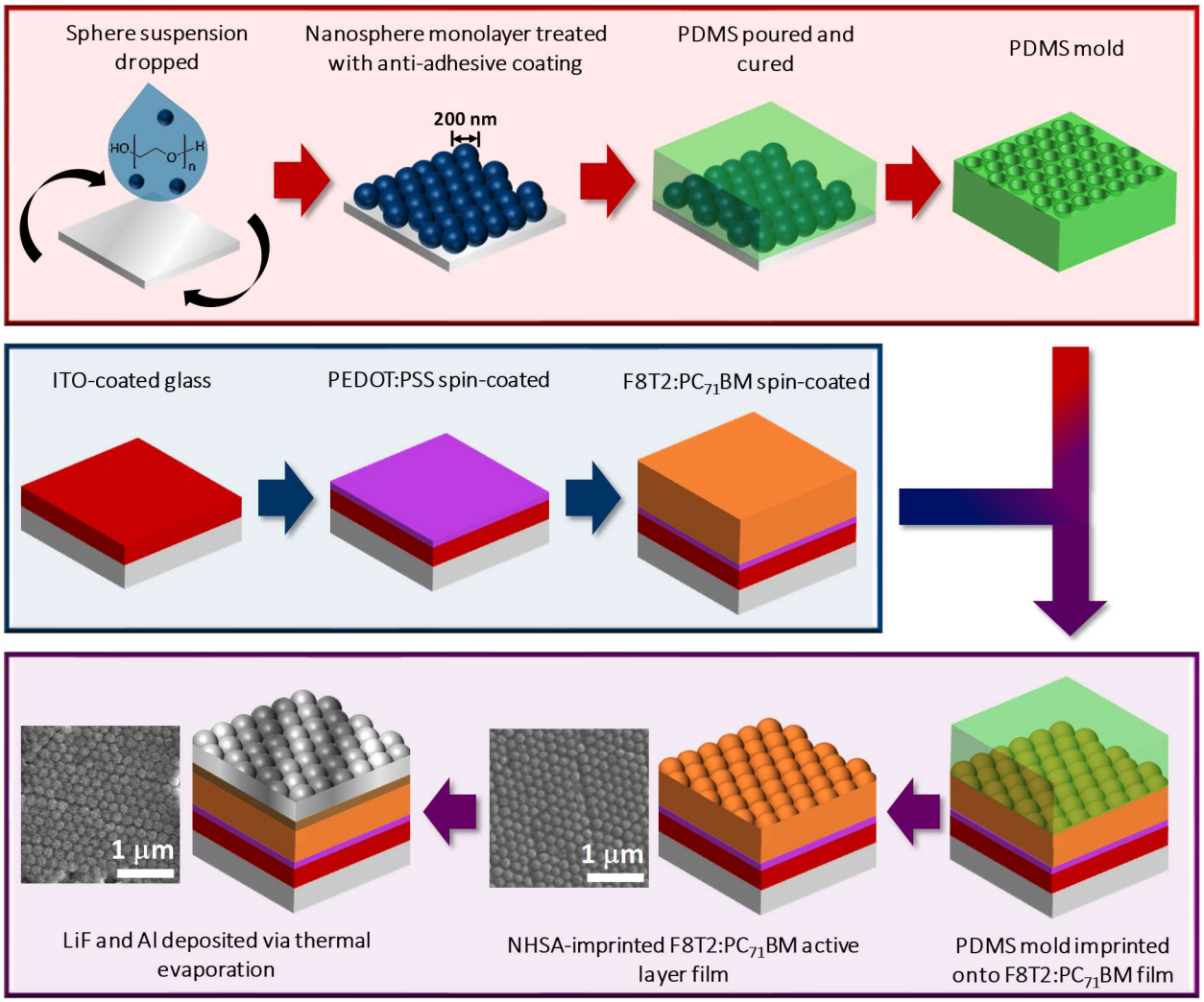

Figure 5-7. Schematic of the procedure for making NHSA PDMS molds, imprinting into the top surface of active layers, and transferring to LiF and Al top electrodes. The SEM images of the NHSA-top active layer and the NHSA-top Al electrode are included in the bottom panel.

Many previous works have realized pattern transfer to the top surface of the active layer by applying temperature and pressure during imprinting.[74, 156, 157] Because the active layer in this work was composed of a 100:4 weight ratio blend of the soft polymer F8T2 and organic molecule $PC_{71}BM$, the film could be imprinted by wetting the PDMS mold with the same solvent used for dissolving the active layer components and placing the mold on the film without applying pressure or any additional temperature beyond the annealing temperature. The NHSA, consisting of hexagonally arranged 200 nm diameter nanohemispheres, was successfully incorporated into the

top surface of the active layer and transferred to the thermally deposited LiF electron transport layer and top Al electrode, as shown in the SEM images included in Fig. 5-7.

Since active layer film thickness is known to impact device performance,[30, 33, 51, 52, 123] the NHSA- and flat-top active layers with target thicknesses of 125, 230, 380 and 470 nm were fabricated and the thickness of NHSA- and flat-top films were measured by profilometry and compared. The device structure and the active layer for 3D-FDTD simulations were built to match the experimental device structure and active layer thicknesses, and Fig. 5-8 illustrates how the NHSA-top active layer film thickness was measured and accounted for in 3D-FDTD simulations and includes all relevant film thickness data. The average NHSA-top film thickness was obtained by measuring the height difference between multiple hemispheres (marked by a yellow panel in Fig. 5-8a and yellow line in Fig. 5-8d) and the scratched bottom (marked as a yellow line to the left in Fig. 5-8a). The thickness corresponding to the top of hemispheres was measured from the hemisphere peaks to the scratched bottom (marked as blue lines in Fig. 5-8a). The thickness corresponding to the area between hemispheres was measured from the dips between hemispheres to the scratched bottom (marked as green lines in Fig. 5-8a). At least three different locations on each film were measured to calculate the film thicknesses reported in Fig. 5-8b. Notably, the measured average film thickness of the NHSA-top films is very similar to that of the flat-top films, as demonstrated in Fig. 5-8b. As shown in Fig. 5-8b, the average thicknesses of NHSA-top films are very close to the flat-top target film thicknesses, so film thickness will not be considered as contributing to any difference in performance between NHSA- and flat-top devices.

Figure 5-8c and d provide cross-sectional and top-view illustrations, respectively, to demonstrate how the experimental film thickness was used to build NHSA-top active layers in simulations. Generally, the thickness in the area between nanohemispheres was used to

build the planar portion of the active layer and then 200 nm diameter nanohemispheres were added on top. Fig. 5-8c shows a sample 3D-FDTD-simulated active layer that mimics the experimental NHSA-top active layer with a measured average thickness of 125 nm.

a)

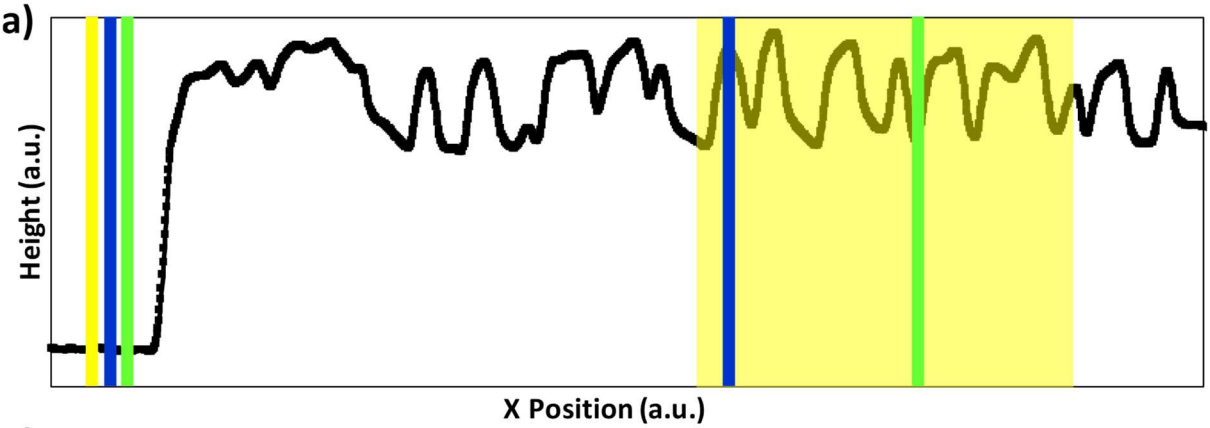

b)

Flat-top Films		NHSA-top Films				
Measured	Simulated	Measured (Average)	Measured (Top)	Simulated (Top)	Measured (Between)	Simulated (Between)
124.7 ± 1.4	125	127.1 ± 4.0	183.8 ± 6.0	200	98.9 ± 1.2	100
229.7 ± 7.2	230	244.0 ± 5.9	304.3 ± 5.2	305	207.5 ± 5.4	205
379.6 ± 3.9	380	380.2 ± 1.7	427.7 ± 6.6	455	323.7 ± 6.7	355
472.7 ± 15	470	476.2 ± 4.7	532.9 ± 10	545	437.6 ± 10.7	445

c)

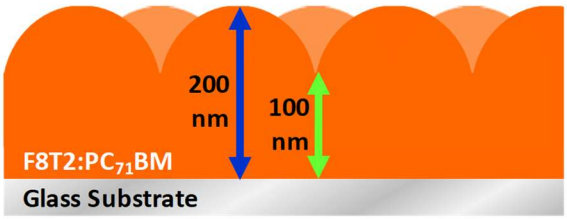

d)

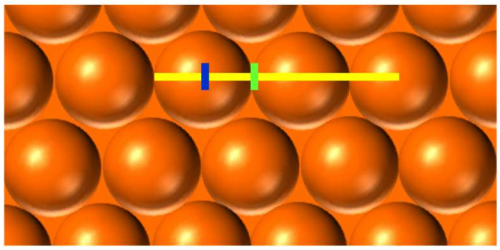

Figure 5-8. (a) Sample profilometry data for an NHSA-top film. (b) The thickness of NHSA- and flat-top films fabricated and simulated in this work. Thickness of each film was measured from at least three locations via profilometry. All values are reported in nm. (c-d) Schematic drawings of (c) cross-sectional and (d) top views of the NHSA. Film thicknesses, for a sample film with an average thickness of 125 nm, are marked in (c).

5.3.3 *Impact of NHSA-Tops on Device Performance*

NHSA- and flat-top devices, with an overall device structure of ITO/PEDOT:PSS/F8T2:$PC_{71}BM$ (100:4)/LiF/Al were fabricated with the four target active layer

thicknesses. Since the 3D-FDTD simulations show that the active layer absorbance and electric field behavior gradually change with increasing active layer thickness, we focused the evaluation on the thin (125 nm) and thick (470 nm) devices with both NHSA- and flat-tops, and the photoresponse data is provided in Fig. 5-9. Current density-voltage characteristics for thin and thick devices are provided in Fig. 5-9a and b, respectively, both in the dark and under monochromatic 330 nm illumination. For thin devices (Fig. 5-9a), the magnitude of the photocurrent density produced by NHSA- and flat-top devices are similar, but NHSA-top devices produce lower dark current density. As observed in Fig. 5-9b, the dark current density of thick devices is about one-two orders of magnitude lower than that of thin devices, because the series resistance and charge extraction difficulty increase with increasing active layer thickness.[1] Dark and photocurrent densities of thick NHSA-top devices are slightly higher than those of flat-top devices. For both thin and thick devices, incorporating the NHSA-top results in shifts in the voltages where the minimum dark and illuminated current are obtained, referred to as V_0 and open-circuit voltage (V_{OC}), respectively. For thin devices (Fig. 5-9a), NHSA- and flat-top devices exhibit V_{OC} values of 0.76 and 0.24, respectively, while the V_0 values are both close to 0 V, and for thick devices (Fig. 5-9b) NHSA- and flat-top devices exhibit V_0 values of -0.48 and -0.08, respectively, and similar V_{OC} values of 0.20 and 0.32 V, respectively. These shifts may be indicative of an additional built-in bias related to the electric field enhancements provided by plasmonic NHSA-tops. It is also hypothesized that these shifts could be related to changes in the microstructure and morphology at the top interface of the active layer, because the V_{OC} in organic photodiodes is known to depend on the active layer materials and morphology, interfacial layers, and the nature of the electrode contacts.[158-161]

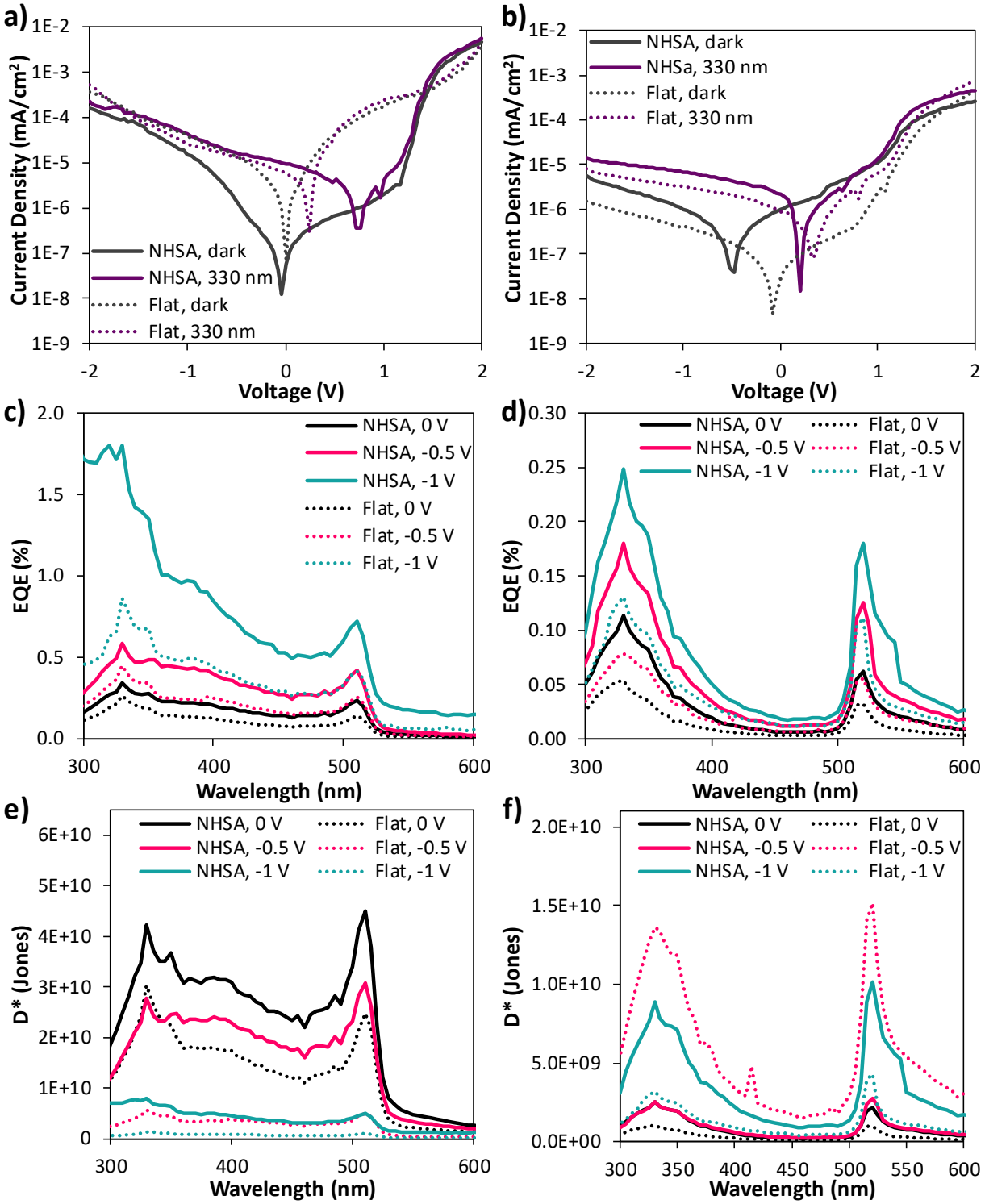

Figure 5-9. (a-b) Current density-voltage characteristics, (c-d) EQE spectra, (e-f) D* spectra for thin (a, c, e) thin and (b, d, f) thick devices.

External quantum efficiency (EQE) spectra of thin and thick devices are shown in Fig. 5-9c and d, respectively, and represents the ratio of charge carriers produced by a device to photons

incident on the device, thereby indicating the photoresponse strength. The spectra in Fig. 5-9c and d exhibit a consistent spectral shape with peaks around 330 and 515 nm, corresponding to the edges of the active layer absorption peak (Fig. 5-4). Light at these wavelengths is absorbed weakly, enabling it to penetrate the active layer and be absorbed at the top of the device. Since $PC_{71}BM$ clusters are known to be more concentrated at the top of the active layer, light absorbed in this physical region can most effectively engage the reverse-bias photoresponse mechanism.[51] For thick devices, a pronounced dip corresponding to the active layer absorbance peak, between about 400-500 nm, is observed in the EQE spectra in Fig. 5-9d. Light within this spectral region is absorbed quickly and therefore has a low penetration depth, precluding it from reaching the top of the active layer and contributing significantly to photoresponse as previously observed.[30, 51] This agrees with the 3D-FDTD-simulated electric field distributions shown in Fig. 5-6, which demonstrate that the electric field in the spectral range between about 400-500 nm is strong at the bottom of the active layer and decays quickly with depth into the active layer.

For both NHSA- and flat-top devices, EQE increases with increasing reverse bias. Regardless of the active layer thickness and the bias applied, NHSA-top devices produce higher EQE values than flat-top devices, indicating that the nanostructures achieve the desired performance enhancement. Under a -1 V bias and 330 nm illumination, thin NHSA- and flat-top devices produce peak EQE values of 1.8 and 0.86%, and thick NHSA- and flat-top devices produce EQE values of 0.25 and 0.13%, respectively. The photoresponse strength is diminished for thicker devices due to the increased difficulty of charge extraction from thicker active layers.[1] It should be noted that the significant increase in EQE values produced by the thin NHSA-top device under a -1 V bias and illumination with increasingly short wavelengths is an indication that the device is approaching unstable behavior, because the lamp power in this spectral region (Fig. 3-1) is very

weak. The spectrum levels off at a reasonable value, so this data is still reliable, but this is considered the reverse-bias limit of device stability for the thin device. Devices with the same structure but thicker active layers were previously shown to be stable under reverse biases as strong as -40 V,[51] so it is anticipated that the thick devices in this work would maintain stable behavior under strong reverse biases. However, increasing the reverse bias was found to diminish the NHSA-top impact because the strong applied bias overwhelmed the plasmonic enhancements to the internal electric field. Therefore, in the interest of maintaining stable behavior for all evaluated devices and examining the impact of NHSA-tops, our discussion focuses on device behavior under small applied reverse biases.

Specific detectivity (D*), which accounts for the noise within devices and therefore provides an indication of photoresponse sensitivity, is provided for thin and thick devices in Fig. 5-9e and f, respectively. Noise currents for thin and thick devices with NHSA- and flat-tops were obtained by performing a Fast Fourier Transform on measured dark current over time and are reported in Table 5-2. As shown in Fig. 5-9e, thin NHSA-top devices exhibit consistently higher D* values than flat-top devices, achieving peak D* values of 4.2×10^{10} and 3.0×10^{10} Jones, respectively, under 0 V bias and 330 nm illumination, which are competitive with those reported for other organic UV photodetectors.[162-164] In this case, the maximum D* value is obtained without any applied bias because the noise current is minimized in this condition. For thick devices, NHSA-top devices exhibit a higher D* values than flat-top devices under 0 and -1 V biased, with peak D* values of 8.9×10^{9} and 3.2×10^{9} Jones, respectively, under -1 V bias and 330 nm illumination. However, NHSA-top devices exhibit lower D* values than flat-top devices under -0.5 V bias due to a higher noise current (Table 5-2). Thick flat-top devices achieve the maximum D* value of 1.4×10^{10} Jones under -0.5 V bias and 330 nm illumination.

Table 5-2. Dark and noise currents of thin and thick NHSA- and flat-top devices under varied applied biases.

Device	Bias (V)	Dark current (A)	FFT noise (A/√Hz)
Thin, Flat	-1	-1.7×10^{-10}	3.1×10^{-11}
	-0.5	-3.3×10^{-11}	3.7×10^{-12}
	0	-1.5×10^{-11}	4.1×10^{-13}
Thin, NHSA	-1	-1.6×10^{-9}	1.1×10^{-11}
	-0.5	-5.8×10^{-11}	9.9×10^{-13}
	0	-2.6×10^{-11}	3.8×10^{-13}
Thick, Flat	-1	4.7×10^{-12}	1.9×10^{-12}
	-0.5	4.1×10^{-12}	2.7×10^{-13}
	0	4.4×10^{-12}	2.4×10^{-12}
Thick, NHSA	-1	4.4×10^{-11}	1.3×10^{-12}
	-0.5	4.4×10^{-11}	3.4×10^{-12}
	0	4.9×10^{-11}	2.1×10^{-12}

EQE spectra for NHSA- and flat-top devices with intermediate active layers are shown in Fig. 5-10. Devices with a 230 nm active layer are represented in Fig. 5-10a-b. Without any applied bias, NHSA-top devices exhibit slightly stronger photoresponse compared to flat-top devices, producing EQE values of 0.19 and 0.16%, respectively, under 330 nm illumination, but when a reverse bias is applied the NHSA enhancement diminishes and disappears. Under -0.5 V, NHSA- and flat-top devices produce similar photoresponse, with peak EQE values of 0.34 and 0.40%, respectively, under 350 and 330 nm illumination, respectively, and under -1 V bias NHSA-top devices produce inferior photoresponse throughout the entire spectral range. It should be noted that the photoresponse of flat-top devices is unstable, as is indicated by the dramatic increase in EQE values exhibited under incident illumination with increasingly short wavelengths, which is shown more clearly in Fig. 5-10b. The optical intensity of the incident light is very weak in the spectral range between about 250-360 nm, and unlike the spectrum for the NHSA-top thin device in Fig. 5-9c, the spectrum in Fig. 5-10b does not level off but continues to increase dramatically in this spectral range for increasingly short wavelengths, indicating unreliable device behavior.

This instability has been previously observed in similar devices, and is thought to occur through a mechanism similar to avalanche breakdown.[51]

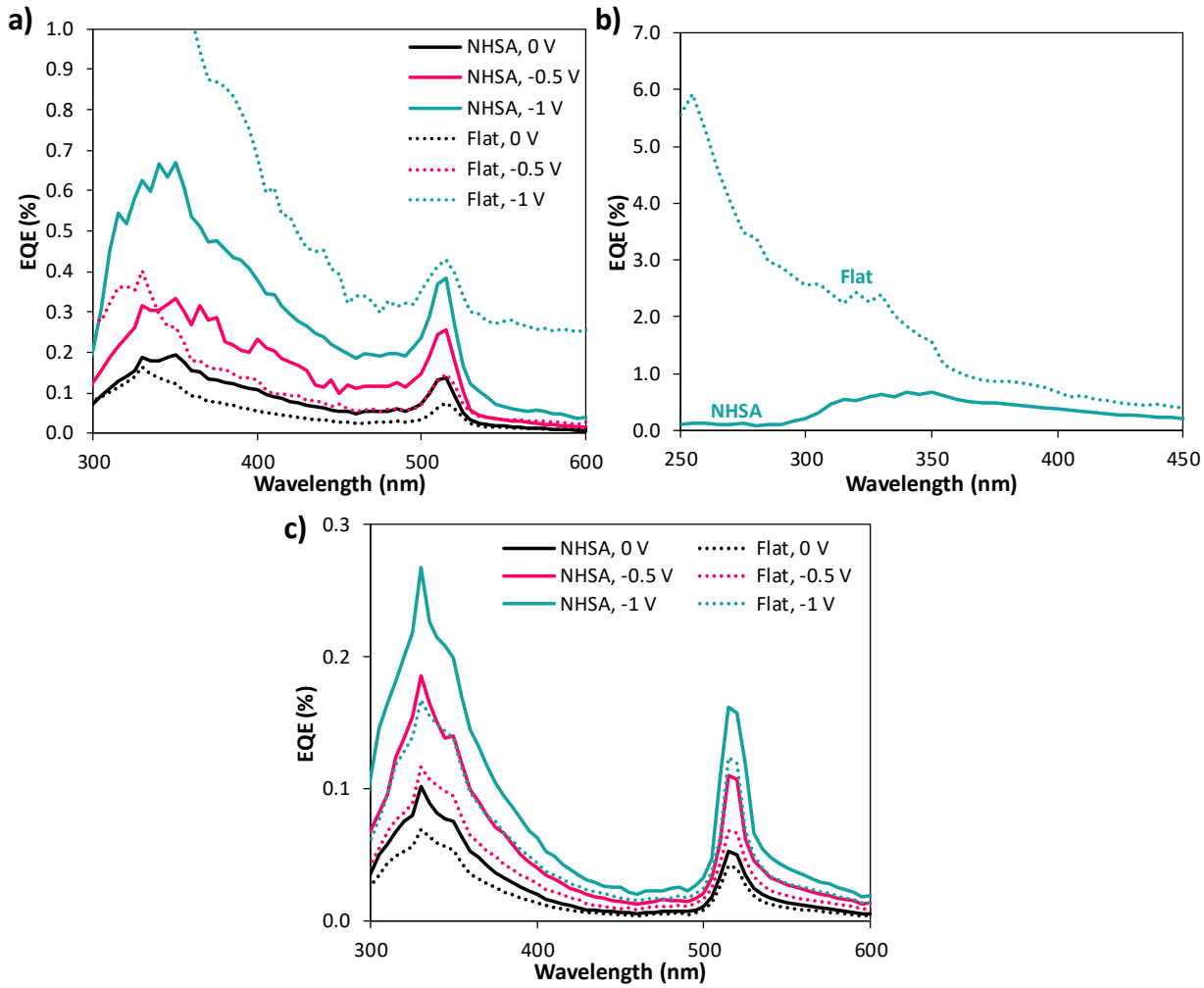

Figure 5-10. EQE spectra for NHSA- and flat-top devices with active layer thicknesses of (a-b) 230 nm and (c) 380 nm. Spectra for devices with 230 nm active layer are shown for an extended range of short wavelength illumination to demonstrate the relative instability of this data.

EQE Spectra for devices with active layer thicknesses of 380 nm are provided in Fig. 5-10d. For these devices, with and without an applied reverse bias, NHSA-top devices produce higher EQE values than flat-top devices, achieving peak EQE values of 0.27 and 0.17%, respectively, under -1 V bias and 330 nm illumination.

The on-off response speed of thin and thick devices with NHSA- and flat-tops were collected under 0 and -0.5 V bias and 330 nm illumination and are shown in Fig. 5-11 along with calculated

rise and fall times for each device and testing condition. As shown in Fig. 5-11a, without any applied bias, thin NHSA-top devices respond faster than flat-top devices, with rise (fall) times of 0.34 s (0.54 s) and 0.36 s (0.77 s), respectively. The rise times are similar in magnitude, while the fall time is significantly shorter for the NHSA-top device than the flat-top device. The faster photoresponse might be attributed to the plasmonic enhancements to the electric field (Figs. 5-5a and 5-6a), which acts as a small built-in bias. Increasing the bias applied to a device improves its response speed, due to faster charge carrier transport and decreased capacitance.[1] In fact, when a -0.5 V bias is applied (Fig. 5-11b), the overall response speed increases and NHSA- and flat-top devices exhibit rise (fall) times of 0.31 s (0.44 s) and 0.23 s (0.28 s), respectively.

For thick devices, the plasmonic enhancement to the response speed is not clearly observed. Without any applied bias, shown in Fig. 5-11c, NHSA- and flat-top devices exhibit similar rises times of 0.35 and 0.30 s, respectively, while the NHSA-top device fall time of 0.52 s is slower than the 0.34 s fall time of the flat-top device. When the bias is increased to -0.5 V (Fig. 5-11d), the response speed is very similar for both NHSA- and flat-top devices, which exhibit rise (fall) times of 0.33 s (0.46 s) and 0.30 s (0.41 s), respectively. It is hypothesized that the similarity of the response speeds for thick NHSA- and flat-top devices is related to the internal electric field distributions, which were relatively similar for thick NHSA- and flat-top devices (Figs. 5-5d and 5-6d), so the response speed of NHSA-top devices does not benefit from this plasmonic effect.

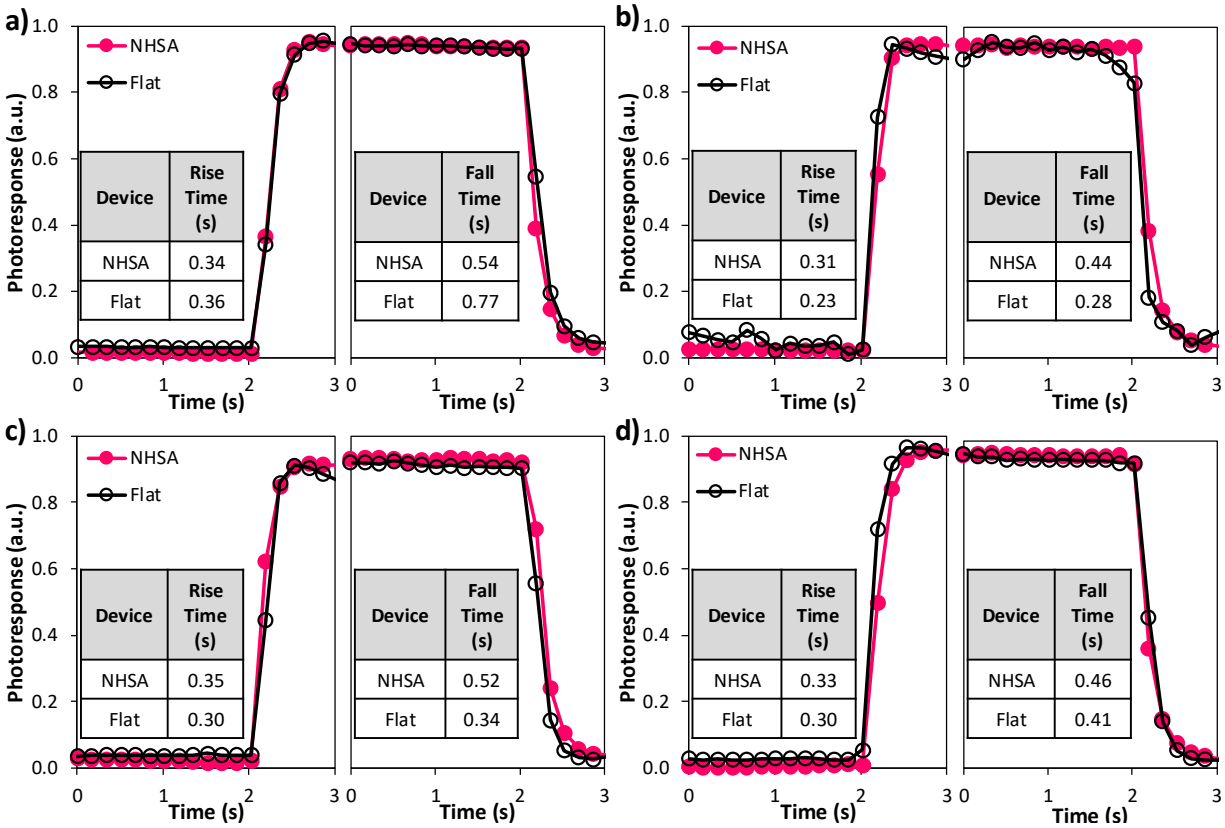

Figure 5-11. On-off response speed for (a,b) thin and (c,d) thick devices with both NHSA- and flat- tops. The response speed was measured under 330 nm illumination and (a,c) 0 V bias and (b,d) -0.5 V bias. The calculated rise and fall times are included as an inset in each plot.

The performance enhancement that the NHSA-tops provide can be attributed to two main factors. The first is angular light reflection that occurs when light that penetrates the active layer reflects off the NHSA nanostructured active layer/LiF/Al electrode interface at the top of the devices. Instead of reflecting straight back, as it does in flat-top devices, light is reflected at an angle, increasing its path length within the active layer and thereby improving light absorption within the active layer, as is demonstrated for the 3D-FDTD-simulated thin NHSA-top devices compared to the flat-top devices in Fig. 5-3a. The second performance-enhancing effect of the NHSA-tops is provided through SPPs that occur at the nanostructured active layer/LiF/Al electrode interface. These localized surface plasmon resonances confine and enhance the local electric field in the nanohemispheric region of the active layer, as demonstrated in Figs. 5-5 and

5-6. The enhanced electric field acts as a small, additional built-in bias, which improves both the photoresponse strength and sensitivity (Figs. 5-9 and 5-10) and the response speed (Fig. 5-11).

5.4 CONCLUSION

Nanohemisphere arrays were incorporated into organic UV photodetectors by imprinting into the top surface of the active layer, and the pattern was then transferred to the LiF electron transport layer and top Al electrode. 3D-FDTD simulation results showed that NHSA-top devices with thin active layers exhibit a clear UV absorbance enhancement and strong confined electric fields in the nanohemispheric region of the active layer upon NHSA incorporation, in comparison to flat-top control devices. The impact of NHSA-tops on the absorbance and electric field in device active layers diminishes with increasing active layer thickness. NHSA molds were fabricated by nanosphere lithography and imprinted into device active layers, and devices with varied active layer thicknesses were fabricated and evaluated. Thin NHSA-top devices demonstrated superior performance compared to flat-top devices, producing peak D* values of 4.2×10^{10} and 3.0×10^{10} Jones, respectively, under 0 V bias and 330 nm illumination, and faster on-off response speed. This work demonstrated that imprinting an NHSA into the top surface of the active layer is an effective method for incorporating plasmonic nanostructures into the top electrodes of organic ultraviolet photodetectors for improved photoresponse. This method can also be applied to incorporate plasmonic nanostructures into other optoelectronic devices to enhance device performance.

Chapter 6. CONCLUSIONS AND OUTLOOK

6.1 CONCLUSIONS

The research presented here has focused on developing and improving the performance of organic ultraviolet photodetectors by optimizing the active layer materials, morphology and thickness to extend established photoresponse mechanisms into the UV spectral range and by incorporating plasmonic nanostructures for optical and electronic performance enhancements. The overarching goal of the work has been to improve the photoresponse strength, selectivity, and tunability while maintaining stable, controllable, predictable device behavior. The conclusions and insights obtained contribute to the ever-expanding field of photodetection, expediting the design process and improving the performance and applicability of photodetectors that employ novel and emerging technologies.

Photodetection is an essential component of modern technology, with applications in consumer products, communications, imaging, scientific research, environmental monitoring, industrial process control, missile detection, and many other fields. The technology has advanced alongside other optoelectronic devices, such as solar cells, LEDs, and lasers. One such advancement was the utilization of organic active materials, which offer flexibility and solution processability, and are more cost-effective and tunable compared to inorganic materials. In photodetection, new technologies are often introduced in the visible-infrared spectral region and are slow to extend to ultraviolet devices, despite the applicability of photodetectors with UV-selective response in fields including imaging, flame and missile detection, environmental monitoring, and scientific research.

The first portion of my work therefore focused on optimizing the active layers of conventional organic photodiode photodetectors to extend the established photoresponse mechanisms of

photomultiplication and charge collection narrowing into the UV spectral region. These mechanisms were first reported in devices with strong visible and infrared detection but had not yet been applied in UV photodetectors. We started with active layers composed of the polymer electron donor poly(9,9-dioctylfluorene-alt-bithiophene) (F8T2) and the fullerene-derivative electron acceptor [6,6]-phenyl-C_{71}-butyric acid methyl ester ($PC_{71}BM$). F8T2 was chosen because of its wide bandgap, yielding strong UV absorption and ensuring UV-selective photoresponse in the resulting device. F8T2 and $PC_{71}BM$ were blended in 100:1 and 100:4 weight ratios, so that the $PC_{71}BM$ formed isolated clusters within the F8T2 layer. During the photomultiplication process, photogenerated excitons are separated at the F8T2-$PC_{71}BM$ interface, and the electrons transfer into $PC_{71}BM$ and become trapped. The accumulation of trapped charges bends the active layer energy bands and enables charges to be injected from the cathode, transported through the active layer, and collected at the anode. In this way, multiple charge carriers can be collected per incident photon and external quantum efficiency EQE values over 100% can be achieved.

In this case, because of the active layer morphology and thickness, the photoresponse spectra exhibited two peaks at either edge of the active layer absorption peak with a dip in between. These photodetectors therefore produced one UV-selective response peak and one that was not UV-selective. Typically, photodetectors are operated under an applied reverse bias to minimize noise and improve photoresponse sensitivity. Increasing the reverse bias increases the strength and speed of the photoresponse produced, but in these devices an additional benefit was observed. We found that the UV-selective response peak was more sensitive to the applied bias than the non-UV-selective peak, so increasing the applied reverse bias improved the UV-selectivity in addition to improving response strength and speed.

We next explored an organic-inorganic hybrid active layer utilizing the polymer donor poly[bis(4-phenyl)(2,4,6-trimethylphenyl)amine] (PTAA), which also has strong, UV-selective absorption, with embedded ZnO nanoparticles acting as electron acceptors and traps. Because PTAA has superior hole mobility to F8T2 and ZnO has significant UV-selective absorption, while $PC_{71}BM$ does not, these devices produced overall stronger photoresponse compared to the F8T2:$PC_{71}BM$ system. With this PTAA:ZnO active layer, the charge collection narrowing (CCN) mechanism was investigated and successfully employed in UV-selective photodetection after being first established in visible-infrared detection. Charge collection narrowing utilizes the active layer thickness as a control handle for tuning photoresponse between broad- and narrowband. When the active layer is thin, all absorbed light contributes to the photoresponse, and broadband photomultiplication is achieved. When the thickness is increased, light within the active layer absorption peak is absorbed quickly and therefore cannot penetrate the entire active layer. It only generates excitons in the lower portion of the active layer, which produces a response-suppressing space charge region. Light at the short-wavelength edge of the absorption peak produces the same result due to its inherently low penetration depth. Only light at the long-wavelength edge of the absorption peak can penetrate the active layer. This light reflects off the top electrode and establishes an interference pattern within the layer that enables it to be absorbed and generate excitons throughout the layer, resulting in bulk exciton generation and a significant contribution to photoresponse.

Thus, increasing the active layer thickness effectively narrows the spectral photoresponse to a single peak at the long-wavelength edge of the active layer absorption peak. For the PTAA:ZnO system, this corresponded to about 420 nm, yielding UV-selective photoresponse that could be tuned between broad- and narrowband simply by changing the active layer thickness. This is a

relatively easy parameter to adjust during device fabrication, so this response-tuning mechanism of CCN could enable easy fabrication of multiple devices with distinct spectral photoresponse.

In addition to exploring different UV-selective active layer materials and optimizing them for strong, selective, tunable UV photodetection, we also incorporated plasmonic nanostructures into device electrodes. While this is a popular approach for improving optoelectronic device performance, there are relatively few instances of plasmonic enhancements utilized in UV-selective systems. Al was chosen as a plasmonic material because it is abundant, cost-effective, easily processable, and is well-suited to support surface plasmon polaritons (SPPs) that are excited under UV illumination. Two types of nanostructure incorporation were pursued, including an Al nanohole array (Al-NHA) used as a transparent conducting electrode and a nanohemisphere array (NHSA) imprinted into the top active layer/electrode interface. Both nanopatterns provided plasmonic enhancement to the local electric field intensity and subsequently device performance.

An Al-NHA was employed as a transparent conducting bottom electrode in conventional organic devices, using the F8T2:$PC_{71}BM$ active layer investigated in our early work. 3-dimensional finite-difference time-domain (3D-FDTD) electromagnetic simulations were used to evaluate the electric field intensity and active layer absorbance strength and UV-selectivity, and Al-NHAs were found to provide a significant enhancement to the electric field intensity in the lower portion of devices, compared to control devices based on ITO. The pattern geometry of the Al-NHAs was varied, within reasonable fabrication constraints, and the optimal pattern was found to be a hexagonal NHA with a hole diameter of 175 nm and a pitch (center-to-center distance) of 200 nm. These NHAs were fabricated by nanosphere lithography, where 200 nm diameter spheres were deposited by drop-coating and then exposed to plasma etch, Al deposition, and liftoff steps to produce Al-NHAs with a diameter, pitch, and thickness of 175, 200, and 30 nm, respectively.

Devices based on both Al-NHA and control ITO electrodes were then fabricated and evaluated, with device structures of [ITO or Al-NHA]/PEDOT:PSS/F8T2:$PC_{71}BM$/LiF/Al. Due to the relatively low transmittance of Al-NHAs, the photoresponse strength of the Al-NHA-based devices was lower than ITO-based device under the typical reverse bias testing conditions. The spectral behavior, however, was unaffected by the Al-NHA and matched that observed in our early work. Notably, Al-NHA-based devices benefitted from low dark and noise currents, enabling them to produce similar specific detectivity (D*) values to ITO-based devices despite having weaker photoresponse. The most notable feature of the Al-NHA-based devices was observed under forward bias. While ITO-based devices produced increasingly unstable two-peak spectra under forward bias, the electrode symmetry of Al-NHA-based devices unlocked a distinct photoresponse spectra under forward bias containing a single peak that corresponds to the active layer absorbance peak. This spectral behavior results from hole diffusion, which is aided by applied forward bias. Al-NHA-based devices exhibited this behavior more strongly and clearly than devices based on planar Al electrodes, indicating that the NHAs support a plasmonic enhancement to the local electric field that acts as an additional forward bias, increasing the driving force for hole diffusion and enabling a bias-dependent photoresponse tunability. This yields a device that, depending on the operating conditions, could be used in multiple photodetection applications.

Nanosphere lithography was also used to incorporate NHSAs into the top electrode of ITO-based devices with the same conventional organic photodiode structure. In this case, the nanosphere monolayer was used to produce a PDMS mold that was then imprinted into the top surface of the active layer, producing a hexagonal array of 200 nm diameter hemispheres. The impacts of these NHSA-tops were evaluated through 3D-FDTD simulations and were found to enhance both the UV absorbance of the active layer and the electric field intensity at the top active

layer interface in simulated devices. The enhanced electric field intensity acts as an additional reverse bias, improving both the strength and speed of the resultant photoresponse. In addition to this plasmonic enhancement, incorporating NHSAs also improved the photoresponse strength through optical light scattering, where light is reflected off the top device interface at an angle and therefore follows an extended path through the active layer, improving its absorption. Two distinct arrays of plasmonic nanostructures have thus been successfully incorporated into organic ultraviolet photodetectors, yielding improvements to the photoresponse strength, speed, and tunability while maintaining good UV-selectivity due to the selection of both the active layer material and the plasmonic metal Al.

6.2 OUTLOOK

My work has played a significant role in extending both established photoresponse mechanisms, such as photomultiplication and charge collection narrowing, and emerging plasmonic enhancements, through Al-NHA and NHSA incorporation, into the UV spectral range of photodetection. This contributes to the advancement of photodetector research, which continually reaches toward new technologies and applications, such as fully flexible, stretchable, conformable devices, low-driving voltages, increasingly strong, sensitive, and fast photoresponse, and devices utilizing double-sided illumination. In general, photodetectors have a wide variety of applications, which complicates the device design process. For some applications, such as communications, response speed is the most important performance criterion. For applications like imaging and color spectroscopy, wavelength-selectivity is the highest priority. For other applications, such as environmental monitoring and missile detection, device sensitivity and specificity are the most critical features.

This variety in applications and performance criteria makes designing photodetectors a complex and difficult problem, as it is nearly impossible to optimize a device without a specific application in mind. Therefore, it is critical that the field have a strong "toolbox" at hand to expedite the design and optimization process. The tools would include the material selection, device architecture, and controllable physical parameters of the device structure and operation, including layer thicknesses and morphology, operating voltage, etc. For this toolbox to be useful, each tool must be well understood. The individual impact on device performance, relevant underlying device physics and response mechanisms, reasonable working ranges, processability, and competitive and/or constructive interactions with other device parameters must be thoroughly investigated and understood. The response mechanisms that these tools engage, such as photomultiplication, CCN, electric field enhancements, and light scattering, and the observable device performance that they produce, must be equally well understood. When this is accomplished, the perfect photodetector for any selected application can be designed and produced quickly, easily, and cost-effectively.

My work has focused on improving our understanding of these relationships between physical parameters, device working mechanisms, and device performance, particularly within the UV spectral range. Active layer material, morphology, and thickness each impact the working mechanisms that devices can engage and the photoresponse that is produced, and the extent to which each parameter can influence the photoresponse depends on the other parameters. The material determines whether UV-selective response is possible, while the morphology and thickness together determine whether response mechanisms like photomultiplication and CCN can be achieved. All three parameters, together, ultimately determine what mechanisms will be utilized and what the resulting photoresponse strength and spectral selectivity will be. Plasmonic

nanostructures are another physical parameter that we can control and utilize to unlock new photoresponse behavior, such as bias-dependent response switching, in addition to enhancing existing working mechanisms within devices through light scattering and electric field improvements. The extent to which these effects are felt, however, depends on the active layer thickness and morphology, the device structure, and the applied bias. Additionally, other aspects of device architecture, including electrode materials and interfacial layers, must be selected with a full understanding of their impact on photoresponse mechanisms and device stability.

Photodetection is an essential component in modern technology, and while the field has advanced along with the general field of optoelectronics, the efficient design of these devices depends on a constantly expanding knowledge of the relationship between material properties, physical parameters, working mechanisms, and device performance. The wide variety of technologies and photodetection solutions available within the field, and our thorough understanding of how they can be engaged and utilized, mean that we will continuously improve our ability to meet the ever growing and changing photodetection needs of modern technology.

REFERENCES

1. Kasap, S. O., *Principles of Electronic Materials and Devices*. McGraw-Hill: New York, NY, 2006.

2. Bhattacharya, P., *Semiconductor Optoelectronic Devices*. Prentice Hall: 1996.

3. Will photonics replace electronics? https://electrosome.com/will-photonics-replace-electronics/.

4. Blaen, P. J.; Khamis, K.; Lloyd, C. E. M.; Bradley, C.; Hannah, D.; Krause, S., Real-time monitoring of nutrients and dissolved organic matter in rivers: Capturing event dynamics, technological opportunities and future directions. *Science of the Total Environment* **2016,** *569*, 647-660.

5. Environics RanidPRO200 Product Page. https://www.environics.fi/us/product-gallery/ranidvision-products/.

6. Exactly what's so great about night vision binoculars? http://bestnightvisionbinocular.blogspot.com/2015/01/exactly-whats-so-great-about-night.html.

7. Schurman, K. CMOS Image Sensor. https://www.lifewire.com/cmos-image-sensor-493271.

8. Hsiao, C. C.; Peng, C. Y.; Liu, T. S., An optical lever approach to photodetector measurements of the pickup-head flying height in an optical disk drive. *Measurement Science and Technology* **2006,** *17* (8), 2335-2342.

9. Laubach, R. T., PHOTODETECTOR SENSES MOTION IN NOISY SURROUNDINGS. *Electronics* **1972,** *45* (21), 101-&.

10. Razeghi, M.; Rogalski, A., Semiconductor ultraviolet detectors. *Journal of Applied Physics* **1996,** *79* (10), 7433-7473.

11. Kedadra, A.; Traiche, M., Photomultiplier and avalanche photodiode detection performance for LiDAR application to environment studies. *Journal of Applied Remote Sensing* **2014,** *8*, 15.

12. Gurin, N. T.; Novikov, S. G.; Korneev, I. V.; Shtan'ko, A. A.; Rodionov, V. A., Position-sensitive photodetector for rotation-angle transducers. *Technical Physics Letters* **2011,** *37* (3), 271-273.

13. Research, N. P. Organic Photovoltaic Solar Cells. https://www.nrel.gov/pv/organic-photovoltaic-solar-cells.html.

14. Baeg, K. J.; Binda, M.; Natali, D.; Caironi, M.; Noh, Y. Y., Organic Light Detectors: Photodiodes and Phototransistors. *Advanced Materials* **2013,** *25* (31), 4267-4295.

15. Soehnge, H.; Ouhtit, A.; Ananthaswamy, O. N., Mechanisms of induction of skin cancer by UV radiation. *Frontiers in Bioscience* **1997,** *2*, d538-51.

16. Gorokhov, E. V.; Magunov, A. N.; Feshchenko, V. S.; Altukhov, A. A., Solar-blind UV flame detector based on natural diamond. *Instruments and Experimental Techniques* **2008,** *51* (2), 280-283.

17. Land, H. B. Arc Flash Detection System. US20080094612 A1, April 24, 2008.

18. Moses, W. W.; Choong, W. S.; Hull, G.; Payne, S.; Cherepy, N.; Valentine, J. D., Photodetectors for scintillator proportionality measurement. *Nuclear Instruments & Methods in Physics Research Section A-Accelerators Spectrometers Detectors and Associated Equipment* **2009,** *610* (1), 45-49.

19. Dennis, P. N. J., *Photodetectors: An Introduction to Current Technology*. Plenum Press: New York, NY, 1986.

20. BenMoussa, A.; Soltani, A.; Schuhle, U.; Haenen, K.; Chong, Y. M.; Zhang, W. J.; Dahal, R.; Lin, J. Y.; Jiang, H. X.; Barkad, H. A.; BenMoussa, B.; Bolsee, D.; Hermans, C.; Kroth, U.; Laubis, C.; Mortet, V.; De Jaeger, J. C.; Giordanengo, B.; Richter, M.; Scholze, F.; Hochedez, J. F., Recent developments of wide-bandgap semiconductor based UV sensors. *Diamond and Related Materials* **2009,** *18* (5-8), 860-864.

21. Chen, Q.; Khan, M. A.; Sun, C. J.; Yang, J. W., Visible-blind ultraviolet photodetectors based on GaN p-n junctions. *Electronics Letters* **1995,** *31* (20), 1781-1782.

22. Liu, Y.; Gorla, C. R.; Liang, S.; Emanetoglu, N.; Lu, Y.; Shen, H.; Wraback, M., Ultraviolet detectors based on epitaxial ZnO films grown by MOCVD. *Journal of Electronic Materials* **2000,** *29* (1), 69-74.

23. Zhu, H.; Shan, C. X.; Yao, B.; Li, B. H.; Zhang, J. Y.; Zhao, D. X.; Shen, D. Z.; Fan, X. W., High Spectrum Selectivity Ultraviolet Photodetector Fabricated from an n-ZnO/p-GaN Heterojunction. *Journal of Physical Chemistry C* **2008,** *112* (51), 20546-20548.

24. Yu, J.; Shan, C. X.; Huang, X. M.; Zhang, X. W.; Wang, S. P.; Shen, D. Z., ZnO-based ultraviolet avalanche photodetectors. *Journal of Physics D-Applied Physics* **2013,** *46* (30), 5.

25. Yu, J.; Shan, C. X.; Qiao, Q.; Xie, X. H.; Wang, S. P.; Zhang, Z. Z.; Shen, D. Z., Enhanced Responsivity of Photodetectors Realized via Impact Ionization. *Sensors* **2012,** *12* (2), 1280-1287.

26. Knoll, G. F., *Radiation Detection and Measurement*. John Wiley & Sons, Inc: Hoboken, NJ, 2000.

27. Sariciftci, N. S.; Smilowitz, L.; Heeger, A. J.; Wudl, F., Photoinduced electron-transfer from a conducting polymer to buckminsterfullerene. *Science* **1992,** *258* (5087), 1474-1476.

28. Yu, G.; Gao, J.; Hummelen, J. C.; Wudl, F.; Heeger, A. J., Polymer photovoltaic cells - enhanced efficiencies via a network of internal donor-acceptor heterojunctions. *Science* **1995,** *270* (5243), 1789-1791.

29. Schilinsky, P.; Waldauf, C.; Brabec, C. J., Recombination and loss analysis in polythiophene based bulk heterojunction photodetectors. *Applied Physics Letters* **2002,** *81* (20), 3885-3887.

30. Li, L. L.; Zhang, F. J.; Wang, J.; An, Q. S.; Sun, Q. Q.; Wang, W. B.; Zhang, J.; Teng, F., Achieving EQE of 16,700% in P3HT: PC71BM based photodetectors by trap-assisted photomultiplication. *Scientific Reports* **2015,** *5*, 7.

31. Li, L. L.; Zhang, F. J.; Wang, W. B.; An, Q. S.; Wang, J.; Sun, Q. Q.; Zhang, M., Trap-Assisted Photomultiplication Polymer Photodetectors Obtaining an External Quantum Efficiency of 37500%. *ACS Applied Materials & Interfaces* **2015,** *7* (10), 5890-5897.

32. Guo, F. W.; Yang, B.; Yuan, Y. B.; Xiao, Z. G.; Dong, Q. F.; Bi, Y.; Huang, J. S., A nanocomposite ultraviolet photodetector based on interfacial trap-controlled charge injection. *Nature Nanotechnology* **2012,** *7* (12), 798-802.

33. Armin, A.; Jansen-van Vuuren, R. D.; Kopidakis, N.; Burn, P. L.; Meredith, P., Narrowband light detection via internal quantum efficiency manipulation of organic photodiodes. *Nature Communications* **2015,** *6*, 8.

34. Xu, X. B.; Chueh, C. C.; Jing, P. F.; Yang, Z. B.; Shi, X. L.; Zhao, T.; Lin, L. Y.; Jen, A. K. Y., High-Performance Near-IR Photodetector Using Low-Bandgap MA(0.5)FA(0.5)Pb(0.5)Sn(0.5)I(3) Perovskite. *Advanced Functional Materials* **2017,** *27* (28), 6.

35. Fang, Y.; Armin, A.; Meredith, P.; Huang, J., Accurate characterization of next-generation thin-film photodetectors. *Nature Photonics* **2019,** *13*, 1-4.

36. Li, L. L.; Zhang, F. J.; Wang, W. B.; Fang, Y. J.; Huang, J. S., Revealing the working mechanism of polymer photodetectors with ultra-high external quantum efficiency. *Physical Chemistry Chemical Physics* **2015,** *17* (45), 30712-30720.

37. Kielar, M.; Dhez, O.; Pecastaings, G.; Curutchet, A.; Hirsch, L., Long-Term Stable Organic Photodetectors with Ultra Low Dark Currents for High Detectivity Applications. *Scientific Reports* **2016,** *6*, 11.

38. Wang, X.; Zhou, D. L.; Wang, H. Y.; Jin, H.; Yu, J. S., Solution-processed, fullerene-free organic ultraviolet photodetectors using thermally activated delayed fluorescence materials as electron acceptor. *Journal of Physics D-Applied Physics* **2019,** *52* (2), 7.

39. Wang, X.; Huang, J.; Li, J.; Yu, J. S., Effect of organic electron blocking layers on the performance of organic photodetectors with high ultraviolet detectivity. *Journal of Physics D-Applied Physics* **2016,** *49* (7), 7.

40. Zhu, L.; Dai, Q.; Hu, Z. F.; Zhang, X. Q.; Wang, Y. S., Organic Deep Ultraviolet Photodetector With Response Peak Focusing on 270 nm Using the Acceptor BAlq. *IEEE Photonics Technology Letters* **2011,** *23* (23), 1835-1837.

41. Shao, D. L.; Yu, M. P.; Sun, H. T.; Xin, G. Q.; Lian, J.; Sawyer, S., High-Performance Ultraviolet Photodetector Based on Organic-Inorganic Hybrid Structure. *ACS Applied Materials & Interfaces* **2014,** *6* (16), 14690-14694.

42. Guo, D. Y.; Shan, C. X.; Qu, S. N.; Shen, D. Z., Highly Sensitive Ultraviolet Photodetectors Fabricated from ZnO Quantum Dots/Carbon Nanodots Hybrid Films. *Scientific Reports* **2014,** *4*, 6.

43. Chen, C. H.; Lee, C. T., High Detectivity Mechanism of ZnO-Based Nanorod Ultraviolet Photodetectors. *IEEE Photonics Technology Letters* **2013,** *25* (4), 348-351.

44. Edmunds Optics. Silicon Detectors.

45. Wan, X.; Xu, Y.; Guo, H. W.; Shehzad, K.; Ali, A.; Liu, Y.; Yang, J. Y.; Dai, D. X.; Lin, C. T.; Liu, L. W.; Cheng, H. C.; Wang, F. Q.; Wang, X. M.; Lu, H.; Hu, W. D.; Pi, X. D.; Dan, Y. P.; Luo, J. K.; Hasan, T.; Duan, X. F.; Li, X. M.; Xu, J. B.; Yang, D. R.; Ren, T. L.; Yu, B., A self-powered high-performance graphene/silicon ultraviolet photodetector with ultra-shallow junction: breaking the limit of silicon? *Npj 2D Materials and Applications* **2017,** *1*, 8.

46. Pan, S. S.; Liu, Q. W.; Zhao, J. G.; Li, G. H., Ultrahigh Detectivity and Wide Dynamic Range Ultraviolet Photodetectors Based on BixSn1-xO2 Intermediate Band. Semiconductor. *ACS Applied Materials & Interfaces* **2017,** *9* (34), 28737-28742.

47. Liu, L.; Yang, C.; Patane, A.; Yu, Z. G.; Yan, F. G.; Wang, K. Y.; Lu, H. X.; Li, J. M.; Zhao, L. X., High-detectivity ultraviolet photodetectors based on laterally mesoporous GaN. *Nanoscale* **2017,** *9* (24), 8142-8148.

48. Suzuki, A.; Suzuki, H.; Maruhashi, H.; Banya, S.; Akiyama, T.; Oku, T., Effect of annealing on photovoltaic properties and microstructure of conventional and inverted organic solar cells using active bilayer based on liquid-crystal semiconducting polymer and fullerene. *International Journal of Energy Research* **2014,** *38* (12), 1541-1550.

49. Kinder, L.; Kanicki, J.; Petroff, P., Structural ordering and enhanced carrier mobility in organic polymer thin film transistors. *Synthetic Metals* **2004,** *146* (2), 181-185.

50. Yasuda, T.; Yonezawa, K.; Ito, M.; Kamioka, H.; Han, L.; Moritomo, Y., Photovoltaic Properties and Charge Dynamics in Nanophase-Separated F8T2/PCBM Blend Films. *Journal of Photopolymer Science and Technology* **2012,** *25* (3), 271-276.

51. Esopi, M. R.; Calcagno, M.; Yu, Q. M., Organic Ultraviolet Photodetectors Exhibiting Photomultiplication, Low Dark Current, and High Stability. *Advanced Materials Technologies* **2017,** *2* (8), 9.

52. Esopi, M. R.; Zheng, E. J.; Zhang, X. Y.; Cai, C.; Yu, Q. M., Tuning the spectral response of ultraviolet organic-inorganic hybrid photodetectors via charge trapping and charge collection narrowing. *Physical Chemistry Chemical Physics* **2018,** *20* (16), 11273-11284.

53. Shen, L.; Fang, Y. J.; Wei, H. T.; Yuan, Y. B.; Huang, J. S., A Highly Sensitive Narrowband Nanocomposite Photodetector with Gain. *Advanced Materials* **2016,** *28* (10), 2043.

54. Lin, Q. Q.; Armin, A.; Burn, P. L.; Meredith, P., Filterless narrowband visible photodetectors. *Nature Photonics* **2015,** *9* (10), 687.

55. Ding, G.; Deng, J.; Zhou, L.; Gan, Q.; Hwang, J. C. M.; Dierolf, V.; Bartoli, F. J.; Mazuir, C.; Schoenfeld, W. V., Al nanogrid electrode for ultraviolet detectors. *Optics Letters* **2011,** *36* (18), 3663-3665.

56. Yokogawa, S.; Burgos, S. P.; Atwater, H. A., Plasmonic Color Filters for CMOS Image Sensor Applications. *Nano Letters* **2012,** *12* (8), 4349-4354.

57. Schuller, J. A.; Barnard, E. S.; Cai, W. S.; Jun, Y. C.; White, J. S.; Brongersma, M. L., Plasmonics for extreme light concentration and manipulation. *Nature Materials* **2010,** *9* (3), 193-204.

58. Brongersma, M. L., Plasmonic Photodetectors, Photovoltaics, and Hot-Electron Devices. *Proceedings of the IEEE* **2016,** *104* (12), 2349-2361.

59. Arredondo, B.; de Dios, C.; Vergaz, R.; Criado, A. R.; Romero, B.; Zimmermann, B.; Wurfel, U., Performance of ITO-free inverted organic bulk heterojunction photodetectors: Comparison with standard device architecture. *Organic Electronics* **2013,** *14* (10), 2484-2490.

60. Barnes, W. L.; Dereux, A.; Ebbesen, T. W., Surface plasmon subwavelength optics. *Nature* **2003,** *424* (6950), 824-830.

61. Atwater, H. A.; Polman, A., Plasmonics for improved photovoltaic devices. *Nature Materials* **2010,** *9* (3), 205-213.

62. Genet, C.; Ebbesen, T. W., Light in tiny holes. *Nature* **2007,** *445* (7123), 39-46.

63. Salomon, L.; Grillot, F.; Zayats, A. V.; de Fornel, F., Near-field distribution of optical transmission of periodic subwavelength holes in a metal film. *Physical Review Letters* **2001,** *86* (6), 1110-1113.

64. Zhang, J. X.; Zhang, L. D.; Xu, W., Surface plasmon polaritons: physics and applications. *Journal of Physics D-Applied Physics* **2012,** *45* (11), 19.

65. Berini, P., Surface plasmon photodetectors and their applications. *Laser & Photonics Reviews* **2014,** *8* (2), 197-220.

66. Chang, S. H.; Gray, S. K.; Schatz, G. C., Surface plasmon generation and light transmission by isolated nanoholes and arrays of nanoholes in thin metal films. *Optics Express* **2005,** *13* (8), 3150-3165.

67. Wang, H.; Lim, J. W.; Mota, F. M.; Jang, Y. J.; Yoon, M.; Kim, H.; Hu, W.; Noh, Y. Y.; Kim, D. H., Plasmon-mediated wavelength-selective enhanced photoresponse in polymer photodetectors. *Journal of Materials Chemistry C* **2017,** *5* (2), 399-407.

68. Liang, Z. Q.; Sun, J.; Jiang, Y. Y.; Jiang, L.; Chen, X. D., Plasmonic Enhanced Optoelectronic Devices. *Plasmonics* **2014,** *9* (4), 859-866.

69. Richardson, B. J.; Zhu, L.; Yu, Q. M., Design and development of plasmonic nanostructured electrodes for ITO-free organic photovoltaic cells on rigid and highly flexible substrates. *Nanotechnology* **2017,** *28*.

70. Kim, Y.; Bicanic, K.; Tan, H. R.; Ouellette, O.; Sutherland, B. R.; de Arguer, F. P. G.; Jo, J. W.; Liu, M. X.; Sun, B.; Liu, M.; Hoogland, S.; Sargent, E. H., Nanoimprint-Transfer-Patterned Solids Enhance Light Absorption in Colloidal Quantum Dot Solar Cells. *Nano Letters* **2017,** *17* (4), 2349-2353.

71. Liu, Y.; Lang, F.; Dittrich, T.; Steigert, A.; Fischer, C. H.; Kohler, T.; Plate, P.; Rappich, J.; Lux-Steiner, M. C.; Schmid, M., Enhancement of photocurrent in an ultra-thin perovskite solar cell by Ag nanoparticles deposited at low temperature. *RSC Advances* **2017,** *7* (3), 1206-1214.

72. Lan, W. X.; Wang, Y. W.; Singh, J.; Zhu, F. R., Omnidirectional and Broadband Light Absorption Enhancement in 2-D Photonic-Structured Organic Solar Cells. *ACS Photonics* **2018,** *5* (3), 1144-1150.

73. Du, Q. G.; Ren, H. J.; Wu, L.; Bai, P.; Png, C. E.; Sun, X. W.; Kam, C. H.; de Sterke, C. M., Light absorption mechanism in organic solar cells with hexagonal lattice nanohole aluminum transparent electrodes. *Journal of Optics* **2015,** *17* (8), 5.

74. Wang, H. L.; Haroldson, R.; Balachandran, B.; Zakhidov, A.; Sohal, S.; Chan, J. Y.; Hu, W., Nanoimprinted Perovskite Nanograting Photodetector with Improved Efficiency. *ACS Nano* **2016,** *10* (12), 10921-10928.

75. Du, B. W.; Yang, W. Q.; Jiang, Q.; Shan, H. Y.; Luo, D. Y.; Li, B. W.; Tang, W. C.; Lin, F.; Shen, B.; Gong, Q. H.; Zhu, X.; Zhu, R.; Fang, Z. Y., Plasmonic-Functionalized Broadband Perovskite Photodetector. *Advanced Optical Materials* **2018,** *6* (8), 8.

76. Luo, X.; Du, L. L.; Wen, Z. W.; Lv, W. L.; Zhao, F. Y.; Jiang, X. Y.; Peng, Y. Q.; Sun, L.; Li, Y.; Rao, J. W., Remarkably enhanced red-NIR broad spectral absorption via gold

nanoparticles: applications for organic photosensitive diodes. *Nanoscale* **2015,** *7* (34), 14422-14433.

77. Hou, J. L.; Fischer, A.; Yang, S. C.; Benduhn, J.; Widmer, J.; Kasemann, D.; Vandewal, K.; Leo, K., Plasmon-Induced Sub-Bandgap Photodetection with Organic Schottky Diodes. *Advanced Functional Materials* **2016,** *26* (31), 5741-5747.

78. Lee, Y. H.; Lee, T. K.; Kim, H.; Song, I.; Lee, J.; Kang, S.; Ko, H.; Kwak, S. K.; Oh, J. H., A Flexible High-Performance Photoimaging Device Based on Bioinspired Hierarchical Multiple-Patterned Plasmonic Nanostructures. *Small* **2018,** *14* (13), 9.

79. Zheng, B. Y.; Wang, Y. M.; Nordlander, P.; Halas, N. J., Color-Selective and CMOS-Compatible Photodetection Based on Aluminum Plasmonics. *Advanced Materials* **2014,** *26* (36), 6318-6323.

80. Knight, M. W.; King, N. S.; Liu, L. F.; Everitt, H. O.; Nordlander, P.; Halas, N. J., Aluminum for Plasmonics. *ACS Nano* **2014,** *8* (1), 834-840.

81. Taguchi, A.; Saito, Y.; Watanabe, K.; Yijian, S.; Kawata, S., Tailoring plasmon resonances in the deep-ultraviolet by size-tunable fabrication of aluminum nanostructures. *Applied Physics Letters* **2012,** *101* (8), 4.

82. Boltasseva, A.; Atwater, H. A., Low-Loss Plasmonic Metamaterials. *Science* **2011,** *331* (6015), 290-291.

83. Zhu, A. Y.; Kuznetsov, A. I.; Luk'yanchuk, B.; Engheta, N.; Genevet, P., Traditional and emerging materials for optical metasurfaces. *Nanophotonics* **2017,** *6* (2), 452-471.

84. Gerard, D.; Gray, S. K., Aluminium plasmonics. *Journal of Physics D-Applied Physics* **2015,** *48* (18), 14.

85. Gong, T.; Munday, J. N., Aluminum-based hot carrier plasmonics. *Applied Physics Letters* **2017,** *110* (2), 5.

86. Katsume, T.; Hiramoto, M.; Yokoyama, M., Photocurrent multiplication in naphthalene tetracarboxylic anhydride film at room temperature. *Applied Physics Letters* **1996,** *69* (24), 3722-3724.

87. Hiramoto, M.; Imahigashi, T.; Yokoyama, M., Photocurrent multiplication in organic pigment films. *Applied Physics Letters* **1994,** *64* (2), 187-189.

88. Wang, W. B.; Zhang, F. J.; Bai, H. T.; Li, L. L.; Gao, M. L.; Zhanga, M.; Zhan, X. W., Photomultiplication photodetectors with P3HT: fullerene-free material as the active layers exhibiting a broad response. *Nanoscale* **2016,** *8* (10), 5578-5586.

89. Gong, X. O.; Tong, M. H.; Park, S. H.; Liu, M.; Jen, A.; Heeger, A. J., Semiconducting Polymer Photodetectors with Electron and Hole Blocking Layers: High Detectivity in the Near-Infrared. *Sensors* **2010,** *10* (7), 6488-6496.

90. Zhou, X. K.; Yang, D. Z.; Ma, D. G., Extremely Low Dark Current, High Responsivity, All-Polymer Photodetectors with Spectral Response from 300 nm to 1000 nm. *Advanced Optical Materials* **2015,** *3* (11), 1570-1576.

91. Skompska, M., Hybrid conjugated polymer/semiconductor photovoltaic cells. *Synthetic Metals* **2010,** *160* (1-2), 1-15.

92. Hamasaki, T.; Morimune, T.; Kajii, H.; Minakata, S.; Tsuruoka, R.; Nagamachi, T.; Ohmori, Y., Fabrication and characteristics of polyfluorene based organic photodetectors using fullerene derivatives. *Thin Solid Films* **2009,** *518* (2), 548-550.

93. Burkhard, G. F.; Hoke, E. T.; McGehee, M. D., Accounting for Interference, Scattering, and Electrode Absorption to Make Accurate Internal Quantum Efficiency Measurements in Organic and Other Thin Solar Cells. *Advanced Materials* **2010,** *22* (30), 3293.

94. Burkhard, G. F.; Hoke, E. T., *Transfer Matrix Optical Modeling*. McGehee Group: Stanford Univ., 2011.

95. Lumerical, Inc. FDTD Solutions. https://www.lumerical.com/tcad-products/fdtd/.

96. Lumerical, Inc. Material Database (Optical). https://kb.lumerical.com/en/materials_material_database_optical.html.

97. Malitson, I. H., INTERSPECIMEN COMPARISON OF REFRACTIVE INDEX OF FUSED SILICA. *Journal of the Optical Society of America* **1965,** *55* (10P1), 1205-&.

98. RefractiveIndex.INFO Optical constants of Fused silica (fused quartz). https://refractiveindex.info/?shelf=glass&book=fused_silica&page=Malitson.

99. Verilhac, J. M., Recent developments of solution-processed organic photodetectors. *European Physical Journal-Applied Physics* **2013,** *63* (1), 7.

100. Michaelson, H. B., WORK FUNCTION OF ELEMENTS AND ITS PERIODICITY. *Journal of Applied Physics* **1977,** *48* (11), 4729-4733.

101. Kim, H.; Shin, M.; Kim, Y., Influence of thermal annealing on the deformation of a lithium fluoride nanolayer in polymer : fullerene solar cells. *EPL* **2008,** *84* (5), 5.

102. Saracco, E.; Bouthinon, B.; Verilhac, J. M.; Celle, C.; Chevalier, N.; Mariolle, D.; Dhez, O.; Simonato, J. P., Work Function Tuning for High-Performance Solution-Processed Organic Photodetectors with Inverted Structure. *Advanced Materials* **2013,** *25* (45), 6534-6538.

103. Street, R. A., Electronic Structure and Properties of Organic Bulk-Heterojunction Interfaces. *Advanced Materials* **2016,** *28* (20), 3814-3830.

104. Richardson, B. J.; Zhu, L. Z.; Yu, Q. M., Inverted hybrid solar cells based on pyrite FeS2 nanocrystals in P3HT: PCBM with enhanced photocurrent and air-stability. *Solar Energy Materials and Solar Cells* **2013,** *116*, 252-261.

105. Hau, S. K.; Yip, H. L.; Baek, N. S.; Zou, J. Y.; O'Malley, K.; Jen, A. K. Y., Air-stable inverted flexible polymer solar cells using zinc oxide nanoparticles as an electron selective layer. *Applied Physics Letters* **2008,** *92* (25), 3.

106. Richardson, B. J.; Wang, X. Z.; Almutairi, A.; Yu, Q. M., High efficiency PTB7-based inverted organic photovoltaics on nano-ridged and planar zinc oxide electron transport layers. *Journal of Materials Chemistry A* **2015,** *3* (10), 5563-5571.

107. Hu, X. W.; Wang, K.; Liu, C.; Meng, T. Y.; Dong, Y.; Liu, S. J.; Huang, F.; Gong, X.; Cao, Y., High-detectivity inverted near-infrared polymer photodetectors using cross-linkable conjugated polyfluorene as an electron extraction layer. *Journal of Materials Chemistry C* **2014,** *2* (45), 9592-9598.

108. Kim, S.; Lee, J.; Dao, V. A.; Lee, S.; Balaji, N.; Ahn, S.; Hussain, S. Q.; Han, S.; Jung, J.; Jang, J.; Lee, Y.; Yi, J., Effects of LiF/Al back electrode on the amorphous/crystalline silicon heterojunction solar cells. *Materials Science and Engineering B-Advanced Functional Solid-State Materials* **2013,** *178* (9), 660-664.

109. Schlaf, R.; Parkinson, B. A.; Lee, P. A.; Nebesny, K. W.; Jabbour, G.; Kippelen, B.; Peyghambarian, N.; Armstrong, N. R., Photoemission spectroscopy of LiF coated Al and Pt electrodes. *Journal of Applied Physics* **1998,** *84* (12), 6729-6736.

110. Gong, X.; Tong, M. H.; Xia, Y. J.; Cai, W. Z.; Moon, J. S.; Cao, Y.; Yu, G.; Shieh, C. L.; Nilsson, B.; Heeger, A. J., High-Detectivity Polymer Photodetectors with Spectral Response from 300 nm to 1450 nm. *Science* **2009,** *325* (5948), 1665-1667.

111. Konstantatos, G.; Sargent, E. H., Nanostructured materials for photon detection. *Nature Nanotechnology* **2010,** *5* (6), 391-400.

112. Greenham, N. C.; Peng, X. G.; Alivisatos, A. P., Charge separation and transport in conjugated-polymer/semiconductor-nanocrystal composites studied by photoluminescence quenching and photoconductivity. *Physical Review B* **1996,** *54* (24), 17628-17637.

113. Rauch, T.; Boberl, M.; Tedde, S. F.; Furst, J.; Kovalenko, M. V.; Hesser, G. N.; Lemmer, U.; Heiss, W.; Hayden, O., Near-infrared imaging with quantum-dot-sensitized organic photodiodes. *Nature Photonics* **2009,** *3* (6), 332-336.

114. Li, W. H.; Guo, H.; Wang, Z.; Dong, G. F., Narrowband Organic Photodiodes Based on Green Light Sensitive Squarylium. *Journal of Physical Chemistry C* **2017,** *121* (28), 15333-15338.

115. Chen, H. Y.; Lo, M. K. F.; Yang, G. W.; Monbouquette, H. G.; Yang, Y., Nanoparticle-assisted high photoconductive gain in composites of polymer and fullerene. *Nature Nanotechnology* **2008,** *3* (9), 543-547.

116. Pacholski, C.; Kornowski, A.; Weller, H., Self-assembly of ZnO: From nanodots, to nanorods. *Angewandte Chemie-International Edition* **2002,** *41* (7), 1188-+.

117. Parker, I. D., Carrier tunneling and device characteristics in polymer light-emitting-diodes. *Journal of Applied Physics* **1994,** *75* (3), 1656-1666.

118. Saunders, B. R.; Turner, M. L., Nanoparticle-polymer photovoltaic cells. *Advances in Colloid and Interface Science* **2008,** *138* (1), 1-23.

119. Xu, Y.; Schoonen, M. A. A., The absolute energy positions of conduction and valence bands of selected semiconducting minerals. *American Mineralogist* **2000,** *85* (3-4), 543-556.

120. Djurisic, A. B.; Ng, A. M. C.; Chen, X. Y., ZnO nanostructures for optoelectronics: Material properties and device applications. *Progress in Quantum Electronics* **2010,** *34* (4), 191-259.

121. Habisreutinger, S. N.; Leijtens, T.; Eperon, G. E.; Stranks, S. D.; Nicholas, R. J.; Snaith, H. J., Carbon Nanotube/Polymer Composites as a Highly Stable Hole Collection Layer in Perovskite Solar Cells. *Nano Letters* **2014,** *14* (10), 5561-5568.

122. McCulloch, I.; Heeney, M., Polytriarylamine Semiconductors. Material Matters, 2009; Vol. 4.3.

123. Miao, J. L.; Zhang, F. J.; Du, M. D.; Wang, W. B.; Fang, Y., Photomultiplication type narrowband organic photodetectors working at forward and reverse bias. *Physical Chemistry Chemical Physics* **2017,** *19* (22), 14424-14430.

124. Wang, W. B.; Zhang, F. J.; Du, M. D.; Li, L. L.; Zhang, M.; Wang, K.; Wang, Y. S.; Hu, B.; Fang, Y.; Huang, J. S., Highly Narrowband Photomultiplication Type Organic Photodetectors. *Nano Letters* **2017,** *17* (3), 1995-2002.

125. Oba, F.; Choi, M.; Togo, A.; Tanaka, I., Point defects in ZnO: an approach from first principles. *Science and Technology of Advanced Materials* **2011,** *12* (3), 14.

126. Zheng, X. G.; Li, Q. S.; Hu, W.; Chen, D.; Zhang, N.; Shi, M. J.; Wang, J. J.; Zhang, L. C., Photoconductive properties of ZnO thin films grown by pulsed laser deposition. *Journal of Luminescence* **2007,** *122*, 198-201.

127. Li, H. G.; Wu, G.; Shi, M. M.; Yang, L. G.; Chen, H. Z.; Wang, M., ZnO/poly(9,9-dihexylfluorene) based inorganic/organic hybrid ultraviolet photodetector. *Applied Physics Letters* **2008,** *93* (15), 3.

128. Jin, Y. Z.; Wang, J. P.; Sun, B. Q.; Blakesley, J. C.; Greenham, N. C., Solution-processed ultraviolet photodetedtors based on colloidal ZnO nanoparticles. *Nano Letters* **2008,** *8* (6), 1649-1653.

129. Gogurla, N.; Sinha, A. K.; Santra, S.; Manna, S.; Ray, S. K., Multifunctional Au-ZnO Plasmonic Nanostructures for Enhanced UV Photodetector and Room Temperature NO Sensing Devices. *Scientific Reports* **2014,** *4*, 9.

130. Ebbesen, T. W.; Lezec, H. J.; Ghaemi, H. F.; Thio, T.; Wolff, P. A., Extraordinary optical transmission through sub-wavelength hole arrays. *Nature* **1998,** *391* (6668), 667-669.

131. Cheng, C. W.; Liao, Y. J.; Liu, C. Y.; Wu, B. H.; Raja, S. S.; Wang, C. Y.; Li, X. Q.; Shih, C. K.; Chen, L. J.; Gwo, S., Epitaxial Aluminum-on-Sapphire Films as a Plasmonic Material Platform for Ultraviolet and Full Visible Spectral Regions. *ACS Photonics* **2018,** *5* (7), 2624-2630.

132. Lumerical, Inc. Using the boundary conditions tab. https://kb.lumerical.com/en/ref_sim_obj_boundary_conditions_tab.html.

133. Li, H. H., Refractive index of alkali halides and its wavelength and temperature derivatives. Journal of Physical and Chemical Reference Data, 1976; Vol. 5.

134. RefractiveIndex.INFO Optical Constants of Lithium Fluoride (LiF). https://refractiveindex.info/?shelf=main&book=LiF&page=Li.

135. Galvan, D. D.; Spackova, B.; Slaby, J.; Sun, F.; Ho, Y. H.; Homola, J.; Yu, Q. M., Surface-Enhanced Raman Scattering on Gold Nanohole Arrays in Symmetrical Dielectric Environments Exhibiting Electric Field Extension. *Journal of Physical Chemistry C* **2016,** *120* (44), 25519-25529.

136. Wang, B. M.; Ruud, C. J.; Price, J. S.; Kim, H.; Giebink, N. C., Graded-Index Fluoropolymer Antireflection Coatings for Invisible Plastic Optics. *Nano Letters* **2019,** *19* (2), 787-792.

137. Xu, S. P.; Lei, Y., Template-Assisted Fabrication of Nanostructured Arrays for Sensing Applications. *ChemPlusChem* **2018,** *83* (8), 741-755.

138. Ho, C. C.; Chen, P. Y.; Lin, K. H.; Juan, W. T.; Lee, W. L., Fabrication of Monolayer of Polymer/Nanospheres Hybrid at a Water-Air Interface. *ACS Applied Materials & Interfaces* **2011,** *3* (2), 204-208.

139. Prevo, B. G.; Velev, O. D., Controlled, rapid deposition of structured coatings from micro- and nanoparticle suspensions. *Langmuir* **2004,** *20* (6), 2099-2107.

140. Choi, J. Y.; Alford, T. L.; Honsberg, C. B., Solvent-Controlled Spin-Coating Method for Large-Scale Area Deposition of Two-Dimensional Silica Nanosphere Assembled Layers. *Langmuir* **2014,** *30* (20), 5732-5738.

141. Liu, J.; Chen, C. Y.; Yang, G. S.; Chen, Y. S.; Yang, C. F., Effect of the Fabrication Parameters of the Nanosphere Lithography Method on the Properties of the Deposited Au-Ag Nanoparticle Arrays. *Materials* **2017,** *10* (4), 15.

142. Purwidyantri, A.; Chen, C. H.; Hwang, B. J.; Luo, J. D.; Chiou, C. C.; Tian, Y. C.; Lin, C. Y.; Cheng, C. H.; Lai, C. S., Spin-coated Au-nanohole arrays engineered by nanosphere lithography for a Staphylococcus aureus 16S rRNA electrochemical sensor. *Biosensors & Bioelectronics* **2016,** *77*, 1086-1094.

143. Mikac, L.; Ivanda, M.; Gotic, M.; Janicki, V.; Zorc, H.; Janci, T.; Vidacek, S., Surface-enhanced Raman spectroscopy substrate based on Ag-coated self-assembled polystyrene spheres. *Journal of Molecular Structure* **2017,** *1146*, 530-535.

144. He, Y. Z.; Larsen, G. K.; Ingram, W.; Zhao, Y. P., Tunable Three-Dimensional Helically Stacked Plasmonic Layers on Nanosphere Monolayers. *Nano Letters* **2014,** *14* (4), 1976-1981.

145. Ingram, W. M.; Han, C. Q.; Zhang, Q. J.; Zhao, Y. P., Optimization of Ag-Coated Polystyrene Nanosphere Substrates for Quantitative Surface-Enhanced Raman Spectroscopy Analysis. *Journal of Physical Chemistry C* **2015,** *119* (49), 27639-27648.

146. Weekes, S. M.; Ogrin, F. Y.; Murray, W. A.; Keatley, P. S., Macroscopic arrays of magnetic nanostructures from self-assembled nanosphere templates. *Langmuir* **2007,** *23* (3), 1057-1060.

147. Sirotkin, E.; Apweiler, J. D.; Ogrin, F. Y., Macroscopic Ordering of Polystyrene Carboxylate-Modified Nanospheres Self-Assembled at the Water-Air Interface. *Langmuir* **2010,** *26* (13), 10677-10683.

148. Stavroulakis, P. I.; Christou, N.; Bagnall, D., Improved deposition of large scale ordered nanosphere monolayers via liquid surface self-assembly. *Materials Science and Engineering B-Advanced Functional Solid-State Materials* **2009,** *165* (3), 186-189.

149. Chen, K.; Rajeeva, B. B.; Wu, Z. L.; Rukavina, M.; Dao, T. D.; Ishii, S.; Aono, M.; Nagao, T.; Zheng, Y. B., Moire Nanosphere Lithography. *ACS Nano* **2015,** *9* (6), 6031-6040.

150. Wu, Z. L.; Chen, K.; Menz, R.; Nagao, T.; Zheng, Y. B., Tunable multiband metasurfaces by moire nanosphere lithography. *Nanoscale* **2015,** *7* (48), 20391-20396.

151. Jang, D.; Kim, Y.; Kim, T. Y.; Koh, K.; Jeong, U.; Cho, J., Force-assembled triboelectric nanogenerator with high-humidity-resistant electricity generation using hierarchical surface morphology. *Nano Energy* **2016,** *20*, 283-293.

152. Park, C.; Lee, T.; Xia, Y. N.; Shin, T. J.; Myoung, J.; Jeong, U., Quick, Large-Area Assembly of a Single-Crystal Monolayer of Spherical Particles by Unidirectional Rubbing. *Advanced Materials* **2014,** *26* (27), 4633.

153. Chong, M. A. S.; Zheng, Y. B.; Gao, H.; Tan, L. K., Combinational template-assisted fabrication of hierarchically ordered nanowire arrays on substrates for device applications. *Applied Physics Letters* **2006,** *89* (23), 3.

154. Wu, Z. L.; Li, W.; Yogeesh, M. N.; Jung, S. Y.; Lee, A. L.; McNicholas, K.; Briggs, A.; Bank, S. R.; Belkin, M. A.; Akinwande, D.; Zheng, Y. B., Tunable Graphene Metasurfaces with Gradient Features by Self-Assembly-Based Moire Nanosphere Lithography. *Advanced Optical Materials* **2016,** *4* (12), 2035-2043.

155. Cheng, F.; Fang, G. J.; Fan, X.; Huang, H. H.; Zheng, Q.; Qin, P. L.; Lei, H. W.; Li, Y. F., Enhancing the performance of P3HT:ICBA based polymer solar cells using LiF as electron collecting buffer layer and UV-ozone treated MoO3 as hole collecting buffer layer. *Solar Energy Materials and Solar Cells* **2013,** *110*, 63-68.

156. Pourdavoud, N.; Wang, S.; Mayer, A.; Hu, T.; Chen, Y. W.; Marianovich, A.; Kowalsky, W.; Heiderhoff, R.; Scheer, H. C.; Riedl, T., Photonic Nanostructures Patterned by Thermal Nanoimprint Directly into Organo- Metal Halide Perovskites. *Advanced Materials* **2017,** *29* (12), 7.

157. Wei, J.; Xu, R. P.; Li, Y. Q.; Li, C.; Chen, J. D.; Zhao, X. D.; Xie, Z. Z.; Lee, C. S.; Zhang, W. J.; Tang, J. X., Enhanced Light Harvesting in Perovskite Solar Cells by a Bioinspired Nanostructured Back Electrode. *Advanced Energy Materials* **2017,** *7* (20), 7.

158. Mihailetchi, V. D.; Koster, L. J. A.; Blom, P. W. M., Effect of metal electrodes on the performance of polymer : fullerene bulk heterojunction solar cells. *Applied Physics Letters* **2004,** *85* (6), 970-972.

159. Gadisa, A.; Svensson, M.; Andersson, M. R.; Inganas, O., Correlation between oxidation potential and open-circuit voltage of composite solar cells based on blends of polythiophenes/fullerene derivative. *Applied Physics Letters* **2004,** *84* (9), 1609-1611.

160. He, Z. C.; Zhong, C. M.; Huang, X.; Wong, W. Y.; Wu, H. B.; Chen, L. W.; Su, S. J.; Cao, Y., Simultaneous Enhancement of Open-Circuit Voltage, Short-Circuit Current Density, and Fill Factor in Polymer Solar Cells. *Advanced Materials* **2011,** *23* (40), 4636.

161. Vandewal, K.; Tvingstedt, K.; Gadisa, A.; Inganas, O.; Manca, J. V., On the origin of the open-circuit voltage of polymer-fullerene solar cells. *Nature Materials* **2009,** *8* (11), 904-909.

162. Qi, J.; Qiao, W. Q.; Zhou, X. K.; Yang, D. Z.; Zhang, J. D.; Ma, D. G.; Wang, Z. Y., High-Detectivity All-Polymer Photodetectors with Spectral Response from 300 to 1100 nm. *Macromolecular Chemistry and Physics* **2016,** *217* (15), 1683-1689.

163. Yang, D. Z.; Zhou, X. K.; Wang, Y. P.; Vadim, A.; Alshehri, S. M.; Ahamad, T.; Ma, D. G., Deep ultraviolet-to-NIR broad spectral response organic photodetectors with large gain. *Journal of Materials Chemistry C* **2016,** *4* (11), 2160-2164.

164. Wang, X.; Wang, H. Y.; Zhou, D. L.; Jin, H.; Yu, J. S., Semitransparent indium-tin-oxide-free non-fullerene organic photodetectors with double-side ultraviolet selective responses. *Materials Letters* **2018,** *230*, 289-292.

VITA

Monica Esopi is originally from Dallas, Pennsylvania and received her B.S. in Chemical Engineering from Penn State in May 2014. She began graduate work at the University of Washington in September 2014, joining the Yu Research Group and received her Master of Science in Chemical Engineering at the University of Washington in Seattle, WA in 2017. She is expected to receive her Doctor of Philosophy in Chemical Engineering at the University of Washington in Seattle, WA in 2019.

Publications from Graduate Studies:

1. **Esopi, M.R.**; Zheng, E.J.; Yu, Q.M., Narrowband Ultraviolet Photodetectors based on Photodiode. *To be submitted as an invited review to Journal of Materials Chemistry C.*
2. **Esopi, M.R.**; Yu, Q.M., Incorporating Aluminum Plasmonic Nanohemisphere Arrays into Organic Ultraviolet Photodetectors for Improved Photoresponse. *Submitted to ACS Nano.*
3. **Esopi, M.R.**; Yu, Q.M., Plasmonic Aluminum Nanohole Arrays as Transparent Conducting Electrodes for Organic Ultraviolet Photodetectors with Bias-Dependent Photoresponse. *ACS Applied Nano Materials.* DOI: 10.1021/acsanm.9b00902.
4. **Esopi, M.R.**; Zheng, E.J.; Zhang, X.Y.; Cai, C.; Yu, Q.M., Tuning the spectral response of ultraviolet organic–inorganic hybrid photodetectors via charge trapping and charge collection narrowing. *Physical Chemistry Chemical Physics*. 2018, 20, 11273 – 11284.
5. **Esopi, M.R.**; Calcagno, M.; Yu, Q.M., Organic Ultraviolet Photodetectors Exhibiting Photomultiplication, Low Dark Current, and High Stability. *Advanced Materials Technologies* 2017, 2 (8), 9.

6. Zhang, X.Y.; Zheng, E.J.; **Esopi, M.R.**; Cai, C.; Yu, Q.M., Flexible Narrowband Ultraviolet Photodetectors with Photomultiplication Based on Wide Band Gap Conjugate Polymer and Inorganic Nanoparticles. *ACS Applied Materials & Interfaces.* 2018, 10 (28), 24064.
7. Zheng, E.J.; Zhang, X.Y.; Zhou, B.Y.; **Esopi, M.R.**; Cai, C.; Lin, Y.-Y.; Yu, Q.M., Narrowband Ultraviolet Photodetectors Based on Nanocomposite Thin Films with High Gain and Low Driving Voltage. *ACS Applied Materials & Interfaces.* 2018, 10 (48), 41552.

Oral Presentations from Graduate Studies:

1. "Nanostructured Al Electrode for Plasmonic Enhancement of Organic Ultraviolet Photodetectors with High Gain", oral presentation, MRS Fall Meeting, Boston, MA, November 29th, 2017.
2. "Impact of Device Architecture and Active Layer Morphology on Organic Ultraviolet Photodetector Performance", oral presentation, MRS Fall Meeting, Boston, MA, November 29th, 2017.
3. "Investigation of the microstructures of F8T2:PC71BM blends and their effects on bulk heterojunction ultraviolet photodetectors", oral presentation, SPIE Photonics West, San Francisco, CA, February 15th, 2016.
4. "3D-FDTD simulations for the design and optimization of nanostructures and the resulting plasmonic enhancement in organic ultraviolet photodetector performance", oral presentation, SPIE Photonics West, San Francisco, CA, February 18th, 2016.

Publications from Undergraduate Studies:

1. Akhade, S.A.; Bernstein, N.J.; **Esopi, M.R.**; Regula, M.J.; Janik, M.J., A simple method to approximate electrode potential-dependent activation energies using density functional theory. *Catalysis Today.* 2017. 288, 63-73.
2. Nie, X.; **Esopi, M.R.**; Janik, M.J.; Asthagiri, A., Selectivity of CO2 reduction on copper electrodes:the role of the kinetics of elementary steps. *Angewandte Chemie Int. Ed.* 2013. 52, 2459–2462.
3. Yeh, K.Y.; Restaino, N.A.; **Esopi, M.R.**; Maranas, J.K.; Janik, M.J., The adsorption of bisulfate and sulfate anions over a Pt(1 1 1) electrode: A first principle study of adsorption configurations, vibrational frequencies and linear sweep voltammogram simulations. *Catalysis Today.* 2013. 202, 20–35.

Oral Presentations from Undergraduate Studies:

1. "Electrode potential dependent activation barriers approximated with density functional theory", oral presentation at the National AIChE Conference, San Francisco, CA, November 7th, 2013.